O-GlcNAc Regulation of Mitochondrial Function and Energy Metabolism

Ee Phie Tan
B.Sc., University of Iowa, 2011

Submitted to the graduate degree program in Biochemistry and Molecular Biology and the Graduate Faculty of the University of Kansas in partial fulfillment of the requirements for the degree of Doctor of Philosophy.

Co-Chairperson: Russell Swerdlow, M.D.

Co-Chairperson: Chad Slawson, Ph.D.

Gerald Carlson, Ph.D.

Antonio Artigues, Ph.D.

Hao Zhu, Ph.D.

Date Defended: 18 April 2017

The dissertation committee for Ee Phie Tan certifies that this is the approved version of the following dissertation:

O-GlcNAc Regulation of Mitochondrial Function and Energy Metabolism

Co-Chairperson: Russell Swerdlow, M.D.

Co-Chairperson: Chad Slawson, Ph.D.

Date Approved: 18 April 2017

Abstract

O-GlcNAc is a post-translational modification (PTM) of a single *N*-acetylglucosamine sugar attachment on serine or threonine residues of nuclear, cytoplasmic, and mitochondrial proteins. Two opposing enzymes facilitate the modification; O-GlcNAc transferase (OGT) adds the modification, while O-GlcNAcase (OGA) removes it. The addition and the removal of O-GlcNAc, termed O-GlcNAc cycling, is often a dynamic process sensitive to changes in the cellular environment. Disruptions in O-GlcNAcylation contribute to diseases such as diabetes, cancer, and neurodegeneration. Accumulative chronic dysfunctional mitochondria also lead to the development of disease; and importantly, O-GlcNAcylation regulates mitochondrial function.

In order to test our first hypothesis that disruptions in O-GlcNAc cycling affect mitochondrial function by changing the mitochondrial proteome, we employed a proteomics screen using SH-SY5Y neuroblastoma cells. We found that OGT and OGA overexpression severely disrupted the mitochondrial proteome, including proteins involved in the respiratory chain and TCA cycle. Furthermore, mitochondrial morphology in the over-expressing cells had disorganized cristae and altered shape and size. Both cellular respiration and glycolysis is impaired. These data support that O-GlcNAc cycling was essential for the proper regulation of mitochondrial function.

We next investigated how sustained elevations in cellular O-GlcNAc levels would alter the metabolic profile of the cell. We elevated cellular O-GlcNAc levels by either treating SH-SY5Y cells with low levels of glucosamine (GlcN), the metabolic substrate of OGT, or the OGA inhibitor Thiamet-G (TMG). We found cellular respiration was altered and ATP levels were lower in these cells with sustained elevated O-GlcNAc. Additionally, these cells produce significantly less reactive oxygen species (ROS). Both GlcN and TMG treated cells have

elongated mitochondria, while mitochondrial fusion/fission protein expressions were decreased. RNA-sequencing analysis showed that the transcriptome is reprogrammed and NRF2 anti-oxidant response is down-regulated. Importantly, sustained O-GlcNAcylation in mice brain and liver validated the metabolic phenotypes seen in cells, whereas liver OGT knockdown elevated ROS levels, impaired mitochondrial respiration, and increased NRF2 anti-oxidant response. Furthermore, we discovered from an indirect calorimetric study that sustained elevated O-GlcNAc promoted weight loss and lowered respiration, skewing mice toward using carbohydrates as their main energy source. Here, our results demonstrated that sustained elevation in O-GlcNAcylation, coupled with increased OGA expression, reprograms energy metabolism and can potentially impact the development of metabolic diseases. Altogether, these studies provide new evidence supporting the role of O-GlcNAc as a critical regulator of mitochondrial function and energy metabolism.

Acknowledgment

I would like to take this opportunity to thank my mentor, Dr. Chad Slawson, who has supported me unconditionally throughout my graduate career. I have been able to advance my scientific ability tremendously during these five 'painful' graduate school years, truly because of him. His confidence and faith in me, and his generosity and forgiveness towards me are the reasons I used to push myself to continuously be fearless in science and to be my best. The second person that I would like to thank is Dr. Christopher Stipp from the University of Iowa, who was the first person that raised my interests in science. His patience and scientific wisdom inspired me to want to pursue science. I would especially like to thank Dr. Gerald Carlson, who is also one of my committee members, for his encouragement when I encountered some bumpy roads during my graduate school years, and his wise advice on navigating myself to be a better person. Certainly, his advice was proven to be useful! Furthermore, I am grateful to all of my committee members, including Drs. Russell Swerdlow, Antonio Artigues and Hao Zhu for constantly challenging me to become a better scientist during the course of my graduate career. I am thankful for all the faculty, staff, and students in the Biochemistry and Molecular Biology department as my scientific community.

Most importantly, I am eternally grateful to my parents and siblings, who always believed in me and cheered me on as I endured all the challenges I encountered. They are certainly my role models to look up to and have helped cultivate my grit in life. I would like to dedicate this dissertation to my parents David Tan and Wan Yiong Yeong, and my sister Sofia Tan and brother Philip Tan.

I would like to thank all those friends who made my journey through graduate school an invaluable experience, and also acknowledge the network of individuals who have given me

support throughout my graduate career, especially Drs. Francesca Duncan (Northwestern University), Maite Villar, Mike Werle, Aric Rogers (MDI Biological Laboratory), Sadie Wignall (Northwestern University), Johnathan Labbadia (Northwestern University), Pedro Reis Rodrigues (The Scripps Research Institute), Sornakala Ganeshkumar, Chooi Ying Sim, Melody Chambers, Steven McGreal, Robert Tessman, Lezi E, Jane Lu, Zhen Zhang, Miranda Machacek, Anish Potnis, Kellyann Jones-Jamtgaard, Pedro Rodrigues, Jeremy Hollis, Nikita Divekar, Timothy Mullen, Amanda Cara, Renee Brielmann, Rachel Gomez, and Gabriel Warner.

Table of Contents

List of Figures

List of Tables

Chapter 1: Introduction

1.1 Overview

Chronic mitochondrial deterioration resulting in uncontrolled reactive oxygen species (ROS) generation can impair cellular energy metabolism and lead to the development of complex metabolic diseases. These diseases include Alzheimer's (AD), diabetes and cancer [1-3]. Therefore, mitochondria must acquire different regulatory mechanisms to properly maintain their function. Phosphorylation and acetylation regulate mitochondrial function, and these modifications are altered during disease states [4-7]. For example, high levels of mitochondrial acetylation negatively impact mitochondrial function, as acetylation predominantly deactivates proteins involved in the electron transport chain (ETC), tricarboxylic acid cycle (TCA) and ROS detoxification [8]. However, emerging evidence points to O-GlcNAc as a key regulator of mitochondrial function.

O-GlcNAcylation is a post-translational modification (PTM) involving the attachment of a single β-N-acetylglucosamine to serine/threonine amino acid residues of nuclear, cytoplasmic, and mitochondrial proteins. The modification is dynamically regulated by the opposing functions of two specific enzymes: O-GlcNAc transferase (OGT) adds the modification, whereas O-GlcNAcase (OGA) removes it. Furthermore, the OGT metabolic substrate, UDP-GlcNAc, is synthesized via the hexosamine biosynthetic pathway (HBP) linking several metabolic inputs with O-GlcNAcylation (**Figure 1**) [9]. Ultimately, these metabolic inputs make O-GlcNAc a nutrient sensor capable of influencing many cellular processes, including transcription, translation, and mitochondrial function.

Indication that O-GlcNAc regulates mitochondrial function comes from initial studies demonstrating that both OGT [10] and OGA [11] localize to the mitochondria. Furthermore, the

pyrimidine nucleotide carrier 1 (PNC1) transports UDP-GlcNAc into the mitochondria to provide substrate for OGT [11], allowing electron transport chain (ETC) subunits to be modified by O-GlcNAc [12]. Potentially, O-GlcNAcylation of ETC complexes modulates both the ETC function and energy metabolism. Importantly, aberrant O-GlcNAcylation is also linked to metabolic diseases [13, 14]; however, it is still unclear what is the role of O-GlcNAcylation in relation to these metabolic diseases. Evidence supports O-GlcNAc cycling as a global regulator for energy metabolism, and delineating O-GlcNAc's regulatory roles in mitochondrial function is essential.

1.2 Mitochondria: Metabolic Factories

Mitochondria are key cellular organelles that harbor several important metabolic pathways such as the tricarboxylic acid (TCA) cycle, the urea cycle, and oxidative phosphorylation. More than just harvesting chemical energy from nutrients to make adenosine triphosphate (ATP), the mitochondria are responsible for an array of cellular functions. These functions include sugar and fatty acid catabolism, amino acid metabolism, calcium homeostasis, synthesis of heme, iron-sulfur (Fe-S) clusters and steroids, and apoptosis regulation [15]. The intermediates generated through different metabolic pathways of the mitochondria, such as ATP [16], acetyl CoA [17], and succinyl CoA[18], are important substrates for the different PTMs, including phosphorylation, acetylation and succinylation. Additionally, mitochondria are the main site for free radical generation, which are major signaling molecules in cell [19]. Therefore, mitochondria are major metabolic hubs in controlling cellular function.

Chronic impairment in mitochondrial functions can lead to the development of complex metabolic diseases, such as Alzheimer's and cancer. For example, one evolving hypothesis, the mitochondrial cascade hypothesis, argues that the development of Alzheimer's is a result of

chronic mitochondrial deterioration. The mitochondrial cascade hypothesis is based on the idea that an individual's baseline mitochondrial function is defined by gene inheritance, and that inherited and environmental factors determine the rates of mitochondrial functional changes [20]. And as we age, the efficacy of mitochondrial respiration diminishes. The increased electron leakage from the electron transport chain increases ROS generation and lowers ATP generation. The progressive mitochondrial deterioration leads to global cellular damage and enhances diseases progression [1-3]. In support of this hypothesis, several studies demonstrate that in the brains of AD patients and AD mice prior to the formation of amyloid plaques, the TCA cycle and oxidative phosphorylation are suppressed, and the elevation of free radical production increases oxidative stress [21-24]. Subsequently, the prolonged exposure to large concentrations of ROS in neurons can have a deleterious effect on DNA, RNA and proteins, and more importantly, this phenomenon also induces cross-linking of Aβ and APP fragments for further aggregation [25, 26]. Furthermore, studies using various AD models, such as AD brain and human platelet mitochondria, have also reported that deficiencies in the fission and fusion of mitochondria, and in enzymes involved in the electron transport chain (ETC) and tricarboxylic acid cycle (TCA), are present in AD [27, 28]. Altogether, these studies have provided strong evidence for the important role of improper mitochondrial regulation in the development of AD.

1.3 O-GlcNAc: A Nutrient/Stress Sensing Modification

Broadly defined, nutrient sensing is a cell's ability to determine the concentrations of metabolites, and to act accordingly to change cellular function. Most PTMs are derived from metabolites that are linked to metabolic inputs used to signal appropriate cellular action [2]. O-GlcNAc is a PTM of the attachment of a single *N*-acetylglucosamine to serine/threonine residues of nuclear, cytoplasmic and mitochondrial proteins. Both OGT and OGA are nutrient sensors

that facilitate the addition and removal of O-GlcNAcylation in response to changes in cellular nutrients and metabolic state. Importantly, O-GlcNAc acts as a nutrient sensing modification through the activity of the hexosamine biosynthetic pathway (HBP). The HBP is tightly regulated by its rate-limiting enzyme glutamine fructose-6-phosphate aminotransferase 1 (GFAT1). This pathway integrates signals from glucose, amino acid, fatty acid and nucleotide metabolisms (**Figure 1**) to synthesize the substrate of OGT, UDP-GlcNAc. Because UDP-GlcNAc synthesis relies on the integration of multiple metabolic pathways, O-GlcNAcylation can sense changes in nutrients [29]. Since O-GlcNAc regulates mitochondrial function, changes in nutrients could lead to changes in mitochondrial function. Potentially, chronic disruptions in O-GlcNAc's nutrient sensing ability could mediate mitochondrial deterioration leading to the development of metabolically related diseases. In spite of this, the mechanism is unclear in which O-GlcNAc regulates mitochondrial function and warrants further investigation.

1.4 O-GlcNAc Regulates Metabolism

Cumulative evidence supports O-GlcNAc as essential in controlling mitochondrial function influencing energy metabolism. Both O-GlcNAc cycling enzymes, OGT [10] and OGA, localize to the mitochondria [11]. OGT substrate, UDP-GlcNAc, is transported into the mitochondria by pyrimidine nucleotide carrier 1 (PNC1) [11]. Furthermore, majority of the ETC subunits are modified by O-GlcNAc, and changes in O-GlcNAcylation levels alter mitochondrial respiration. For example, when O-GlcNAcylation is elevated via short-term high glucose treatment, ETC activity is suppressed in rat cardiomyocytes [30]; whereas, short-term OGA inhibition increased mitochondrial respiration in rats [12]. Recently, several studies also demonstrated genetic ablation of OGT that significantly reduced basal O-GlcNAcylation produced severe metabolic

phenotypes [31-33]. Together, these data demonstrate that O-GlcNAc is essential for the proper regulation of mitochondrial function and energy metabolism.

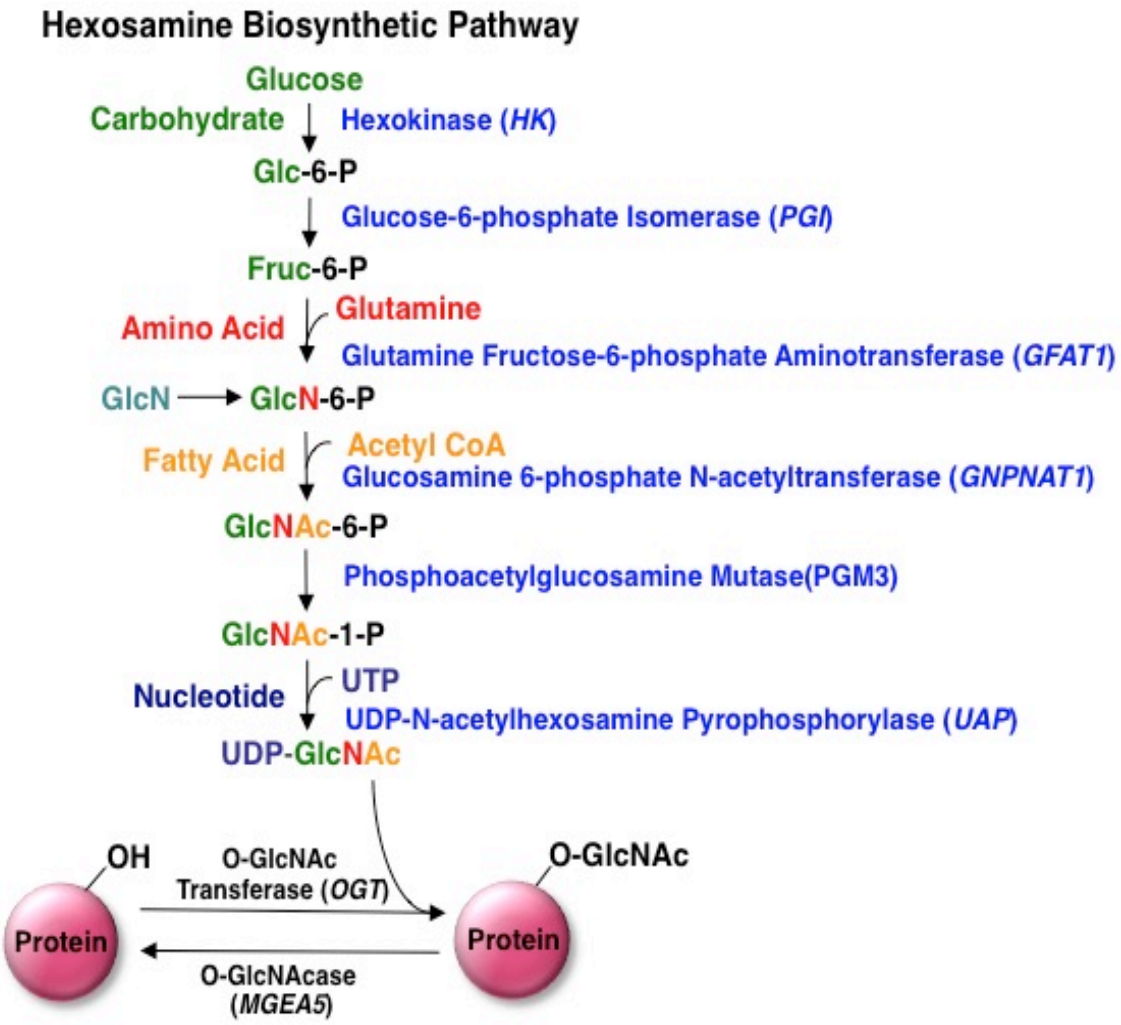

Figure 1: Schematic representation of the Hexosamine Biosynthetic Pathway (HBP) and O-GlcNAc modification.

Modified from Slawson et al. [9]

Chapter 2: O-linked β-*N*-Acetylglucosamine Cycling is Important in Regulating Mitochondrial Function

Reproduced with permission from Tan, E.P., Villar, M.T., E, L., Lu, J., Selfridge, J.E., Artigues, A., Swerdlow, R.H., and Slawson, C. (2013). ***Altering O-linked β-N-Acetylglucosamine Cycling Disrupts Mitochondrial Function.*** *The Journal of Biological Chemistry 289(21):14719-30*

2.1 Introduction

O-GlcNAc is the post-translational addition of a single N-acetylglucosamine residue to cytoplasmic and nuclear proteins [34]. The O-GlcNAc modification is ubiquitously found in all higher eukaryotes. O-GlcNAc transferase (OGT) is the enzyme responsible for the addition of O-GlcNAc to intracellular proteins, while O-GlcNAcase (OGA) removes the modification from intracellular proteins [35]. These enzymes are expressed in all mammalian cells, with highest expression levels in brain [34]. The addition or removal of O-GlcNAc is termed O-GlcNAc cycling, and altering O-GlcNAc cycling rates affects metabolic pathways, stress response, and cell cycle progression [34-36].

In the past several years, multiple groups have demonstrated links between metabolic disorders and O-GlcNAcylation. For example, several proteins involved in insulin signaling, including IRS1, are modified by O-GlcNAc. OGT localizes to the plasma membrane shortly after insulin binding to the insulin receptor, suggesting that relocation of OGT to the membrane suppresses insulin signaling by O-GlcNAcylating IRS1 [37-40]. Elevated glucose levels impair glycogen synthase function through increased O-GlcNAcylation of glycogen synthase [41]. Furthermore, chronic hyperglycemia causes an increase in O-GlcNAcylation of CRTC2 (cyclic adenosine monophosphate response element–binding protein 2), thereby promoting increased gluconeogenesis through interactions with the CREB transcription factor [42]. Concomitantly,

the transcription factor FOXO1 is O-GlcNAcylated, which increases the transcription of gluconeogenesis genes such as glucose-6-phosphatase and phosphoenolpyruvate carboxykinase [43]. Together, these data demonstrate the importance of O-GlcNAcylation in regulating metabolic function.

Mitochondrial function is also regulated by O-GlcNAc. Several respiratory chain proteins are modified by O-GlcNAc, and increased O-GlcNAcylation impairs respiration [44, 45]. A splice variant of OGT (mOGT) localizes to the mitochondria [44, 46, 47], and in INS-1 cells mOGT over-expression causes cellular apoptosis [48]. Recently, several studies suggest that chronic hypoglycemia increases O-GlcNAcylation, and promotes metabolic disease by inducing mitochondrial dysfunction [49, 50]. For example, changes in cellular glucose levels in cardiac myocytes are linked to altered O-GlcNAcylation, which in turn leads to changes in mitochondrial function [44, 51]. Rats selected for low running capacity had increased mitochondrial O-GlcNAcylation, suggesting that increased mitochondrial O-GlcNAcylation impair respiration [52]. Together, these data demonstrate a critical role for O-GlcNAcylation in the regulation of mitochondrial function.

To more fully address how alterations in O-GlcNAc processing enzymes affect mitochondrial function, we performed a proteomics based study in a neuronal cell line in which we quantified changes in mitochondrial protein expression after over-expression of OGT or OGA. Over-expression of either enzyme caused alterations in the expression of proteins involved in the respiratory chain, as well as a reduction in several TCA cycle proteins. Mitochondrial morphology was greatly altered, and cellular respiration and glycolysis rates were significantly reduced. Together, our data demonstrate that both O-GlcNAc processing enzymes regulate

mitochondrial and cytosolic bioenergetic fluxes and infrastructure. Our data imply that mitochondrial function is sensitive to O-GlcNAc cycling.

2.2 Methods

2.2.1 Antibodies

All antibodies were used at a 1:1000 dilution for immunoblotting unless otherwise noted. COX IV antibody was purchased from Invitrogen (A21348). The following antibodies were purchased from Abcam: Metaxin-1 (AB104966), ACADM (AB92461), NDUFA5 (AB183706), NDUFA9 (AB14713). Actin (A2066) and GFP (G6539) were from Sigma. Antibodies for OGT (AL-28, Al-35), OGA (341), and O-GlcNAc (110.6) were a kind gift from the laboratory of Gerald Hart in the department of Biological Chemistry at the Johns Hopkins University School of Medicine.

2.2.2 Cell Culture

SY5Y neuroblastoma cells were cultured in DMEM (Sigma) supplemented with 10% Fetal Bovine Serum (FBS, Gemini) and 1% penicillin/streptomycin (Invitrogen). For SILAC culture, SY5Y cells were cultured in DMEM (Cambridge Isotope, DMEM-500) supplemented with unlabeled arginine, lysine, and tyrosine (Sigma A8094, L5501, T8566), DMEM supplemented with ^{13}C6-arginine, 4,4,5,5-D4-lysine, and tyrosine (Cambridge Isotope CLM-2265 and DLM-2640), or DMEM supplemented with ^{13}C6-^{15}N4-arginine, ^{13}C6-^{15}N2-lysine, and tyrosine (Cambridge Isotope CNLM-539 and CNLM-291). All SILAC media were supplemented with 10% dialyzed Fetal Bovine Serum (Gemini 100-108) and 1% penicillin/streptomycin. Cells were passaged at least 5 times in labeled media before performing an experiment. Cells were infected with OGT, OGA, or GFP virus at a multiplicity of infection (MOI) of 75. Cells were

then harvested for either MS analysis or respiration analysis 48 or 24 hours post-infection respectively.

2.2.3 Mitochondrial Isolation

All mitochondria were isolated using the modified nitrogen cavitation method described by Gottlieb and Adachi [53]. At least 2 x 10^8 cells were used. The cells were digested off the plate with trypsin, washed twice with pre-chilled PBS, and resuspended into 3 mL of the isolation medium (225 mM mannitol, 75 mM sucrose, 5 mM Hepes, 1 mM EGTA, pH 7.4 at 4 °C). The cell suspension was collected into a pre-chilled cavitation chamber (nitrogen bomb; Parr Instrument Company, Moline IL) and was subjected to 900 psi for 15-min period. The collected cell suspension from the cavitation chamber was centrifuged at 1500 x g for 3 min to pellet the cell debris (heavy particles, or fractions of cells). The supernatant was collected and centrifuged at 20,000 x g for 10 min. The pellet (crude mitochondrial fraction) was washed three times with 500 µl of isolation medium. The final pellet was resuspended in 100 µl of NP-40 Lysis Buffer (20 mM Tris-HCl pH 7.4, 150 mM NaCl, 1 mM EDTA, 1 mM DTT, 40 mM GlcNAc, and 1% NP-40, all reagents from Sigma) and lysed on ice for 30 min with occasional vortexing.

2.2.4 Peptide Identification and Computational Analysis

Peaks Studio (version 7.0 BSI, Waterloo, ON, Canada) was used to analyze the mass spectra. The following criteria were used for the searches: data refinement was performed with no merged scans, with precursor charge correction and with no filtering. *De novo* sequencing was performed with a mass tolerance of 25 ppm for the parent and 0.4 for the fragment ions, using trypsin as enzyme specificity, carbamidomethyl cysteine as a fixed modification and variable modifications of oxidation (M), deamidation (N, Q), pyroGlu from Q. Since proteins were isotopically labeled, variable modification for K (+4.03 and +8.01 for medium and heavy label,

respectively) and R (+6.02 and 10.02 for medium and heavy label, respectively) were also considered. A maximum of 3 variable modifications and 2 missed cleavages per peptide were allowed. The resulting peptide sequences were searched against a human IPI protein database (version 3.87). Estimation of false discovery rate (FDR) was conducted by searching all spectra against a decoy-fusion (inverted) database. Peptide identifications were accepted if they could be established at a FDR less than 1%. For protein identification, proteins were accepted if they could be established at a Peaks protein probability score (-10lgP) better than 20 with a minimum of two unique peptides per protein. Proteins that contained similar peptides and could not be differentiated based on MS/MS analysis alone were grouped to satisfy the principle of parsimony, only the top ranked protein sequence was reported in the results section. For protein quantification the Peaks Q module included in the Peaks Studio (Peaks studio v7.0) was used. For precursor ion quantification, the mass tolerance was set to 0.2 Da and a retention time tolerance of 1 min, using an upper bound charge state of 4. For each experimental data set, protein ratios were calculated relative to the control (GFP cells) and were calculated on the average of total peak intensities of the top 3 unique peptides identified per protein group. For each protein group, the data of at least 2 experimental data sets from all searches were combined and averaged. Only proteins that showed a 1.5-fold expression change were considered noteworthy.

2.2.5 Electron Microscopy

SY5Y cells were cultured on Thermanox® Coverslips and infected with a 75 MOI of GFP, OGT, or OGA adenovirus 24 hours prior to fixation. Cells were fixed with 2% glutaraldehyde in 0.1 M cacodylate buffer, pH 7.4, and were post-fixed with 1% osmium tetroxide/0.3% potassium

ferricynide. The cells were then dehydrated in a graded series of 50, 70, 80, 95 and 100% ethanol. Cells on coverslips were embedded in 100% epoxy resin, and the resin was cured overnight at 60°C. Thin sections of 70-90 nm were cut on a Reichert Ultracut-S (Reichert Technologies, Buffalo, NY), stained with uranyl acetate and lead citrate. Images were captured at 80kV with JEOL JEM-1400 Transmission Electron Microscope (JEOL USA Inc., Peabody, MA) equipped with a Lab6 gun at the University of Kansas Medical Center EM Core laboratory.

2.2.6 Cellular Respiration and Glycolysis Measurement

To measure cellular respiration and glycolysis, we used an XF24 flux analyzer (Seahorse Bioscience, North Billerica, MA). All cellular respiration and glycolysis assays were performed in a Seahorse 24-well cell culture plate in conjunction with an XF24 sensor cartridge at least three separate times. SY5Y cells were seeded as a monolayer with a density of 65,000 cells per well and were infected with OGT, OGA, or GFP virus for 24 hours prior to experimental assays. For respiration assays, cells were incubated in unbuffered DMEM (DMEM 8.3 g/L Sigma D5030-1L pH 7.4), 25 mM glucose, Phenol Red (15 mg/L Sigma P-5530), 200 mM GlutaMax-1, NaCl (1.85 g/L), at 37° in a CO_2 free incubator for 1 hour prior to loading the plate in the XF24 to allow temperature and pH equilibrium. The oxygen consumption rate (OCR) was measured over a period of 100 min during which oligomycin (0.5 μM), FCCP (0.3 μM), and both antimycin A (0.2 μM) and rotenone (0.1 μM) were sequentially added to each well at specified time points. For glycolysis assays, cells were incubated in glycolysis stress test base glucose free medium (DMEM 8.3 g/L Sigma D5030-1L pH 7.4) containing 40 μM Phenol Red (Sigma P-5530), 2 mM L-glutamine, and NaCl (1.85 g/L) at 37 °C in a CO_2 free incubator for 1 hour prior to loading the plate in the XF24 to allow temperature and pH equilibrium. The extracellular acidification rate (ECAR) was measured over a period of 100 min. Glucose (25 mM),

oligomycin (1 μM), and 2-Deoxy-D-glucose (2-DG) (100 mM) were added to each well sequentially at specified time points during the assay.

2.2.7 Statistical Analysis

For comparisons of data containing three groups, we used one-way ANOVA followed by Tukey's post hoc tests to compare mean differences of groups at a significance threshold of $P < 0.05$.

2.3 Results

2.3.1 OGT/OGA Overexpression Alters Mitochondrial O-GlcNAcylation and Protein Expression

In order to determine how changes in O-GlcNAc cycling affect mitochondria protein expression, we over-expressed either OGT or OGA through adenoviral-mediated infection. Importantly, we chose to use the full length OGT over the mitochondrial form of OGT because we wanted to determine how changes in O-GlcNAc cycling would affect expression of both nuclear encoded mitochondrial genes and subsequently any mitochondrial-encoded genes. Since neuronal function is highly dependent on oxidative metabolism, we used as a model cell line SY5Y neuroblastoma cells. We selected this line because of its rapid expansion, its ease of over-expression, its neuronal background (OGT and OGA expression is robust in brain), and because SY5Y cells are relatively sensitive to changes in mitochondrial function [54]. After over-expression we isolated a heavy membrane preparation enriched for mitochondria, and measured O-GlcNAcylation levels. Green Fluorescent Protein (GFP) was used as a control for adenoviral infection. GFP-expressing control mitochondria contained numerous O-GlcNAcylated proteins. Both OGT and OGA expression robustly increased in the respectively transfected cells. Over-

expressing the nuclear-cytoplasmic form of OGT dramatically increased O-GlcNAc levels while OGA over-expression profoundly reduced O-GlcNAc levels (**Figure 2**).

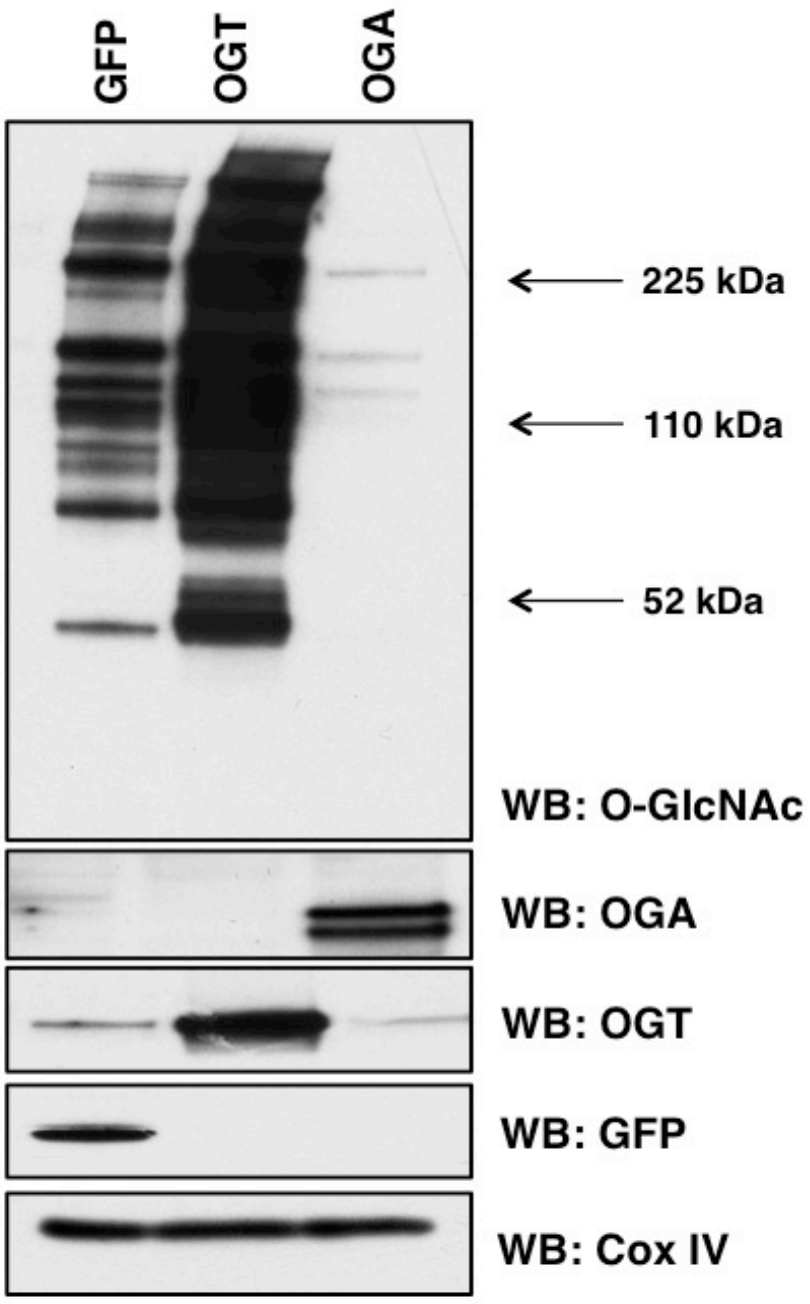

Figure 2: OGT or OGA over-expression alters mitochondrial O-GlcNAcylation. Mitochondria were purified from SY5Y cells expressing GFP, OGT, or OGA and probed for total O-GlcNAc. As expected, total O-GlcNAc levels are increased in OGT expressing cells and decreased in OGA expressing cells. COX IV was used as a loading control.

Next, we generated SILAC (Stable Isotope Labeling of Amino Acids on Cell Culture) labeled SY5Y cells in order to determine how OGT/OGA over-expression changes the expression of mitochondrial proteins. Labeled cells expressing GFP (grown in light isotopic medium), OGT (grown in medium isotopic medium), or OGA (grown in heavy isotopic medium) were lysed, mitochondria purified, and equal amounts of mitochondrial proteins were combined and separated via gel electrophoresis. In gel-digestion of stained proteins was performed, followed by a cleanup step using a protein trap and reverse phase HPLC separation. Separated proteins were then injected into a high mass accuracy Thermofinnigan FT-LTQ mass spectrometer. Both sequence composition and quantitative information were collected in a single scan. Peptide and protein identifications below a false discovery rate of 1% are reported. PEAKS Software suite was used for identification and quantification analysis (**Figure 3A**). We repeated this experiment two more times, but switched SILAC labels for the cells expressing GFP, medium media, OGT, heavy media, or OGA, light media, for example. From each experimental set, we were able to identify numerous proteins from each in-gel digested band (**Figure 3B**).

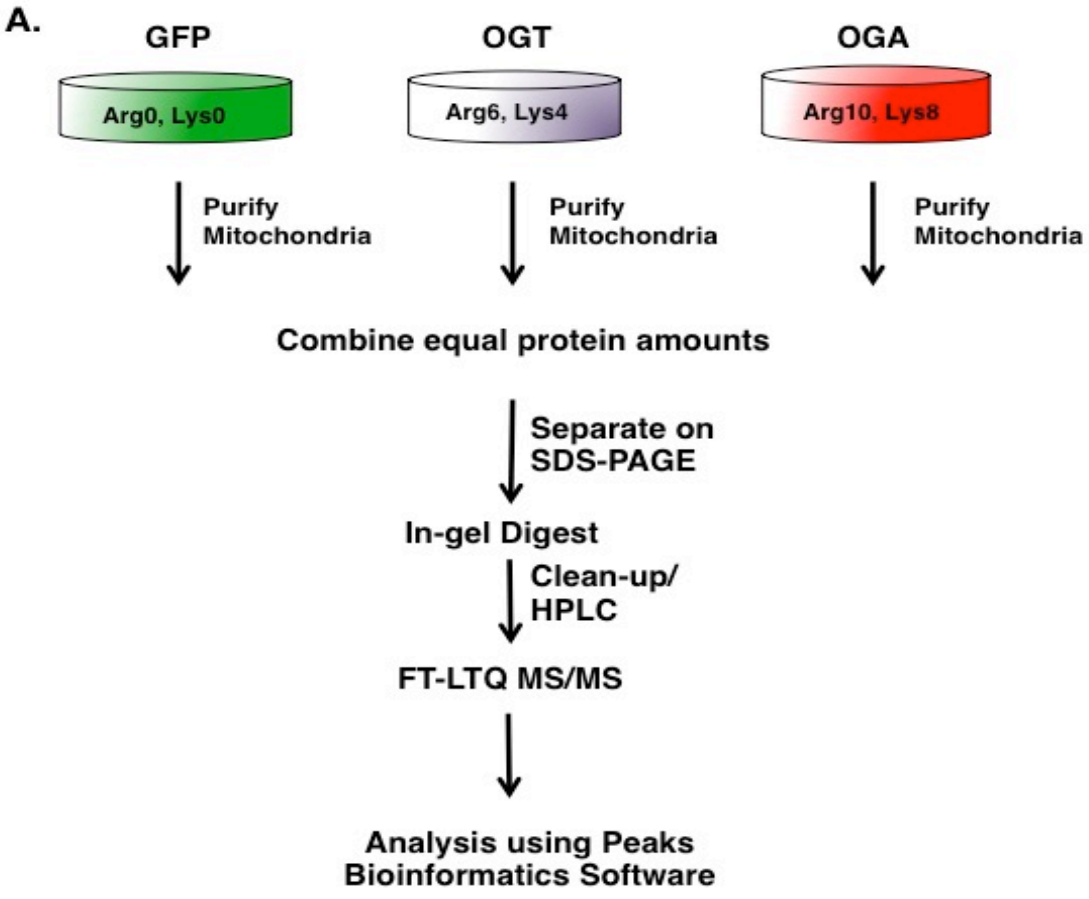
A.
GFP
OGT
OGA
Arg0, Lys0
Arg6, Lys4
Arg10, Lys8
Purify Mitochondria
Purify Mitochondria
Purify Mitochondria
Combine equal protein amounts
Separate on SDS-PAGE
In-gel Digest
Clean-up/ HPLC
FT-LTQ MS/MS
Analysis using Peaks Bioinformatics Software

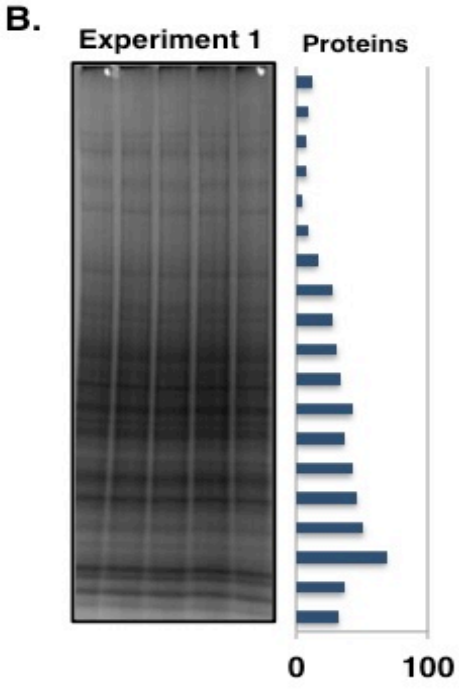
B.
Experiment 1
Proteins
0
100

Figure 3: Purification of SILAC labeled mitochondria from SY5Y cells.
(**A**) Schematic of SILAC sample processing. Mitochondria from light, medium, and heavy labeled SY5Y cells were purified and combined in equal protein amounts. The samples were separated by gel electrophoresis, stained, and bands excised. The excised bands were processed by in-gel trypsin digestion. Peptides were separated via HPLC and analyzed by a FT-LTQ mass spectrometer. SILAC quantification was performed using the PEAKS software package. (**B**) Image of Coomassie blue-stained gel after electrophoretic separation. The bar graph on the right side indicates the total number of proteins identified in each band.

In the first experiment, we determined a total of 507 protein identifications in the crude mitochondrial preparation; experiment 2 yielded 350 protein identifications; and experiment 3 yielded 768 protein identifications (**Figure 4A**). 152 of the identified proteins were found in all experimental replicates. We identified a total of 234, 146, and 242 mitochondrial proteins, respectively, from the 3 experimental replicates (**Figure 4B**). We grouped the identified mitochondrial proteins into classes according to function (**Figure 5**). Of the 345 unique mitochondrial proteins identified, the most abundant class included those that mediate mitochondrial protein translation, while proteins involved in cellular respiration were the next largest class of proteins identified.

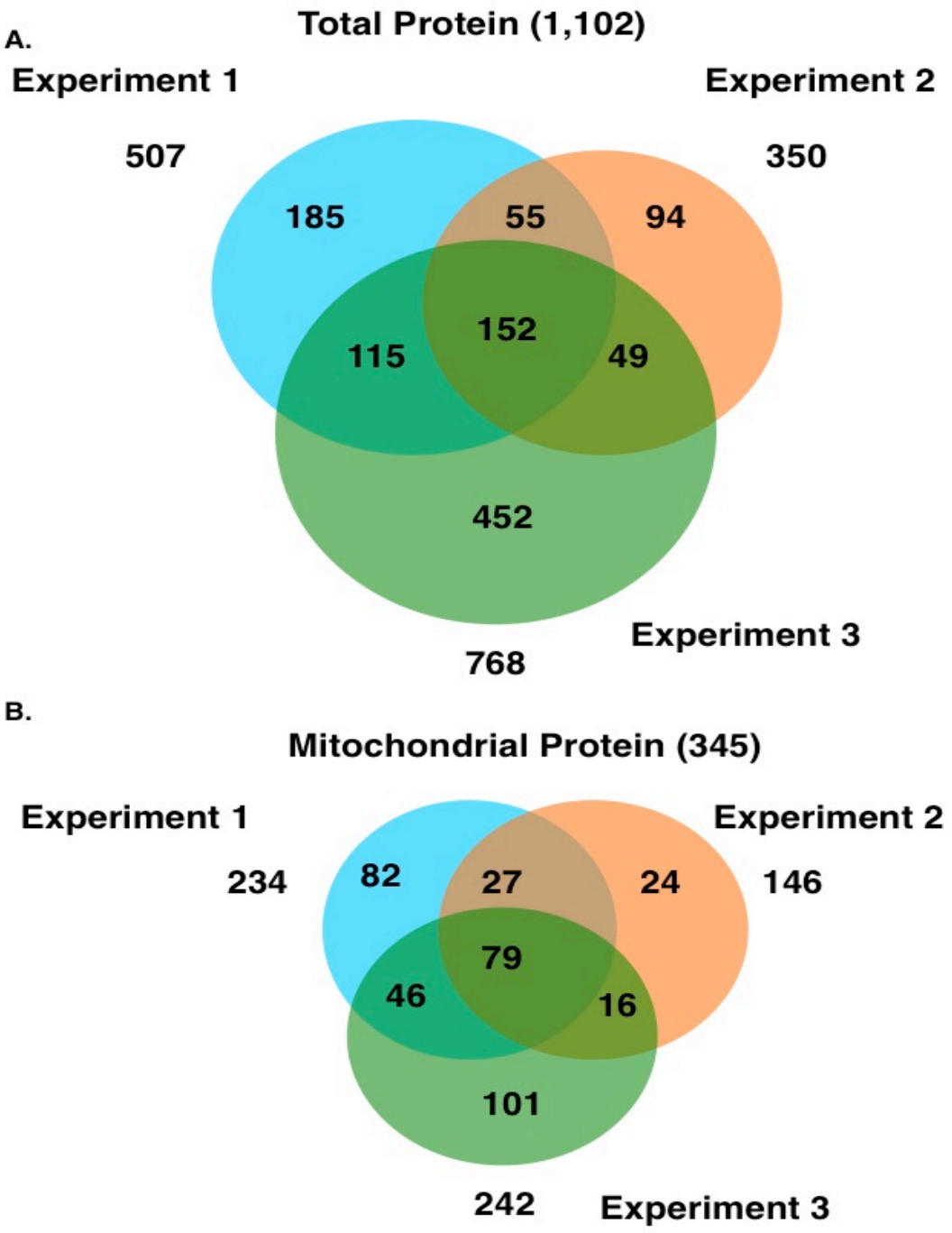

Figure 4: Proteomic identification of isolated proteins.
(**A**) Venn diagram indicating the total number of identified proteins from 3 independent replicate experiments. (**B**) Venn diagram showing the total number of mitochondrial proteins identified from 3 independent replicate experiments.

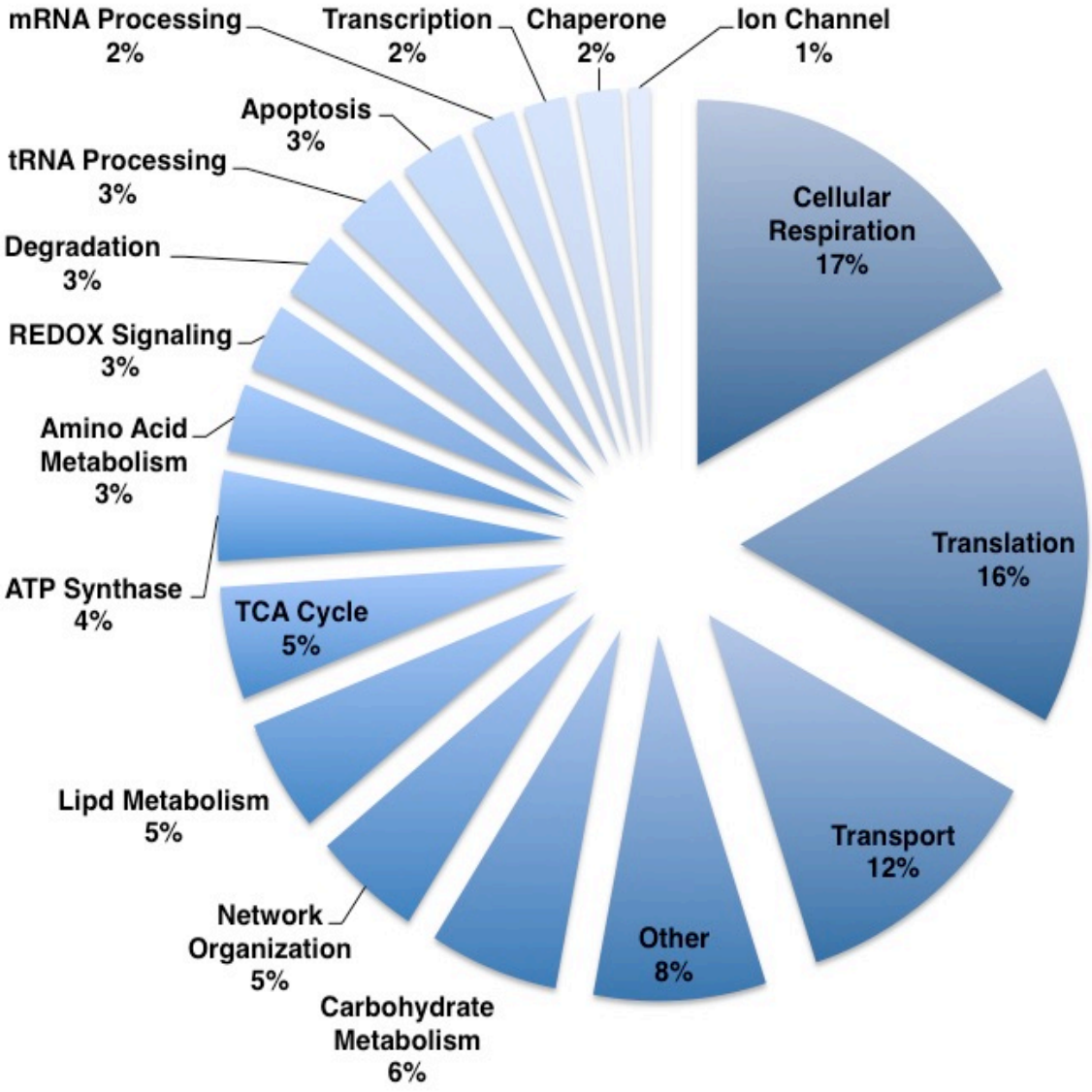

Figure 5: Functional class distribution of identified mitochondrial proteins.
Identified proteins were distributed into biological functional class. Components of mitochondrial protein expression and cellular respiration were the two largest identified classes of proteins.

2.3.2 OGT/OGA Overexpression Impacts Electron Transport Chain and TCA Protein Expression

Next, we quantified the differences in protein expression of the OGT or OGA over-expressing cells compared to the GFP expressing control cells. Including non-mitochondrial proteins, from the combined replicates we were able to quantify 1102 total proteins. We considered proteins whose expression changed greater than 1.5-fold to be noteworthy, with 571 proteins showing large expression changes in the total extract (**Figure 6A**), while 107 proteins changed in the mitochondrial extract (**Figure 6B**). In most cases the increase or decrease in protein expression of OGT or OGA expressing cells was similar. (**Figure 6A-B**).

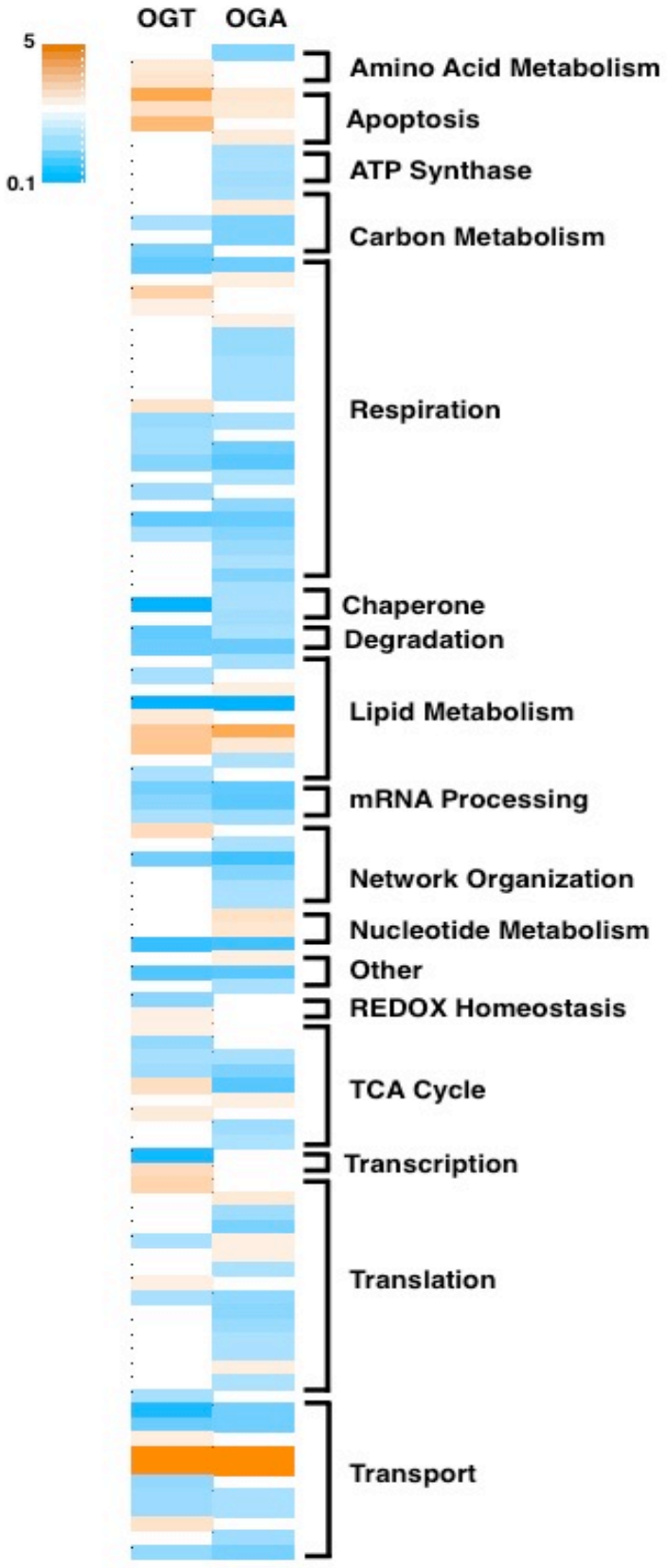
OGT
OGA
5
0.1
Amino Acid Metabolism
Apoptosis
ATP Synthase
Carbon Metabolism
Respiration
Chaperone
Degradation
Lipid Metabolism
mRNA Processing
Network Organization
Nucleotide Metabolism
Other
REDOX Homeostasis
TCA Cycle
Transcription
Translation
Transport

Figure 6: Quantification of SILAC labeled mitochondrial proteins from OGT and OGA over-expressing SY5Y cells

(**A-B**) The relative fold changes in total quantified proteins (**A**) or mitochondrial proteins (**B)** were plotted after OGT over-expression (dark green) or OGA over-expression (light orange). Red lines indicate 1.5-fold change cut-off.

OGA and OGT over-expressing cells demonstrated similar patterns of mitochondrial protein change. Almost all the mitochondrial protein functional categories demonstrated a decrease in protein expression, although some transport and apoptosis proteins were increased in the over-expressing cells (**Figure 7 and Table 1**). Next, we performed orthogonal validation via western blots on several mitochondrial proteins whose expression changed in the proteomic study. Again, we enriched mitochondria from SY5Y cells, but we also included the cytosolic fraction as well on the gels. By including the cytosolic fraction, we could determine if protein transport into the mitochondria was altered and potentially a mechanism for changes in protein expression. We then blotted for a variety of proteins. We determined no change in COX4 (Cytochrome c oxidase subunit 4) according to the proteomics; therefore, we used COX4 as a mitochondrial protein load control (**Figure 8**). The complex 1 protein NDUFA9 (NADH dehydrogenase [ubiquinone] 1 alpha subcomplex) was decreased in the OGA over-expression proteomics and validated via western blotting. On the other hand, complex 1 protein NDUFA5 was increased in OGT over-expressing cells but decreased in the OGA over-expressing cells. Showing expression decreases in both OGT/OGA over-expressing cells was the outer mitochondrial membrane protein Metaxin-1 (MTX1). The β-oxidation protein ACADM (Medium-chain specific acyl-CoA dehydrogenase) was decreased in OGT over-expressing cells and increased in the OGA over-expressing cells, agreeing with the proteomics data (**Figure 8**).

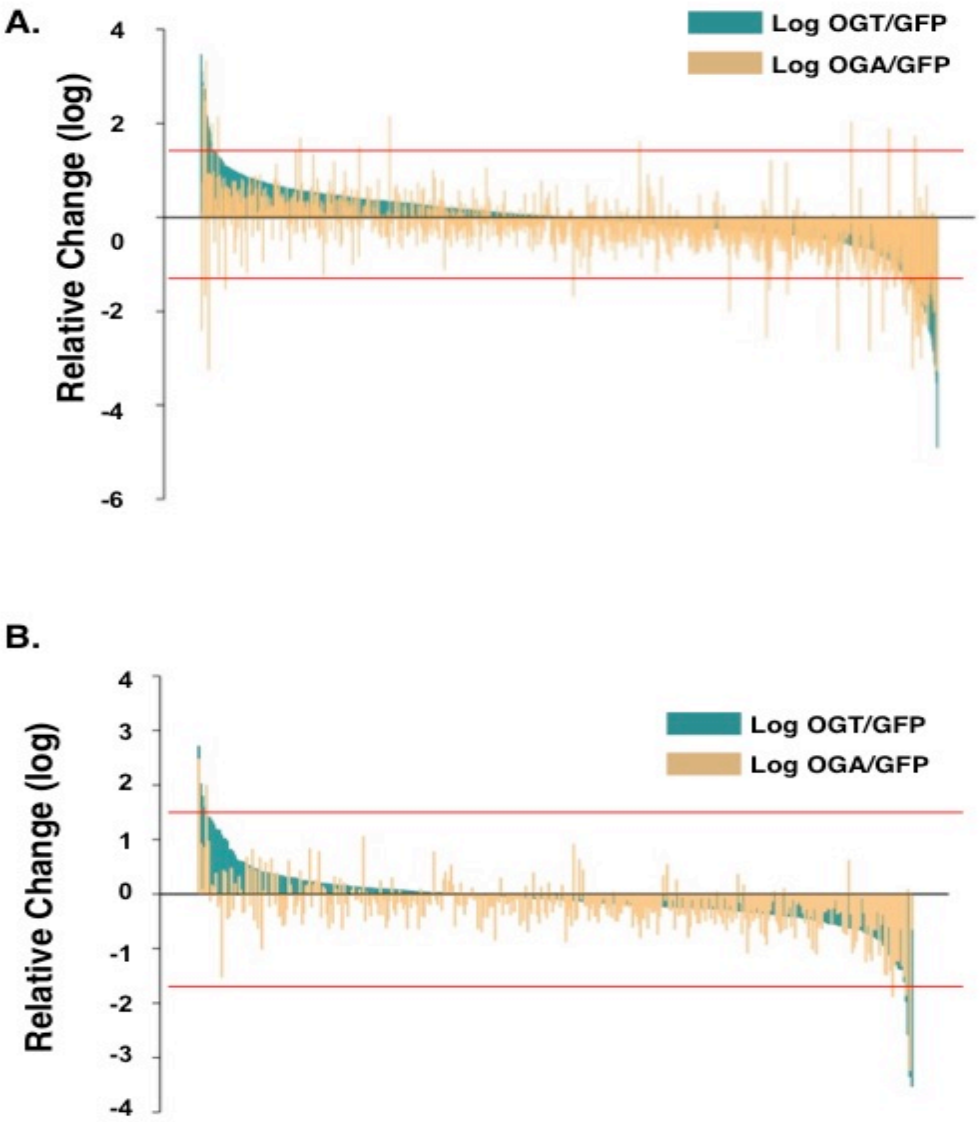

Figure 7: OGT/OGA over-expression alters mitochondrial protein expression
Heat map of proteins demonstrating a greater than 1.5-fold expression change in the OGT/OGA over-expressing cells normalized to GFP control cells. Heat map scale ranges from increased protein expression (orange) to decreased protein expression (teal). Proteins were grouped according to their functional class.

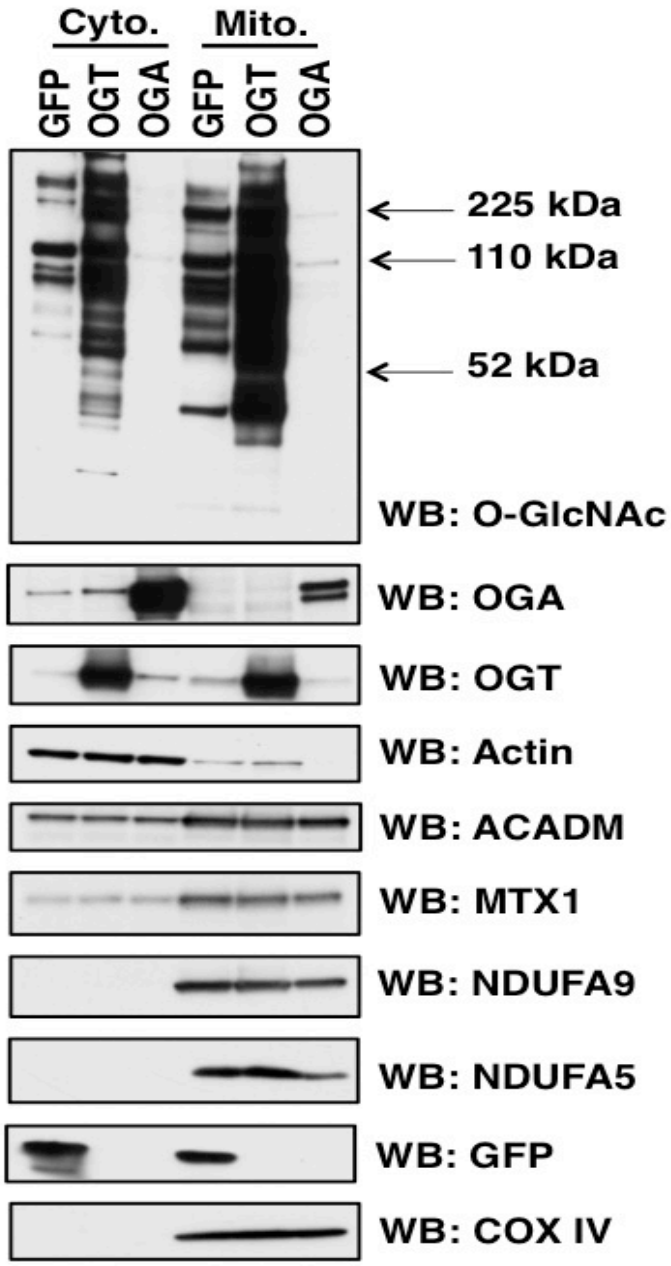

Figure 8: Orthogonal validation of mitochondrial protein expression
Mitochondria and cytosolic fractions were prepared from SY5Y cells. Samples were separated on SDS-PAGE and probed for specific proteins. COX4 is used as a mitochondria load control while actin was a cytoplasmic load control. ACADM, NDUFA9, NDUFA5, and MTX1 expression mirrored the expression changes in the proteomic studies.

Table 1: Complete list of protein expression changed after OGT/OGA overexpression

SampleDescription	OGT-fold	OGA-fold	Function
Tax_Id=9606 Gene_Symbol=ALDH18A1 Isoform Short of Delta-1-pyrroline-5-carboxylate synthase	_	0.51	**Amino Acid Metabolism**
Tax_Id=9606 Gene_Symbol=GLUD1 Uncharacterized protein	1.76	_	**Amino Acid Metabolism**
Tax_Id=9606 Gene_Symbol=PYCR1 Pyrroline-5-carboxylate reductase	1.96	_	**Amino Acid Metabolism**
Tax_Id=9606 Gene_Symbol=AIFM1 Isoform 1 of Apoptosis-inducing factor 1_ mitochondrial	4.06	1.89	**Apoptosis**
Tax_Id=9606 Gene_Symbol=BAX Isoform Sigma of Apoptosis regulator BAX	2.15	1.78	**Apoptosis**
Tax_Id=9606 Gene_Symbol=DIABLO Isoform 2 of Diablo homolog_ mitochondrial	3.47	_	**Apoptosis**
Tax_Id=9606 Gene_Symbol=FAM162A Uncharacterized protein	_	1.72	**Apoptosis**
Tax_Id=9606 Gene_Symbol=ATP5I ATP synthase_ H+ transporting_ mitochondrial F0 complex_ subunit E	_	0.63	**ATP Synthase**
Tax_Id=9606 Gene_Symbol=ATP5L ATP synthase subunit g_ mitochondrial	_	0.64	**ATP Synthase**
Tax_Id=9606 Gene_Symbol=ATP5L Uncharacterized protein	_	0.61	**ATP Synthase**
Tax_Id=9606 Gene_Symbol=ALDH2 Aldehyde dehydrogenase_ mitochondrial	_	0.64	**Carbon Metabolism**
Tax_Id=9606 Gene_Symbol=MTHFD2 Bifunctional methylenetetrahydrofolate dehydrogenase/cyclohydrolase_ mitochondrial	_	1.71	**Carbon Metabolism**
Tax_Id=9606 Gene_Symbol=MTHFD2 cDNA FLJ52745_ highly similar to Bifunctional methylenetetrahydrofolatedehydrogenase/cyclohydrolase_ mitochondrial	0.64	0.47	**Carbon Metabolism**
Tax_Id=9606 Gene_Symbol=MTHFD2 Uncharacterized protein	_	0.47	**Carbon Metabolism**
Tax_Id=9606 Gene_Symbol=PDHX Pyruvate dehydrogenase protein X component_ mitochondrial	0.46	_	**Carbon Metabolism**
COX6C	0.39	0.43	**Cellular Respiration**
NDUFA13_ highly similar to NADH dehydrogenase (ubiquinone) 1 alpha subcomplex subunit 13	_	1.58	**Cellular Respiration**

Tax_Id=9606 Gene_Symbol=COX6B1 Cytochrome c oxidase subunit 6B1	2.63	_	**Cellular Respiration**
Tax_Id=9606 Gene_Symbol=ETFB Isoform 1 of Electron transfer flavoprotein subunit beta	1.51	_	**Cellular Respiration**
Tax_Id=9606 Gene_Symbol=GBAS	_	1.52	**Cellular Respiration**
Tax_Id=9606 Gene_Symbol=NDUFA11 Isoform 2 of NADH dehydrogenase [ubiquinone] 1 alpha subcomplex subunit 11	_	0.57	**Cellular Respiration**
Tax_Id=9606 Gene_Symbol=NDUFA11 NADH dehydrogenase [ubiquinone] 1 alpha subcomplex subunit 11 isoform 2	_	0.57	**Cellular Respiration**
Tax_Id=9606 Gene_Symbol=NDUFA2 NADH dehydrogenase [ubiquinone] 1 alpha subcomplex subunit 2	_	0.62	**Cellular Respiration**
Tax_Id=9606 Gene_Symbol=NDUFA4 NADH dehydrogenase [ubiquinone] 1 alpha subcomplex subunit 4	_	0.63	**Cellular Respiration**
Tax_Id=9606 Gene_Symbol=NDUFA5 Uncharacterized protein	_	0.62	**Cellular Respiration**
Tax_Id=9606 Gene_Symbol=NDUFA5 Uncharacterized protein	2.02	_	**Cellular Respiration**
Tax_Id=9606 Gene_Symbol=NDUFA6 NADH dehydrogenase [ubiquinone] 1 alpha subcomplex subunit 6	0.57	0.64	**Cellular Respiration**
Tax_Id=9606 Gene_Symbol=NDUFA8 NADH dehydrogenase [ubiquinone] 1 alpha subcomplex subunit 8	0.61	_	**Cellular Respiration**
Tax_Id=9606 Gene_Symbol=NDUFA9 NADH dehydrogenase [ubiquinone] 1 alpha subcomplex subunit 9_ mitochondrial	0.61	0.42	**Cellular Respiration**
Tax_Id=9606 Gene_Symbol=NDUFAF2 Mimitin_ mitochondrial	0.51	0.36	**Cellular Respiration**
Tax_Id=9606 Gene_Symbol=NDUFB11 Neuronal protein	_	0.65	**Cellular Respiration**
Tax_Id=9606 Gene_Symbol=NDUFB6 NADH dehydrogenase [ubiquinone] 1 beta subcomplex subunit 6	0.60	_	**Cellular Respiration**
Tax_Id=9606 Gene_Symbol=NDUFB9 NADH dehydrogenase [ubiquinone] 1 beta subcomplex subunit 9	_	0.55	**Cellular Respiration**

Tax_Id=9606 Gene_Symbol=NDUFC2;NDUFC2-KCTD14 Uncharacterized protein	0.38	0.40	**Cellular Respiration**
Tax_Id=9606 Gene_Symbol=NDUFS1 NADH-ubiquinone oxidoreductase 75 kDa subunit_ mitochondrial isoform 4	0.64	0.51	**Cellular Respiration**
Tax_Id=9606 Gene_Symbol=NDUFS4 NADH dehydrogenase [ubiquinone] iron-sulfur protein 4_ mitochondrial	_	0.57	**Cellular Respiration**
Tax_Id=9606 Gene_Symbol=NIPSNAP1 protein NipSnap homolog 1 isoform 2	_	0.65	**Cellular Respiration**
Tax_Id=9606 Gene_Symbol=NNT NAD(P) transhydrogenase_ mitochondrial	_	0.50	**Cellular Respiration**
Tax_Id=9606 Gene_Symbol=HSP90AA1 Isoform 1 of Heat shock protein HSP 90-alpha	_	0.63	**Chaperone**
Tax_Id=9606 Gene_Symbol=HSPA2 Heat shock-related 70 kDa protein 2	0.09	0.64	**Chaperone**
Tax_Id=9606 Gene_Symbol=PPIF Peptidyl-prolyl cis-trans isomerase F_ mitochondrial	_	0.61	**Chaperone**
Tax_Id=9606 Gene_Symbol=AFG3L2 Similar to AFG3 ATPase family gene 3-like 2 (Fragment)	0.38	0.64	**Degradation**
Tax_Id=9606 Gene_Symbol=CLPX ATP-dependent Clp protease ATP-binding subunit clpX-like_ mitochondrial	0.41	0.40	**Degradation**
GPD2	_	0.62	**Lipid Metabolism**
Tax_Id=9606 Gene_Symbol=ACADM cDNA_ FLJ78845_ highly similar to Medium-chain specific acyl-CoA dehydrogenase_ mitochondrial	0.63	_	**Lipid Metabolism**
Tax_Id=9606 Gene_Symbol=ACADM Isoform 2 of Medium-chain specific acyl-CoA dehydrogenase_ mitochondrial	_	1.57	**Lipid Metabolism**
Tax_Id=9606 Gene_Symbol=ACADM Putative uncharacterized protein DKFZp686M24262	0.10	0.11	**Lipid Metabolism**
Tax_Id=9606 Gene_Symbol=ACADVL cDNA FLJ56425_ highly similar to Very-long-chain specific acyl-CoAdehydrogenase_ mitochondrial	1.76	_	**Lipid Metabolism**
Tax_Id=9606 Gene_Symbol=FDXR cDNA FLJ36801 fis_ clone ADRGL2007810_ highly similar to NADPH:adrenodoxin oxidoreductase_ mitochondrial	2.96	3.98	**Lipid Metabolism**
Tax_Id=9606 Gene_Symbol=FDXR cDNA FLJ59386_ highly similar to NADPH:adrenodoxin oxidoreductase_ mitochondrial	3.01	1.81	**Lipid Metabolism**

Tax_Id=9606 Gene_Symbol=HADH Isoform 2 of Hydroxyacyl-coenzyme A dehydrogenase_ mitochondrial	_	0.66	**Lipid Metabolism**
Tax_Id=9606 Gene_Symbol=HADHB cDNA FLJ56214_ highly similar to Trifunctional enzyme subunit beta_ mitochondrial	0.65	_	**Lipid Metabolism**
Tax_Id=9606 Gene_Symbol=DHX30 Isoform 2 of Putative ATP-dependent RNA helicase DHX30	0.44	0.38	**mRNA Processing**
Tax_Id=9606 Gene_Symbol=DHX30 Isoform 3 of Putative ATP-dependent RNA helicase DHX30	0.52	0.36	**mRNA Processing**
Tax_Id=9606 Gene_Symbol=PNPT1 59 kDa protein	0.65	0.60	**mRNA Processing**
Tax_Id=9606 Gene_Symbol=ATAD3A Isoform 2 of ATPase family AAA domain-containing protein 3A	2.25	_	**Network Organization**
Tax_Id=9606 Gene_Symbol=FIS1 Mitochondrial fission 1 protein	_	0.65	**Network Organization**
Tax_Id=9606 Gene_Symbol=IMMT Isoform 1 of Mitochondrial inner membrane protein	0.43	0.27	**Network Organization**
Tax_Id=9606 Gene_Symbol=IMMT Uncharacterized protein	_	0.50	**Network Organization**
Tax_Id=9606 Gene_Symbol=IMMT Uncharacterized protein	_	0.64	**Network Organization**
Tax_Id=9606 Gene_Symbol=IMMT Uncharacterized protein	_	0.64	**Network Organization**
Tax_Id=9606 Gene_Symbol=AK2 Isoform 1 of Adenylate kinase 2_ mitochondrial	_	2.07	**Nucleotide Metabolism**
Tax_Id=9606 Gene_Symbol=AK2 Isoform 6 of Adenylate kinase 2_ mitochondrial	_	1.87	**Nucleotide Metabolism**
Tax_Id=9606 Gene_Symbol=NME4 Nucleoside diphosphate kinase_ mitochondrial	0.26	0.28	**Nucleotide Metabolism**
Tax_Id=9606 Gene_Symbol=C21orf33 Isoform Long of ES1 protein homolog_ mitochondrial	_	1.59	**Other**
Tax_Id=9606 Gene_Symbol=PMPCB Mitochondrial-processing peptidase subunit beta	0.33	0.35	**Other**
Tax_Id=9606 Gene_Symbol=SCCPDH Probable saccharopine dehydrogenase	_	0.64	**Other**
Tax_Id=9606 Gene_Symbol=GLRX5 Glutaredoxin-related protein 5_ mitochondrial	0.52	_	**REDOX Homeostasis**
Tax_Id=9606 Gene_Symbol=PRDX5 Isoform Mitochondrial of Peroxiredoxin-5_ mitochondrial	1.52	_	**REDOX Homeostasis**

Tax_Id=9606 Gene_Symbol=OGDH 2-oxoglutarate dehydrogenase_ mitochondrial	1.51	_	**TCA Cycle**
Tax_Id=9606 Gene_Symbol=OGDH cDNA FLJ59557_ highly similar to 2-oxoglutarate dehydrogenase E1 component_ mitochondrial	0.56	_	**TCA Cycle**
Tax_Id=9606 Gene_Symbol=ACO2 Aconitate hydratase_ mitochondrial	0.64	0.63	**TCA Cycle**
Tax_Id=9606 Gene_Symbol=ACO2 cDNA FLJ50886_ highly similar to Aconitate hydratase_ mitochondrial	0.60	0.47	**TCA Cycle**
Tax_Id=9606 Gene_Symbol=DLST;DLSTP1 cDNA FLJ55034_ highly similar to Dihydrolipoyllysine-residue succinyltransferase component of 2- oxoglutarate dehydrogenase complex_ mitochondrial	2.12	0.35	**TCA Cycle**
Tax_Id=9606 Gene_Symbol=IDH3A Isoform 2 of Isocitrate dehydrogenase [NAD] subunit alpha_ mitochondrial	_	1.55	**TCA Cycle**
Tax_Id=9606 Gene_Symbol=SUCLG1 Succinyl-CoA ligase [GDP-forming] subunit alpha_ mitochondrial	1.71	_	**TCA Cycle**
Tax_Id=9606 Gene_Symbol=SUCLG2 Uncharacterized protein	_	0.60	**TCA Cycle**
Tax_Id=9606 Gene_Symbol=TBRG4 cDNA FLJ56153_ highly sim...	_	0.66	**Transcription**
Tax_Id=9606 Gene_Symbol=TFB2M Dimethyladenosine transferase 2_ mitochondrial	0.17	_	**Transcription**
Tax_Id=9606 Gene_Symbol=DAP3 28S ribosomal protein S29_ mitochondrial	2.26	_	**Translation**
Tax_Id=9606 Gene_Symbol=DAP3 28S ribosomal protein S29_ mitochondrial isoform 2	2.53	_	**Translation**
Tax_Id=9606 Gene_Symbol=GFM1 Isoform 1 of Elongation factor G_ mitochondrial	_	1.77	**Translation**
Tax_Id=9606 Gene_Symbol=MRPL11 Isoform 1 of 39S ribosomal protein L11_ mitochondrial	_	0.60	**Translation**
Tax_Id=9606 Gene_Symbol=MRPL22 Isoform 1 of 39S ribosomal protein L22_ mitochondrial	_	0.47	**Translation**
Tax_Id=9606 Gene_Symbol=MRPL41 39S ribosomal protein L41_ mitochondrial	0.65	1.53	**Translation**
Tax_Id=9606 Gene_Symbol=MRPL9 cDNA FLJ59179_ highly similar to 39S ribosomal protein L9_ mitochondrial	_	1.53	**Translation**
Tax_Id=9606 Gene_Symbol=MRPS17 28S ribosomal protein S17_ mitochondrial precursor	_	0.64	**Translation**
Tax_Id=9606 Gene_Symbol=MRPS22 Uncharacterized protein	1.54	_	**Translation**

Tax_Id=9606 Gene_Symbol=MRPS23 28S ribosomal protein S23_ mitochondrial	0.64	0.55	**Translation**
Tax_Id=9606 Gene_Symbol=MRPS28 Uncharacterized protein	_	0.53	**Translation**
Tax_Id=9606 Gene_Symbol=MRPS5 Isoform 1 of 28S ribosomal protein S5_ mitochondrial	_	0.58	**Translation**
Tax_Id=9606 Gene_Symbol=MRPS7 28S ribosomal protein S7_ mitochondrial	_	0.65	**Translation**
Tax_Id=9606 Gene_Symbol=MRPS9 28S ribosomal protein S9_ mitochondrial	_	0.64	**Translation**
Tax_Id=9606 Gene_Symbol=MRRF Isoform 3 of Ribosome-recycling factor_ mitochondrial	_	1.60	**Translation**
Tax_Id=9606 Gene_Symbol=VARS Valyl-tRNA synthetase	_	0.66	**Translation**
Tax_Id=9606 Gene_Symbol=VDAC3 Uncharacterized protein	0.64	_	**Transport**
Tax_Id=9606 Gene_Symbol=LOC285556 hypothetical protein LOC285556	0.18	0.44	**Transport**
Tax_Id=9606 Gene_Symbol=MTX1 Isoform 2 of Metaxin-1	0.41	0.43	**Transport**
Tax_Id=9606 Gene_Symbol=SCP2 non-specific lipid-transfer protein isoform 4 proprotein	1.63	_	**Transport**
Tax_Id=9606 Gene_Symbol=SCP2 non-specific lipid-transfer protein isoform 8 proprotein	6.53	5.55	**Transport**
Tax_Id=9606 Gene_Symbol=SCP2 non-specific lipid-transfer protein isoform 8 proprotein	6.53	5.55	**Transport**
Tax_Id=9606 Gene_Symbol=SLC25A22 Uncharacterized protein	0.55	_	**Transport**
Tax_Id=9606 Gene_Symbol=SLC25A3 Isoform B of Phosphate carrier protein_ mitochondrial	0.58	0.64	**Transport**
Tax_Id=9606 Gene_Symbol=SLC25A3 Isoform B of Phosphate carrier protein_ mitochondrial	0.58	0.64	**Transport**
Tax_Id=9606 Gene_Symbol=SLC25A3 Uncharacterized protein	2.02	_	**Transport**
Tax_Id=9606 Gene_Symbol=TIMM17B Mitochondrial import inner membrane translocase subunit Tim17-B	_	0.60	**Transport**
Tax_Id=9606 Gene_Symbol=TOMM20 Mitochondrial import receptor subunit TOM20 homolog	0.56	0.46	**Transport**

Both OGT and OGA over-expressing cells caused similar expression changes in mitochondrial metabolic pathways. For example, several TCA cycle proteins had altered expression. First, the protein PDHX (pyruvate dehydrogenase protein X component) of the pyruvate dehydrogenase complex, the entry point for acetyl-CoA into the TCA cycle, was deceased in OGT over-expression cells (**Figure 9**). OGA over-expressing cells reduced SUCLG2 (succinyl-CoA ligase GDP-forming beta) of the succinyl-CoA synthetase complex expression while increasing IDH3A (isocitrate dehydrogenase [NAD] subunit alpha) expression of the isocitrate dehydrogenase complex. OGT over-expressing cells increased the expression of both subunits of the α-ketoglutarate dehydrogenase complex, although, one isoform of OGDH (2-oxoglutarate dehydrogenase) was decreased in the OGT over-expressing cells. Both over-expressing cell types exhibited reduced aconitase (ACO2) expression. Not only did OGT/OGA over-expression affect the TCA cycle, but several respiratory chain subunits also had altered expression levels. Complex 1, 4, and ATP synthase subunits showed reduced expression (**Figure 10**). Importantly, protein expression of other subunits of complex 1 and the ETF (electron transfer flavoprotein) complex were increased.

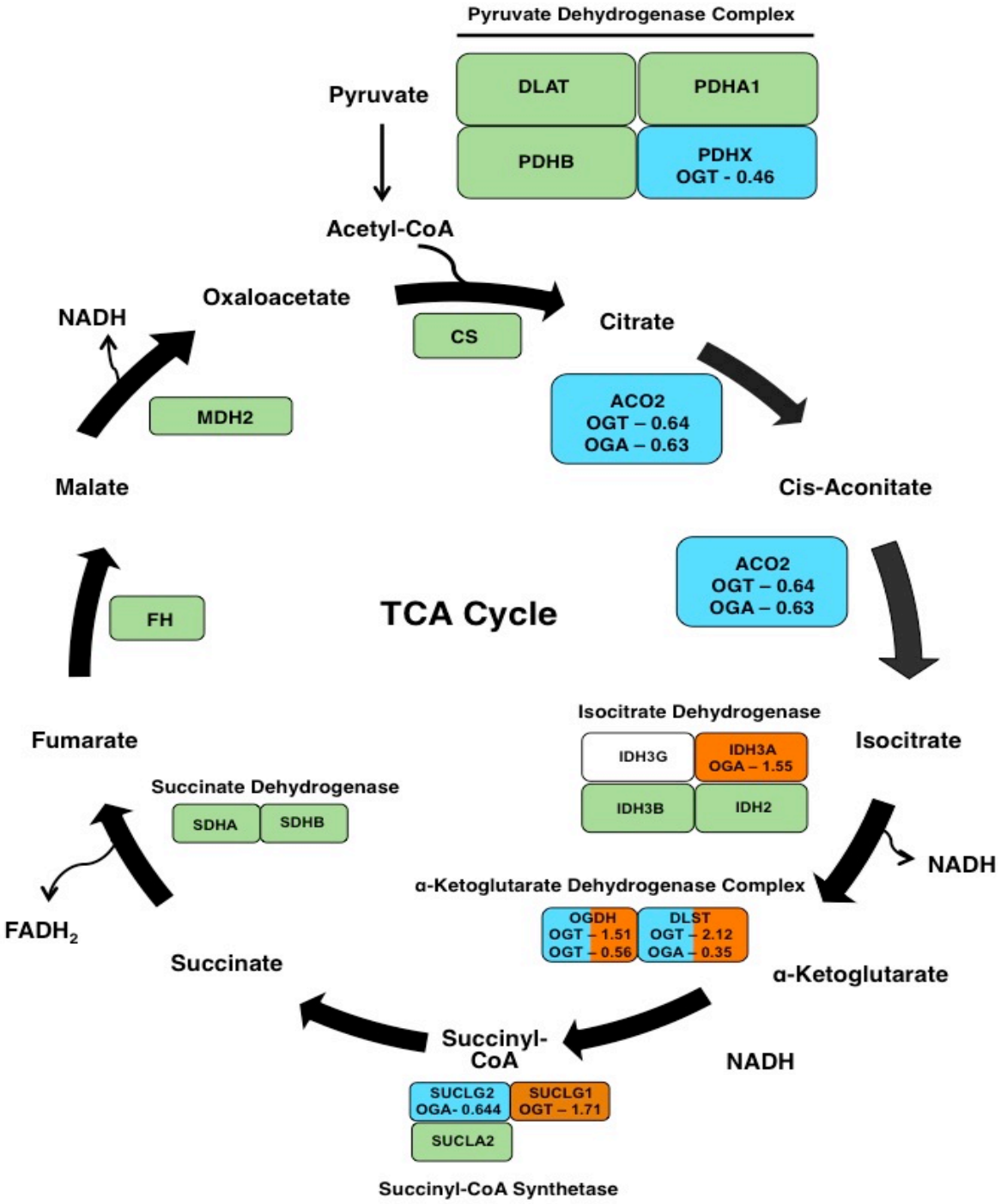

Figure 9: TCA cycle protein expression is altered in OGT/OGA over-expressing cells
Cartoon of the TCA cycle shows enzymes of the cycle shown in blocks. Teal blocks list proteins whose expression decreased in OGT or OGA over-expressing cells. The fold change induced by either OGT or OGA is listed in the box as well. Green blocks indicate no expression changes while proteins in white blocks were not identified.

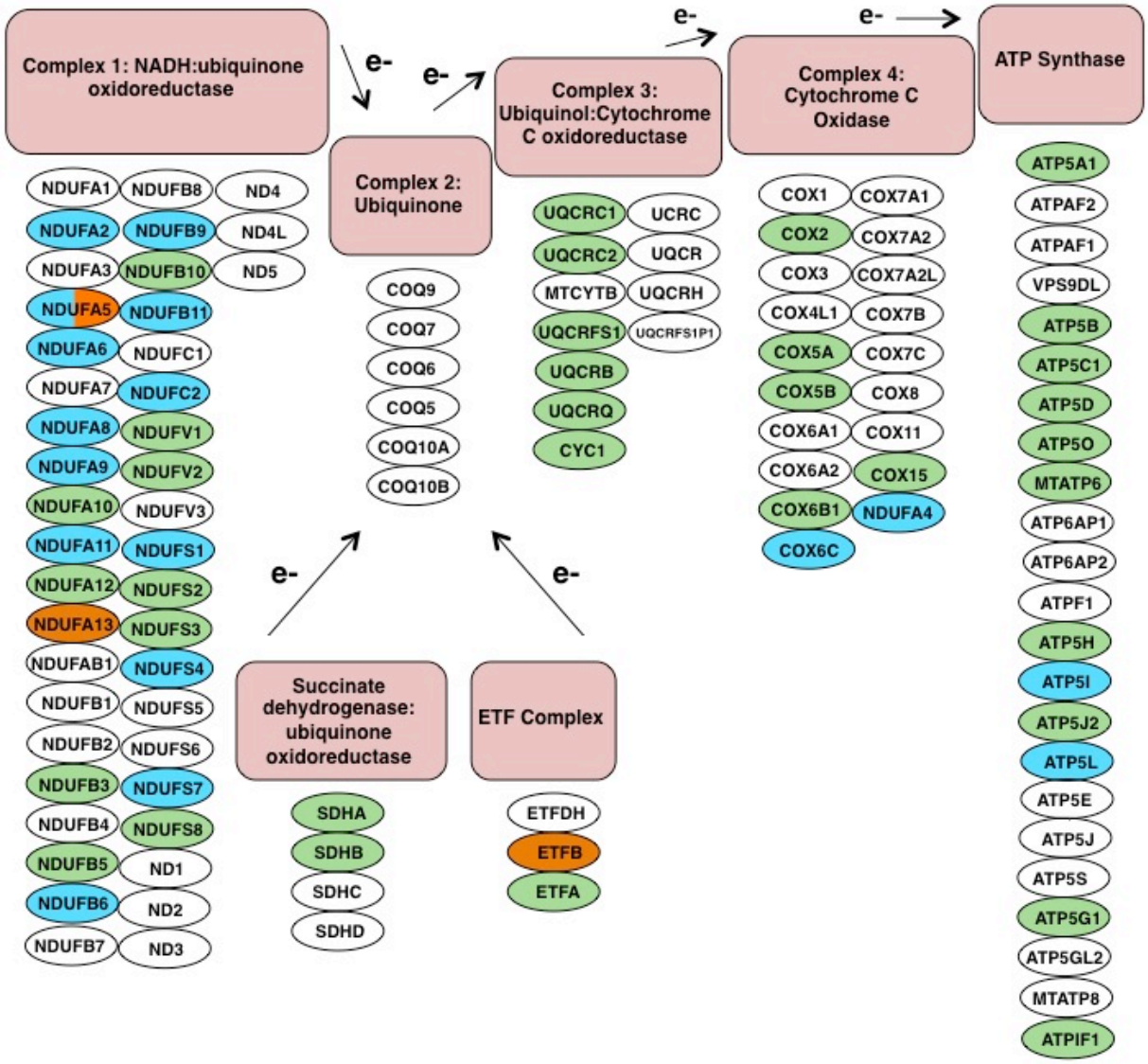

Figure 10: Components of the electron transport chain are altered in OGT or OGA over-expressing cells

In the schematic, electron transport chain proteins (circles) are categorized according to respiratory complex. Green circles indicate identified proteins whose expression does not change; teal circles are proteins whose expression decreases, and orange circles are proteins whose expression increases. White circles are proteins that were not identified in the screen.

2.3.3 Altered O-GlcNAc Cycling Disrupts Mitochondrial Morphology

Next, we used transmission electron microscopy to assess if mitochondrial morphology was disrupted in the OGT/OGA over-expressing cells. Mitochondria from these cells showed a lack of cristae or apparent errors in fission or fusion when compared to GFP control mitochondria (**Figure 11A**). After quantification, OGT/OGA over-expressing cells contained 40-50% abnormal mitochondria compared to 10% in the GFP control cells (**Figure 11B**).

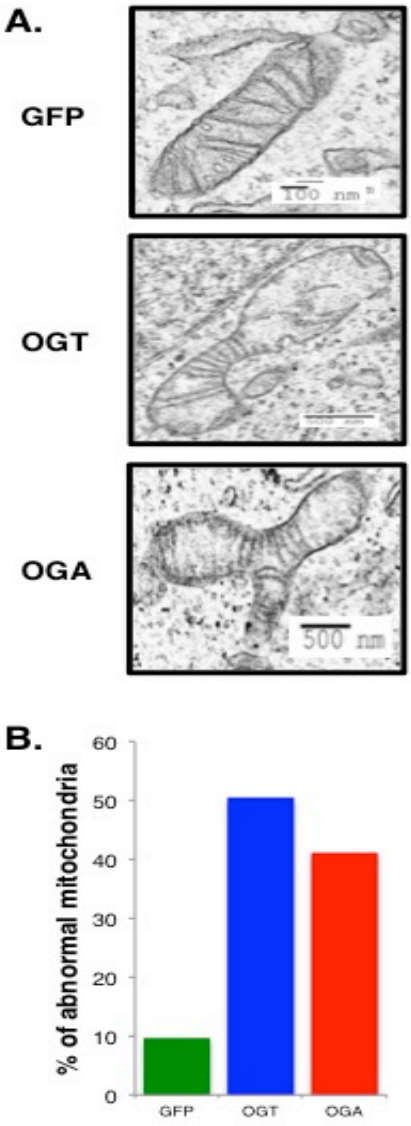

Figure 11: Mitochondrial morphology is disrupted in OGT/OGA over-expressing cells
(**A**) Mitochondria morphology was observed after GFP, OGT, or OGA adenoviral infection by transmission electron microscopy. Scale bars are indicated on each image. (**B**) Mitochondria from the over-expression cells with aberrant morphology and lack of cristae were quantified. The percentage of abnormal mitochondria were calculated and plotted. Counted mitochondria number (n): nGFP = 62, nOGT = 87, nOGA = 85.

2.3.4 OGT/OGA Overexpression Impairs Cellular Respiration and Glycolysis

Since OGT and OGA over-expression altered respiratory chain protein expression and mitochondrial morphology, we measured cellular respiration using an XF24 analyzer. First, we determined the basal respiration rate in these cells. OGA over-expressing cells had significantly decreased baseline oxygen consumption rates compared to GFP control cells (**Figure 12A**). Following this measurement oligomycin, an ATP synthase inhibitor, was added. This compound allows for the measurement of the proton leak rate, which determines mitochondrial thermogenesis. Thermogenesis was modestly reduced in the OGT and OGA over-expressing cells (**Figure 12B)**. From this set of data, we calculated the percentage of total mitochondrial oxygen consumption used for ATP production. Under basal conditions, the percentage of mitochondrial oxygen consumption supporting ATP production was slightly lower in OGA over-expressing cells (**Figure 12C**). Next, we added FCCP (Carbonyl cyanide 4-trifluoromethoxy-phenylhydrazone) in order to depolarize the membrane. From these data, we calculated the mitochondria reserve capacity. OGT/OGA over-expressing cells had little reserve capacity as compared to control cells (**Figure 12D**). Accordingly, the absolute maximal respiration rate was significantly reduced in the OGT/OGA over-expressing cells (**Figure 12E**). Overall, these cells appeared to be bioenergetically stressed even under basal conditions, as the amount of oxygen they consumed under those conditions represented a higher percentage of their total oxygen consumption capacity (**Figure 12F**).

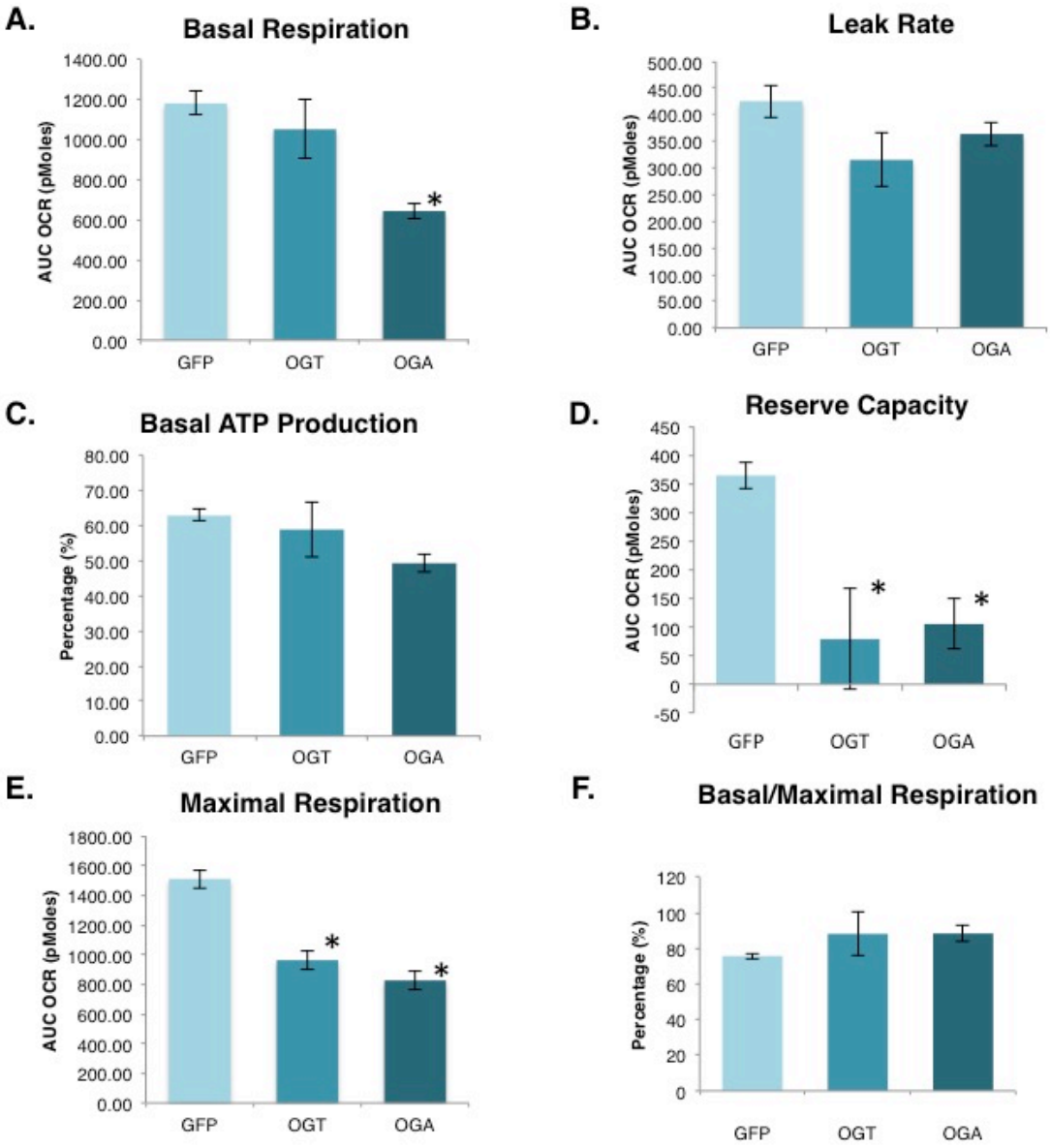

Figure 12: OGT/OGA over-expressing cells have reduced cellular respiration

(**A**) Basal mitochondria respiration (OCR) is measured in SY5Y over-expression cells using an XF24 analyzer. (**B**) ATP synthase inhibitor oligomycin is added to the cells to block ATP production, allowing for the measurement of the proton leak rate. (**C**) The percentage of oxygen consumed to generate ATP under basal respiration conditions was calculated from the proton leak and basal respiration measurements. (**D**) FCCP, which depolarizes the mitochondrial outer membrane, was added to cells to measure the maximal increase in oxygen consumption. Reserve capacity was calculated by subtracting maximal oxygen consumption from basal consumption (**E**) Antimycin and rotenone, which inhibits complex I and II of the ETC, was added to measure the non-mitochondrial oxygen consumption. Maximal respiration was calculated by subtracting non-mitochondrial respiration from the highest rate of oxygen consumption. (**F**) The respiration capacity being utilized at the basal level was calculated by using the ratio of basal respiration

over the maximal respiration. Mean ± SEM, replicate number (n): 7, *$P < 0.05$ GFP vs OGT/OGA.

Lastly, we measured cell glycolysis flux to ascertain if the over-expressing cells were shifting towards a more anaerobic pattern of energy production. Cells were placed into the XF24 analyzer and starved of glucose for 1 hour. After starvation, glucose was added back to cells and the extracellular acidification rate was measured. Both OGT and OGA over-expressing cells had significantly lower basal glycolysis rates (**Figure 13A**). After the addition of oligomycin, we measured the glycolysis rate that resulted when mitochondrial ATP production was inhibited, and used this parameter to calculate the glycolysis reserve capacity. These cells had a lower glycolysis capacity than control cells (**Figure 13B**), and OGA over-expressing cells did show a significant reduction in maximal capacity compared to control cells (**Figure 13C**). Finally, we calculated the percentage of glycolysis capacity being used by these cells under unstressed conditions. No significant difference was found between the control and over-expression cells (**Figure 13D**). Therefore, with over-expression of either OGT or OGA the basal and maximal glycolysis rates were proportionally reduced.

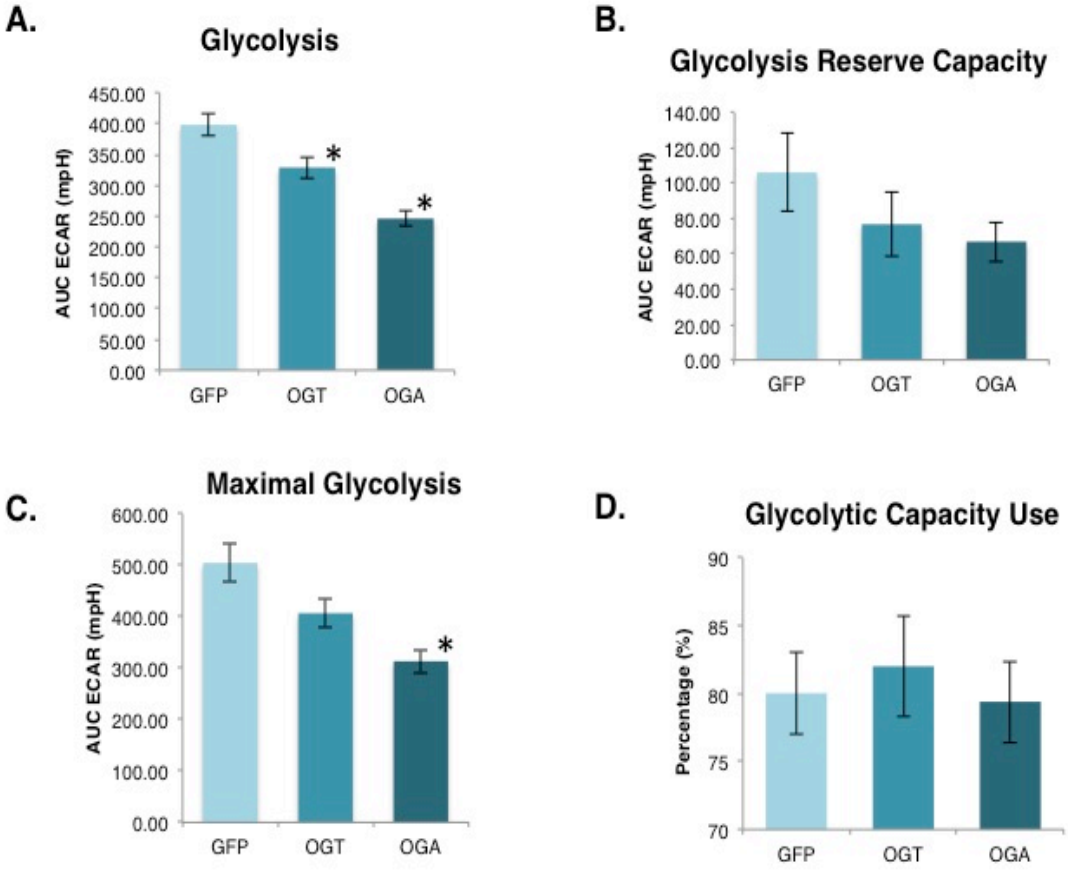

Figure 13: Glycolysis is lower in OGT/OGA over-expressing cells

(**A**) Extracellular acidification rate (ECAR) was measured after the addition of glucose to starved SY5Y over-expression cells allowing for the glycolysis calculation. (**B**) ATP synthase inhibitor oligomycin was added to block ATP production causing an increase in extracellular acidification rate. Glycolytic reserve capacity was calculated by subtracting the maximal ECAR from the basal ECAR. (**C**) The addition of 2-deoyglucose blocks glycolysis, allowing for the measurement of the non-glycolytic ECAR. Maximal glycolytic rate was calculated by subtracting non-glycolytic ECAR from maximal ECAR. (**D**) Glycolytic capacity use under basal condition was calculated by using the ratio of basal glycolysis over the maximal glycolysis. Mean ± SEM, replicate number (n): 7, $*P < 0.05$ GFP vs OGT/OGA.

2.4 Discussion

Increasing evidence points to a critical role for OGT and OGA in regulating mitochondrial function. We decided to explore how increased OGT or OGA cellular expression affects mitochondrial protein expression and function. By employing a proteomics-based approach to explore how O-GlcNAc cycling affects mitochondria function, we demonstrate that OGT or OGA over-expression resulted in altered mitochondrial protein expression. Proteins showing the greatest expression changes were protein transport, translation, and respiration chain proteins. The alteration in mitochondrial protein expression had a deleterious effect on the morphology of the mitochondria; furthermore, the respiration capacity was dramatically impaired after OGT/OGA over-expression. Together these data suggest a complicated and important role for O-GlcNAc cycling in the homeostasis of mitochondrial protein expression and function.

As expected, mitochondrial proteins identified in the SILAC experiment were composed primarily of proteins critical for mitochondrial function, such as respiration, translation, and transport proteins. Since we over-expressed either the nuclear/cytoplasmic forms OGT or OGA, then protein expression changes are likely due to a variety of cellular defects. Altered O-GlcNAc cycling affects both transcription and translation. Both OGT and OGA are important in modulating gene transcription [55]. For example, RNA polymerase II is modified by O-GlcNAc [56], and O-GlcNAcylation of RNAP promotes the formation of the transcriptional preinitiation complex [57]; however, for transcriptional elongation to proceed, OGA needs to remove the O-GlcNAc to facilitate the phosphorylation of the RNAP C-terminal tail and elongation [57]. O-GlcNAcylation is also important for proper protein translation, with alterations to cellular O-GlcNAc levels impinging on the function of the translational machinery [58].

Potentially, transcriptional or translational changes in mitochondrial transport proteins such as the Translocase of the Mitochondrial Outer Membrane (TOMM) family can then have a secondary effect on mitochondrial protein expression. In fact, we measured declines in TOMM20 as well as TIMM17B (Translocase of Mitochondrial Inner Membrane). We can envision impairment of mitochondrial protein transport into the mitochondria causing an increase of mitochondrial proteins in the cytoplasm and a decrease within the mitochondria. Although, the proteins examined in the orthogonal validation were altered in the mitochondria; cytoplasmic expression appeared to mirror the mitochondrial expression, suggesting that the proteins we validated did not appear to have problems entering the mitochondria (**Figure 8**). Besides potential expression changes being caused by alterations in transcription, translation or protein transport into the mitochondria, OGT/OGA over-expression could lead to alternative processing of mRNA transcripts, leading to expression changes in isoforms or splice variants of a given protein. We potentially see this occurring with proteins such as the TCA cycle protein OGDH and ACADM, which is involved in fatty acid β-oxidation.

The expressions of numerous respiratory chain proteins are also regulated by O-GlcNAc cycling (**Figure 10**). We identified 24 NADH dehydrogenase ubiquinone 1 (NDUF) members from complex 1 of the electron transport chain. The expression of several of these family members was altered in the OGT/OGA over-expression cells. For example, NDUFA9 protein expression was decreased in OGA over-expression cells; interestingly, NDUFA9 is O-GlcNAcylated at Ser156 [44]. O-GlcNAcylation of NDUFA9 was increased in cardiac myocytes exposed to high glucose conditions, which correlated with impaired mitochondrial function. Mitochondrial function and a decrease in NDUFA9 O-GlcNAcylation were partially restored under these high glucose conditions after adenoviral-mediated expression of OGA [44]. Similar

to our study, OGA over-expression also lowered NDUFA9 expression in these cells [44], suggesting that OGA expression influences NDUFA9 expression. These data also suggest an important role for maintaining homeostatic levels of O-GlcNAc in the regulation of Complex 1 proteins. Complex 1 deficiency is the most common electron transport chain defect [59]. Mutations in complex 1 proteins or gain/loss of expression alter complex 1 assembly and impair the electron transport chain, leading to numerous physiological consequences [59]. Disease or age-related changes to the O-GlcNAc cycling rate, therefore, could profoundly affect complex 1 subunit expression and holoenzyme function.

Morphologic disruption of the mitochondria (**Figure 11**), manifesting here as perturbed cristae formation, would associate with abnormal respiration chain formation. Not surprisingly, the measured declines in respiratory chain protein expression and disrupted mitochondrial morphology lead to a reduced basal oxygen consumption in the over-expression cells (**Figure 12**). Further, overexpression of OGA pushed basal mitochondrial respiration towards its maximum capacity, which was itself reduced. Interestingly, OGT and OGA over-expressing cells did not attempt to compensate for this apparent respiration stress by increasing glycolysis, as overall glycolysis flux in these cells is decreased (**Figure 13**). Therefore, the net effect of altered O-GlcNAc cycling is a reduction in both the oxidative metabolism infrastructure and glycolysis, a combination expected to place cells in a state of relative bioenergetic jeopardy.

In conclusion, we have demonstrated that altered O-GlcNAc cycling rates impact mitochondrial protein expression, morphology, and respiration. We show that over-expression of the O-GlcNAc cycling enzymes OGT or OGA cause, respectively, an increase or decrease in O-GlcNAc levels. Importantly, OGT/OGA over-expression will increase the rate of addition and removal of the O-GlcNAc modification and disruption of the basal rate of O-GlcNAc cycling

impairs cellular function [60]. These data argue that mitochondrial function is directly related to the rate of O-GlcNAc cycling, and alteration of basal O-GlcNAc cycling rates either by disease or aging would have a profound effect on mitochondrial function. Moving forward, subsequent investigation into how altered O-GlcNAcylation affects mitochondrial protein expression and function in metabolic diseases such as diabetes, Alzheimer's, or cancer should be a high priority

Chapter 3: O-GlcNAc is a Critical Regulator for Mitochondrial Function and Energy Metabolism

Reproduced with permission from Tan, E.P., McGrea, S.R., Graw, S., Tessman, R., Koppel, S.J., Dhakal, P., Zhang, Z., Machacek, M., Zachara, N.E., Koestler, D.C., Peterson, K.R., Thyfault, J.P., Swerdlow, R.H., Krishnamurthy, P., DiTacchio, L., Apte, U., and Slawson, C. (2017). ***Sustained O-GlcNAcylation Reprograms Mitochondrial Function to Regulate Energy Metabolism.*** *Submitted.*

3.1 Introduction

Chronically impaired mitochondrial respiration and uncontrolled reactive oxygen species (ROS) generation contribute to complex, chronic diseases [61]. Treatment with glucosamine (GlcN), a common amino-sugar, improved mitochondrial function and extended lifespan in both *C. elegans* and mice. GlcN treatment increased mitochondrial respiration and transiently induced mitochondrial ROS generation, followed by a significant reduction in ROS [62]. The initial transient ROS induction promotes mitochondrial biogenesis and improves anti-oxidant response, resulting in lifespan extension [62]. Interventions that improve mitochondrial function and reduce uncontrolled ROS production will have widespread clinical applications in the treatment of chronic disease. Here, we assert that O-GlcNAc regulates mitochondrial function and the oxidative stress response.

O-GlcNAc post-translational modifications connect nutrient sensing with mitochondrial dysfunction. O-GlcNAcylation is the addition of a single O-linked β-D-*N*-acetylglucosamine sugar moiety to serine or threonine residues in nuclear, cytoplasmic, and mitochondrial proteins [63]. O-GlcNAcylation is facilitated by two functionally opposing enzymes, O-GlcNAc transferase (OGT) catalyzes the addition of O-GlcNAc, whereas, O-GlcNAcase (OGA)

hydrolyzes the modification [63]. During catalysis, OGT uses the nucleotide sugar UDP-GlcNAc generated from the hexosamine biosynthetic pathway (HBP). The HBP is tightly regulated by the enzyme glutamine fructose-6-phosphate aminotransferase 1 (GFAT1). GlcN feeds into the HBP downstream of GFAT1 and increases cellular O-GlcNAcylation by elevating the synthesis of UDP-GlcNAc [64]. Therefore, GlcN influence on mitochondrial function and lifespan extension could be mediated by O-GlcNAc. Because UDP-GlcNAc synthesis relies on the integration of multiple metabolic pathways, O-GlcNAcylation can reflect changes in nutrients [29]. Chronic disruptions in O-GlcNAcylation due to nutrient imbalance influences metabolic diseases [13, 14].

O-GlcNAc is a key regulator of mitochondrial function. Both OGT [10] and OGA localize to the mitochondria [11], and the Pyrimidine Nucleotide Carrier 1 (PNC1) transports UDP-GlcNAc into the mitochondria, providing substrate for OGT [11]. Electron transport chain (ETC) subunits are modified by O-GlcNAc [12], suggesting that O-GlcNAc modulates ETC activity. Short-term high glucose treatment elevates O-GlcNAcylation but suppresses ETC activity and ATP production in rat cardiomyocytes [30], whereas, short-term OGA inhibition in rats increased oxygen consumption in isolated mitochondria [12]. OGT or OGA overexpression in SH-SY5Y neuroblastoma cells alters the mitochondrial proteome, including several TCA cycle and ETC proteins [65]. The loss of ETC protein expression adversely affected mitochondrial shape and impaired respiration. These data indicate O-GlcNAc is essential for the proper regulation of mitochondrial function and energy metabolism.

Here, we report that increasing O-GlcNAcylation in cell lines and mice by inhibiting OGA or GlcN supplementation reprograms mitochondrial function and changes energy metabolism. Sustained elevation in O-GlcNAc lowered respiration and reduced ROS generation.

These changes were due to transcriptional reprograming of the proteome and a decrease in the transcription factor Nuclear factor (erythroid-derived)-like 2 (NRF2)-mediated oxidative stress response. In contrast, OGT liver knockdown severely impaired mitochondrial function, increased ROS levels, and activated the NRF2 antioxidant response. Together, these data demonstrates distinct roles for O-GlcNAc in modulating mitochondrial function, and provides new insights into how pharmacological targeting of O-GlcNAc protects against aging and metabolic diseases.

3.2 Methods

3.2.1 Cell Culture

Both SH-SY5Y and NT2 cells were cultured in DMEM media (Sigma), 44 mM sodium bicarbonate (Sigma), 5 mM galactose (Fisher), 15 mg/L phenol red (Sigma), and supplemented with 10% fetal bovine serum (FBS; Gemini), 1% penicillin/streptomycin (Sigma), 1% GlutaMAX (Gibco). First, cells were adapted to the 5 mM galactose media for two weeks prior to treatment with 10 μM Thiamet-G (TMG, S.D. Specialty Chemicals) or 0.35 mM glucosamine (GlcN, Sigma) for at least three weeks prior to experiments. Media were replenished daily.

3.2.2 Animal Protocols and Models

The University of Kansas Medical Center Animal Care and Use Committee approved all experiments in this study. Two-month-old male C57Bl/6J mice were purchased from Jackson Laboratory (Bar Harbor, ME). All mice were housed using a standard 12 h light/dark cycle with access to chow and water ad libitum. Mice were treated with a 50 mg/kg Thiamet-G intraparietal injection every other morning for 15 days for a total of 8 doses per mouse. After completion of dosing, mice were fasted for 16 hrs before isoflurane (Fisher) anesthesia assisted cervical dislocation on day 16.

Ogt^{tm1Gwh} mice were obtained from Natasha Zachara, PhD at John Hopkins University and liver specific KO of OGT was performed by treating male mice with $5.0x10^{11}$ virus particles of AAV8.TBG.PI.Cre.rBG vector (University of Pennsylvania vector core) dissolved in 200uL of sterile PBS via IP injection.

3.2.3 Cell Lysis and Immunoblotting

Cells were lysed, samples prepared for SDS-PAGE, and immunoblotted as described previously [65]. At least three independent experiments were repeated for all immunoblotting. Relative protein levels were analyzed using ImageJ 3.2 (NIH) and were normalized to actin or GAPDH [66].

3.2.4 Cell Respiration, Isolated Mitochondrial Respiration and Glycolysis Measurement

An XF24 analyzer (Agilent Seahorse XF Technology, Santa Clara, CA) was used to measure cellular respiration and glycolysis. 75,000 control, TMG, or GlcN treated cells were seeded per well in a Seahorse 24-well cell culture plate 24 h prior to experimental assay. For respiration assays, cells were incubated in unbuffered DMEM (Sigma), 25 mM Glucose (Sigma), Phenol Red (Sigma), 200 mM GlutaMax-1 (Gibco), NaCl (Fisher), at 37°C in a CO_2 free incubator for 1 h prior to loading. OCR was measured over a period of 100 min. Drugs oligomycin (0.5 μM, Sigma), FCCP (0.5 μM, Sigma), antimycin A (0.2 μM, Sigma) and rotenone (0.1 μM, Sigma) were added to each well sequentially at various time points during the assay [65].

For animal tissues, 15 μg per well of mouse liver or brain mitochondria was prepared in mitochondrial assay solution (MAS) [67]. Respiration was initiated by adding mitochondria, followed by sequential addition 6 mM ADP (Sigma), 1 μM FCCP (Sigma), 1 μM oligomycin (Sigma) and 4 μM antimycin A (Sigma) [67].

For glycolysis assays, ECAR was measured over a period of 100 min. Glucose (25 mM) oligomycin (1 μM), and 2-Deoxy-D-glucose (2-DG, 100 mM, Sigma) were added at specific time points during the assay [65].

3.2.5 Statistical Analysis

Statistical significance of all results, with the exception of the 24-hour time-point Avg RER, locomotion, and Avg EE, were assessed using a two-sample t-test with $p < 0.05$ considered to be statistically significant. All data were generated using at least three independent experiments and were represented as mean ± standard error. The 24 h time point Avg RER, locomotion, and Avg EE were assessed using permutation test with $p < 0.05$ considered to be statistically significant.

3.2.6 Antibodies

All primary and secondary antibodies used for immunoblotting were used at a concentration of 1:1,000 and 1:10,000 dilution respectively. Anti-O-linked *N*-acetylglucosamine antibody (RL2, ab2739) was purchased from Abcam. Both anti-OGT (AL-34) and OGA (345) were gracious gifts from the Laboratory of Gerald Hart in the Department of Biological Chemistry at the Johns Hopkins University School of Medicine. Anti-actin (A2066), NRF2 (ab62352), mTFA (ab47517), GAPDH (ab9484), Oxidative Stress Defense (Catalase, SOD1, TRX, smooth muscle Actin) Cocktail (ab179843), PRX Pathway (TRX, TXNRD1, PRX1) Cocktail (ab184868), Citrate Synthase (ab96600) and NADPH Oxidase 4 (ab79971) were purchased from Abcam. Anti-DLP1 (611113) was purchased from BD Biosciences, anti-Mfn1 (sc-50330) and anti-p53 (sc-126) were purchased from Santa Cruz. Anti-cleaved PARP (9542) and anti-lamin B1 (D4Q4Z) were purchased from Cell Signaling Technology, and anti-Mfn2 (M6444) was purchased from Sigma.

3.2.7 Mitochondrial Purification from Cells and Tissues.

Mitochondria were isolated from SH-SY5Y cells using the modified cavitation method described previously [65]. Briefly, 2 x 10^8 cells were trypsin-digested off the plate and washed twice with pre-chilled PBS, then resuspended into 3 mL of the mitochondrial isolation medium. The cell suspensions were transferred into a pre-chilled cavitation chamber (nitrogen bomb; Parr Instrument Company, Moline, IL) and subjected to 900 psi for 15 min. Subsequently, the pressurized cell suspension was collected from the cavitation chamber, followed by centrifugation at 1,000 x g for 10 min to pellet the cell debris. The clear supernatant was collected and centrifuged at 12,000 x g for 15 min. Crude mitochondrial pellet was washed three times with 500 µl of isolation medium. Washed pellet was lysed with NP-40 lysis buffer.

Both mouse brain and liver mitochondria were isolated using the modified method of two differential centrifugations [67]. Promptly after euthanasia (brain < 30 s, liver < 1 min), tissues were rinsed twice with ice cold PBS, homogenized (Teflon glass homogenizer with 15 strokes), and extracted in ~10 volumes of mitochondrial isolation buffer (MSHE+BSA). All subsequent steps were performed on ice. Homogenate was centrifuged at 800 x g for 10 min at 4 °C. Supernatant was decanted through 2 layers of cheesecloth to a new tube, followed by further centrifugation at 8,000 xg for 10 min at 4 °C. Mitochondrial pellet was washed once with MSHE+BSA and final pellet was resuspended with minimal volume of MSHE+BSA. Total protein concentration was determined using BCA protein assay kit (Thermo Fisher Scientific) per manufacturer's instruction.

3.2.8 Total RNA Isolation and Reverse Transcription (RT)-PCR

Total RNA was isolated by using TRI reagent solution (Ambion) per manufacturer's instruction. Approximately 2 x 10^6 cells were resuspended in 1 mL TRI reagent solution; then 200 µl of chloroform (Fisher) was added to extract RNA. Upon centrifugation, an equal amount of isopropanol (Fisher) was added to the upper layer solution containing RNA. RNA pellets were precipitated by centrifugation, washed once with 70% ethanol, air-dried, and the pellet was dissolved in nuclease free water (Life Technologies) [68].

RNA concentration was measured using a Nanodrop 2000c (Thermo) and 1 µg of total RNA was reverse transcribed using iScript Reverse Transcription Supermix (Bio-rad) per manufacturer's instruction. Total volume of 20 µl of each completed reaction mix was incubated in a thermal cycler (Model 2720, Applied Biosystems). Protocol was as followed: priming 5 min at 25 °C, RT 30 min at 42 °C, and RT inactivation 5 min at 85 °C. cDNA products were diluted with nuclease free water, 1:10 dilution, and analyzed by qPCR [68].

3.2.9 qPCR Assay

qPCR assays on cDNA samples were done using SsoAdvanced Universal SYBR Green Supermix (Bio-Rad) per manufacturer's instruction. 2 µl of cDNA were used with a total reaction volume of 20 ul. Primers used for OGT were: F, CATCGAGAATATCAGGCAGGAG; R, CCTTCGACACTGGAAGTGTATAG [68]; OGA were: F, TTCACTGAAGGCTAATGGCTCCCG; R, ATGTCACAGGCTCCGACCAAGT [68]; GAPDH were: F, CCACATCGCTCAGACACCAT; R, CCAGGCGCCCAATACG; GFAT1 were: F, AGCCCTCTGTTGATTGGTGT; R, TCCATCTGGAGTGTTTGCAC; Nrf2 were: F, CCAGCACATCCAGTCAGAAA; R, GCATGCAGTCATCAAAGTACAAA; TXNRD1 were: F, GCAATCCAGGCAGGAAGATT; R, AGGCCACAAGCACCATATTC; GNG1 were: F,

GAGCAGCTTCGCAAAGAA; R, AGGATCCTCTCCAGAACG; TFPI2 were: F, CAGGTTTCCAGATGAAGCTACT; R, GAGTCACATTGGCAGAGCA; ATF4 were: F, GAGAGAAGATGGTAGCAGCAAA; R, TTCTTCTGGCGGTACCTAGT; and IGF2 were: F, CCTGGAGACGTACTGTGCTA; R, GACTGCTTCCAGGTGTCATATT. A 96-well PCR plate (Midsci) with the reaction mixture was loaded onto CFX96 Touch Real-Time PCR Detection System (Bio-Rad). The protocol was as follow: polymerase activation and DNA denaturation 30 s at 95 °C, amplification denaturation 5 s at 95 °C and annealing 30 s at 60 °C with 40 cycles, and melt curve 65-95 °C with 0.5 °C increment 5s/step.

3.2.10 OGA Activity Assay

Whole cell extract samples (60 µg/reaction) were lysed using NP-40 lysis buffer. O-GlcNAcase activity was assayed in a total reaction volume of 200 µl (including 10 µl of 500 mM sodium cacodylate (Sigma), pH 6.4, 3% BSA (Sigma), 2 µl of 100 mM *p*-Nitrophenyl-*N-acetyl-β-D-glucosaminide* (Sigma), water, and cell extract) at 37 °C for up to two hours. Reactions were stopped with 100 µl of 500 mM sodium carbonate (Sigma) every 30 min subsequently and the absorbance at 400 nm was measured using a plate reader (BioTek Instrument). One unit is the amount of enzyme required to catalyze the release of *p*-nitrophenyl from 1 pmol of *p*NP-O-GlcNAc/min at 37°C [69]. These samples were assayed in a 96-well plate (pureGrade S-781671, BRAND*plates*).

3.2.11 JC-1 Staining for Mitochondrial Membrane Potential

Mitochondrial membrane potential was analyzed with the potential-dependent dye JC-1 (Life Technologies). 2 µM of JC-1 in Hanks' Balanced Salt solution (HBSS, Sigma) was added to 2 x 10^6 cells per sample at 37 °C, 5% CO_2 for 30 min. Cells were washed once and resuspended in

500 µl of warm HBSS. Cells were analyzed by flow cytometers with 488 nm excitation and gated for singlet cells excluding cell debris. JC-1 dye exhibits a potential-dependent accumulation in mitochondria via a fluorescence emission shift from green (~529 nm) to red (~590 nm). Mitochondrial polarization was determined by red/green intensity ratio.

3.2.12 Transmission Electron Microscopy

Long-term TMG and GlcN treated SY5Y cells were prepared for electron microscopic experiments as previously described [65]. Cells were seeded and cultured on Thermanox (Fisher) coverslips 24 h prior to fixation. Cells were fixed with 2% glutaraldehyde in 0.1 M cacodylate buffer, pH 7.4, and post fixed with 1% osmium tetraoxide/0.3% potassium ferricyanide. Cells were dehydrated in a graded series of 50, 70, 80, 95 and 100% ethanol. Coverslips were embedded in 100% epoxy resin, and the resin was cured overnight at 60°C. Thin sections of 70 – 90 nm were cut on a Reichert Ultracut-S (Reichert Technologies, Buffalo, NY) and stained with uranyl acetate and lead citrate. Images were captured at 80 kV using a JEOL JEM-1400 Transmission Electron Microscope (JEOL USA, Peabody, MA) equipped with a Lab6 gun at the University of Kansas Medical Center EM Core Laboratory.

3.2.13 Complex I Activity Assay

Crude isolated mitochondria were used for the complex I activity. A modified method following the decrease in NADH absorbance at 340 nm that occurs when ubiquinone (CoQ1, Sigma) is reduced to ubiquinol was used for the complex I activity assay. CoQ1 (50 µM) was used to initiate the reaction at 30°C. After 5 min, rotenone (10 µM) was added to obtain non-complex I activity. Total protein concentration was measured using the DC assay kit (Bio-rad) as instructed by the manufacturer. Finally, complex I activity was expressed as nano moles per min per milligram of protein [70].

3.2.14 Cytochrome c Oxidase and Citrate Synthase Activity Assays

Complex IV (COXIV) and citrate synthase (CS) Vmax activities in TMG or GlcN treated SH-SY5Y cells were evaluated in both whole cell and isolated mitochondria. Whole cells were trypsinized and washed twice with ice-cold 1X PBS, and then pelleted by centrifuging at 1,000 x g for 3 min. The whole cell pellets were resuspended in ice-cold PBS at a concentration of 30 x 10^6 cells/mL. Mitochondria were isolated as described before. A total of 40 x 10^6 cells were used for the mitochondrial isolation and the mitochondria pellets were resuspended in 400 µl of the mitochondrial isolation buffer. Both whole cell and isolated mitochondrial COXIV and CS Vmax activities in non-treated and TMG- or GlcN-treated SH-SY5Y cells were determined as previously described [71]. COXIV Vmax activity was normalized both to protein concentration and to CS activity.

3.2.15 Immunofluorescence Microscopy

Cells were cultured on microscope slides (Fisher) and were washed with 1X PBS, and fixed with 4% Paraformaldehyde (Sigma) for 20 min. Cells were permeabilized with 0.1% Triton X-100 (Sigma) in ice cold PBS and then blocked with a TBST blocking solution (0.2% azide, 0.2% powdered dry milk, 12% chicken serum, 1% BSA, 100 mM glycine, 0.1% Triton-X 100 in TBST, pH 7.5) for 1 h. Tom20 (1:500) in TBST blocking buffer was applied overnight. Slides were washed with TBST and incubated with fluorescent secondary antibodies (1:500 mouse Alexa-fluor 488 nm Life Technologies) for 1 h. DAPI solution (PBS, 0.01% Triton-X 100, 0.001% DAPI, Sigma) was applied for 20 min. Finally, slides were washed and mounted on cover slips using ProLong Gold Anti-fade (Life Technologies) [66].

3.2.16 cDNA Library Preparation

cDNA library was prepared using Illumina TruSeq Stranded mRNA sample preparation kit (Illumina) as manufacturer's instruction. Total RNA was isolated using the same method as previously described and 800 ng of the total RNA per reaction was used to initiate the protocol.

3.2.17 RNA Sequencing Analysis

The quality of RNA sequencing results was first assessed using FastQC (0.11.2). Then, RSEM (1.2.22) was utilized to align the reads to the human reference genome HG38 and to calculate gene expression values. EdgeR (3.14.0) was then used to normalize the expression values using the TMM-method (weighted trimmed mean of M-values), and for differential expression analyses. First, the negative binomial conditional common likelihood was maximized to estimate a common dispersion value across all genes (estimateCommonDisp). Next, tagwise dispersion values were estimated by an empirical Bayes method based on weighted conditional maximum likelihood (estimateTagwiseDisp). Finally, the differential gene expression was calculated by computing genewise exact tests for differences in the means between two groups of negative-binomially distributed counts. Hierarchical clustering analysis was determined using Euclidean distance. The following R-packages were utilized for calculations and visualizations: gplots and edgeR.

To reduce the burden of multiple testing in differential gene expression analyses, a filter was initially applied to reduce the number of genes. Genes were removed if they did not present a meaningful gene expression across all samples; only genes with cpm (counts per million) of >10 in least two samples were considered in differential expression analyses involving the heat

map, volcano plots, and pie chart. A cpm of >100 threshold was used for the IPA analysis. The Benjamini and Hochberg procedure was used to control the false discovery rate (FDR).

3.2.18 Pathway and Gene Set Enrichment Analysis (GSEA)

Ingenuity Pathway Analysis (IPA) software (Ingenuity® QIAGEN, www.ingenuity.com) was used to compare biological functions or canonical pathways in non-treated, long-term TMG- or GlcN-treated SH-SY5Y cells. Flexible format and Illumina HumanRef-8 v3.0 array platforms were the only parameters altered from default IPA settings for the Core analyses used to evaluate upregulated and downregulated genes (fold change > 1.3, $p < 0.05$).

GSEA analysis was done using the javaGSEA desktop software. The default settings were used, except the permutation type was set to Gene_set with 1000 permutation type, and the metric for ranking genes was set to Diff_of_Classes (normalized expression data used were $\log_2$ transformed) when executing GSEA. All five gene set collections (c1-c6, h1) were queried from the Molecular Signatures Database (MSigDB) version 3.1.

3.2.19 ROS Detection Assay

Cells were analyzed for reactive oxygen species levels using a ROS-ID Total ROS Detection Kit (Enzo Life Sciences) per manufacturer's protocol. Briefly 2 x 10^5 cells/well of control, prolonged TMG- or GlcN-treated cells were seeded in a 96-well plate (pureGrade BRAND*plates* Midsci) a day prior to the assay. Cells were treated with ROS detection reagent at 37°C for 1 h and ROS level was measured via a fluorescence plate reader (TECAN Infinite M200, Switzerland) and quantified as level of fluorescence per cell. For both liver and brain, isolated mitochondria, superoxide levels were determined using MitoSOX (Life Technology) as instructed by manufacturer. Briefly, 150 µg/well of isolated mitochondria was resuspended in ice

cold MAS (w/o rotenone) added with substrates (5 mM succinate, 5 mM malate, 5 mM glutamate), then stained with MitoSOX at a concentration of 3.5 μM at 37°C for 10 min. The mitochondria were washed once with MAS, and transferred into a 96-well plate (pureGrade BRAND*plates* Midsci). Superoxide level was detected via fluorescence plate reader with excitation wavelength at 510 nm and emission wavelength at 590 nm.

3.2.20 ATP Level Determination

Cellular ATP level was determined by using a CellTiter-Glo Luminescent Cell Viability Assay Kit (Promega) per manufacturer's instruction. Briefly 2 x 10^5 cells/well were seeded in a 96-well plate (pureGrade BRAND*plates* Midsci) a day prior to the assay. Cells were treated with ATP detection reagent at room temperature for 10 min. Cellular ATP levels were determined by measuring the luminescent signal on a plate reader (TECAN Infinity M200).

3.2.21 Nuclear Extraction

Cells were harvested and pelleted, then resuspended in hypotonic buffer (20 mM HEPES, 50 mM NaF, 5 mM $Na_2P_2O_7$, 50 mM *N*-acetylglucosamine, 1 mM EDTA, 1 mM EGTA, 1 mM DTT, 1 mM PMSF, protease inhibitor mixture, pH 7.5) followed by centrifugation. Supernatant (cytoplasmic content) was saved and nuclear pellet was washed with hypotonic buffer then lysed with NP-40 lysis buffer and centrifuged for 20 min at 20,000 xg. Resulting supernatants were used for protein determination via Bradford assay (Bio-rad). The protein levels were analyzed via immunoblotting, and anti-lamin B1 was used for nuclear content loading control. Actin was used for cytoplasmic content.

3.2.22 Oxidative Stress and Cell Viability Assay

Prolonged TMG- or GlcN-treated cells were incubated with different concentrations of H_2O_2 (50 μM, 100 μM, Sigma) for 7 h prior to cell viability determination via Annexin V (Life

Technologies) and propidium iodide (PI, Life Technologies) staining. Annexin V-FITC/PI double labeling method was used per manufacturer's instructions to determine cell viability after acute oxidative stress. Cells were digested with 2% BSA trypsin, washed once with 1X PBS and incubated with Annexin V/PI mixture then subjected to a BD LSR II flow cytometer (BD Biosciences) and analyzed with BD FACSDiva software (BD Biosciences) for cell viability determination.

3.2.23 Cycloheximide Treatment

Cells were treated with 50 μg/mL of cycloheximide (CHX, Sigma) and harvested at different time-points for up to 6 h. Immunoblotting was performed to determine NRF2 protein stability after prolonged TMG or GlcN treatment. p53 was used as positive control for the CHX treatment.

3.2.24 Body Composition and Indirect Calorimetry Measurement

Fat mass, lean mass, and water mass were measured with an EchoMRI 4 in1-1100 analyzer (EchoMRI; Houston, TX)

Prior to the indirect calorimetry measurements, mice were housed individually for 5 days. Subsequently, mice were transferred and housed in the calorimetric chamber (Promethion High Definition Continuous Respiratory system for mice, Sable Systems Inc) for 3-5 days. The chamber measured food intake, energy expenditure, substrate utilization, and various outcomes of the mice for baseline measurement calibration. Then, mice were transferred back to the normal individual cage. 50mg/kg of TMG or saline dosage was delivered to each mouse via peritoneal injection every other day for up to two weeks. During the last five days of injection, mice were transferred back into the calorimetric chamber and parameters measured as previously

mentioned (saline vs TMG injection). These experiments were repeated twice and each repeat included eight mice.

3.3 Results

3.3.1 Thiamet-G (TMG) or Glucosamine (GlcN) Treatment Alter Mitochondrial Bioenergetic Capacity

Prolonged treatment with GlcN improves mitochondrial function and extends lifespan in both *C. elegans* and mice [62]. We hypothesized that sustained elevation of O-GlcNAcylation would alter energy metabolism. To determine how O-GlcNAcylation affects energy metabolism, we treated SH-SY5Y neuroblastoma cells with either Thiamet-G (TMG, 10 μM) or GlcN (0.35 mM) for at least three weeks prior to harvesting these cells. TMG is a highly selective OGA inhibitor [72], while GlcN feeds into the hexosamine biosynthetic pathway after GFAT1, increasing cellular pools of UDP-GlcNAc [64]. In contrast to GlcN, which can influence a variety of metabolic pathways, TMG precisely manipulates O-GlcNAcylation by targeting OGA.

Both TMG- and GlcN-treated SH-SY5Y cells increased total and mitochondrial O-GlcNAc levels (**Figure A.1A-B**). OGT protein and transcript levels were reduced, whereas OGA protein and transcript levels were increased in response to elevated O-GlcNAcylation, and GFAT1 protein level was decreased in TMG treated cells (**Figure A.1A** and **D**) [68]. OGA specific activity was increased in GlcN-treated SH-SY5Y cells (**Figure A.1E**). Similar results were found in NT2 human teratocarcinoma cells treated with TMG or GlcN (**Figure A.1C**).

Prolonged elevation of O-GlcNAc altered cellular respiration (**Figure A.1F**). TMG lowered baseline oxygen consumption rates (OCR), whereas GlcN increased baseline OCR (**Figure 14A**). Under basal conditions, *in vivo* ATP production was lower in the presence of TMG but higher in GlcN-treated cells (**Figure A.1I**). Neither treatment affected the proton leak

rate (**Figure 14B**). The maximum respiratory rate was increased in GlcN cells while TMG was similar to control cells (**Figure A.1G**). SH-SY5Y cells grown in oxidative media regardless of TMG or GlcN-treatment have no reserve capacity (**Figure A.1H**) showing that these cells were respiring at their maximum capacity. To eliminate any cell type specific effects, we performed the respiration assays in NT2 cells. TMG-treated NT2 cells replicated the data from SH-SY5Y cells (**Figure A.1K-O**). GlcN-treated NT2 cells mirrored the TMG-treated results from SH-SY5Y/NT2 cells showing lower respiration rates (**Figure A.1K-P**).

The total cellular ATP levels in both TMG- and GlcN-treated SH-SY5Y cells and in TMG-treated NT2 cells were lower (**Figure 14C, Figure A.1P**). TMG treatment caused both SH-SY5Y and NT2 cells to produced significantly less ATP, while GlcN-treated SH-SY5Y cells produced and consumed more energy due to increased phosphorylation of GlcN to GlcN-6-P by hexose kinase (HK) [64]. Of note, GlcN had no effect on AMP activated protein kinase activity (data not shown).

Since oxidative phosphorylation and glycolysis are interdependent energy producing pathways [73], we examined glycolytic energy production by measuring cellular glycolytic flux. Both TMG- and GlcN-treated SH-SY5Y cells had lower basal glycolytic rates (**Figure 14D**), and TMG-treated NT2 cells had a lower basal glycolytic rate. GlcN treated NT2 cells showed no changes (**Figure A.1Q**).

3.3.2 TMG or GlcN Treatment Increased Complex I and Complex IV Activity and Elevated Cellular NAD^+/NADH Ratio

Because prolonged TMG treatment lowered cellular respiration, we postulated that the ETC complex activity was lower. Mitochondria isolated from both TMG- and GlcN-treated SH-SY5Y

cells had increased Complex I activity (**Figure 14E**). TMG also elevated COXIV activity (**Figure 14F, Figure A.2A-B**). Since isolated ETC complex activity did not correspond to the *in vitro* respiration measurements, we considered whether the observed decrease in OCR was due to reduced concentration of NADH available for respiration. The NAD^+ concentration was elevated in TMG but reduced in GlcN-treated cells (**Figure 14G**) while the NADH concentration was decreased in both TMG- and GlcN-treated SH-SY5Y cells (**Figure 14H**). The NAD^+ and NADH ratio skewed toward NAD^+ for both TMG- and GlcN-treated cells (**Figure 14I**). To ascertain whether altered cellular respiration was due to changes in mitochondrial membrane potential, we probed for mitochondrial membrane polarization differences in TMG or GlcN-treated SH-SY5Y cells. TMG significantly enhanced mitochondrial hyperpolarization (**Figure 14J**).

3.3.3 Prolonged TMG or GlcN Treatment Promotes Elongated Mitochondria

To assess whether mitochondrial morphology was changed in TMG- or GlcN-treated SH-SY5Y cells, we used transmission electron microscopy to visualize the mitochondria. Mitochondria from both treated cells were longer in shape compared to control mitochondria (**Figure 14K**). Confocal imaging data agreed with the electron microscopy data showing longer mitochondria in TMG- or GlcN-treated cells (**Figure 14L**). Mitofusin 1 (MFN1), Mitofusin 2 (MFN2), and Dynamin-like protein (DLP1), which facilitate mitochondrial fusion and fission, were lower in TMG-treated cells; however, GlcN treatment increased the DLP1 protein levels (**Figure A.2C**).

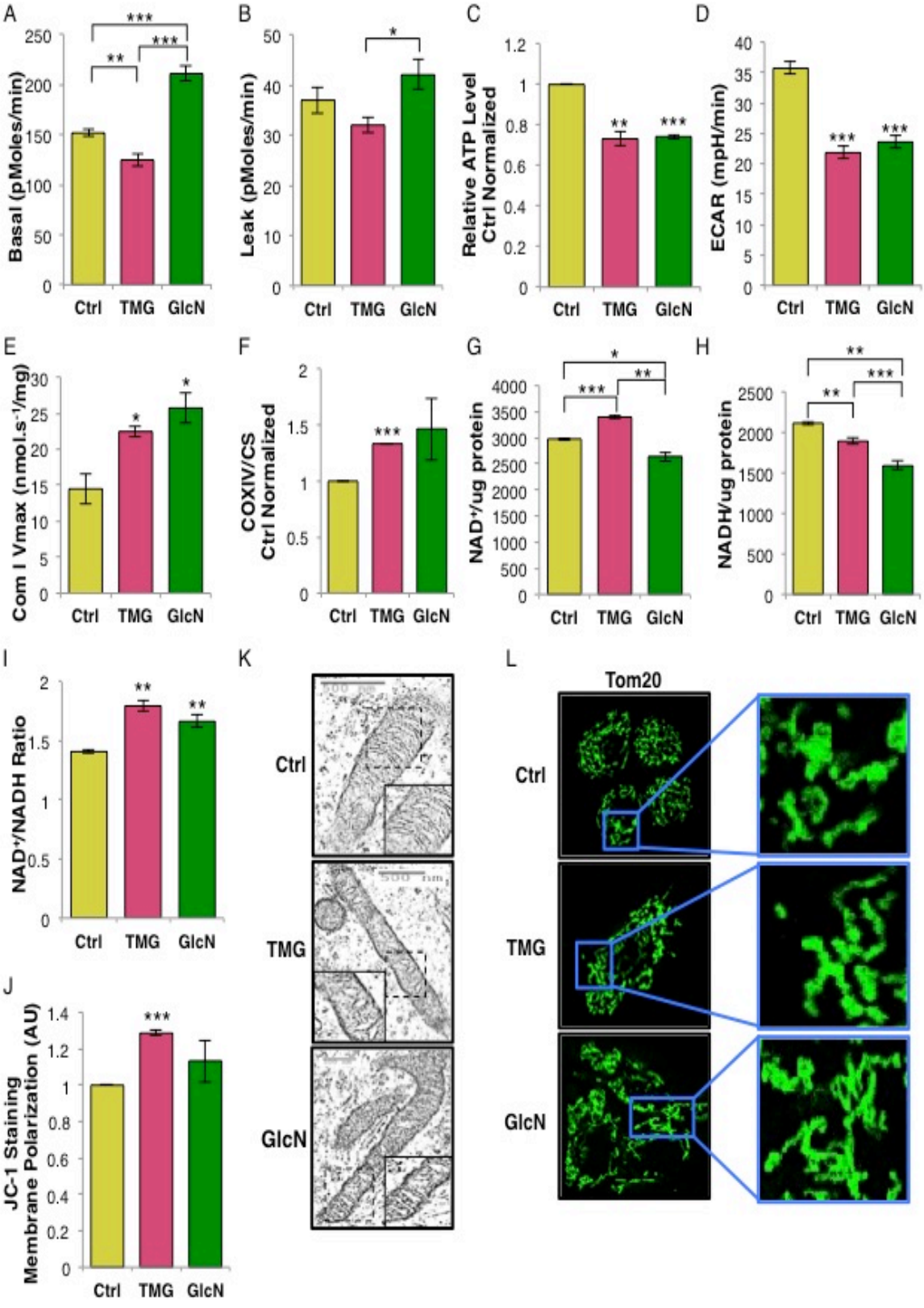
A
Basal (pMoles/min)
Ctrl
TMG
GlcN
B
Leak (pMoles/min)
C
Relative ATP Level Ctrl Normalized
D
ECAR (mpH/min)
E
Com I Vmax (nmol.s-1/mg)
F
COXIV/CS Ctrl Normalized
G
NAD+/ug protein
H
NADH/ug protein
I
NAD+/NADH Ratio
J
JC-1 Staining Membrane Polarization (AU)
K
L
Tom20

Figure 14: Thiamet-G (TMG) or glucosamine (GlcN) treatment altered mitochondrial bioenergetics, elevated cellular NAD^+/NADH ratio, enhanced mitochondrial hyperpolarization, and promoted longer mitochondria

(A) Basal respiration **(B)** leak rate in O-GlcNAc elevated SH-SY5Y cells were determined using XF24 analyzer (average ± SEM, n=6). **(C)** Relative ATP level representative plot (average ± SEM, n=4) showed both TMG (10 μM) and GlcN (0.35 mM) treated SH-SY5Y cells maintained low cellular ATP levels. Displayed relative ATP levels were average value of each replicated result normalized with control. **(D)** ECAR was measured using XF24 analyzer (average ± SEM, n=6). **(E)** Complex I Vmax (average ± SEM, n=3) normalized with total protein concentration, **(F)** complex IV (COXIV) Vmax normalized with citrate synthase (CS) activity (average ± SEM, n=3). **(G)** NAD^+ and **(H)** NADH levels were altered **(I)** NAD^+/NADH ratio (average ± SEM, n=4) normalized with protein concentration. (**J**) Membrane potential was measured using JC-1 (average ± SEM, n=3) **(K)** Transmission Electron microscopy and **(L)** confocal staining with TOM20. * indicates significance $p < 0.05$. ** indicates significance $p < 0.01$. *** indicates significance $p < 0.001$.

3.3.4 Prolonged TMG or GlcN Altered the Transcriptome

We considered whether the observed mitochondrial changes were mediated by alterations in the transcriptome. Next Generation RNA-Sequencing (RNA-seq) analysis found 8793 genes differentially expressed in TMG- or GlcN-treated SH-SY5Y cells. Only genes with high sequencing counts (cpm: counts per million of >10 in at least two of the three biological replicate samples) were considered in the differential expression analyses (**Figure A.3A-C and Table 2)**. A total of 75 genes for TMG treatment and 196 genes for GlcN treatment were elevated, while 117 genes for TMG treatment and 269 genes for GlcN treatment were reduced (p-value < 0.05) (**Figure 15A**). Among these genes, 36 genes from TMG and 74 genes from GlcN treatment were increased 1.5-fold or more, while 73 genes from TMG and 200 genes from GlcN decreased 1.5-fold or more (**Figure 15A**). All genes selected for orthogonal validation agreed with the RNA sequencing results (Tissue Factor Pathway Inhibitor 2 (*TFPI2*), Guanine nucleotide binding protein, gamma subunit 1 (*GNG1*), Activating Transcription Factor 4 (*ATF4*), and Insulin-like growth factor 2 (I*GF2*) (**Figure A.3E** and **Table 3-4**). As a positive control (**Figure A.1D**), the RNA-Seq data showed that *OGA (MGEA5)* gene expression was increased in both TMG- and GlcN-treatment (**Table 3-4**) [68].

Table 2: Complete list of differentially expressed genes after TMG/GlcN treatment

	cnt1	cnt2	cnt3	tmg1	tmg2	tmg3	glcn1	glcn2	glcn3
ABCB4	62.09	98.7	66.75	358.77	295.66	435.75	198.55	177.51	170.16
ABR	777.99	936.18	1194.05	579.93	785.52	1018.91	495.58	423.16	415.56
ACP6	160.58	190.84	126.33	60.8	42.99	47.81	168.23	143.72	78.55
ADAMTS2	238.53	356.72	212.88	143.51	131.64	169.98	40.48	62.41	42.29
ADAMTS3	374.2	312.73	253.78	1197.88	1298.15	1024.95	841.47	887.1	1025.98
AES	430.28	392.41	505.72	144.26	293.84	457.87	180.71	111.7	147.56
AFF3	68.99	71.03	72.29	224.23	320.64	256.2	66.82	35.36	85.56
AHNAK	6340.59	9097.32	8103.01	7010.88	5679.5	8280.15	4199.07	3999.81	3130.33
AK5	208.37	223.92	231.5	674.68	710.99	655.97	368.4	365.3	240.65
ARHGAP36	1261.64	1623.18	1191.36	479.35	464.22	633.5	1154.25	864.98	774.28
ARL6IP4	320.04	321.17	406.97	109.61	251.79	315.49	141.61	80.87	97.38
ATCAY	202.52	223.98	207.51	106.63	149.63	232.14	45.23	80.24	62.42
ATF4	1660.59	1674.92	2091.45	910.86	1108.38	1638.15	858.43	722.46	605.13
ATP7A	1696.22	1454.64	1261.25	1943.32	1876.4	1553.37	2809.92	2937.85	3166.57
ATRNL1	293.28	293.94	296.93	789.29	650.3	682.55	461.23	593.64	520.54
AUP1	274.65	256.15	400.31	108.62	163.13	344.03	76.28	82.42	99.66
BAALC	192.4	246.36	180.33	613.89	442.17	655.86	341.09	466.3	439.35
BANF1	1504.18	1584.26	2641.16	600.92	966.2	1666.73	883.72	622.18	577.94
BCL2	358.64	384.41	470.71	1396.21	1089.14	854.89	515.6	529.62	787.34
BEND4	1077.08	877.99	1023.72	576.03	379.94	385.96	807.98	846.31	1060.21
BMP7	132.59	197.63	180.4	182.52	194.76	322.21	75.87	63.92	43.3
C11orf1	996.42	943.92	858.82	352.78	498.73	454.97	947.36	745.35	622.25
C18orf32	1186.99	924.75	535.64	1304.44	1198.94	1081.92	1586.53	1899.48	2749.15
C7	6170.27	7804.25	5754.6	16958.65	13564.5	14668.07	4463.96	5070.23	4173.44
CACNA2D2	454.36	394.41	735.13	259.1	386.33	421.93	255.88	145.9	138.95
CALM3	931.39	1091.26	2463.72	492.59	708.84	1161.81	600.56	424.03	412.53
CALR	3749.42	4307.29	5293.28	1624.4	2638.88	4152.56	2273.08	1478.54	1552.58
CAPNS1	1394.3	1785.39	1492.97	625.83	1297.04	2410.89	651.6	459.93	622.23
CC2D2A	112.4	158.23	173.29	412.59	363.42	320.04	197.49	185.11	203.4
CFL1	5928.11	7010.4	10653.88	2634.04	4933.62	9702.47	3046.63	2115.07	3030.31
CHD3	1121.15	1333.26	1916.13	1141.07	1133.74	1815.71	727.82	619.77	505.45
CHGB	1202.7	1382.85	1787.6	1063.34	1193.64	1207.73	899.69	572.95	436.99
CIZ1	521.37	607.19	1053.51	204.29	436.43	496.28	358.81	220.63	202.39
CKMT1A	226.32	175.63	207.76	107.54	225.77	305.22	63.23	53.65	24.99
CLMP	512.67	465.63	405.25	1460.99	1067.17	850.65	511.17	845.76	850.78
CLPB	498.29	482.71	455.01	192.33	265.12	352.75	267.66	187.58	178.22
CNOT3	290.52	251.74	520.8	117.59	202.93	235.83	153.03	85.64	82.57
CPE	925.88	831.99	808.63	2370.85	2165.05	2017.97	1022.99	1111.17	1342.13

CPEB2	161.18	184.54	245.76	686.65	505.49	485.9	383.9	475.43	611.14
CPS1	135.09	195.03	190.31	51.83	30.64	40	175.68	181.7	225.52
CXCL12	595.89	481.75	474.89	1178.95	1044.42	899.5	216.01	195.24	235.59
DBH	787.46	888.83	2362.98	212.26	321.2	525.94	713.41	387.83	295.02
DCN	550.22	627.13	579.27	1076.3	1367.46	1310.86	791.5	556.66	807.49
DCX	602.43	572.35	580.78	3051.51	2321.19	2096.69	641.43	645.19	708.82
DGKK	133.32	235.33	198.11	73.75	54.42	56.33	125.48	98.62	67.47
DKK1	2552.09	2530.13	1665.43	7460.33	7138.21	6931.06	4839.77	5261.84	6437.85
DKK2	158.01	102.2	234.33	627.84	637.29	545.42	402.56	481.97	978.62
DLG2	898.89	765.22	1017.13	468.4	357.15	397.6	663.34	682.63	637.34
DOCK10	69.91	60.67	70.65	271.07	293.32	238.16	93.39	88.44	78.53
DPYD	257.27	270.19	193.09	498.29	590.84	496.5	409.09	406.66	457.1
DUSP4	861.82	946.49	990.19	2027.03	1676.14	1949.86	1001.98	969.47	959.53
DYNC1I1	87.99	131.74	153.3	319.9	277.25	396.41	205.75	226.75	259.76
EIF3G	522.75	529.91	2323.32	143.49	299.22	597.03	233.08	128.76	221.49
EPAS1	872.68	1012.27	1084.11	1096.23	1024.21	1010.01	367.11	270.79	258.76
ERP29	1957.75	2454.79	3025.93	1089.98	1563.92	2067.58	1256.98	872.52	783.34
ESRRG	728.4	576.39	853.01	1872.56	1779.01	1345.02	830.21	1162.95	1659.28
FADS2	424.99	464.72	555.74	157.45	272.89	522.66	164.79	102.6	121.83
FAM101B	290.42	400.74	478.46	1003.1	881.92	1151.32	727.87	634.19	546.17
FAM124A	156.33	144.35	184.05	622.86	627.56	648.49	263.35	276.97	219.5
FBN1	767.53	1202.11	1041.89	2131.68	1431.23	1666.03	548.7	490.78	397.71
FBN2	180.36	268.4	309.58	77.73	71.97	93.43	239.98	182.54	166.13
FEZ1	187.27	283.24	177.83	202.3	268.71	290.12	96.62	80.86	49.35
FGL1	931.35	600.4	521.1	211.28	183.47	184.96	731.68	786.94	925.29
FHOD3	322.34	389.52	417.44	811.31	678.67	876.48	507	479.11	363.29
FILIP1L	69.68	75.2	103.22	252.14	260.85	199.91	98.3	120.71	130.88
FLOT1	827.44	807.18	941.46	288	597.81	785.41	401.66	258.83	254.74
GABRB3	25.96	26.41	52.44	355.79	290.58	230.77	16.5	34.88	59.37
GALNT13	503.41	334.61	538.95	1566.62	1442.85	1213.15	732.9	855.73	995.77
GAREM	268.9	210.81	345.84	1057.37	749.44	687.94	601.18	679.92	945.42
GDI1	990.05	1064.9	2063.87	447.45	774.15	1055.48	579.6	392.18	313.14
GNAI2	1010.34	1047.06	1636.84	544.12	949.79	1004.56	708.98	442.2	363.49
GNAO1	167.86	166.42	307.05	134.54	141.32	184.83	80.7	75.67	72.49
GNG11	1389.5	1217.13	1321.26	6146.85	5291.77	5138.5	2907.17	3686.59	3908.62
GPC3	452.8	588.92	391.85	1178.94	1613.22	1484.17	1107.75	692.61	556.8
GREM1	149.3	90.47	88.3	705.58	764.69	449.84	14.3	54.63	71.46
GYG2	229.47	266.84	180.96	112.61	122.92	155.07	79.29	50.88	56.38
HAND1	1914.94	2254.88	2957.52	1217.8	2059.18	1613.91	1238.62	905.7	839.73
HGS	146.77	179.26	341.46	64.77	115.92	178.59	70.28	56	70.47

HMGA1	270.74	242.01	1396.95	86.69	194.21	225.16	113.22	104.37	147.99
HTRA1	265.47	362.62	231.03	222.24	221.17	279.48	129.01	81.38	100.68
HYOU1	1126.2	1252.92	1937.22	597.94	779.32	1125.68	739.25	513.51	500.41
IGF2	2305.5	2251.25	4105.37	1081.28	972.4	1001.5	1331.14	940.43	1028
IL17RD	1192.8	1371.08	1192.53	3895.6	3018.8	3366.09	1927.9	2077.27	1826.44
INPP5F	483.11	372.23	596.33	1315.48	1045.23	972.85	705.12	894.95	796.42
IQGAP2	149	79.99	165.33	481.34	557.45	514.54	220.7	220.76	255.73
ITM2A	363.24	329.89	238.77	1034.44	1049.61	1257.65	532.89	530.48	752.1
KCNK1	75.95	42.5	76.25	249.15	221.25	199.88	50.03	90.13	124.82
LAMP5	186.43	252.31	209.08	461.41	622.27	850.32	194.93	166.55	122.84
LUM	327.24	261.48	196.35	516.22	727.82	595.36	636.95	659.52	923.27
MAB21L2	2064.24	2530.54	5030.29	978.63	979.39	1228.93	1784.46	1624.73	1584.8
MAOB	557.05	557.88	526.29	580.01	576.59	705.84	250.31	203.9	134.93
MAP6	551.2	539.94	508.11	458.43	406.33	473.04	294.46	253.88	245.67
MBOAT7	117.36	174.42	213.81	83.71	112.4	153.94	52.99	58	42.29
MEIS1	488.13	509.21	492.76	997.57	936.48	858	650.59	599.33	648.41
MEST	494.12	497.31	405.29	431.52	333.47	356.15	276.92	192.66	192.31
MGEA5	1575.94	1529.83	1427.78	5208.08	5002.22	4842.91	3050.3	3265.57	3071.93
MGP	594.75	802.51	483.12	837.12	1035.63	1262.92	269.12	241.97	262.78
MGST1	132.71	151.32	164.5	501.28	529.32	511.35	332.84	350.68	381.59
MMS19	1022.34	1022.47	1049.58	497.28	692.46	984.26	615.53	396.31	415.83
MSX2	118.01	87.99	86.47	357.77	349.36	359.3	182.7	196.08	276.86
NAV1	802.86	1002.85	1185.33	1430.08	1125.86	1447.99	525.63	506.98	381.61
NCALD	172.03	232.49	270.24	657.75	439.23	571.94	271.68	331.24	346.09
NEBL	148.85	144.47	142.26	680.66	708.44	508.27	550.16	509.24	717.87
NEFL	391.34	332.88	678.69	2168.56	1022.15	1217.42	421.81	411.73	479.25
NEFM	544.32	460.21	768.98	1442.04	1594.7	1507.58	400.72	335.39	293
NID1	1923.33	2568.49	2736.5	2494.42	2028.97	1968	1421.47	1258.88	1215.28
NMNAT2	263.95	242.65	251.46	222.24	178.92	278.38	91.3	108.01	106.72
NOVA2	465.82	845.03	907.43	416.57	480.17	505.23	420.96	208.66	185.27
NR2F1	175.46	239.44	223.89	681.66	646.05	529.5	415.01	474.6	555.77
NRCAM	2209.15	1898.57	2718	10059.39	8775.74	7783.81	2990.38	3757.91	3847.2
NRIP1	214.35	227.42	190.84	73.75	103.99	55.36	201.33	219.21	200.77
NT5E	52.72	88.29	86.97	321.9	228.08	298.67	185.99	168.05	218.47
NUDC	1688.99	2190.09	2428.35	790.27	1204.96	1764.63	1084.95	894.11	729.98
OLFML3	802.86	913.05	1272.9	628.83	1065.7	972.73	510.65	432.92	471.2
PCDHGA7	65.5	82.38	143.25	319.27	297.92	445.9	223.32	145.62	158.02
PCLO	621.61	591.02	789.29	285.02	313.49	273.22	453.99	459.5	326.23
PDE7B	33.88	26.52	28.48	234.2	223.96	174.4	67.19	89.25	114.76
PDGFRA	1648.03	1666.08	1938.42	2179.51	1899.99	1857.01	720.17	843.87	932.34
PEG10	2200.77	1909.7	2578.58	8315.4	5031	4748.38	2764.93	3257.92	3415.26

PIPOX	162.15	189.83	181.54	55.78	57.09	72.16	92.58	26.85	37.26
PITPNA-AS1	51.02	69.11	18.86	76.97	96.95	49.37	134.78	197.29	176.36
PKM	11375.91	13099.14	23798.11	5098.45	10596.83	12734.92	8359.77	4636.07	4308.37
PLCXD3	384.24	270.66	333.33	2324.01	2536.46	1684.2	509.98	673.17	954.48
PLEKHA6	1222.88	1281.98	1845.03	1169.98	982.85	1215.15	736.17	815.13	670.57
PLK2	218.72	176.83	181.87	680.67	576.64	527.36	291.23	355.98	285.95
PLOD2	201.26	132.32	142.6	62.79	34.99	48.85	140.12	238.01	240.62
PPEF1	60.03	29.66	59.51	272.07	267.82	226.47	114	79.77	84.57
PRELID1	1471.13	1545.98	1842.62	418.07	735.2	1668.28	596.23	419.9	683.64
PRICKLE1	253.96	409.57	291.27	873.45	651.93	881.29	414.67	390.94	313.96
PROM1	151.34	135.82	166.03	472.39	312.35	337.04	274.89	253.9	254.73
PRR14	180.52	210.22	253.65	78.72	190.78	198.61	81.76	74.02	59.41
PSMC3	1025.51	1407.06	1177.23	575.01	906.62	1274.5	665.26	449.83	451.08
PTGER2	500.32	432.44	237.89	1056.37	1104.18	889.92	1069.17	1081.43	1339.11
PTMS	2737.78	3325.59	8436.18	1102.2	2614.57	3010.76	1671.83	940.34	959.54
PTPRM	121.84	129.08	144.79	387.67	273.7	373.08	91.21	93.5	98.66
PTX3	64.1	59.95	50.09	241.17	260.76	271.03	146.87	156.18	225.51
RAB3IP	486.39	460.35	601.2	260.11	252.89	216.9	436.88	466.13	500.4
RAPGEF4	142.14	157.47	111.07	411.59	354.59	362.52	235.64	227.6	232.58
RBP1	603.72	586.56	1220.06	319.89	429.9	879.91	254.02	224.19	213.45
RCOR2	140.18	172.67	202.09	62.78	75.41	141.08	58.54	38.15	44.3
RD3	110.56	90.74	52.48	347.81	293.05	406	99.49	142.95	124.84
RELN	1591.45	2660.06	2381.69	3366.42	2449.24	2747.31	1200.74	1115.46	1065.26
RERG	48.31	30.71	34.7	236.19	213.32	216.85	51.66	22.63	55.36
RIMS1	37.02	33.28	51.7	234.2	271.44	202.03	61.19	61.18	73.49
RP11-481F24.3	1233.8	975.01	745.14	2707.46	2360.84	2314.47	2029.75	2590.85	2092
RPH3A	316.32	403.02	790.36	603.92	838.29	849.39	181.1	175.17	104.72
RPL28	1393.38	1694.68	1909.4	777.32	1098.79	1520.13	917.39	815.05	617.21
RPS11	2914.79	3111.75	19002.77	1033.43	1638.89	7441.65	687.93	467.25	1547.49
SCN9A	746.9	739.66	957.3	2025.45	1915.83	1512.58	1004.46	1306.34	1563.44
SERPINF1	97.79	86.43	67.05	168.41	328.42	406.95	150.88	117.3	77.54
SERTAD4	267.15	254.51	341.62	684.65	673.28	534.82	337.64	410.08	510.46
SEZ6L	77.06	112.04	142.45	495.3	463.42	493.26	95.78	108.97	79.54
SGK1	395.94	353.74	305.14	1617.44	1748.23	1849.9	474.99	479.67	534.63
SHOX2	448.63	415.94	530	1208.85	922.38	777.26	708.44	748.85	693.72
SLC6A2	1015.39	1034.95	997.21	1904.68	1720.76	2181.71	1762.46	1646.93	1439.06
SLC8A3	55.34	79.72	75.12	347.81	295.82	273.25	101.48	114.13	67.47
SSR4	441.27	366.44	388.13	104.63	196.66	301.61	192.24	109.45	87.61
SV2C	31.02	49.06	37.6	345.82	289.64	297.67	211.38	189.3	231.57
TFPI2	474	479.41	350.93	7765.29	7406.82	5752.03	1802.24	2203.53	3197.76

TKT	912.04	1219.88	1287.29	369.72	708.24	1190.39	457.34	294.37	415.82
TMEM100	148.91	125.57	142.08	444.48	353.66	382.71	153.56	112.74	182.22
TMEM178B	148.6	158	230.4	256.12	209.74	237.03	64.63	70.65	65.44
TMSB10	1877.09	2226.65	3204.51	961.68	1625.92	4402.15	561.85	500.6	959.5
TNNT2	450.4	359.48	505.66	95.66	175.58	279.27	171.59	104.35	98.68
TRAP1	1051.21	1102.03	1664.87	334.84	705.34	772.03	685.23	367.67	367.82
TRIB2	854.18	1187.61	898.29	2524.32	2014.04	1998.83	1326.99	1582.39	1593.85
TSHZ2	62.02	81.26	104.66	341.84	314.48	142.37	56.35	43.3	49.43
TUBA1B	9503.45	10830.43	14342.84	3623.41	6614.62	11027.88	3707.38	2390.08	3460.9
TWIST1	922.23	889.05	1333.63	2586.11	1932.39	1948.87	1501.59	1750.35	2106.33
UBA52	1633.63	2079.09	2038.32	875.28	1321.68	2712.93	759.03	660.67	893.15
UNC5D	13.32	19.75	30.19	188.36	222.35	144.65	40.83	5.61	26.17
UNC79	364.67	313.4	428.23	445.47	438.88	452.86	150.26	179.32	177.2
USP11	1055.87	1096.77	1204.09	351.78	772.39	1154.28	546.04	283.28	355.42
VAMP2	611.3	650.72	1141.64	394.64	533.73	586.74	446.74	302.17	270.85
VAT1	1559.13	1721.33	1234.1	578	1268.28	1682.75	778.46	484.58	505.45
VSTM2A	224.3	235.82	273.66	97.67	109.93	85.06	211.32	175.69	215.46
VSTM4	74.15	46.78	87.63	213.28	215.92	250.8	79.66	75.58	94.63
XYLT1	69.9	64.13	69.25	226.23	190.42	233.81	96.87	102.15	72.5
ZYX	116.33	170.69	369.51	51.81	56.8	178.09	65.36	38.99	41.28

Table 3: Genes list of significantly (p<0.05) up-regulated or down-regulated after TMG treatment

	logFC	logCPM	PValue
TFPI2	3.974315389	7.984336724	3.40E-49
GNG11	2.048433269	8.062998042	1.01E-22
SGK1	2.277471985	6.065222981	2.15E-22
PLCXD3	2.699059303	6.381448599	4.55E-20
MGEA5	1.702261181	7.965254798	7.53E-20
DCX	2.060765891	6.596177586	3.19E-18
NRCAM	1.934288314	8.568472697	4.99E-17
IL17RD	1.424414076	7.421823589	1.57E-12
DKK1	1.644288922	8.595270368	2.21E-12
IGF2	-1.532544968	7.026821053	1.60E-09
CPE	1.323266754	6.765710761	2.45E-09
RP11-481F24.3	1.290595996	7.201935817	1.45E-08
MAB21L2	-1.622228417	7.272067617	1.71E-08
PEG10	1.406166131	8.206085404	2.77E-08
TRIB2	1.124861201	6.916130214	7.63E-07
C7	1.167612531	9.406382224	8.70E-07
SCN9A	1.129965883	6.668730579	5.86E-06
DUSP4	0.98720095	6.620099707	6.29E-06
TWIST1	1.012814552	7.015622298	1.81E-05
SLC6A2	0.902559617	6.887559136	2.20E-05
MANF	-0.97916434	7.073468586	2.93E-05
ESRRG	1.182273941	6.54602197	3.33E-05
ASCL1	-0.796494691	8.569181531	7.81E-05
GPS2	-1.475796159	6.922239736	0.000127915
FSTL1	0.764377934	8.143356395	0.000140223
SIPA1L1	0.904099364	6.434242443	0.0001465
FRMD6	0.906722651	6.423991918	0.000202817
XPR1	0.842826623	8.079487425	0.000326395
PRKCA	0.765950988	8.480749557	0.000336453
MTUS1	-0.810318467	6.720087742	0.000351102
AZIN1	0.835720005	9.34268067	0.000370476
HDAC9	0.904693051	7.291180258	0.000378629

FAT1	-0.752040827	8.025525536	0.000465052
CREB3L2	0.800895347	6.555216452	0.000469756
SORCS1	0.702804894	7.704984428	0.000630729
ITGA1	-0.72265724	7.047001389	0.000655617
RIMS3	-0.916268416	8.579287327	0.000679593
LIMA1	0.693236361	7.107553024	0.000755359
AARS	-1.041876727	6.681350405	0.000872145
STAC	0.618234474	7.702113648	0.001219615
CHRNA3	-0.723569954	9.283428145	0.001396019
NOMO1	-0.862037417	7.771738954	0.001591809
PPM1G	-0.98249157	8.574637675	0.001938814
ZPR1	-0.769295093	7.416296754	0.002295731
LGR5	0.612682686	8.492114432	0.002434399
MRPL37	-0.976214847	7.637839562	0.003333965
EIF3C	-1.026933741	10.75841222	0.00348991
AMZ2	-0.629571914	8.460266234	0.003660173
CSNK2B	-0.82997636	7.510070449	0.004847854
PTMS	-1.134915161	7.749769069	0.005305841
CDON	-0.606847892	7.0078246	0.005528275
ADAM22	0.574450099	8.082423309	0.005588434
PPP1R11	-0.776560451	7.968385626	0.006083876
ALCAM	0.619969531	8.503937758	0.006522808
NUDC	-0.772413173	6.792171458	0.007019238
EDNRA	0.658950937	7.136645592	0.007034996
TCF12	0.514909174	8.101024402	0.007053281
RAD21	0.673633968	9.577534675	0.007476604
GAR1	-0.802816833	6.7542483	0.007688859
CDC25B	-0.760981608	7.004003099	0.007946699
RNF150	0.570552744	7.411099445	0.007960745
CTDNEP1	-0.698431838	7.377677381	0.008055964
UBE3C	0.516917015	7.427738308	0.008152032
DOCK7	0.521155094	8.428808865	0.008155624
FTSJ3	-0.884046023	6.969777419	0.008211142

ELAVL4	-0.660712706	8.92847878	0.008359706
EBNA1BP2	-0.746411625	6.993256334	0.008541209
PPFIBP1	0.526424519	7.156633307	0.009218237
FN1	0.584957968	7.406644996	0.009453243
TANC2	0.581402146	7.063223169	0.010169279
MDH2	-0.876874588	6.794050353	0.010232305
CKS2	0.6368953	7.445938462	0.010466104
ERP29	-0.682263947	7.030170382	0.010606499
POM121C	-0.695631769	7.004598091	0.011098191
MT-CO3	-1.227853996	13.19784594	0.011106659
THOC5	-0.71295444	6.887044763	0.011654324
SMC6	-0.546932292	7.222632701	0.012938452
BRE	-0.740280557	7.689313486	0.013188866
GPC6	-0.690137144	6.794176685	0.013245586
PTBP1	-1.183514144	7.132030275	0.013301863
TSC22D1	0.543653501	7.287426899	0.013749817
UBE2C	-0.670668518	6.722297448	0.014793118
TENM3	-0.590358012	7.317308789	0.015293699
ASNS	-0.596327379	8.713388339	0.015307451
TMEM97	-0.525088624	7.312664816	0.015438755
CD46	0.574788982	7.440134619	0.015493012
SF3B2	-0.813660562	8.831230396	0.015602109
TBX3	-0.54493534	8.728892988	0.015685141
ZNF627	0.51722737	6.793599458	0.015800986
NBEA	0.479935278	7.51802842	0.015963637
ABHD2	0.533289827	7.302460159	0.015969993
RET	-0.533897749	8.851087406	0.01601111
P4HB	-0.706254071	7.574752079	0.016282525
MAZ	-0.712648443	8.139140992	0.016313182
AKAP9	-0.494027396	7.697876451	0.016510384

UBE2L3	-0.80721758	7.589486513	0.016552814
SUPT6H	-0.774025763	7.043424732	0.01657952
IMPDH2	-0.727170212	7.353090857	0.016751588
PPIB	-0.789567779	8.751017828	0.017175562
ATAD2	0.475084659	7.90645691	0.017206476
CNN3	0.504264401	8.577025795	0.017258069
MALAT1	0.483375018	7.339203293	0.017687501
CALR	-0.691395808	7.875427446	0.018067103
TLN2	-0.591540317	6.755797925	0.018244469
WARS	-0.563930867	7.363492942	0.018288284
NAV2	0.502379735	6.857300206	0.019235683
TCAF1	0.547181196	9.354532693	0.019970265
BAG6	-0.74698734	7.464953772	0.020501202
NEDD8	-0.57853253	7.611533897	0.020812679
ZMIZ1	-0.635594903	7.915685255	0.021128002
HAND1	-0.572008201	7.022438286	0.021133806
SMARCA1	0.466729889	8.090071558	0.021270031
DAXX	-0.635336572	6.863198027	0.021664842
FNDC3A	0.496811075	7.88847881	0.02182937
CLIP3	-0.852965081	7.407963873	0.021843053
ZMAT2	-0.531162094	6.909940284	0.022096076
KLHDC3	-0.751347562	7.241338002	0.022791483
ATF4	-0.596270729	6.611322335	0.023073957
CLPTM1L	-0.551346166	7.096490119	0.023304574
XIST	-0.531085678	9.440920395	0.023342366
NCSTN	-0.581791732	7.090979139	0.024430641
UBAC2	-0.494430848	7.366223592	0.024664675
CFAP97	-0.55037668	7.125539279	0.024982466
GNG5	-0.615180579	8.544140665	0.025011986
PPP1R10	-0.649988033	6.762570837	0.025195653
MPV17	-0.588286449	7.065128221	0.025881037

MT-ATP6	-1.159920927	13.07305454	0.026005844
AK2	-0.47783234	7.758020521	0.026581472
TFAP2B	0.480740601	7.386584245	0.026771089
LRRN3	-0.50825704	8.404482363	0.026821324
BUD31	-0.580403107	7.74115614	0.026871668
CHMP4B	-0.58273011	6.843367991	0.027273808
SEC23B	-0.463246017	7.486818053	0.027346597
IRF2BP2	0.5093795	7.264786382	0.028121064
MCCC2	-0.445282251	8.015567323	0.028970421
SSRP1	-0.655187182	8.722625177	0.028978838
SARS	-0.612948603	7.449126189	0.029090394
H3F3B	0.512040267	9.756314258	0.029571005
PSMC4	-0.676344975	6.788810725	0.029620917
AFAP1	-0.485935841	6.90889694	0.029926016
MT-CO2	-1.016751331	14.05800818	0.030375754
UBR5	0.448036772	7.813890489	0.030994807
POLR2H	-0.555441462	6.835715306	0.031129857
ID2	0.56325906	8.015145563	0.031274698
PTDSS1	-0.54849364	7.499481218	0.03141721
CETN2	-0.487230186	7.017210086	0.031601298
TUBA1B	-0.730659217	9.151440654	0.031643051
PKM	-0.79058477	9.671057409	0.031929466
CERK	-0.450201272	8.105680291	0.03218758
PPP2R5E	0.432660442	7.900399134	0.032612417
POLR2A	-0.834773764	7.087055602	0.032742537
MAGI2-AS3	-0.588311604	7.206015915	0.033086028
UBAP2L	-0.694194823	8.490312113	0.033545911
NAT10	-0.552699278	7.193540109	0.03358678
LINC00665	-0.600417696	7.421999379	0.033625882
STT3A	-0.506456737	7.677946311	0.03369268

RPL35	-0.609828322	6.635443688	0.034048363
RERE	-0.545363082	7.132047495	0.034649325
PDCD11	-0.574919317	7.492894518	0.034829288
TENM4	-0.54734415	6.697226231	0.034978287
RAD50	-0.424015801	8.033194909	0.035811552
KIAA0100	-0.509305854	7.980113726	0.035930253
TRAK2	0.427916012	7.068273404	0.036327304
CDK6	-0.629461946	9.22387697	0.036914719
MAPK1	0.403920802	7.044887938	0.037523153
FABP5	0.46059264	6.988679239	0.037855408
TMX4	0.470648742	7.099597454	0.038933877
NDFIP1	0.426255978	8.466402049	0.038995421
PMPCA	-0.539834563	6.916608077	0.039178313
DYNLT1	-0.453987805	8.424423504	0.039964143
CIRBP	-0.523272032	6.763159124	0.040949801
JAK1	0.398300871	7.717623211	0.042444903
STARD4	0.560615298	6.821007386	0.043783788
PSME1	-0.594407247	7.288375279	0.044137683
VPS39	-0.463902402	7.351606323	0.044175796
TLN1	-0.689618228	7.540808926	0.044426814
PRMT5	-0.587111509	8.325262667	0.044911139
ZC3H13	-0.425567994	8.072920026	0.046122211
DLST	0.561831892	6.851242186	0.046333118
ABLIM1	0.407822267	8.091731788	0.046869633
IQGAP1	0.408367593	8.015551266	0.046887081
ELF2	0.4393446	6.731004387	0.046964476
EP400	-0.458006277	7.075043425	0.047077892
GTF2A2	-0.408809607	7.680856841	0.047162908
SNRPN	-0.517187341	7.76207455	0.047188755
DNMT1	-0.511923551	7.562221354	0.047727604
RNF214	-0.475111191	7.194348488	0.048416562
ATL2	0.434027032	7.353977098	0.048603872

CCND1	0.487429487	9.323533105	0.049048184
KCTD20	0.426584195	8.588293549	0.04934024
GCN1L1	-0.569440023	7.3108849	0.049475995
NEK1	-0.460217125	6.985472017	0.049477908

Table 4: Gene list of significantly (p<0.05) up-regulated or down-regulated genes after prolonged GlcN treatment

	logFC	logCPM	PValue
TFPI2	2.449549276	7.984336724	4.27E-22
GNG11	1.400880484	8.062998042	8.64E-12
MGEA5	1.029759892	7.965254798	2.20E-08
IGF2	-1.415111687	7.026821053	2.30E-08
DKK1	1.274701245	8.595270368	3.95E-08
TUBA1B	-1.879917667	9.151440654	7.54E-08
RP11-481F24.3	1.162426643	7.201935817	3.10E-07
HAND1	-1.279389647	7.022438286	3.71E-07
ERP29	-1.376501598	7.030170382	3.76E-07
ATF4	-1.33553956	6.611322335	5.32E-07
PDGFRA	-1.091817707	6.88888152	5.60E-07
PTMS	-2.046182301	7.749769069	9.76E-07
ATP7A	0.994206259	7.337665669	1.41E-06
CALR	-1.354956856	7.875427446	4.83E-06
RELN	-0.99206582	7.327970415	1.42E-05
AHNAK	-1.076559642	8.917657368	1.46E-05
TMSB10	-1.870704304	7.146039288	1.72E-05
NUDC	-1.242362228	6.792171458	1.75E-05
NID1	-0.912566093	7.252899644	1.82E-05
RPS11	-3.22548531	8.36363387	2.35E-05
MYL6	-1.061201889	7.996649405	3.63E-05
CFL1	-1.546174471	8.733514764	3.84E-05
C18orf32	1.218130265	6.754779215	4.23E-05
NEDD8	-1.027447717	7.611533897	4.62E-05
PKM	-1.505232604	9.671057409	5.78E-05
UBA52	-1.333477997	6.814546944	6.44E-05
CAPNS1	-1.451744755	6.541698801	7.24E-05
SUPT6H	-1.284650185	7.043424732	8.34E-05
GAP43	-	7.530240071	8.61E-05

	0.779216082		
PLCXD3	1.098396638	6.381448599	0.000101694
UBC	-1.399370809	9.485955683	0.00012405
FLNB	-1.054081826	6.962606714	0.000150823
IMPDH2	-1.156659038	7.353090857	0.000160469
AKAP12	-0.809030747	6.787146944	0.00016659
MPP6	0.850937415	7.235000472	0.00016691
SSRP1	-1.133396883	8.722625177	0.000179628
RPL7A	-1.244465491	7.4213187	0.00018936
MANF	-0.871614147	7.073468586	0.000194654
GNB2L1	-1.2240911	7.547941363	0.00021181
GAPDH	-1.262893693	10.0902515	0.000222794
GANAB	-1.023214928	8.211212754	0.000237194
CIRBP	-0.9442862	6.763159124	0.000248837
NOMO1	-1.000695714	7.771738954	0.000257103
UBE2I	-1.049636975	8.115504563	0.000257817
HDAC9	0.930311296	7.291180258	0.000258633
EIF3I	-1.144167785	7.376246758	0.000283796
CDC25B	-1.043907968	7.004003099	0.000293597
FTSJ3	-1.219236098	6.969777419	0.000294765
UBAP2L	-1.186122857	8.490312113	0.000319863
RPL29	-1.096950136	9.193880883	0.00032508
SMARCC2	-1.087339026	7.300937992	0.000351224
NBEA	0.712396317	7.51802842	0.000356862
FAT1	-0.765544444	8.025525536	0.000367826
FRMD6	0.868642632	6.423991918	0.000370383
P4HB	-1.04549002	7.574752079	0.000408307
CLIP3	-1.317846172	7.407963873	0.000452579
MAP1A	-1.116638013	6.664603258	0.000461457

CHGA	-1.268354165	7.438226481	0.000510925
CD63	-0.895370821	7.839260571	0.000536769
EIF3C	-1.214081436	10.75841222	0.000582845
RPL35	-0.993311222	6.635443688	0.000601764
QARS	-1.222550602	6.941977028	0.000603939
CTDNEP1	-0.904537968	7.377677381	0.00062902
MAB21L2	-0.967090374	7.272067617	0.000632616
POLR2A	-1.350853688	7.087055602	0.000633538
SLC39A1	-0.954783093	6.691312588	0.000835626
RPL10	-1.315804457	7.855640214	0.000840155
AARS	-1.03977848	6.681350405	0.000897923
PPM1G	-1.050372577	8.574637675	0.000936779
ANXA2	-0.860435794	8.367700311	0.001037822
S100A10	-0.900264302	6.924309517	0.001137347
MCM3	-0.658699767	7.911133648	0.001173992
MRPL37	-1.080091503	7.637839562	0.001196051
PSMD2	-0.928406368	7.358599115	0.001314969
NOP56	-0.726286439	7.850050755	0.001331374
SSR2	-0.913752596	8.103371435	0.001350133
RGS4	-0.657522844	8.401062865	0.001357951
CKS1B	-0.660488747	7.792235171	0.001390785
TWIST1	0.752714522	7.015622298	0.001397533
RPL18A	-1.192914417	7.351885612	0.001419253
ABCF1	-1.019670892	6.734491684	0.00154863
RPS18	-1.058620299	10.37371853	0.001624468
MDH2	-1.077851179	6.794050353	0.001668437
NOMO3	-0.958839472	7.238961612	0.001688511
AFAP1	-0.7039821	6.90889694	0.001718838

PSME1	-0.929705961	7.288375279	0.001743191
DAXX	-0.868244207	6.863198027	0.001775445
MKI67	-0.747689275	8.569323556	0.00188046
POM121C	-0.851596529	7.004598091	0.001934554
SETDB1	-0.831736823	7.847568759	0.002017257
RPS15A	-0.837645542	9.97400285	0.00201729
IL17RD	0.614346014	7.421823589	0.002037409
RPL26	-0.745592051	9.701854615	0.002079022
EEF2	-0.994067338	8.817360808	0.002097463
CSNK2B	-0.903683018	7.510070449	0.002195241
RPLP0	-1.115316482	9.717400177	0.002236339
SLC6A2	0.648355535	6.887559136	0.002247475
RPS3	-0.947471519	10.54016106	0.002361594
YIPF4	0.719401214	7.011829971	0.002412642
PPP2R5E	0.609956712	7.900399134	0.002624983
HUWE1	-0.806315759	8.779912743	0.002705815
RPL41	-0.996726326	9.778364457	0.002834304
PTDSS1	-0.762332768	7.499481218	0.00287259
SPARC	-0.646927276	8.543539304	0.002936573
SLC4A8	-0.618033071	7.361169902	0.0030232
NCSTN	-0.767778464	7.090979139	0.003073275
ATP5J2	-1.052840053	6.972619815	0.003076987
CACNG4	-0.758677273	7.322199509	0.00307967
KIF20A	-0.758480324	7.237190861	0.00354331
TENM3	-0.710714609	7.317308789	0.003554218
RPL12	-0.943227154	9.45141067	0.003664619
EEF1G	-1.055158341	10.2400586	0.00373831
RPS27	-	10.15260232	0.003750255

	0.773356915		
SMN2	0.57950038	7.832268092	0.003784391
HAT1	0.750059426	6.710903936	0.003969555
BRD2	-0.798209445	7.085629549	0.004142737
SEC24C	-0.771494257	7.5126224	0.004161356
SFRP1	-0.679631882	7.438536355	0.004235332
ARF3	-0.64333804	7.630591759	0.004305669
ACACA	-0.738824251	7.683161139	0.004373437
TLN1	-0.979205919	7.540808926	0.004516241
EIF4A1	-0.855668751	10.70555321	0.004533314
ATL2	0.624208475	7.353977098	0.004637697
MMP2	-0.887883808	6.911105807	0.00477092
RPL27	-0.789934282	8.890944811	0.004810893
PRMT5	-0.823990018	8.325262667	0.00503439
UBE2C	-0.766146097	6.722297448	0.005459595
FOXM1	-0.673777831	6.845013745	0.005480087
RPS4X	-0.835130403	11.59372685	0.005527749
RPL32	-0.892950377	9.850476809	0.005590872
SPTAN1	-0.749443924	8.406872594	0.005602003
CEP44	0.751318747	7.946345157	0.005755674
FDFT1	-0.676513169	8.031042705	0.005764419
ZWILCH	0.68116595	6.991362982	0.00583738
MZT1	0.856832499	7.200653965	0.005893811
SNRPA	-0.927066607	6.6612562	0.005920381
CCDC25	0.598452386	6.863724597	0.005930061
LIMA1	0.565326949	7.107553024	0.005957992
NRCAM	0.616146235	8.568472697	0.006018163
ACTR6	0.803625714	6.696332746	0.006032362
TRRAP	-0.600171683	7.738996983	0.006287822
MMP16	0.709177388	6.772804339	0.006364951
RERE	-0.705083641	7.132047495	0.006449983
HDLBP	-0.805103949	8.756848215	0.006618269

ICA1	-0.575553805	7.570555811	0.006619576
RPL36A	-0.699011048	9.526002269	0.006820403
DDX39B	-0.621456332	7.975360576	0.006961993
AGPS	0.564570998	7.704238311	0.007003106
RAD1	0.580377877	6.955470888	0.00704437
DCP2	0.650519857	7.125352994	0.00713944
SLC6A15	0.577438896	6.97252449	0.00727042
ARHGEF2	-0.78031508	6.72884992	0.007373756
VCP	-0.774321937	8.342207436	0.007428919
DCK	0.688474788	6.96419796	0.00744561
AATF	-0.806540936	6.872945729	0.007482898
EIF4G1	-0.706917237	8.022366495	0.007589612
CRMP1	-0.804904001	7.462212511	0.007740171
MAD2L1	0.6376872	8.133537319	0.007801153
KRAS	0.684820319	6.996256626	0.00796092
SEP6	-0.609164778	8.345705899	0.007970812
PACS1	-0.800720499	6.783206458	0.008090056
TRIB2	0.597201737	6.916130214	0.008262241
SF3B2	-0.889440512	8.831230396	0.008295734
CHD4	-0.737497657	8.841874977	0.008361105
ESRRG	0.744728199	6.54602197	0.008581295
RFC3	0.563171996	7.17292876	0.00860644
TENM4	-0.681720549	6.697226231	0.008740565
SCN9A	0.649198785	6.668730579	0.008885445
RET	-0.579482451	8.851087406	0.008977665
PM20D2	0.638223924	7.01836256	0.009047824
MAZ	-0.773613904	8.139140992	0.009207079
SARS	-0.732181625	7.449126189	0.009273848
ZNF512	-0.555408711	7.99040199	0.009457014
PRPF8	-0.834760956	9.685375011	0.00963452
PSMB7	-	7.235679873	0.009711272

	0.727956917		
EBNA1BP2	-0.733089419	6.993256334	0.009782487
TMEM167A	0.639409034	7.753360893	0.00983525
DNMT1	-0.668873607	7.562221354	0.009837584
IGF2R	-0.592953568	6.870804615	0.009946033
ACIN1	-0.642461085	7.442737952	0.010093296
TMSB4X	-0.715184758	7.855200311	0.010228081
NDUFS5	-0.609778616	7.899946954	0.010263996
UBA1	-0.797236696	7.079383668	0.010322846
RPL37A	-0.894477313	8.274734907	0.01039317
IER3IP1	0.637503727	6.760418352	0.010426087
PPP1R10	-0.743974382	6.762570837	0.010539677
MYH10	-0.597498194	8.590632499	0.010557975
WRN	0.57680754	6.812570166	0.010589966
PPA2	0.584666401	7.052682313	0.010621163
TSNAX	0.677498888	7.559712178	0.010692415
KNTC1	0.521812007	7.385276901	0.010814285
DDB1	-0.789183116	8.896145766	0.010824649
PGD	-0.748030067	7.024148494	0.010828651
CERS2	-0.715389949	8.738537837	0.011048614
MT-CO3	-1.228666502	13.19784594	0.011055031
USP1	0.573950768	7.35725584	0.011623638
BAG6	-0.813704696	7.464953772	0.011715432
BUD31	-0.660381525	7.74115614	0.011898487
NCAPG	0.538895563	7.352033599	0.011993385
RPL18	-0.830177803	7.004954257	0.012001174
MAP9	0.572623367	7.308828496	0.012097032
SEH1L	0.531568546	7.626968001	0.012166801
SND1	-0.824524663	8.593465519	0.012411452
SOD1	-0.546118945	7.927965277	0.012532181
CASC3	-0.600136446	7.915392048	0.012612724

CCNC	0.705235943	6.677367037	0.012675998
YY1AP1	-0.658425462	6.924581188	0.012776883
EP400	-0.574685737	7.075043425	0.012849797
C6orf62	0.542806199	7.484205128	0.013342723
CMPK1	0.66072971	6.707208464	0.013545926
LARP1	-0.550406093	7.576201989	0.013733488
RPS16	-0.808168435	8.022021186	0.014099674
RPL38	-0.707950902	10.00736928	0.014156962
UHMK1	0.586236814	7.558897537	0.014287435
PITPNA	-0.572224219	6.833321905	0.014316427
COPA	-0.614062843	8.938574056	0.014355688
STARD4	0.681003543	6.821007386	0.014434392
RIMS3	-0.656240482	8.579287327	0.0145643
RB1	0.553879463	7.85310158	0.014925876
SMC2	0.526218926	7.787049526	0.014951571
PSMC4	-0.755834284	6.788810725	0.015230787
BNIP2	0.554001485	6.969841001	0.015297166
CCT3	-0.716741768	10.08242527	0.015344614
DCAF13	0.542195013	7.830765596	0.015673761
UBR4	-0.625690888	8.00843422	0.015761273
TTC8	0.523502302	8.100822882	0.015828415
ATP1A1	-0.63018381	8.6461645	0.015909115
RNF11	0.685100389	6.727516365	0.015909417
SMARCB1	-0.763859903	6.836947687	0.015912008
CDK1	0.65449131	7.879598216	0.016043545
ICE2	0.516364882	7.145945949	0.016098486
ZPR1	-0.604940122	7.416296754	0.016265433
CENPH	0.605621328	7.466403305	0.016496252
MFN1	0.599206145	6.715247344	0.016720707
SNRNP200	-0.734677044	9.625119196	0.01677819
NCAM1	-0.55147354	7.620459395	0.016854109
ARID1A	-0.539824616	7.09999454	0.016925311

LAMC1	-0.538555825	8.460123093	0.017007916
ACTR1A	-0.684527826	7.508053133	0.017031741
ZMAT2	-0.553957777	6.909940284	0.017061988
NAT10	-0.620650527	7.193540109	0.017146121
FTH1	-0.67921641	10.58979242	0.017158094
PDCD11	-0.649147429	7.492894518	0.017287096
RNF10	-0.593204373	7.342929869	0.017343642
CEBPZ	0.475961429	7.925583275	0.017531781
SPTBN1	-0.592042479	8.886429184	0.017570762
SAFB	-0.637424821	7.372130865	0.017633644
FUNDC2	-0.64358153	7.768551483	0.01775531
STIP1	-0.69127169	8.811040089	0.017783344
THOC5	-0.669142133	6.887044763	0.017864025
PA2G4	-0.648111642	9.112591306	0.018008156
UBE2L3	-0.795557755	7.589486513	0.018172899
CBFB	0.703332894	6.904897168	0.018253823
GTF2A1	0.618844647	6.983776761	0.018352446
FNTA	0.477656588	7.58847535	0.018391283
CD164	0.686927483	7.260505416	0.018436526
EIF3D	-0.682392139	8.514206669	0.01848299
UBA6	0.581579426	7.115459934	0.018486879
MAT2B	0.550741813	7.430974584	0.018575729
HIP1	-0.586275616	6.795428511	0.018671586
ARL5B	0.62235564	7.385961169	0.018691811
PHF6	0.537538285	7.927563334	0.018910978
SCG2	-0.499942438	6.918525441	0.018961941
C1orf112	0.476728967	6.929970554	0.018975063
SRPR	-0.623579396	6.908883782	0.019254143
CKS2	0.581759577	7.445938462	0.019301158
EIF1AX	0.698255698	8.298949822	0.019373384
HOOK3	0.563931747	6.913164497	0.01940759
NDUFB9	-0.683828572	6.973963778	0.019434354
GMFB	0.690219098	7.392405567	0.019613501

TMEM165	0.521524523	7.039863927	0.019887733
DYNC1LI1	0.513185913	6.990195465	0.020007663
SNRPN	-0.606026147	7.76207455	0.020210175
PPIA	-0.662215713	10.97911734	0.020282527
C7	-0.545587372	9.406382224	0.020391364
GGCT	0.49424728	7.282774654	0.020448593
GPS2	-0.881208997	6.922239736	0.020455783
MT-ATP6	-1.208888682	13.07305454	0.020471926
GTF3C6	0.522733675	8.29411623	0.02114604
PPIP5K2	0.522578637	7.017621913	0.02121959
SMAD9	0.633606902	7.717361504	0.021234545
DR1	0.642032937	7.458048374	0.021298702
C14orf132	-0.490692873	7.588519753	0.021445418
PLXNA4	-0.497705128	7.804488271	0.021459352
RPN1	-0.569862634	8.182041117	0.021565617
RNF130	-0.528230312	6.855189249	0.02171543
OSTC	0.553977859	7.331965259	0.021737994
PPP1R11	-0.647721324	7.968385626	0.021929147
TPM1	-0.517358886	9.033555243	0.021963848
PRC1	-0.474864854	7.963396862	0.022258974
ID2	0.595614455	8.015145563	0.022825072
ATP11C	0.491682441	7.003226685	0.02294183
ECHDC1	0.599902403	6.861418435	0.02295611
KDM3B	-0.479753467	7.517559129	0.023136132
ASXL1	-0.530197124	6.976883533	0.023436778
WDR36	0.502866781	7.172501832	0.023531701
SOGA1	-0.632629455	6.847462532	0.023542551
THOC3	-0.521400525	6.987629437	0.023579514
PCNA	0.534217703	8.981790186	0.023683686
NAE1	0.577662666	7.232312345	0.023700541
STT3A	-0.538691871	7.677946311	0.023982997

COX7C	0.539637674	7.033128702	0.024358263
XPNPEP1	-0.51705682	6.814916709	0.024404862
SRSF11	0.530030416	7.903983898	0.024554145
LRRC58	0.643890773	6.780720558	0.024664326
JAM2	-0.489466027	6.938709053	0.024856031
G2E3	0.691420291	6.741750614	0.025158807
SPCS3	0.607757251	6.966560864	0.02517903
CCDC90B	0.59390345	6.807165431	0.025330841
DDX24	-0.580561	8.372791718	0.025551272
ADSS	0.453373629	7.374256693	0.025551974
NUDCD3	-0.567178097	7.36528815	0.025557214
GNPNAT1	0.550681541	7.591550715	0.025914652
FAM98B	0.506125364	7.527517404	0.025988397
ASCL1	-0.446866795	8.569181531	0.026002839
LSM5	0.616351534	8.181851511	0.026022315
OSBPL8	0.526478052	7.21479431	0.026100384
TMEM106B	0.59573737	7.231479994	0.026113432
CDON	-0.485652611	7.0078246	0.026119988
POLR2M	0.547581428	7.159183699	0.026290652
PSMD12	0.489125873	8.249937634	0.026407304
GCSH	0.524065189	7.310630424	0.026857462
USMG5	0.563745341	7.377173494	0.026897771
TMEM30A	0.55102192	7.849612154	0.026917315
ARNT	-0.448124848	7.588450097	0.027023973
TFAM	0.536775231	7.238324589	0.027384851
NDC80	0.515990727	6.825341431	0.027501917
HAUS6	0.497044384	7.503734266	0.027725176
WIPI2	-0.504375865	6.773379804	0.027746182
SMG7	-0.532716513	8.348162119	0.027989765
MTPN	0.585120335	10.06923325	0.028157416
SF3B6	0.478313408	7.952346408	0.028296054
YKT6	-0.555280612	7.535864988	0.028472171
TWF1	0.689926572	6.927530248	0.028525407
CYCS	0.633041606	8.419434912	0.028610661
RPL6	-0.529514861	10.72676553	0.02865775
DEPDC1	0.583857943	6.742471195	0.028665198
GULP1	0.681354217	7.253071095	0.028707305

NES	-0.616366567	9.214172583	0.029100777
UXT	-0.73432444	6.787524068	0.029152751
LTN1	0.516865405	7.2472387	0.029168979
SAP30BP	-0.562826004	7.214673687	0.029559357
ACTB	-0.629683485	11.6785997	0.029647613
TMX3	0.588144213	6.659098527	0.029656312
EGLN1	0.572705063	6.829437454	0.029666026
ERC1	-0.547597571	6.73223718	0.029919791
GSTM3	-0.7487231	6.933423974	0.029945921
CTSB	-0.632680577	7.845931199	0.029993108
VPS13A	0.479187185	6.684107939	0.030300953
RAD21	0.544372769	9.577534675	0.030404265
GCN1L1	-0.627736397	7.3108849	0.030527259
STRAP	0.473996474	8.945718768	0.030697514
HIGD1A	0.542298614	7.0127987	0.030786342
XPO1	0.52884387	9.370407101	0.030790216
TP53BP2	-0.549729203	7.405747318	0.030797176
VPS26B	-0.535177871	6.854521171	0.030816934
KMT2A	-0.529556472	7.63970236	0.030830004
EID1	0.682005873	8.279743343	0.030874475
H2AFY2	-0.585974046	6.942115336	0.030934962
CD46	0.511975868	7.440134619	0.031007583
KCTD12	0.592893311	7.427404919	0.031137575
BLOC1S6	0.454844004	7.215829354	0.031366392
GON4L	-0.588020084	6.824164549	0.031579528
ATP11B	0.473839955	6.952190087	0.032207808
SRP68	-0.503289134	7.790219698	0.03228419
ZBTB44	0.501026351	7.070238659	0.033009098
STAG2	0.475366305	8.057609458	0.033124777
SEC14L1	-0.521427612	6.909749389	0.033626925
CCZ1	0.438259614	8.398980931	0.033816862
TOR1AIP2	0.449262301	7.542236873	0.033866578
MRPL9	-	7.53490675	0.034092372

	0.507292898		
PPIB	-0.701221648	8.751017828	0.034099479
TLE4	0.441754831	6.798673105	0.034132896
MALAT1	0.431437911	7.339203293	0.034242072
SLC7A2	0.441425173	7.988861349	0.034380428
PPP2CB	0.420943412	7.416619151	0.034380807
KDELR1	-0.605106858	6.746939746	0.03440662
EXTL2	0.488275838	7.273557849	0.034426432
PURB	0.495093403	8.145382898	0.034487529
NAA15	0.458689281	8.072056543	0.034705333
SOCS4	0.562252875	6.755806882	0.035006224
SCRN1	-0.459078684	8.468773471	0.035567933
RPS6	-0.564538316	9.943868117	0.035606921
PFDN5	-0.570007782	8.145984891	0.035707386
PRKD3	0.491728899	8.18603757	0.035882594
ABCE1	0.528202237	8.075550887	0.035976579
GNG12	0.486971165	7.582135339	0.036471776
TLN2	-0.523388326	6.755797925	0.036559026
SGK1	0.476590583	6.065222981	0.036622195
RPL3	-0.628572575	9.54478926	0.036778936
CAPZA2	0.610555175	7.410070211	0.03736812
PPP1CB	0.598881591	8.552653266	0.03785458
RFWD2	0.398954167	7.396916794	0.037885057
MAP4	-0.564871021	8.757519887	0.037967424
PPP3R1	0.403489288	7.954328608	0.038014055
RPL10A	-0.715157412	10.1174482	0.038324659
STARD3NL	0.444598728	7.314185085	0.038996223
HK1	-0.646342554	7.37144133	0.039244919
MCM7	-0.60963435	7.244267667	0.039292398
BZW1	0.517243924	9.483454137	0.039611884
ADO	0.424823422	7.34393212	0.039666453
MT-ND5	-1.08099704	11.3921962	0.039691753
KIAA0100	-0.498778869	7.980113726	0.039947844
RAF1	-0.42510671	7.014396999	0.039985939
FAM208A	0.453296834	7.169718832	0.039997722
BRIP1	0.452416501	7.070592948	0.040321359

ZNF3	-0.4695101	7.656415219	0.040392913
SNX7	0.426471908	7.558749456	0.040409874
CRTAP	-0.499374727	8.358040186	0.040521704
TRPM7	0.492725154	6.931745473	0.040652685
EXOC5	0.504949385	7.532718824	0.040848328
DNAJC10	0.444862834	7.712336112	0.041098912
PNO1	0.510120268	6.846447503	0.041197502
HNRNPA0	0.458595539	8.55949452	0.041372721
PDCD4	0.429648778	7.004777498	0.041573843
PCNP	0.536955247	8.352967408	0.041767613
SEC24D	0.373856909	7.791125547	0.041954992
RSBN1L	0.475478447	7.169047314	0.042187338
SLC20A1	-0.429278338	7.197391534	0.042261343
THUMPD3	0.44680257	6.767278038	0.042415024
SIN3A	-0.53258322	7.287836893	0.042592761
C7orf73	0.428421556	7.511267518	0.042726276
DENR	0.4330541	7.809993219	0.043112607
RPS2	-0.663638592	10.29349875	0.043274444
MT-CO2	-0.946278093	14.05800818	0.043617983
CS	-0.553999987	9.382035718	0.043618661
UBE2Q1	-0.464233572	8.006393661	0.043746258
NCAPD2	-0.526114564	8.199127337	0.043900763
MRPL42	0.460995044	7.153197851	0.044020685
COPG1	-0.522697244	6.807995611	0.044119245
GEN1	0.521059619	7.117859347	0.044328841
RPL27A	-0.548524254	10.29231561	0.044341545
SRSF10	0.440295505	7.998350578	0.044430204
NDUFB6	0.777413315	7.28138122	0.044931393
DENND5A	-0.446772557	7.052297083	0.045324949
ECT2	0.47174819	7.79343461	0.045370558
APLP2	-0.483139339	8.767654763	0.045603705
KPNA3	0.459516859	7.331257373	0.046168464
SIKE1	0.483376267	6.923773785	0.046240972
ORC2	0.385126849	7.448399315	0.046279304

RC3H2	0.418712468	7.339394834	0.046308889
MSH2	0.496425736	8.146747115	0.046743655
ARIH2	-0.465788317	6.963631321	0.046887397
EML4	0.455868452	9.075641723	0.046956188
CAND1	0.446081472	8.575612657	0.047091855
GATAD2B	-0.463864272	6.990985567	0.047135895
SF1	-0.550061371	8.770854265	0.047163389
USP33	0.417250209	7.637428035	0.047295601
ATP13A3	0.451534212	7.684347954	0.047470236
CH507-513H4.3	1.71524385	8.866424395	0.047488558
CH507-513H4.4	1.715243851	8.866424395	0.047496103
CH507-513H4.6	1.715243852	8.866424395	0.047500949
ACTR2	0.481151912	9.322584915	0.047544539
RPS25	-0.503202308	9.590099838	0.047663212
SLC4A7	0.491703374	6.712520362	0.047921546
DEK	0.498577957	8.698118689	0.048064857
PTEN	0.457687764	7.815508876	0.04813261
CLTA	-0.498804227	8.297464041	0.049389844
KRR1	0.493663748	6.585563324	0.049425754
CENPU	0.418760387	7.270888839	0.049462329
UBE4B	-0.447380619	7.184125761	0.04949097
DESI2	0.466222975	7.973720163	0.049690195
ADAM22	0.4064219	8.082423309	0.049707012
UBE2K	0.418281214	8.327286796	0.049916693
UTP14A	-0.460348822	7.575680321	0.049931014

13 mitochondrial-encoded polypeptides of ETC complex subunits were found. Of these genes, TMG treatment down-regulated 3 and GlcN treatment down-regulated 4 (**Figure 15B**). Of note, the mitochondrial transcription factor A (TFAM) level, the mitochondrial specific transcription factor [74], was unchanged between treatments (**Figure A.3F)**, suggesting that O-GlcNAc could be modulating the mitochondrial transcriptome by affecting TFAM activity or mitochondrial mRNA stability.

Using gene set enrichment analysis (GSEA) [75] to compare TMG-treated with control gene expression data sets, we identified genes from the insulin signaling pathway, aging, and cancer metastasis enriched in prolonged TMG-treated cells (**Figure A.3G-I**). These data suggested that prolonged O-GlcNAc elevation modulates the progression of chronic metabolic disease.

3.3.5 NRF2-mediated Oxidative Stress Response was Down Regulated

To define biological functions of the altered genes, we performed Ingenuity Pathway Analysis (IPA). A stringent threshold (cpm of > 100) was applied to the gene set to prevent false positives. There were 22 canonical pathways for TMG-treated (**Figure 15C**) and 26 canonical pathways for GlcN-treated cells (**Figure 15D**) were identified (**Table 5-6**). We found 13 pathways overlapped in both TMG and GlcN-treated cells and changed in the same predicted manner (see **Figure 15C-D**). The NRF2-mediated oxidative stress response was identified as down regulated in both TMG and GlcN treated SH-SY5Y cells. These data suggest that both TMG and GlcN treatments could modulate ROS levels.

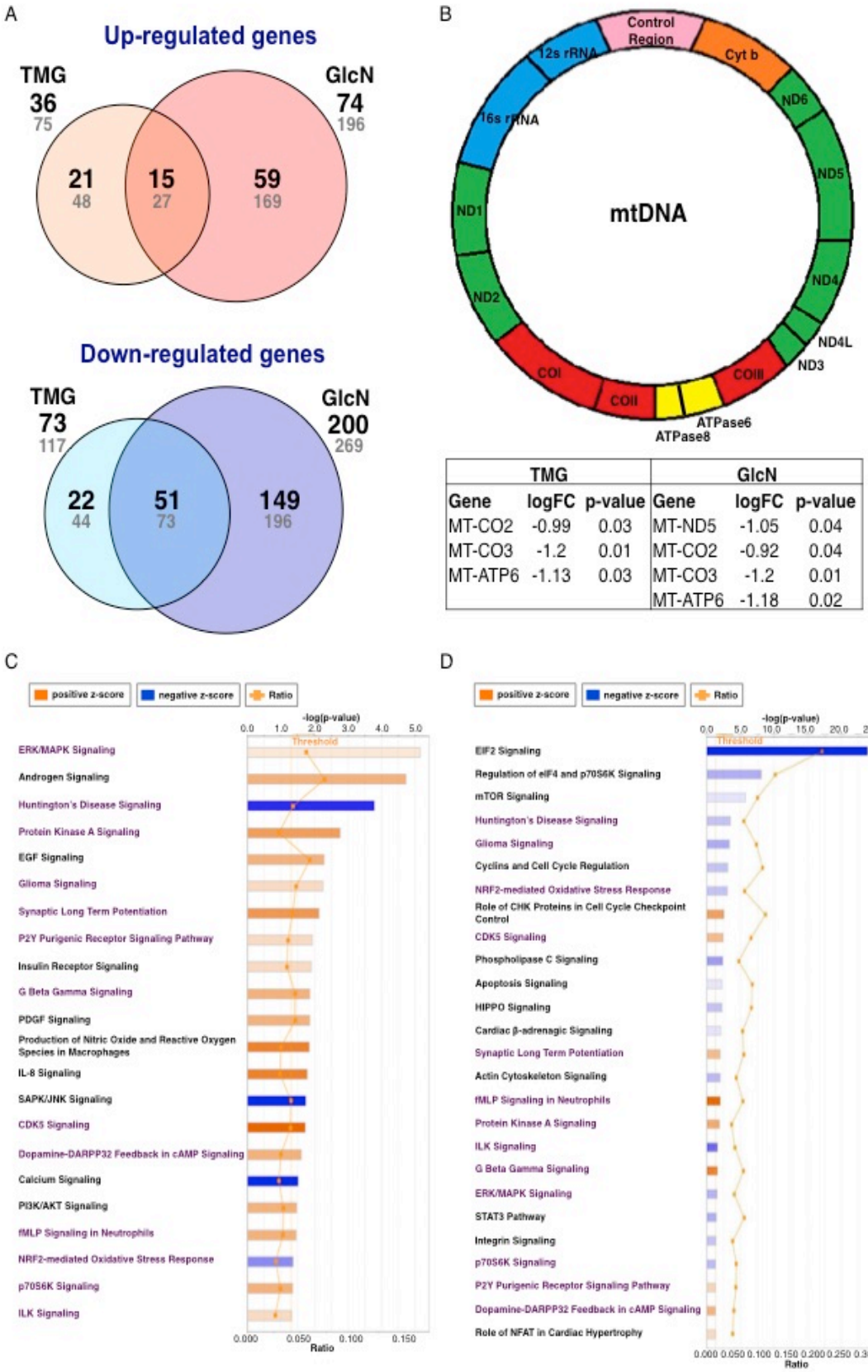

TMG			GlcN		
Gene	logFC	p-value	Gene	logFC	p-value
MT-CO2	-0.99	0.03	MT-ND5	-1.05	0.04
MT-CO3	-1.2	0.01	MT-CO2	-0.92	0.04
MT-ATP6	-1.13	0.03	MT-CO3	-1.2	0.01
			MT-ATP6	-1.18	0.02

Figure 15: TMG or GlcN treatment altered the transcriptome and down-regulated NRF2-mediated oxidative stress response

Representative Venn charts showing number of differentially expressed genes **(A)** up-regulated or down-regulated after TMG or GlcN treatment. Shown in grey are number of genes whose expression was changed ($p < 0.05$) compared to control cells. Numbers in bold represent $p < 0.05$ genes changed more than 1.5-fold (n=3). **(B)** Schematic representation of mitochondrial-encoded genes that were down-regulated. Canonical pathways significantly associated with changes in genes expression after long-term **(C)** TMG and **(D)** GlcN treatment.

Table 5: TMG gene list used for IPA analysis

	logFC	PValue
MAB21L2	-1.622228417	1.71E-08
IGF2	-1.532544968	1.60E-09
GPS2	-1.475796159	0.000127915
MT-CO3	-1.227853996	0.011106659
PTBP1	-1.183514144	0.013301863
MT-ATP6	-1.159920927	0.026005844
PTMS	-1.134915161	0.005305841
AARS	-1.041876727	0.000872145
EIF3C	-1.026933741	0.00348991
MT-CO2	-1.016751331	0.030375754
PPM1G	-0.98249157	0.001938814
MANF	-0.97916434	2.93E-05
MRPL37	-0.976214847	0.003333965
RIMS3	-0.916268416	0.000679593
FTSJ3	-0.884046023	0.008211142
MDH2	-0.876874588	0.010232305
NOMO1	-0.862037417	0.001591809
CLIP3	-0.852965081	0.021843053
POLR2A	-0.834773764	0.032742537
CSNK2B	-0.82997636	0.004847854
SF3B2	-0.813660562	0.015602109
MTUS1	-0.810318467	0.000351102
UBE2L3	-0.80721758	0.016552814
GAR1	-0.802816833	0.007688859
ASCL1	-0.796494691	7.81E-05
PKM	-0.79058477	0.031929466
PPIB	-0.789567779	0.017175562
PPP1R11	-	0.006083876

	0.776560451	
SUPT6H	-0.774025763	0.01657952
NUDC	-0.772413173	0.007019238
ZPR1	-0.769295093	0.002295731
CDC25B	-0.760981608	0.007946699
FAT1	-0.752040827	0.000465052
KLHDC3	-0.751347562	0.022791483
BAG6	-0.74698734	0.020501202
EBNA1BP2	-0.746411625	0.008541209
BRE	-0.740280557	0.013188866
TUBA1B	-0.730659217	0.031643051
IMPDH2	-0.727170212	0.016751588
CHRNA3	-0.723569954	0.001396019
ITGA1	-0.72265724	0.000655617
THOC5	-0.71295444	0.011654324
MAZ	-0.712648443	0.016313182
P4HB	-0.706254071	0.016282525
CTDNEP1	-0.698431838	0.008055964
POM121C	-0.695631769	0.011098191
UBAP2L	-0.694194823	0.033545911
CALR	-0.691395808	0.018067103
GPC6	-0.690137144	0.013245586
TLN1	-0.689618228	0.044426814
ERP29	-0.682263947	0.010606499
PSMC4	-0.676344975	0.029620917
UBE2C	-0.670668518	0.014793118
ELAVL4	-0.660712706	0.008359706
SSRP1	-	0.028978838

	0.655187182	
PPP1R10	-0.649988033	0.025195653
ZMIZ1	-0.635594903	0.021128002
DAXX	-0.635336572	0.021664842
AMZ2	-0.629571914	0.003660173
CDK6	-0.629461946	0.036914719
GNG5	-0.615180579	0.025011986
SARS	-0.612948603	0.029090394
RPL35	-0.609828322	0.034048363
CDON	-0.606847892	0.005528275
LINC00665	-0.600417696	0.033625882
ASNS	-0.596327379	0.015307451
ATF4	-0.596270729	0.023073957
PSME1	-0.594407247	0.044137683
TLN2	-0.591540317	0.018244469
TENM3	-0.590358012	0.015293699
MAGI2-AS3	-0.588311604	0.033086028
MPV17	-0.588286449	0.025881037
PRMT5	-0.587111509	0.044911139
CHMP4B	-0.58273011	0.027273808
NCSTN	-0.581791732	0.024430641
BUD31	-0.580403107	0.026871668
NEDD8	-0.57853253	0.020812679
PDCD11	-0.574919317	0.034829288
HAND1	-0.572008201	0.021133806
GCN1L1	-0.569440023	0.049475995
WARS	-0.563930867	0.018288284
POLR2H	-0.555441462	0.031129857

NAT10	-0.552699278	0.03358678
CLPTM1L	-0.551346166	0.023304574
CFAP97	-0.55037668	0.024982466
PTDSS1	-0.54849364	0.03141721
TENM4	-0.54734415	0.034978287
SMC6	-0.546932292	0.012938452
RERE	-0.545363082	0.034649325
TBX3	-0.54493534	0.015685141
PMPCA	-0.539834563	0.039178313
RET	-0.533897749	0.01601111
ZMAT2	-0.531162094	0.022096076
XIST	-0.531085678	0.023342366
TMEM97	-0.525088624	0.015438755
CIRBP	-0.523272032	0.040949801
SNRPN	-0.517187341	0.047188755
DNMT1	-0.511923551	0.047727604
KIAA0100	-0.509305854	0.035930253
LRRN3	-0.50825704	0.026821324
STT3A	-0.506456737	0.03369268
UBAC2	-0.494430848	0.024664675
AKAP9	-0.494027396	0.016510384
CETN2	-0.487230186	0.031601298
AFAP1	-0.485935841	0.029926016
AK2	-0.47783234	0.026581472
RNF214	-0.475111191	0.048416562
VPS39	-0.463902402	0.044175796
SEC23B	-0.463246017	0.027346597
NEK1	-0.460217125	0.049477908

EP400	-0.458006277	0.047077892
DYNLT1	-0.453987805	0.039964143
CERK	-0.450201272	0.03218758
MCCC2	-0.445282251	0.028970421
ZC3H13	-0.425567994	0.046122211
RAD50	-0.424015801	0.035811552
GTF2A2	-0.408809607	0.047162908
JAK1	0.398300871	0.042444903
MAPK1	0.403920802	0.037523153
ABLIM1	0.407822267	0.046869633
IQGAP1	0.408367593	0.046887081
NDFIP1	0.426255978	0.038995421
KCTD20	0.426584195	0.04934024
TRAK2	0.427916012	0.036327304
PPP2R5E	0.432660442	0.032612417
ATL2	0.434027032	0.048603872
ELF2	0.4393446	0.046964476
UBR5	0.448036772	0.030994807
FABP5	0.46059264	0.037855408
SMARCA1	0.466729889	0.021270031
TMX4	0.470648742	0.038933877
ATAD2	0.475084659	0.017206476
NBEA	0.479935278	0.015963637
TFAP2B	0.480740601	0.026771089
MALAT1	0.483375018	0.017687501
CCND1	0.487429487	0.049048184
FNDC3A	0.496811075	0.02182937
NAV2	0.502379735	0.019235683
CNN3	0.504264401	0.017258069
IRF2BP2	0.5093795	0.028121064
H3F3B	0.512040267	0.029571005
TCF12	0.514909174	0.007053281
UBE3C	0.516917015	0.008152032
ZNF627	0.51722737	0.015800986
DOCK7	0.521155094	0.008155624
PPFIBP1	0.526424519	0.009218237
ABHD2	0.533289827	0.015969993
TSC22D1	0.543653501	0.013749817

TCAF1	0.547181196	0.019970265
STARD4	0.560615298	0.043783788
DLST	0.561831892	0.046333118
ID2	0.56325906	0.031274698
RNF150	0.570552744	0.007960745
ADAM22	0.574450099	0.005588434
CD46	0.574788982	0.015493012
TANC2	0.581402146	0.010169279
FN1	0.584957968	0.009453243
LGR5	0.612682686	0.002434399
STAC	0.618234474	0.001219615
ALCAM	0.619969531	0.006522808
CKS2	0.6368953	0.010466104
EDNRA	0.658950937	0.007034996
RAD21	0.673633968	0.007476604
LIMA1	0.693236361	0.000755359
SORCS1	0.702804894	0.000630729
FSTL1	0.764377934	0.000140223
PRKCA	0.765950988	0.000336453
CREB3L2	0.800895347	0.000469756
AZIN1	0.835720005	0.000370476
XPR1	0.842826623	0.000326395
SLC6A2	0.902559617	2.20E-05
SIPA1L1	0.904099364	0.0001465
HDAC9	0.904693051	0.000378629
FRMD6	0.906722651	0.000202817
DUSP4	0.98720095	6.29E-06
TWIST1	1.012814552	1.81E-05
TRIB2	1.124861201	7.63E-07
SCN9A	1.129965883	5.86E-06
C7	1.167612531	8.70E-07
ESRRG	1.182273941	3.33E-05
RP11-481F24.3	1.290595996	1.45E-08
CPE	1.323266754	2.45E-09
PEG10	1.406166131	2.77E-08
IL17RD	1.424414076	1.57E-12
DKK1	1.644288922	2.21E-12
MGEA5	1.702261181	7.53E-20
NRCAM	1.934288314	4.99E-17
GNG11	2.048433269	1.01E-22

DCX	2.060765891	3.19E-18
SGK1	2.277471985	2.15E-22
PLCXD3	2.699059303	4.55E-20
TFPI2	3.974315389	3.40E-49

Table 6: GlcN gene list used for IPA analysis

	logFC	PValue
RPS11	-3.22548531	2.35E-05
PTMS	-2.046182301	9.76E-07
TUBA1B	-1.879917667	7.54E-08
TMSB10	-1.870704304	1.72E-05
CFL1	-1.546174471	3.84E-05
PKM	-1.505232604	5.78E-05
CAPNS1	-1.451744755	7.24E-05
IGF2	-1.415111687	2.30E-08
UBC	-1.399370809	0.00012405
ERP29	-1.376501598	3.76E-07
CALR	-1.354956856	4.83E-06
POLR2A	-1.350853688	0.000633538
ATF4	-1.33553956	5.32E-07
UBA52	-1.333477997	6.44E-05
CLIP3	-1.317846172	0.000452579
RPL10	-1.315804457	0.000840155
SUPT6H	-1.284650185	8.34E-05
HAND1	-1.279389647	3.71E-07
CHGA	-1.268354165	0.000510925
GAPDH	-1.262893693	0.000222794
RPL7A	-1.244465491	0.00018936
NUDC	-1.242362228	1.75E-05
MT-CO3	-1.228666502	0.011055031
GNB2L1	-1.2240911	0.00021181
QARS	-1.222550602	0.000603939

FTSJ3	-1.219236098	0.000294765
EIF3C	-1.214081436	0.000582845
MT-ATP6	-1.208888682	0.020471926
RPL18A	-1.192914417	0.001419253
UBAP2L	-1.186122857	0.000319863
IMPDH2	-1.156659038	0.000160469
EIF3I	-1.144167785	0.000283796
SSRP1	-1.133396883	0.000179628
MAP1A	-1.116638013	0.000461457
RPLP0	-1.115316482	0.002236339
RPL29	-1.096950136	0.00032508
PDGFRA	-1.091817707	5.60E-07
SMARCC2	-1.087339026	0.000351224
MT-ND5	-1.08099704	0.039691753
MRPL37	-1.080091503	0.001196051
MDH2	-1.077851179	0.001668437
AHNAK	-1.076559642	1.46E-05
MYL6	-1.061201889	3.63E-05
RPS18	-1.058620299	0.001624468
EEF1G	-1.055158341	0.00373831
FLNB	-1.054081826	0.000150823
ATP5J2	-1.052840053	0.003076987
PPM1G	-1.050372577	0.000936779
UBE2I	-1.049636975	0.000257817
P4HB	-1.04549002	0.000408307
CDC25B	-1.043907968	0.000293597
AARS	-1.03977848	0.000897923
NEDD8	-1.027447717	4.62E-05

GANAB	-1.023214928	0.000237194
ABCF1	-1.019670892	0.00154863
NOMO1	-1.000695714	0.000257103
RPL41	-0.996726326	0.002834304
EEF2	-0.994067338	0.002097463
RPL35	-0.993311222	0.000601764
RELN	-0.99206582	1.42E-05
TLN1	-0.979205919	0.004516241
MAB21L2	-0.967090374	0.000632616
NOMO3	-0.958839472	0.001688511
SLC39A1	-0.954783093	0.000835626
RPS3	-0.947471519	0.002361594
MT-CO2	-0.946278093	0.043617983
CIRBP	-0.9442862	0.000248837
RPL12	-0.943227154	0.003664619
PSME1	-0.929705961	0.001743191
PSMD2	-0.928406368	0.001314969
SNRPA	-0.927066607	0.005920381
SSR2	-0.913752596	0.001350133
NID1	-0.912566093	1.82E-05
CTDNEP1	-0.904537968	0.00062902
CSNK2B	-0.903683018	0.002195241
S100A10	-0.900264302	0.001137347
CD63	-0.895370821	0.000536769
RPL37A	-0.894477313	0.01039317
RPL32	-0.892950377	0.005590872
SF3B2	-0.889440512	0.008295734

MMP2	-0.887883808	0.00477092
GPS2	-0.881208997	0.020455783
MANF	-0.871614147	0.000194654
DAXX	-0.868244207	0.001775445
ANXA2	-0.860435794	0.001037822
EIF4A1	-0.855668751	0.004533314
POM121C	-0.851596529	0.001934554
RPS15A	-0.837645542	0.00201729
RPS4X	-0.835130403	0.005527749
PRPF8	-0.834760956	0.00963452
SETDB1	-0.831736823	0.002017257
RPL18	-0.830177803	0.012001174
SND1	-0.824524663	0.012411452
PRMT5	-0.823990018	0.00503439
BAG6	-0.813704696	0.011715432
AKAP12	-0.809030747	0.00016659
RPS16	-0.808168435	0.014099674
AATF	-0.806540936	0.007482898
HUWE1	-0.806315759	0.002705815
HDLBP	-0.805103949	0.006618269
CRMP1	-0.804904001	0.007740171
PACS1	-0.800720499	0.008090056
BRD2	-0.798209445	0.004142737
UBA1	-0.797236696	0.010322846
UBE2L3	-0.795557755	0.018172899
RPL27	-0.789934282	0.004810893
DDB1	-0.789183116	0.010824649

ARHGEF2	-0.78031508	0.007373756
GAP43	-0.779216082	8.61E-05
VCP	-0.774321937	0.007428919
MAZ	-0.773613904	0.009207079
RPS27	-0.773356915	0.003750255
SEC24C	-0.771494257	0.004161356
NCSTN	-0.767778464	0.003073275
UBE2C	-0.766146097	0.005459595
FAT1	-0.765544444	0.000367826
SMARCB1	-0.763859903	0.015912008
PTDSS1	-0.762332768	0.00287259
CACNG4	-0.758677273	0.00307967
KIF20A	-0.758480324	0.00354331
PSMC4	-0.755834284	0.015230787
SPTAN1	-0.749443924	0.005602003
GSTM3	-0.7487231	0.029945921
PGD	-0.748030067	0.010828651
MKI67	-0.747689275	0.00188046
RPL26	-0.745592051	0.002079022
PPP1R10	-0.743974382	0.010539677
ACACA	-0.738824251	0.004373437
CHD4	-0.737497657	0.008361105
SNRNP200	-0.734677044	0.01677819
UXT	-0.73432444	0.029152751
EBNA1BP2	-0.733089419	0.009782487
SARS	-0.732181625	0.009273848
PSMB7	-0.727956917	0.009711272

NOP56	-0.726286439	0.001331374
CCT3	-0.716741768	0.015344614
CERS2	-0.715389949	0.011048614
TMSB4X	-0.715184758	0.010228081
RPL10A	-0.715157412	0.038324659
TENM3	-0.710714609	0.003554218
RPL38	-0.707950902	0.014156962
EIF4G1	-0.706917237	0.007589612
RERE	-0.705083641	0.006449983
AFAP1	-0.7039821	0.001718838
PPIB	-0.701221648	0.034099479
RPL36A	-0.699011048	0.006820403
STIP1	-0.69127169	0.017783344
ACTR1A	-0.684527826	0.017031741
NDUFB9	-0.683828572	0.019434354
EIF3D	-0.682392139	0.01848299
TENM4	-0.681720549	0.008740565
SFRP1	-0.679631882	0.004235332
FTH1	-0.67921641	0.017158094
FDFT1	-0.676513169	0.005764419
FOXM1	-0.673777831	0.005480087
THOC5	-0.669142133	0.017864025
DNMT1	-0.668873607	0.009837584
RPS2	-0.663638592	0.043274444
PPIA	-0.662215713	0.020282527
CKS1B	-0.660488747	0.001390785
BUD31	-0.660381525	0.011898487
MCM3	-0.658699767	0.001173992

YY1AP1	-0.658425462	0.012776883
RGS4	-0.657522844	0.001357951
RIMS3	-0.656240482	0.0145643
PDCD11	-0.649147429	0.017287096
PA2G4	-0.648111642	0.018008156
PPP1R11	-0.647721324	0.021929147
SPARC	-0.646927276	0.002936573
HK1	-0.646342554	0.039244919
FUNDC2	-0.64358153	0.01775531
ARF3	-0.64333804	0.004305669
ACIN1	-0.642461085	0.010093296
SAFB	-0.637424821	0.017633644
CTSB	-0.632680577	0.029993108
SOGA1	-0.632629455	0.023542551
ATP1A1	-0.63018381	0.015909115
ACTB	-0.629683485	0.029647613
RPL3	-0.628572575	0.036778936
GCN1L1	-0.627736397	0.030527259
UBR4	-0.625690888	0.015761273
SRPR	-0.623579396	0.019254143
DDX39B	-0.621456332	0.006961993
NAT10	-0.620650527	0.017146121
SLC4A8	-0.618033071	0.0030232
NES	-0.616366567	0.029100777
COPA	-0.614062843	0.014355688
NDUFS5	-0.609778616	0.010263996
MCM7	-0.60963435	0.039292398
SEP6	-	0.007970812

	0.609164778	
SNRPN	-0.606026147	0.020210175
KDELR1	-0.605106858	0.03440662
ZPR1	-0.604940122	0.016265433
TRRAP	-0.600171683	0.006287822
CASC3	-0.600136446	0.012612724
MYH10	-0.597498194	0.010557975
RNF10	-0.593204373	0.017343642
IGF2R	-0.592953568	0.009946033
SPTBN1	-0.592042479	0.017570762
GON4L	-0.588020084	0.031579528
HIP1	-0.586275616	0.018671586
H2AFY2	-0.585974046	0.030934962
DDX24	-0.580561	0.025551272
RET	-0.579482451	0.008977665
ICA1	-0.575553805	0.006619576
EP400	-0.574685737	0.012849797
PITPNA	-0.572224219	0.014316427
PFDN5	-0.570007782	0.035707386
RPN1	-0.569862634	0.021565617
NUDCD3	-0.567178097	0.025557214
MAP4	-0.564871021	0.037967424
RPS6	-0.564538316	0.035606921
SAP30BP	-0.562826004	0.029559357
ZNF512	-0.555408711	0.009457014
YKT6	-0.555280612	0.028472171
CS	-0.553999987	0.043618661
ZMAT2	-0.553957777	0.017061988

NCAM1	-0.55147354	0.016854109
LARP1	-0.550406093	0.013733488
SF1	-0.550061371	0.047163389
TP53BP2	-0.549729203	0.030797176
RPL27A	-0.548524254	0.044341545
ERC1	-0.547597571	0.029919791
SOD1	-0.546118945	0.012532181
C7	-0.545587372	0.020391364
ARID1A	-0.539824616	0.016925311
STT3A	-0.538691871	0.023982997
LAMC1	-0.538555825	0.017007916
VPS26B	-0.535177871	0.030816934
SMG7	-0.532716513	0.027989765
SIN3A	-0.53258322	0.042592761
ASXL1	-0.530197124	0.023436778
KMT2A	-0.529556472	0.030830004
RPL6	-0.529514861	0.02865775
RNF130	-0.528230312	0.02171543
NCAPD2	-0.526114564	0.043900763
TLN2	-0.523388326	0.036559026
COPG1	-0.522697244	0.044119245
SEC14L1	-0.521427612	0.033626925
THOC3	-0.521400525	0.023579514
TPM1	-0.517358886	0.021963848
XPNPEP1	-0.51705682	0.024404862
MRPL9	-0.507292898	0.034092372
WIPI2	-0.504375865	0.027746182

SRP68	-0.503289134	0.03228419
RPS25	-0.503202308	0.047663212
SCG2	-0.499942438	0.018961941
CRTAP	-0.499374727	0.040521704
CLTA	-0.498804227	0.049389844
KIAA0100	-0.498778869	0.039947844
PLXNA4	-0.497705128	0.021459352
C14orf132	-0.490692873	0.021445418
JAM2	-0.489466027	0.024856031
CDON	-0.485652611	0.026119988
APLP2	-0.483139339	0.045603705
KDM3B	-0.479753467	0.023136132
PRC1	-0.474864854	0.022258974
ZNF3	-0.4695101	0.040392913
ARIH2	-0.465788317	0.046887397
UBE2Q1	-0.464233572	0.043746258
GATAD2B	-0.463864272	0.047135895
UTP14A	-0.460348822	0.049931014
SCRN1	-0.459078684	0.035567933
ARNT	-0.448124848	0.027023973
UBE4B	-0.447380619	0.04949097
ASCL1	-0.446866795	0.026002839
DENND5A	-0.446772557	0.045324949
SLC20A1	-0.429278338	0.042261343
RAF1	-0.42510671	0.039985939
SEC24D	0.373856909	0.041954992
ORC2	0.385126849	0.046279304
RFWD2	0.398954167	0.037885057
PPP3R1	0.403489288	0.038014055

ADAM22	0.4064219	0.049707012
USP33	0.417250209	0.047295601
UBE2K	0.418281214	0.049916693
RC3H2	0.418712468	0.046308889
CENPU	0.418760387	0.049462329
PPP2CB	0.420943412	0.034380807
ADO	0.424823422	0.039666453
SNX7	0.426471908	0.040409874
C7orf73	0.428421556	0.042726276
PDCD4	0.429648778	0.041573843
MALAT1	0.431437911	0.034242072
DENR	0.4330541	0.043112607
CCZ1	0.438259614	0.033816862
SRSF10	0.440295505	0.044430204
SLC7A2	0.441425173	0.034380428
TLE4	0.441754831	0.034132896
STARD3NL	0.444598728	0.038996223
DNAJC10	0.444862834	0.041098912
CAND1	0.446081472	0.047091855
THUMPD3	0.44680257	0.042415024
TOR1AIP2	0.449262301	0.033866578
ATP13A3	0.451534212	0.047470236
BRIP1	0.452416501	0.040321359
FAM208A	0.453296834	0.039997722
ADSS	0.453373629	0.025551974
BLOC1S6	0.454844004	0.031366392
EML4	0.455868452	0.046956188
PTEN	0.457687764	0.04813261
HNRNPA0	0.458595539	0.041372721
NAA15	0.458689281	0.034705333
KPNA3	0.459516859	0.046168464
MRPL42	0.460995044	0.044020685
DESI2	0.466222975	0.049690195
ECT2	0.47174819	0.045370558
ATP11B	0.473839955	0.032207808
STRAP	0.473996474	0.030697514
STAG2	0.475366305	0.033124777
RSBN1L	0.475478447	0.042187338
CEBPZ	0.475961429	0.017531781
SGK1	0.476590583	0.036622195

C1orf112	0.476728967	0.018975063
FNTA	0.477656588	0.018391283
SF3B6	0.478313408	0.028296054
VPS13A	0.479187185	0.030300953
ACTR2	0.481151912	0.047544539
SIKE1	0.483376267	0.046240972
GNG12	0.486971165	0.036471776
EXTL2	0.488275838	0.034426432
PSMD12	0.489125873	0.026407304
ATP11C	0.491682441	0.02294183
SLC4A7	0.491703374	0.047921546
PRKD3	0.491728899	0.035882594
TRPM7	0.492725154	0.040652685
KRR1	0.493663748	0.049425754
GGCT	0.49424728	0.020448593
PURB	0.495093403	0.034487529
MSH2	0.496425736	0.046743655
HAUS6	0.497044384	0.027725176
DEK	0.498577957	0.048064857
ZBTB44	0.501026351	0.033009098
WDR36	0.502866781	0.023531701
EXOC5	0.504949385	0.040848328
FAM98B	0.506125364	0.025988397
PNO1	0.510120268	0.041197502
CD46	0.511975868	0.031007583
DYNC1LI1	0.513185913	0.020007663
NDC80	0.515990727	0.027501917
ICE2	0.516364882	0.016098486
LTN1	0.516865405	0.029168979
BZW1	0.517243924	0.039611884
GEN1	0.521059619	0.044328841
TMEM165	0.521524523	0.019887733
KNTC1	0.521812007	0.010814285
PPIP5K2	0.522578637	0.02121959
GTF3C6	0.522733675	0.02114604
TTC8	0.523502302	0.015828415
GCSH	0.524065189	0.026857462
SMC2	0.526218926	0.014951571
OSBPL8	0.526478052	0.026100384
ABCE1	0.528202237	0.035976579
XPO1	0.52884387	0.030790216

SRSF11	0.530030416	0.024554145
SEH1L	0.531568546	0.012166801
PCNA	0.534217703	0.023683686
TFAM	0.536775231	0.027384851
PCNP	0.536955247	0.041767613
PHF6	0.537538285	0.018910978
NCAPG	0.538895563	0.011993385
COX7C	0.539637674	0.024358263
DCAF13	0.542195013	0.015673761
HIGD1A	0.542298614	0.030786342
C6orf62	0.542806199	0.013342723
RAD21	0.544372769	0.030404265
POLR2M	0.547581428	0.026290652
GNPNAT1	0.550681541	0.025914652
MAT2B	0.550741813	0.018575729
TMEM30A	0.55102192	0.026917315
RB1	0.553879463	0.014925876
OSTC	0.553977859	0.021737994
BNIP2	0.554001485	0.015297166
SOCS4	0.562252875	0.035006224
RFC3	0.563171996	0.00860644
USMG5	0.563745341	0.026897771
HOOK3	0.563931747	0.01940759
AGPS	0.564570998	0.007003106
LIMA1	0.565326949	0.005957992
MAP9	0.572623367	0.012097032
EGLN1	0.572705063	0.029666026
USP1	0.573950768	0.011623638
WRN	0.57680754	0.010589966
SLC6A15	0.577438896	0.00727042
NAE1	0.577662666	0.023700541
SMN2	0.57950038	0.003784391
RAD1	0.580377877	0.00704437
UBA6	0.581579426	0.018486879
CKS2	0.581759577	0.019301158
DEPDC1	0.583857943	0.028665198
PPA2	0.584666401	0.010621163
MTPN	0.585120335	0.028157416
UHMK1	0.586236814	0.014287435
TMX3	0.588144213	0.029656312

KCTD12	0.592893311	0.031137575
CCDC90B	0.59390345	0.025330841
ID2	0.595614455	0.022825072
TMEM106B	0.59573737	0.026113432
TRIB2	0.597201737	0.008262241
CCDC25	0.598452386	0.005930061
PPP1CB	0.598881591	0.03785458
MFN1	0.599206145	0.016720707
ECHDC1	0.599902403	0.02295611
CENPH	0.605621328	0.016496252
SPCS3	0.607757251	0.02517903
PPP2R5E	0.609956712	0.002624983
CAPZA2	0.610555175	0.03736812
IL17RD	0.614346014	0.002037409
NRCAM	0.616146235	0.006018163
LSM5	0.616351534	0.026022315
GTF2A1	0.618844647	0.018352446
ARL5B	0.62235564	0.018691811
ATL2	0.624208475	0.004637697
CYCS	0.633041606	0.028610661
SMAD9	0.633606902	0.021234545
IER3IP1	0.637503727	0.010426087
MAD2L1	0.6376872	0.007801153
PM20D2	0.638223924	0.009047824
TMEM167A	0.639409034	0.00983525
DR1	0.642032937	0.021298702
LRRC58	0.643890773	0.024664326
SLC6A2	0.648355535	0.002247475
SCN9A	0.649198785	0.008885445
DCP2	0.650519857	0.00713944
CDK1	0.65449131	0.016043545
CMPK1	0.66072971	0.013545926
TSNAX	0.677498888	0.010692415
STARD4	0.681003543	0.014434392
ZWILCH	0.68116595	0.00583738
GULP1	0.681354217	0.028707305
EID1	0.682005873	0.030874475
KRAS	0.684820319	0.00796092
RNF11	0.685100389	0.015909417
CD164	0.686927483	0.018436526
DCK	0.688474788	0.00744561

TWF1	0.689926572	0.028525407
GMFB	0.690219098	0.019613501
G2E3	0.691420291	0.025158807
EIF1AX	0.698255698	0.019373384
CBFB	0.703332894	0.018253823
CCNC	0.705235943	0.012675998
MMP16	0.709177388	0.006364951
NBEA	0.712396317	0.000356862
YIPF4	0.719401214	0.002412642
ESRRG	0.744728199	0.008581295
HAT1	0.750059426	0.003969555
CEP44	0.751318747	0.005755674
TWIST1	0.752714522	0.001397533
NDUFB6	0.777413315	0.044931393
ACTR6	0.803625714	0.006032362
MPP6	0.850937415	0.00016691
MZT1	0.856832499	0.005893811
FRMD6	0.868642632	0.000370383
HDAC9	0.930311296	0.000258633
ATP7A	0.994206259	1.41E-06
MGEA5	1.029759892	2.20E-08
PLCXD3	1.098396638	0.000101694
RP11-481F24.3	1.162426643	3.10E-07
C18orf32	1.218130265	4.23E-05
DKK1	1.274701245	3.95E-08
GNG11	1.400880484	8.64E-12
CH507-513H4.3	1.71524385	0.047488558
CH507-513H4.4	1.715243851	0.047496103
CH507-513H4.6	1.715243852	0.047500949
TFPI2	2.449549276	4.27E-22

3.3.6 Prolonged TMG or GlcN Treated Cells Generated Less Reactive Oxygen Species (ROS)

TMG or GlcN could affect cellular ROS levels, including reactive nitrogen species (RNS), hydroxyl radical ($^{\bullet}OH$), hydrogen peroxide (H_2O_2), and superoxide ($O_2^{\bullet-}$) (**Figure 16A**). Total ROS (RNS, $^{\bullet}OH$ and H_2O_2) was reduced in both TMG- and GlcN-treated SH-SY5Y cells (**Figure 16B**). Superoxide levels were reduced in TMG-treated cells (**Figure 16C**). Total ROS and superoxide levels were lower in TMG-treated NT2 cells, while GlcN-treated NT2 cells trended lower (**Figure A.4A-B**). Because NADPH oxidase is a major source of cytoplasmic ROS [76], we found that both TMG and GlcN treatment decreased NADPH oxidase protein levels in SH-SY5Y cells (**Figure A.4C**). Together, these data indicated that prolonged elevations of O-GlcNAcylation suppress ROS production.

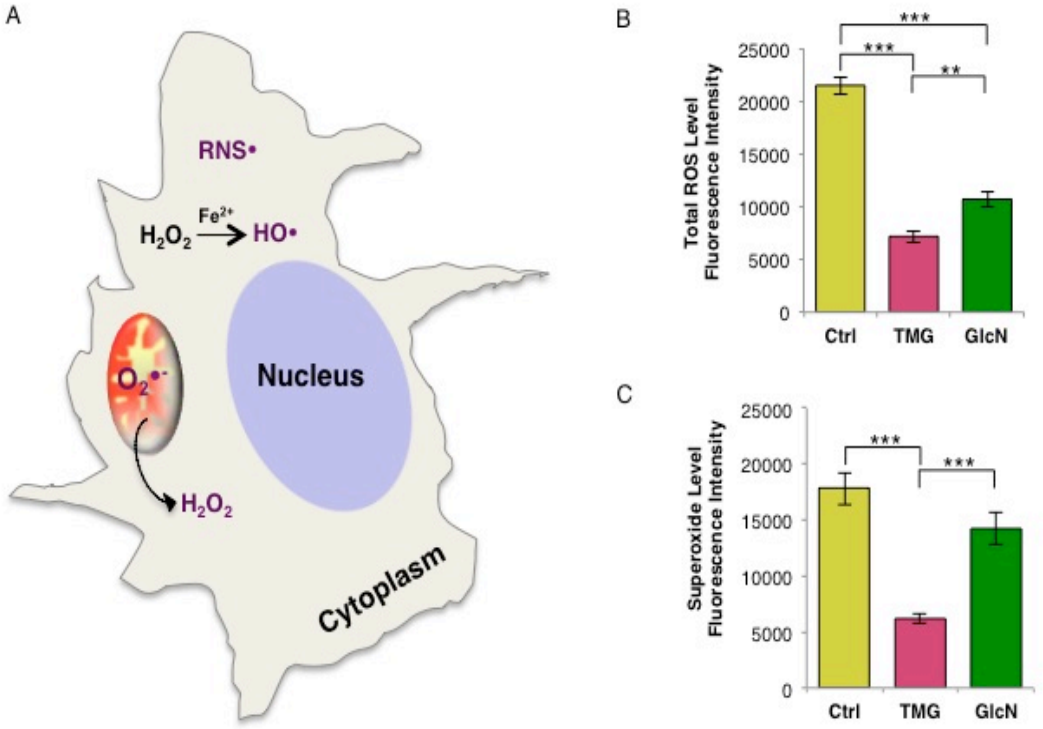

Figure 16: TMG or GlcN cells generated less reactive oxygen species (ROS)
(A) Representative schematic displaying cytoplasmic ROS (total ROS: HO•, H_2O_2, RNS•) and mitochondrial ROS (superoxide: $O_2^{\bullet-}$). **(B)** Total ROS and **(C)** superoxide level (average ± SEM, n=9) were decreased. ROS assay results have been replicated in at least three independent experiments. * indicates significance $p < 0.05$. ** indicates significance $p < 0.01$. *** indicates significance $p < 0.001$.

3.3.7 O-GlcNAc Regulates NRF2 Function

We hypothesized that O-GlcNAc could be directly modulating NRF2 function. TMG lowered NRF2 protein and *NRF2* transcript levels (**Figure 17A-B**). TMG lowered NRF2 target gene Thioredoxin reductase 1 (*TXNRD1*) transcript level (**Figure 17C**) and reduced Superoxide Dismustase 1 (SOD1) and Thioredoxin (TXN) protein levels (**Figure 17D**). However, TXNRD1 and Peroxidase 1 (PRX1) protein expression were not altered (**Figure A.5D**). Interestingly, both TMG and GlcN treatment increased NRF2 O-GlcNAcylation (**Figure 17E**).

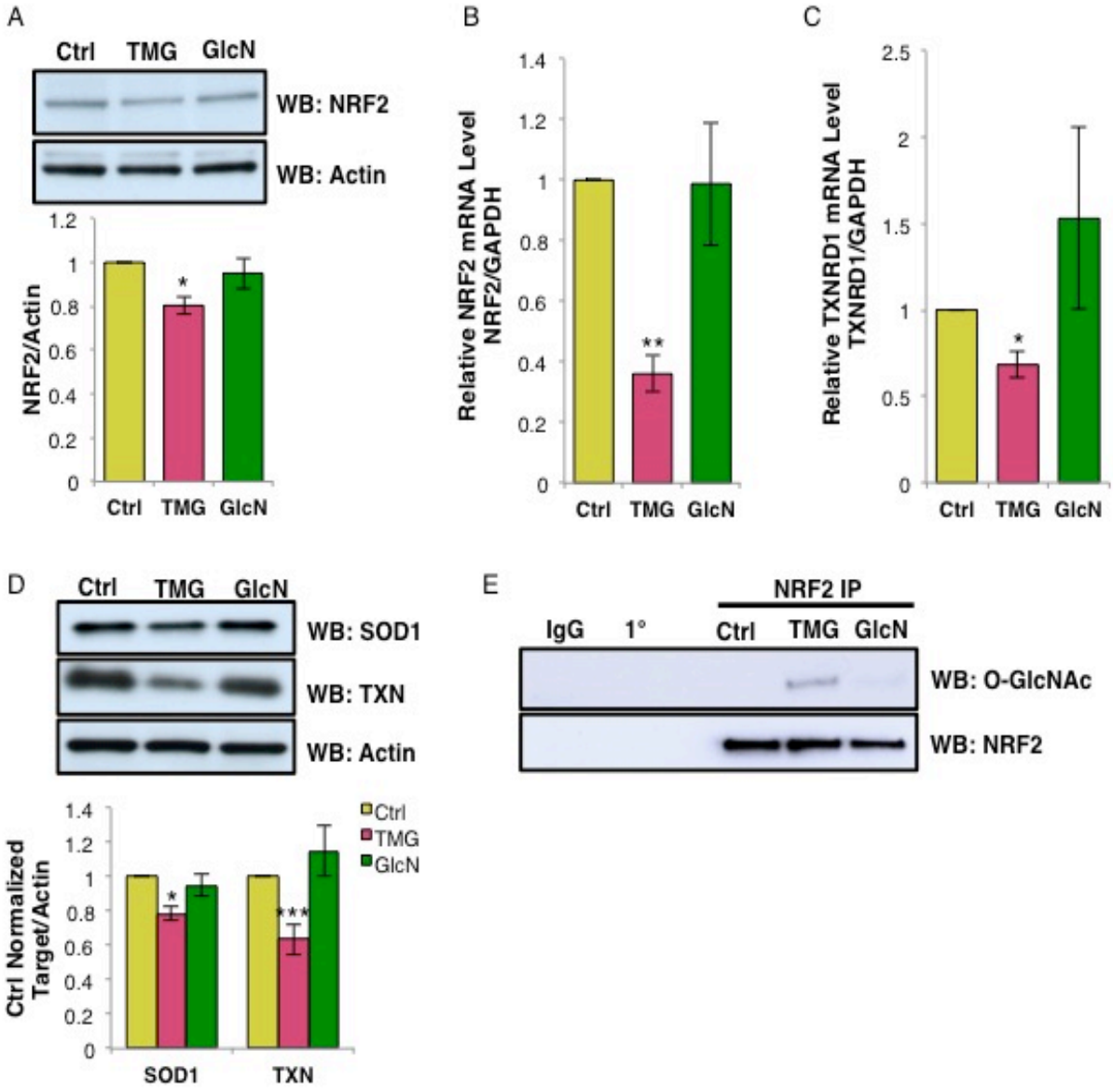

Figure 17: O-GlcNAc regulates NRF2 Function

Representative results shown for **(A)** NRF2 protein level (n=3), **(B)** *NRF2* (n=5) and **(C)** *TXNRD1* (n=4) transcript levels, and **(D)** SOD1 (n=7) and TXN (n=4) protein levels. **(E)** Immunoprecipitation results showed increased NRF2 O-GlcNAcylation (n=3). Protein levels were first normalized with loading control Actin, then normalized to control samples. Transcript levels were measured by qRT-PCR and normalized to *GAPDH* levels. * indicates significance $p < 0.05$. ** indicates significance $p < 0.01$. *** indicates significance $p < 0.001$.

Because O-GlcNAcylation of transcription factors influences their cytolocalization [77], we fractionated the nuclear extract from the cytoplasm, and found increased O-GlcNAcylation did not alter the nuclear-NRF2 protein levels. TMG did reduce the cytoplasmic NRF2 protein levels (**Figure A.5A**). Since O-GlcNAcylation promotes protein stability [78, 79], we pretreated SH-SY5Y cells with cycloheximide (CHX) to inhibit protein translation [80] and harvested cells at different time-points after CHX treatment in relation to control cells. We observed no change in NRF2 protein levels in O-GlcNAc-elevated cells between 0 h to 6 h after CHX treatment (**Figure A.5B**). NRF2 binding partner KEAP1-E3-ligase complex (Kelch-like ECH associated protein 1) promotes degradation of the transcription factor. However, KEAP1 protein levels did not change after TMG and GlcN treatment (**Figure A.5C**), suggesting that the TMG mediated decreased in NRF2 protein level was not due to altered stability of the protein but due to the decrease in the transcript.

MnSOD, a non-NRF2 controlled antioxidant enzyme, is a major antioxidant enzyme present in mitochondria and is essential for the removal of superoxide generated by the ETC complexes [81]. MnSOD protein level was decreased in both TMG- and GlcN-treated SH-SY5Y cells (**Figure A.5E**). Because several antioxidant response pathways were down regulated with TMG and GlcN treatment, we treated SH-SY5Y cells with 50 μM or 100 μM H_2O_2 for upwards of 7 h to induce oxidative stress [82], and measured cell viability. TMG increased cell viability in 100 μM H_2O_2 (**Figure A.5F**). Total O-GlcNAcylation level was robustly increased after oxidative stress induction in control cells (**Figure A.5G**), and the apoptosis marker, cleaved-poly (ADP-ribose) polymerase (PARP) protein, was increased after oxidative stress (**Figure A.5G**). Catalase, TXNRD1, PRDX1, and TXN protein levels were not significantly altered (**Figure**

A.5G). Likely, the increased cell viability in TMG-treated cells was due to increased O-GlcNAcylation mediating other stress response pathways [83].

3.3.8 Prolonged Elevations of O-GlcNAcylation Decreased Mitochondrial Respiration and ROS Generation in Mice Tissue

Because long-term TMG treatment reduced mitochondrial respiration in cell lines, we used TMG to replicate the cell line data in mice. We intraperitoneally injected TMG into C57B6J mice at a concentration of 50 mg/kg [72] every other day for 15 days prior to sacrificing the animals. Liver and brain tissues were then used for subsequent experiments (**Figure 18A**). TMG robustly elevated brain O-GlcNAcylation and OGA expression and reduced OGT protein levels (**Figure 18C**). Similar results were obtained in the livers of TMG-treated mice (**Figure A.6A**).

Next, we purified and pooled mitochondria from four TMG and four control mouse brains and performed *ex vivo* respiration assays [67]. TMG lowered basal respiration (basal, in the presence of substrate, but no ADP) as well as phospho-relating respiration (State 3, + ADP), resting respiration (State 4_0, proton leak rate, + oligomycin), and uncoupled respiration (State 3_u, maximal respiratory rate, + FCCP). Anoxic respiration (+ Antimycin A) was the same between control and TMG-treated mouse brain (**Figure 18E**). TMG reduced liver mitochondrial respiration of State 3 and State 4_0 (**Figure A.6B**). Superoxide level was lower in TMG-treated brain (**Figure 18H**) and liver (**Figure A.6C**). Brain NRF2 protein level was decreased in TMG-injected mice (**Figure 18J**). Sustained inhibition of OGA in mouse brain and liver tissue replicated the data from cell lines suggesting that the metabolic changes seen with TMG were independent of cell type and were an adaptive mechanism to OGA inhibition.

3.3.9 OGT Knockdown Impaired Mitochondrial Respiration and Increased ROS Generation in Mice Liver

To understand how the loss of OGT affects cellular energetics, we generated conditional OGT liver knockout C57B6J mice by intraperitoneal injection of AVV-GFP-Cre virus. Fifteen days after viral injection, liver tissue was harvested (**Figure 18B**). Liver O-GlcNAcylation and OGT protein levels were reduced (**Figure 18D**). OGT knockdown decreased *ex vivo* basal liver respiration, as well as State 3, State 4_0, and State 3_u. No difference was measured in anoxic respiration (**Figure 18G**). In contrast to TMG treatment, the mitochondrial superoxide levels in the OGT knockdown mouse livers were increased (**Figure 18I**). NRF2 protein level and its targeted genes, SOD1 and TXN, were elevated in these OGT knockdown livers (**Figure 18K,L**).

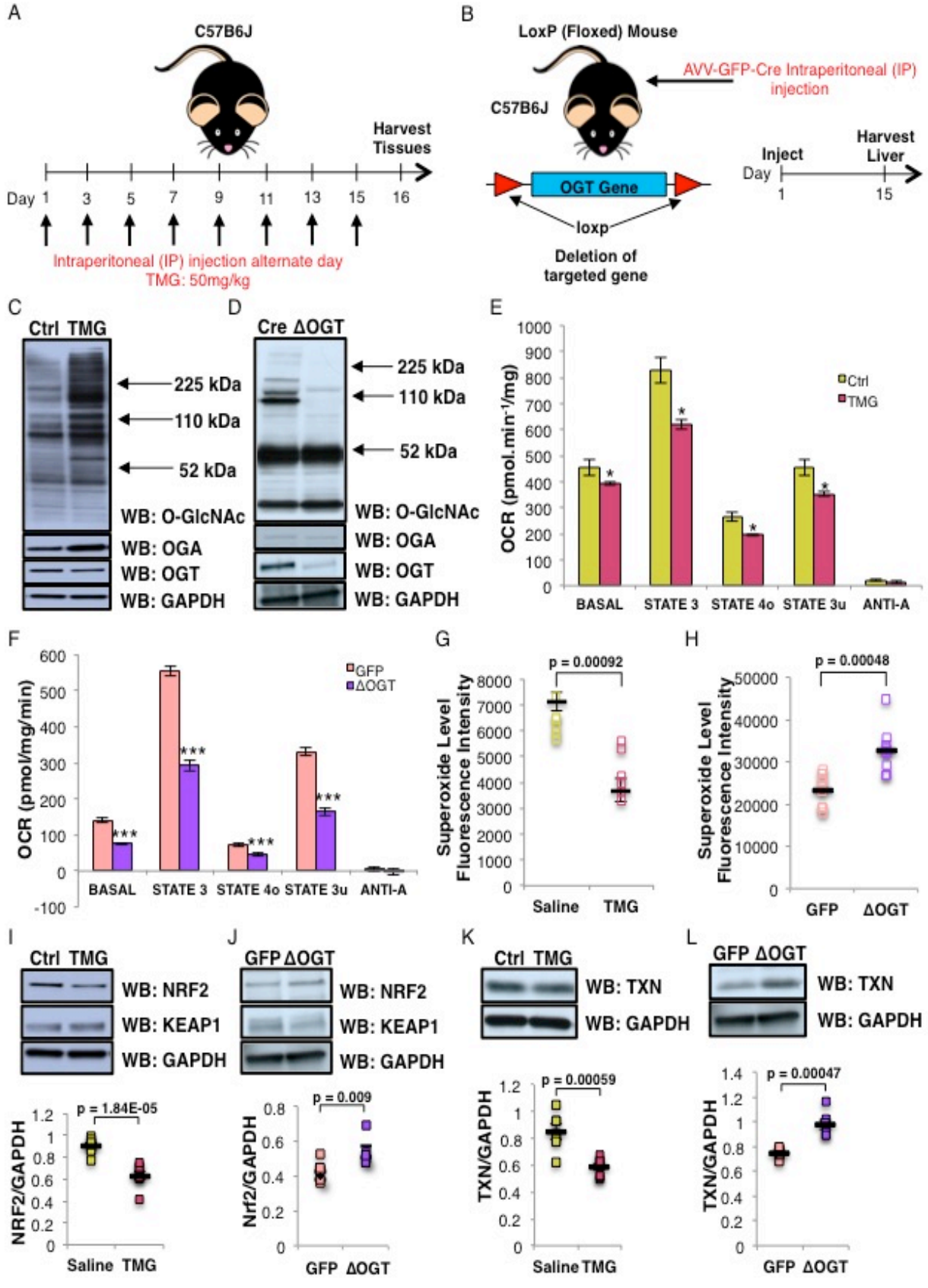
A
C57B6J
Harvest Tissues
Day 1 3 5 7 9 11 13 15 16
Intraperitoneal (IP) injection alternate day
TMG: 50mg/kg
B
LoxP (Floxed) Mouse
C57B6J
AVV-GFP-Cre Intraperitoneal (IP) injection
OGT Gene
loxp
Deletion of targeted gene
Inject Day 1
Harvest Liver 15
C
Ctrl TMG
225 kDa
110 kDa
52 kDa
WB: O-GlcNAc
WB: OGA
WB: OGT
WB: GAPDH
D
Cre ΔOGT
225 kDa
110 kDa
52 kDa
WB: O-GlcNAc
WB: OGA
WB: OGT
WB: GAPDH
E
OCR (pmol.min-1/mg)
Ctrl
TMG
BASAL STATE 3 STATE 4o STATE 3u ANTI-A
F
OCR (pmol/mg/min)
GFP
ΔOGT
BASAL STATE 3 STATE 4o STATE 3u ANTI-A
G
p = 0.00092
Superoxide Level Fluorescence Intensity
Saline TMG
H
p = 0.00048
Superoxide Level Fluorescence Intensity
GFP ΔOGT
I
Ctrl TMG
WB: NRF2
WB: KEAP1
WB: GAPDH
p = 1.84E-05
NRF2/GAPDH
Saline TMG
J
GFP ΔOGT
WB: NRF2
WB: KEAP1
WB: GAPDH
p = 0.009
Nrf2/GAPDH
GFP ΔOGT
K
Ctrl TMG
WB: TXN
WB: GAPDH
p = 0.00059
TXN/GAPDH
Saline TMG
L
GFP ΔOGT
WB: TXN
WB: GAPDH
p = 0.00047
TXN/GAPDH
GFP ΔOGT

Figure 18: Elevated O-GlcNAcylation decreased mitochondrial respiration and ROS generation while OGT liver knockdown impaired mitochondrial respiration and increased ROS generation

(A) Experimental design of TMG dosed mice and **(B)** liver specific-OGT knockdown mice. Total O-GlcNAcylation, OGA, OGT, and GAPDH (loading control) levels in **(C)** TMG-treated mouse brain and **(D)** OGT-knockdown mouse liver (n=11). Oxygen Consumption Rate (OCR) profile on isolated mitochondria from **(E)** long-term TMG-treated mouse brain and **(F)** OGT-knockdown mouse liver. The assays were done using pooled mitochondria from five mice for each condition, and the results were replicated in three independent experiments. Mitochondrial superoxide level (n=6) in **(G)** TMG-treated mouse brain showed decreased superoxide levels, but **(H)** OGT-knockdown mouse liver superoxide was increased. **(I-J)** NRF2, KEAP1, **(K-L)** TXN, and GAPDH (loading control) levels for TMG treated mice (n=8) and OGT-knockdown mice (n=6). Average protein level displayed was normalized to GAPDH. * indicates significance $p < 0.05$. ** indicates significance $p < 0.01$. *** indicates significance $p < 0.001$.

3.3.10 Prolonged O-GlcNAc Elevation Promoted Weight Loss including Reduction of Lean Mass, Fat Free Mass, and Water Mass

Next, we determined whether long-term elevation of O-GlcNAc altered whole body composition. Total body weight of TMG-treated mice was lower after the 2-week treatment period (**Table 7**); however, control mice gained weight (**Figure 19A**). TMG treatment resulted in a reduction in lean mass percentage compared to control mice (**Figure 19B**). Although we did not find a significant difference in the body fat mass percentage (**Figure A.7A**), the free fat mass percentage (all other mass other than fat mass) in TMG-treated mice was lower (**Figure 19C**). Furthermore, TMG treatment reduced body water mass percentage (**Figure A.7E**).

Table 7: Body weight prior and after drug injection

	Before Injection		After Injection	
	Saline	TMG	Saline	TMG
Body weight, g	26.07±0.95	27.44±0.60	26.86±0.88	27.42±0.98
	p = 0.244		p = 0.579	

3.3.11 Long-Term TMG Treatment Lowered Energy Expenditure and Oxygen Consumption, Skewing Mice Toward Carbohydrate Metabolism

Because TMG down regulated mitochondrial respiration and reduced free fat mass body composition, we postulated that the whole-body energy metabolism of the TMG-treated mice would be altered. Two-week TMG treatment reduced total energy expenditure (EE) and resting EE at nighttime (most active) (**Figure 19D-E**), but no changes were measured during the daytime (less active) (**Figure A.7G-H**). When these mice entered the night cycle, the average EE pattern of TMG-treated mice was higher, then declined back to control levels when they re-entered the light cycle (**Figure A.7Q**). TMG-treated mice energy balance (calories from food consumption) was not changed during the light or night cycles (**Figure A.7B, A.7H**).

TMG treatment resulted in a significantly lower OCR especially during the nighttime (O_2 consumption and CO_2 elimination, **Figure 19F-G**). The OCR was not changed significantly during daytime (**Figure A.7J-K**). The Respiratory Exchange Ratio (RER, ratio of whole-body CO_2 production to O_2 consumption) determines the relative contribution of carbohydrates and lipids to overall energy expenditure [84]. The average RER in TMG-treated mice was increased during either the daytime or nighttime cycle, but not significantly (**Figure A.7C, A.7L**). However, basal RER during the daytime cycle was increased in the TMG-treated mice (**Figure A.7M**). Hourly RER at day fifteen following TMG-injection was higher during the daytime cycle in TMG-treated mice, while nighttime RER values in both control and TMG-treated animals were equivalent. Again, when TMG-treated mice re-entered the light cycle, their average hourly RER remained significantly higher compared to control mice (**Figure 19K**). These data showed that TMG-treated mice utilized carbohydrates as their predominant source for energy

throughout a 24-hour cycle, even during the inactive daytime cycle when lipid oxidation is preferred.

3.3.12 TMG Treated Mice were Less Active than Control Mice

Next, we assessed the physical activity of the TMG-treated mice. During the nighttime, TMG-treated mice had less X-, Y-, and Z-axis beam break activity (**Figure A.7D**) and total activity (sum of X- and Y- axis beam breaks) compared to control mice (**Figure 19H, 19L**). No changes between TMG and saline-treated mice during the daytime cycle were found (**Figure 19L, Figure A.7N**). Although locomotion speed was unchanged (**Figure A.7N**), TMG-treated mice walked significantly less distance than control mice during the nighttime cycle (**Figure 19I**). The distance traveled during the daytime cycle was not different (**Figure A.7O**). Finally, TMG treatment increased the sleep duration during the nighttime cycle compared with saline-treated mice (**Figure 19J**), but no change in sleep duration was measured during the daytime cycle (**Figure A.7P**).

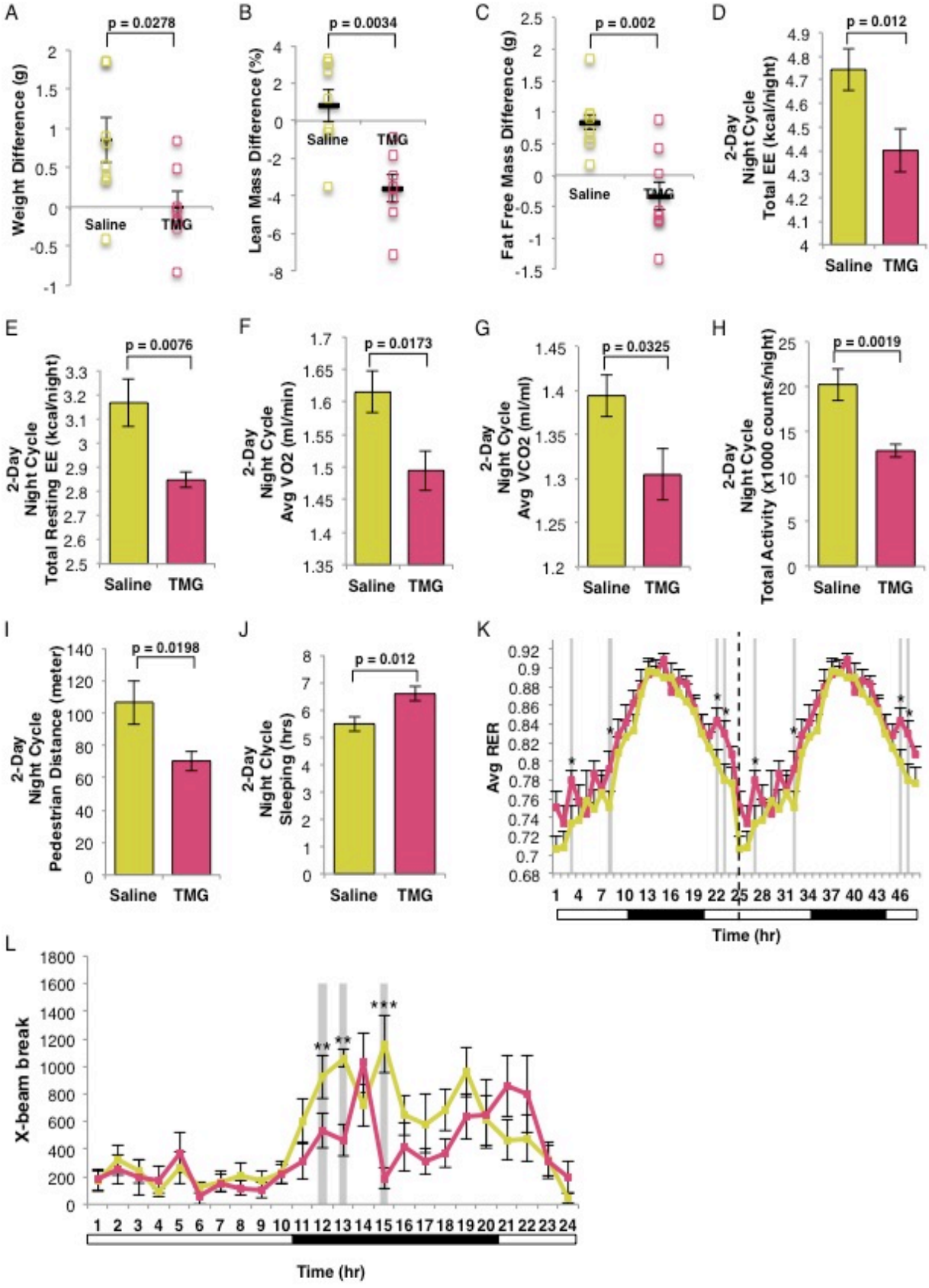
A
p = 0.0278
Weight Difference (g)
Saline
TMG
B
p = 0.0034
Lean Mass Difference (%)
Saline
TMG
C
p = 0.002
Fat Free Mass Difference (g)
Saline
TMG
D
p = 0.012
2-Day Night Cycle Total EE (kcal/night)
Saline
TMG
E
p = 0.0076
2-Day Night Cycle Total Resting EE (kcal/night)
Saline
TMG
F
p = 0.0173
2-Day Night Cycle Avg VO2 (ml/min)
Saline
TMG
G
p = 0.0325
2-Day Night Cycle Avg VCO2 (ml/ml)
Saline
TMG
H
p = 0.0019
2-Day Night Cycle Total Activity (x1000 counts/night)
Saline
TMG
I
p = 0.0198
2-Day Night Cycle Pedestrian Distance (meter)
Saline
TMG
J
p = 0.012
2-Day Night Cycle Sleeping (hrs)
Saline
TMG
K
Avg RER
Time (hr)
L
X-beam break
Time (hr)

Figure 19: O-GlcNAc elevation altered energy metabolism profile in mice

Representative plots shown **(A)** weight, **(B)** lean mass, and **(C)** fat mass differences (n=8) for mice after two weeks of TMG-treatment (50mg/kg). Nocturnal results of **(D)** total energy expenditure (EE), **(E)** total resting EE, **(F)** average oxygen consumption rate, **(G)** carbon dioxide exhaling rate, **(H)** total activity, **(I)** pedestrian distance, and **(J)** sleep duration. **(K)** Double plotted hourly respiration exchange ratio (RER, VCO_2/VO_2) calculated the last day of TMG injection. Dotted line represents blot replication (n=8, * indicates $p < 0.05$). (**L**) Hourly X-beam break plot. Permutation test (10,000 cycles) of hourly RER during light cycle (p=0.034) and X-beam break during night cycle (p=0.0002).

3.4 Discussion

Our data demonstrate a fundamental role for O-GlcNAcylation in regulating mitochondrial function and whole-body energy metabolism. GlcN supplementation increased O-GlcNAcylation and induced a phenotype of increased mitochondrial respiration and reduced ROS production. In contrast to GlcN, TMG-treated cells or mice became less ETC-dependent, maintaining lower oxygen consumption rates due to reduced respiration. Prolonged TMG-treated animals shifted their metabolism toward carbohydrate utilization and reduced their physical activity. In contrast, decreased respiration caused by prolonged TMG treatment did not impair mitochondrial function and generated less ROS. Loss of O-GlcNAcylation by liver specific OGT knockdown lowered and impaired mitochondrial respiration, robustly elevating superoxide levels. Importantly, these results support the notion that O-GlcNAcylation in maintaining proper mitochondrial function while complete loss of O-GlcNAc negatively impacts cellular energetics.

Prolonged inhibition of OGA or elevation in OGT substrate availability led to dramatic changes in mitochondrial respiration, duplicating results from prolonged GlcN treatment in *C. elegans* and mice [62]. However, genetic ablation of OGT dramatically lowers the basal level of O-GlcNAc, producing severe metabolic phenotypes [31-33], while OGT or OGA over-expression impairs respiration [65]. Recently, RNAi mediated knock-out in HeLa cells of the mitochondrial form of OGT (mOGT), which is only expressed in a few mammals including primates [85], in HeLa cells caused mitochondrial fragmentation and reduced membrane potential, while knock-out of both mOGT and the nuclear and cytoplasmic form of OGT lead to a compensatory increase in mitochondrial respiration, partially due to the decrease in mitochondrial content [86]. Even though TMG treatment lowered mitochondrial respiration in our current study, ROS was not increased, suggesting an intervention that raises both O-GlcNAc

and OGA expression promotes a healthier metabolic phenotype than genetic manipulation of OGT or OGA alone.

TMG and to some extent the GlcN-treatment produced a two-stage adaptive process. First, total cellular and mitochondrial O-GlcNAc levels increased, promoting increased respiration [11] and signaling from the mitochondria to the nucleus via increased ROS production [87]. This was followed by O-GlcNAc mediated changes in the transcriptome, resulting in longer mitochondria, reduced energetic demand and ROS generation. Many ETC complex subunits are heavily modified by O-GlcNAc [12], and short-term elevation of O-GlcNAc increased mitochondrial respiration and ATP production in rat cardiomyocytes [11, 12]. The initial induction of respiration caused by increased O-GlcNAcylation transmits a signal to the nucleus that alters gene transcription. After adaptation to sustained elevations in O-GlcNAc, mitochondrial respiration decreases. The changes in respiration are due to a combination of altered gene expression and ETC function. We observed that both *in vivo* complex I and IV activity were increased after TMG treatment, demonstrating that the decreased respiration was not solely due to ETC activity suppression. The mitochondrial membrane was hyperpolarized, suggesting that the ETC was functioning at capacity; however, proton recycling from the intermembrane space into the inner mitochondrial space was decreased. Potentially, the slower proton-recycling rate was due to suppression of ATP synthase caused by a decrease in ATP synthase subunit expression (*ATP6*) or O-GlcNAcylation of ATP synthase subunits [12].

The combination of lower mitochondrial respiration, no change in proton leak rate, and hyperpolarization of the mitochondrial membrane reduced mitochondrial ROS production. Consequently, the decrease in ROS signaling led to lower expression of antioxidant response genes. Under normal conditions, the generation of mitochondrial ROS is needed to induce

antioxidant and growth programs in response to changes in the environment [87]. TMG or GlcN treatment does not preclude the generation of ROS, but the basal ROS level was lowered. Since the cell did not need robust antioxidant responses, NRF2 gene programs were reduced. Under low ROS conditions, KEAP1 constantly degrades NRF2; however, elevated ROS oxidizes cysteine residues on KEAP1 leading to the release of NRF2, translocation into the nucleus, and initiation of antioxidant gene expression including NRF2 itself [88]. The decrease in NRF2 mRNA expression was due to long-term TMG treatment reprograming NRF2 transcription. Likely, the transcriptome reprogramming by TMG or GlcN treatment was due to changes in O-GlcNAc mediated transcriptional and epigenetic regulation. O-GlcNAc not only influences chromatin, but also chromatin readers, writers, and erasers, thus complicating the specific roles of long-term O-GlcNAc elevation in transcriptional reprogramming [89]. Of note, only specific gene networks were affected by long-term increased O-GlcNAcylation, suggesting that the combination of elevated O-GlcNAc and OGA expression must target these networks in some manner. Future investigation into these mechanisms is warranted.

The cellular reprogramming caused by elevations in both O-GlcNAc and OGA has a consequence on the energetic needs of animals. TMG-treated mice shifted their energy metabolism away from oxidative phosphorylation and towards glycolysis. The TMG-treated mice did not show a need for greater energy demand since sleep time was increased, movement was reduced, and energy expenditure were all lower. TMG treatment-induced metabolic changes in the mice would influence chronic diseases. Previously, mitochondrial function was impaired under diabetic conditions [30, 90], with O-GlcNAc levels higher in rat diabetic cardiomyocytes without the concomitant increase in OGA expression. Importantly, adenoviral overexpression of OGA led to improved mitochondrial function and calcium handling in diabetic cardiomyocytes

and improved coronary endothelial cell function in diabetic mice [91, 92]. Furthermore, OGA overexpression lowered O-GlcNAc levels and improved outcomes in mouse models of stretch-induced cardiac hypertrophy [93]. Together, these data demonstrate that sustained elevations in O-GlcNAc without the concurrent increase in OGA expression was detrimental to cells; however, cellular function could be restored with OGA over-expression.

The combination of increased O-GlcNAcylation and OGA expression could restore some metabolic function lost in chronic metabolic diseases such as Alzheimer's disease (AD). TMG and TMG derivatives are actively being investigated as potential therapeutics for AD [94]. The argument for inhibiting OGA in AD patients is that the treatment will increase O-GlcNAcylation of Tau, preventing Tau phosphorylation and subsequent Tau tangles [95-97]. Treatment with TMG does increase Tau O-GlcNAcylation and improve outcomes in animal models of Tauopathies [95]. Our data argue for additional metabolic benefits for brain health after prolonged TMG treatment. Mitochondrial dysfunction is a characteristic of AD, and the mitochondrial cascade hypothesis argues that loss of mitochondrial function over time alters metabolite production and increases the generation of ROS causing neuronal damage and cell death [20]. Screening of adult children of parents with AD demonstrates a decrease in mitochondrial function prior to the onset of any cognitive impairment or increased production of beta-amyloid [98]. The TMG-treated animals had lower mitochondrial respiration and ROS production, but with a shift toward glycolysis which could slow AD development.

Long-term TMG treatment shows no adverse effects on animal health [99], nor does TMG-treatment promotes insulin resistance like less selective OGA inhibitors [100, 101]. O-GlcNAcylation dampens insulin signaling by modifying several proteins in the insulin signaling pathway [102, 103], while OGT can relocate to the plasma membrane after insulin induction

contributing to the ablation of insulin signaling [38, 104]. O-GlcNAcylation is increased in diabetic tissue, suggesting that the increase in glucose availability induces more flux through the HBP, increases O-GlcNAcylation of insulin signaling proteins, and leads to a decrease in responsiveness to insulin [105]. Yet TMG treatment of animals increases O-GlcNAc levels without producing diabetes [99]. We argue that the combination of increased carbohydrate usage, O-GlcNAcylation and OGA expression seen with long-term TMG treatment explains why TMG treatment does not induce diabetes and could potentially make these animals more sensitive to insulin.

In conclusion, long-term elevation in O-GlcNAcylation coupled with an increase in OGA expression modulates mitochondrial function and reprograms the transcriptome to favor a reduction in antioxidant response, and lower ATP production. These profound changes in metabolism caused mice to sleep more, move less, reduced body mass, and increased carbohydrate metabolism (**Figure 7**). These physiological changes suggest that long-term increases in O-GlcNAcylation followed by a concurrent increase in OGA expression changes the metabolic program of animals without causing adverse effects. Potentially, progression of chronic metabolic diseases such as diabetes and Alzheimer's would be positively impacted by a combination of increased O-GlcNAcylation and OGA expression.

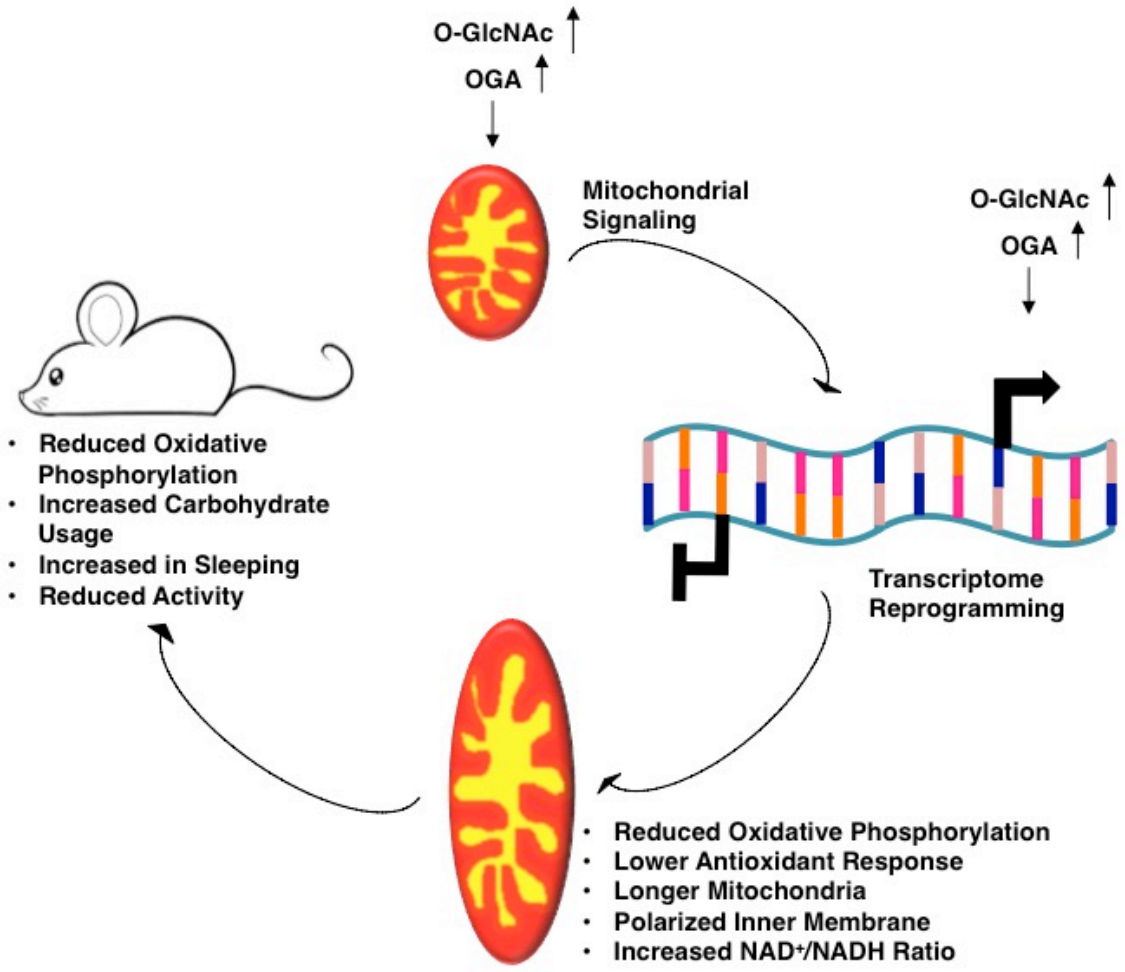

Figure 20: O-GlcNAc regulates energy metabolism by reprogramming mitochondrial function

Representative model for prolonged O-GlcNAcylation and OGA expression leading to transcriptome reprograming of mitochondrial function and energy metabolism.

References

1. Harman, D., *The Free Radical Theory of Aging: Effect of Age on Serum Copper Levels.* J Gerontol, 1965. **20**: p. 151-3.
2. Lopez-Otin, C., et al., *The hallmarks of aging.* Cell, 2013. **153**(6): p. 1194-217.
3. Swerdlow, R.H., *Brain aging, Alzheimer's disease, and mitochondria.* Biochim Biophys Acta, 2011. **1812**(12): p. 1630-9.
4. Kleinridders, A., et al., *Insulin action in brain regulates systemic metabolism and brain function.* Diabetes, 2014. **63**(7): p. 2232-43.
5. Sack, M.N. and T. Finkel, *Mitochondrial metabolism, sirtuins, and aging.* Cold Spring Harb Perspect Biol, 2012. **4**(12).
6. Still, A.J., et al., *Quantification of mitochondrial acetylation dynamics highlights prominent sites of metabolic regulation.* J Biol Chem, 2013. **288**(36): p. 26209-19.
7. Zhao, Y. and B. Zhao, *Oxidative stress and the pathogenesis of Alzheimer's disease.* Oxid Med Cell Longev, 2013. **2013**: p. 316523.
8. Hofer, A. and T. Wenz, *Post-translational modification of mitochondria as a novel mode of regulation.* Exp Gerontol, 2014. **56**: p. 202-20.
9. Slawson, C., R.J. Copeland, and G.W. Hart, *O-GlcNAc signaling: a metabolic link between diabetes and cancer?* Trends Biochem Sci, 2010. **35**(10): p. 547-55.
10. Love, D.C., et al., *Mitochondrial and nucleocytoplasmic targeting of O-linked GlcNAc transferase.* J Cell Sci, 2003. **116**(Pt 4): p. 647-54.
11. Banerjee, P.S., J. Ma, and G.W. Hart, *Diabetes-associated dysregulation of O-GlcNAcylation in rat cardiac mitochondria.* Proc Natl Acad Sci U S A, 2015. **112**(19): p. 6050-5.
12. Ma, J., et al., *O-GlcNAcomic Profiling Identifies Widespread O-Linked beta-N-Acetylglucosamine Modification (O-GlcNAcylation) in Oxidative Phosphorylation System Regulating Cardiac Mitochondrial Function.* J Biol Chem, 2015. **290**(49): p. 29141-53.
13. Bond, M.R. and J.A. Hanover, *O-GlcNAc cycling: a link between metabolism and chronic disease.* Annu Rev Nutr, 2013. **33**: p. 205-29.
14. Dias, W.B. and G.W. Hart, *O-GlcNAc modification in diabetes and Alzheimer's disease.* Mol Biosyst, 2007. **3**(11): p. 766-72.
15. Nunnari, J. and A. Suomalainen, *Mitochondria: in sickness and in health.* Cell, 2012. **148**(6): p. 1145-59.
16. Krebs, E.G., *Historical perspectives on protein phosphorylation and a classification system for protein kinases.* Philos Trans R Soc Lond B Biol Sci, 1983. **302**(1108): p. 3-11.
17. Menzies, K.J., et al., *Protein acetylation in metabolism - metabolites and cofactors.* Nat Rev Endocrinol, 2016. **12**(1): p. 43-60.
18. Choudhary, C., et al., *The growing landscape of lysine acetylation links metabolism and cell signalling.* Nat Rev Mol Cell Biol, 2014. **15**(8): p. 536-50.
19. Schieber, M. and N.S. Chandel, *ROS function in redox signaling and oxidative stress.* Curr Biol, 2014. **24**(10): p. R453-62.
20. Swerdlow, R.H., J.M. Burns, and S.M. Khan, *The Alzheimer's disease mitochondrial cascade hypothesis: progress and perspectives.* Biochim Biophys Acta, 2014. **1842**(8): p. 1219-31.

21. Atamna, H. and W.H. Frey, 2nd, *Mechanisms of mitochondrial dysfunction and energy deficiency in Alzheimer's disease.* Mitochondrion, 2007. **7**(5): p. 297-310.
22. Beal, M.F., *Oxidative damage as an early marker of Alzheimer's disease and mild cognitive impairment.* Neurobiol Aging, 2005. **26**(5): p. 585-6.
23. Blass, J.P., R.K. Sheu, and G.E. Gibson, *Inherent abnormalities in energy metabolism in Alzheimer disease. Interaction with cerebrovascular compromise.* Ann N Y Acad Sci, 2000. **903**: p. 204-21.
24. Santos, R.X., et al., *Alzheimer's disease: diverse aspects of mitochondrial malfunctioning.* Int J Clin Exp Pathol, 2010. **3**(6): p. 570-81.
25. Benzi, G. and A. Moretti, *Are reactive oxygen species involved in Alzheimer's disease?* Neurobiol Aging, 1995. **16**(4): p. 661-74.
26. Demetrius, L.A. and J. Driver, *Alzheimer's as a metabolic disease.* Biogerontology, 2013. **14**(6): p. 641-9.
27. Bonda, D.J., et al., *Mitochondrial dynamics in Alzheimer's disease: opportunities for future treatment strategies.* Drugs Aging, 2010. **27**(3): p. 181-92.
28. Swerdlow, R.H., *Mitochondria and cell bioenergetics: increasingly recognized components and a possible etiologic cause of Alzheimer's disease.* Antioxid Redox Signal, 2012. **16**(12): p. 1434-55.
29. Hart, G.W., *Three Decades of Research on O-GlcNAcylation - A Major Nutrient Sensor That Regulates Signaling, Transcription and Cellular Metabolism.* Front Endocrinol (Lausanne), 2014. **5**: p. 183.
30. Hu, Y., et al., *Increased enzymatic O-GlcNAcylation of mitochondrial proteins impairs mitochondrial function in cardiac myocytes exposed to high glucose.* J Biol Chem, 2009. **284**(1): p. 547-55.
31. Lagerlof, O., et al., *The nutrient sensor OGT in PVN neurons regulates feeding.* Science, 2016. **351**(6279): p. 1293-6.
32. O'Donnell, N., et al., *Ogt-dependent X-chromosome-linked protein glycosylation is a requisite modification in somatic cell function and embryo viability.* Mol Cell Biol, 2004. **24**(4): p. 1680-90.
33. Wang, A.C., et al., *Loss of O-GlcNAc glycosylation in forebrain excitatory neurons induces neurodegeneration.* Proc Natl Acad Sci U S A, 2016. **113**(52): p. 15120-15125.
34. Slawson, C., R.J. Copeland, and G.W. Hart, *O-GlcNAc signaling: a metabolic link between diabetes and cancer?* Trends in biochemical sciences, 2010. **35**(10): p. 547-55.
35. Slawson, C. and G.W. Hart, *O-GlcNAc signalling: implications for cancer cell biology.* Nature reviews. Cancer, 2011. **11**(9): p. 678-84.
36. Bond, M.R. and J.A. Hanover, *O-GlcNAc cycling: a link between metabolism and chronic disease.* Annual review of nutrition, 2013. **33**: p. 205-29.
37. Ball, L.E., M.N. Berkaw, and M.G. Buse, *Identification of the major site of O-linked beta-N-acetylglucosamine modification in the C terminus of insulin receptor substrate-1.* Molecular & cellular proteomics : MCP, 2006. **5**(2): p. 313-23.
38. Yang, X., et al., *Phosphoinositide signalling links O-GlcNAc transferase to insulin resistance.* Nature, 2008. **451**(7181): p. 964-9.
39. Whelan, S.A., M.D. Lane, and G.W. Hart, *Regulation of the O-linked beta-N-acetylglucosamine transferase by insulin signaling.* The Journal of biological chemistry, 2008. **283**(31): p. 21411-7.

40. Whelan, S.A., et al., *Regulation of insulin receptor substrate 1 (IRS-1)/AKT kinase-mediated insulin signaling by O-Linked beta-N-acetylglucosamine in 3T3-L1 adipocytes.* The Journal of biological chemistry, 2010. **285**(8): p. 5204-11.
41. Parker, G., et al., *Hyperglycemia and inhibition of glycogen synthase in streptozotocin-treated mice: role of O-linked N-acetylglucosamine.* The Journal of biological chemistry, 2004. **279**(20): p. 20636-42.
42. Dentin, R., et al., *Hepatic glucose sensing via the CREB coactivator CRTC2.* Science, 2008. **319**(5868): p. 1402-5.
43. Housley, M.P., et al., *O-GlcNAc regulates FoxO activation in response to glucose.* The Journal of biological chemistry, 2008. **283**(24): p. 16283-92.
44. Hu, Y., et al., *Increased enzymatic O-GlcNAcylation of mitochondrial proteins impairs mitochondrial function in cardiac myocytes exposed to high glucose.* The Journal of biological chemistry, 2009. **284**(1): p. 547-55.
45. Burnham-Marusich, A.R. and P.M. Berninsone, *Multiple proteins with essential mitochondrial functions have glycosylated isoforms.* Mitochondrion, 2012. **12**(4): p. 423-7.
46. Suarez, J., et al., *Alterations in mitochondrial function and cytosolic calcium induced by hyperglycemia are restored by mitochondrial transcription factor A in cardiomyocytes.* American journal of physiology. Cell physiology, 2008. **295**(6): p. C1561-8.
47. Love, D.C., et al., *Mitochondrial and nucleocytoplasmic targeting of O-linked GlcNAc transferase.* Journal of cell science, 2003. **116**(Pt 4): p. 647-54.
48. Shin, S.H., D.C. Love, and J.A. Hanover, *Elevated O-GlcNAc-dependent signaling through inducible mOGT expression selectively triggers apoptosis.* Amino acids, 2011. **40**(3): p. 885-93.
49. Bennett, C.E., et al., *Exercise training mitigates aberrant cardiac protein O-GlcNAcylation in streptozotocin-induced diabetic mice.* Life sciences, 2013. **92**(11): p. 657-63.
50. Medford, H.M., J.C. Chatham, and S.A. Marsh, *Chronic ingestion of a Western diet increases O-linked-beta-N-acetylglucosamine (O-GlcNAc) protein modification in the rat heart.* Life sciences, 2012. **90**(23-24): p. 883-8.
51. Ngoh, G.A., et al., *Unique hexosaminidase reduces metabolic survival signal and sensitizes cardiac myocytes to hypoxia/reoxygenation injury.* Circulation research, 2009. **104**(1): p. 41-9.
52. Johnsen, V.L., et al., *Enhanced cardiac protein glycosylation (O-GlcNAc) of selected mitochondrial proteins in rats artificially selected for low running capacity.* Physiological genomics, 2013. **45**(1): p. 17-25.
53. Gottlieb, R.A. and S. Adachi, *Nitrogen cavitation for cell disruption to obtain mitochondria from cultured cells.* Methods in enzymology, 2000. **322**: p. 213-21.
54. Swerdlow, R.H., *Mitochondria in cybrids containing mtDNA from persons with mitochondriopathies.* Journal of neuroscience research, 2007. **85**(15): p. 3416-28.
55. Lewis, B.A., *O-GlcNAcylation at promoters, nutrient sensors, and transcriptional regulation.* Biochimica et biophysica acta, 2013. **1829**(11): p. 1202-6.
56. Kelly, W.G., M.E. Dahmus, and G.W. Hart, *RNA polymerase II is a glycoprotein. Modification of the COOH-terminal domain by O-GlcNAc.* The Journal of biological chemistry, 1993. **268**(14): p. 10416-24.

57. Ranuncolo, S.M., et al., *Evidence of the involvement of O-GlcNAc-modified human RNA polymerase II CTD in transcription in vitro and in vivo.* The Journal of biological chemistry, 2012. **287**(28): p. 23549-61.
58. Zeidan, Q., et al., *O-GlcNAc cycling enzymes associate with the translational machinery and modify core ribosomal proteins.* Molecular biology of the cell, 2010. **21**(12): p. 1922-36.
59. Lazarou, M., et al., *Assembly of mitochondrial complex I and defects in disease.* Biochimica et biophysica acta, 2009. **1793**(1): p. 78-88.
60. Tan, E.P., et al., *O-linked N-acetylglucosamine cycling regulates mitotic spindle organization.* The Journal of biological chemistry, 2013. **288**(38): p. 27085-99.
61. Lezi, E. and R.H. Swerdlow, *Mitochondria in neurodegeneration.* Adv Exp Med Biol, 2012. **942**: p. 269-86.
62. Weimer, S., et al., *D-Glucosamine supplementation extends life span of nematodes and of ageing mice.* Nat Commun, 2014. **5**: p. 3563.
63. Hart, G.W., et al., *Cross talk between O-GlcNAcylation and phosphorylation: roles in signaling, transcription, and chronic disease.* Annu Rev Biochem, 2011. **80**: p. 825-58.
64. Marshall, S., O. Nadeau, and K. Yamasaki, *Dynamic actions of glucose and glucosamine on hexosamine biosynthesis in isolated adipocytes: differential effects on glucosamine 6-phosphate, UDP-N-acetylglucosamine, and ATP levels.* J Biol Chem, 2004. **279**(34): p. 35313-9.
65. Tan, E.P., et al., *Altering O-linked beta-N-acetylglucosamine cycling disrupts mitochondrial function.* J Biol Chem, 2014. **289**(21): p. 14719-30.
66. Tan, E.P., et al., *O-linked N-acetylglucosamine cycling regulates mitotic spindle organization.* J Biol Chem, 2013. **288**(38): p. 27085-99.
67. Rogers, G.W., et al., *High throughput microplate respiratory measurements using minimal quantities of isolated mitochondria.* PLoS One, 2011. **6**(7): p. e21746.
68. Zhang, Z., et al., *O-GlcNAcase Expression is Sensitive to Changes in O-GlcNAc Homeostasis.* Front Endocrinol (Lausanne), 2014. **5**: p. 206.
69. Butkinaree, C., et al., *Characterization of beta-N-acetylglucosaminidase cleavage by caspase-3 during apoptosis.* J Biol Chem, 2008. **283**(35): p. 23557-66.
70. Esteves, A.R., et al., *Mitochondrial respiration and respiration-associated proteins in cell lines created through Parkinson's subject mitochondrial transfer.* J Neurochem, 2010. **113**(3): p. 674-82.
71. E, L. and R.H. Swerdlow, *Lactate's effect on human neuroblastoma cell bioenergetic fluxes.* Biochem Pharmacol, 2016. **99**: p. 88-100.
72. Yuzwa, S.A., et al., *A potent mechanism-inspired O-GlcNAcase inhibitor that blocks phosphorylation of tau in vivo.* Nat Chem Biol, 2008. **4**(8): p. 483-90.
73. Fernie, A.R., F. Carrari, and L.J. Sweetlove, *Respiratory metabolism: glycolysis, the TCA cycle and mitochondrial electron transport.* Curr Opin Plant Biol, 2004. **7**(3): p. 254-61.
74. Fisher, R.P. and D.A. Clayton, *A transcription factor required for promoter recognition by human mitochondrial RNA polymerase. Accurate initiation at the heavy- and light-strand promoters dissected and reconstituted in vitro.* J Biol Chem, 1985. **260**(20): p. 11330-8.
75. Subramanian, A., et al., *Gene set enrichment analysis: a knowledge-based approach for interpreting genome-wide expression profiles.* Proc Natl Acad Sci U S A, 2005. **102**(43): p. 15545-50.

76. Mueller, C.F., et al., *ATVB in focus: redox mechanisms in blood vessels.* Arterioscler Thromb Vasc Biol, 2005. **25**(2): p. 274-8.
77. Housley, M.P., et al., *O-GlcNAc regulates FoxO activation in response to glucose.* J Biol Chem, 2008. **283**(24): p. 16283-92.
78. Ruan, H.B., et al., *O-GlcNAc transferase/host cell factor C1 complex regulates gluconeogenesis by modulating PGC-1alpha stability.* Cell Metab, 2012. **16**(2): p. 226-37.
79. Yang, W.H., et al., *Modification of p53 with O-linked N-acetylglucosamine regulates p53 activity and stability.* Nat Cell Biol, 2006. **8**(10): p. 1074-83.
80. Obrig, T.G., et al., *The mechanism by which cycloheximide and related glutarimide antibiotics inhibit peptide synthesis on reticulocyte ribosomes.* J Biol Chem, 1971. **246**(1): p. 174-81.
81. Sullivan, L.B. and N.S. Chandel, *Mitochondrial reactive oxygen species and cancer.* Cancer Metab, 2014. **2**: p. 17.
82. Tangmansakulchai, K., et al., *Calpastatin overexpression reduces oxidative stress-induced mitochondrial impairment and cell death in human neuroblastoma SH-SY5Y cells by decreasing calpain and calcineurin activation, induction of mitochondrial fission and destruction of mitochondrial fusion.* Mitochondrion, 2016. **30**: p. 151-61.
83. Groves, J.A., et al., *Dynamic O-GlcNAcylation and its roles in the cellular stress response and homeostasis.* Cell Stress Chaperones, 2013. **18**(5): p. 535-58.
84. Pendergast, D.R., J.J. Leddy, and J.T. Venkatraman, *A perspective on fat intake in athletes.* J Am Coll Nutr, 2000. **19**(3): p. 345-50.
85. Trapannone, R., et al., *Nucleocytoplasmic human O-GlcNAc transferase is sufficient for O-GlcNAcylation of mitochondrial proteins.* Biochem J, 2016. **473**(12): p. 1693-702.
86. Sacoman, J.L., et al., *Mitochondrial O-GlcNAc transferase (mOGT) regulates mitochondrial structure, function and survival in HeLa cells.* J Biol Chem, 2017.
87. Reczek, C.R. and N.S. Chandel, *ROS-dependent signal transduction.* Curr Opin Cell Biol, 2015. **33**: p. 8-13.
88. Harder, B., et al., *Molecular mechanisms of Nrf2 regulation and how these influence chemical modulation for disease intervention.* Biochem Soc Trans, 2015. **43**(4): p. 680-6.
89. Zhang, Z., et al., *O-Linked N-Acetylglucosamine (O-GlcNAc) Transferase and O-GlcNAcase Interact with Mi2beta Protein at the Agamma-Globin Promoter.* J Biol Chem, 2016. **291**(30): p. 15628-40.
90. Dassanayaka, S., et al., *High glucose induces mitochondrial dysfunction independently of protein O-GlcNAcylation.* Biochem J, 2015. **467**(1): p. 115-26.
91. Makino, A., et al., *O-GlcNAcase overexpression reverses coronary endothelial cell dysfunction in type 1 diabetic mice.* Am J Physiol Cell Physiol, 2015. **309**(9): p. C593-9.
92. Clark, R.J., et al., *Diabetes and the accompanying hyperglycemia impairs cardiomyocyte calcium cycling through increased nuclear O-GlcNAcylation.* J Biol Chem, 2003. **278**(45): p. 44230-7.
93. Facundo, H.T., et al., *O-GlcNAc signaling is essential for NFAT-mediated transcriptional reprogramming during cardiomyocyte hypertrophy.* Am J Physiol Heart Circ Physiol, 2012. **302**(10): p. H2122-30.

94. Stivers, P.J., et al., *Pharmacological Inhibition of O-GlcNAcase Does Not Increase Sensitivity of Glucocorticoid Receptor-Mediated Transrepression.* PLoS One, 2015. **10**(12): p. e0145151.
95. Yuzwa, S.A., et al., *Pharmacological inhibition of O-GlcNAcase (OGA) prevents cognitive decline and amyloid plaque formation in bigenic tau/APP mutant mice.* Mol Neurodegener, 2014. **9**: p. 42.
96. Yuzwa, S.A., et al., *O-GlcNAc modification of tau directly inhibits its aggregation without perturbing the conformational properties of tau monomers.* J Mol Biol, 2014. **426**(8): p. 1736-52.
97. Yuzwa, S.A., et al., *Increasing O-GlcNAc slows neurodegeneration and stabilizes tau against aggregation.* Nat Chem Biol, 2012. **8**(4): p. 393-9.
98. Mosconi, L., et al., *Reduced mitochondria cytochrome oxidase activity in adult children of mothers with Alzheimer's disease.* J Alzheimers Dis, 2011. **27**(3): p. 483-90.
99. Macauley, M.S., et al., *Elevation of Global O-GlcNAc in rodents using a selective O-GlcNAcase inhibitor does not cause insulin resistance or perturb glucohomeostasis.* Chem Biol, 2010. **17**(9): p. 949-58.
100. Vosseller, K., et al., *Elevated nucleocytoplasmic glycosylation by O-GlcNAc results in insulin resistance associated with defects in Akt activation in 3T3-L1 adipocytes.* Proc Natl Acad Sci U S A, 2002. **99**(8): p. 5313-8.
101. Macauley, M.S., et al., *Elevation of global O-GlcNAc levels in 3T3-L1 adipocytes by selective inhibition of O-GlcNAcase does not induce insulin resistance.* J Biol Chem, 2008. **283**(50): p. 34687-95.
102. Klein, A.L., et al., *O-linked N-acetylglucosamine modification of insulin receptor substrate-1 occurs in close proximity to multiple SH2 domain binding motifs.* Mol Cell Proteomics, 2009. **8**(12): p. 2733-45.
103. Whelan, S.A., et al., *Regulation of insulin receptor substrate 1 (IRS-1)/AKT kinase-mediated insulin signaling by O-Linked beta-N-acetylglucosamine in 3T3-L1 adipocytes.* J Biol Chem, 2010. **285**(8): p. 5204-11.
104. Whelan, S.A., M.D. Lane, and G.W. Hart, *Regulation of the O-linked beta-N-acetylglucosamine transferase by insulin signaling.* J Biol Chem, 2008. **283**(31): p. 21411-7.
105. Copeland, R.J., J.W. Bullen, and G.W. Hart, *Cross-talk between GlcNAcylation and phosphorylation: roles in insulin resistance and glucose toxicity.* Am J Physiol Endocrinol Metab, 2008. **295**(1): p. E17-28.
106. Verdaasdonk, J.S. and K. Bloom, *Centromeres: unique chromatin structures that drive chromosome segregation.* Nature reviews. Molecular cell biology, 2011. **12**(5): p. 320-32.
107. Loncarek, J., et al., *The centromere geometry essential for keeping mitosis error free is controlled by spindle forces.* Nature, 2007. **450**(7170): p. 745-9.
108. Meunier, S. and I. Vernos, *Microtubule assembly during mitosis - from distinct origins to distinct functions?* Journal of cell science, 2012. **125**(Pt 12): p. 2805-14.
109. Seshan, A. and A. Amon, *Linked for life: temporal and spatial coordination of late mitotic events.* Current opinion in cell biology, 2004. **16**(1): p. 41-8.
110. Pfau, S.J. and A. Amon, *Chromosomal instability and aneuploidy in cancer: from yeast to man.* EMBO reports, 2012. **13**(6): p. 515-27.

111. Kunitoku, N., et al., *CENP-A phosphorylation by Aurora-A in prophase is required for enrichment of Aurora-B at inner centromeres and for kinetochore function.* Developmental cell, 2003. **5**(6): p. 853-64.
112. Nigg, E.A., *Mitotic kinases as regulators of cell division and its checkpoints.* Nature reviews. Molecular cell biology, 2001. **2**(1): p. 21-32.
113. Grosstessner-Hain, K., et al., *Quantitative phospho-proteomics to investigate the polo-like kinase 1-dependent phospho-proteome.* Molecular & cellular proteomics : MCP, 2011. **10**(11): p. M111 008540.
114. Carmena, M., et al., *The chromosomal passenger complex activates Polo kinase at centromeres.* PLoS biology, 2012. **10**(1): p. e1001250.
115. Welburn, J.P., et al., *Aurora B phosphorylates spatially distinct targets to differentially regulate the kinetochore-microtubule interface.* Molecular cell, 2010. **38**(3): p. 383-92.
116. Tseng, B.S., et al., *Dual detection of chromosomes and microtubules by the chromosomal passenger complex drives spindle assembly.* Developmental cell, 2010. **18**(6): p. 903-12.
117. Bolton, M.A., et al., *Aurora B kinase exists in a complex with survivin and INCENP and its kinase activity is stimulated by survivin binding and phosphorylation.* Molecular biology of the cell, 2002. **13**(9): p. 3064-77.
118. Petsalaki, E., et al., *Phosphorylation at serine 331 is required for Aurora B activation.* The Journal of cell biology, 2011. **195**(3): p. 449-66.
119. Qi, G., et al., *Nuclear Survivin expression is correlated with malignant behaviors of head and neck cancer together with Aurora-B.* Oral oncology, 2010. **46**(4): p. 263-70.
120. Hayama, S., et al., *Phosphorylation and activation of cell division cycle associated 8 by aurora kinase B plays a significant role in human lung carcinogenesis.* Cancer research, 2007. **67**(9): p. 4113-22.
121. Slawson, C., et al., *Perturbations in O-linked beta-N-acetylglucosamine protein modification cause severe defects in mitotic progression and cytokinesis.* The Journal of biological chemistry, 2005. **280**(38): p. 32944-56.
122. Slawson, C., et al., *A mitotic GlcNAcylation/phosphorylation signaling complex alters the posttranslational state of the cytoskeletal protein vimentin.* Molecular biology of the cell, 2008. **19**(10): p. 4130-40.
123. Wang, Z., et al., *Extensive crosstalk between O-GlcNAcylation and phosphorylation regulates cytokinesis.* Science signaling, 2010. **3**(104): p. ra2.
124. Sakabe, K. and G.W. Hart, *O-GlcNAc transferase regulates mitotic chromatin dynamics.* The Journal of biological chemistry, 2010. **285**(45): p. 34460-8.
125. Clark, R.J., et al., *Diabetes and the accompanying hyperglycemia impairs cardiomyocyte calcium cycling through increased nuclear O-GlcNAcylation.* The Journal of biological chemistry, 2003. **278**(45): p. 44230-7.
126. Ozlu, N., et al., *Binding partner switching on microtubules and aurora-B in the mitosis to cytokinesis transition.* Molecular & cellular proteomics : MCP, 2010. **9**(2): p. 336-50.
127. Sakabe, K., Z. Wang, and G.W. Hart, *Beta-N-acetylglucosamine (O-GlcNAc) is part of the histone code.* Proceedings of the National Academy of Sciences of the United States of America, 2010. **107**(46): p. 19915-20.
128. Yuzwa, S.A., et al., *A potent mechanism-inspired O-GlcNAcase inhibitor that blocks phosphorylation of tau in vivo.* Nature chemical biology, 2008. **4**(8): p. 483-90.

129. Heng, Y.W., et al., *TPPP acts downstream of RhoA-ROCK-LIMK2 to regulate astral microtubule organization and spindle orientation.* Journal of cell science, 2012. **125**(Pt 6): p. 1579-90.
130. DeLuca, J.G., et al., *Kinetochore microtubule dynamics and attachment stability are regulated by Hec1.* Cell, 2006. **127**(5): p. 969-82.
131. Rahal, R. and A. Amon, *Mitotic CDKs control the metaphase-anaphase transition and trigger spindle elongation.* Genes & development, 2008. **22**(11): p. 1534-48.
132. Dephoure, N., et al., *A quantitative atlas of mitotic phosphorylation.* Proceedings of the National Academy of Sciences of the United States of America, 2008. **105**(31): p. 10762-7.
133. Daub, H., et al., *Kinase-selective enrichment enables quantitative phosphoproteomics of the kinome across the cell cycle.* Molecular cell, 2008. **31**(3): p. 438-48.
134. Hutterer, A., et al., *Mitotic activation of the kinase Aurora-A requires its binding partner Bora.* Developmental cell, 2006. **11**(2): p. 147-57.
135. Eyers, P.A., et al., *A novel mechanism for activation of the protein kinase Aurora A.* Current biology : CB, 2003. **13**(8): p. 691-7.
136. Hirota, T., et al., *Aurora-A and an interacting activator, the LIM protein Ajuba, are required for mitotic commitment in human cells.* Cell, 2003. **114**(5): p. 585-98.
137. Walter, A.O., et al., *The mitotic serine/threonine kinase Aurora2/AIK is regulated by phosphorylation and degradation.* Oncogene, 2000. **19**(42): p. 4906-16.
138. Tong, Y., et al., *Pituitary tumor transforming gene 1 regulates Aurora kinase A activity.* Oncogene, 2008. **27**(49): p. 6385-95.
139. Jang, Y.J., et al., *Phosphorylation of threonine 210 and the role of serine 137 in the regulation of mammalian polo-like kinase.* The Journal of biological chemistry, 2002. **277**(46): p. 44115-20.
140. Yang, J., et al., *The catalytic role of INCENP in Aurora B activation and the kinetic mechanism of Aurora B/INCENP.* The Biochemical journal, 2009. **417**(1): p. 355-60.
141. Zeitlin, S.G., R.D. Shelby, and K.F. Sullivan, *CENP-A is phosphorylated by Aurora B kinase and plays an unexpected role in completion of cytokinesis.* The Journal of cell biology, 2001. **155**(7): p. 1147-57.
142. Giet, R. and D.M. Glover, *Drosophila aurora B kinase is required for histone H3 phosphorylation and condensin recruitment during chromosome condensation and to organize the central spindle during cytokinesis.* The Journal of cell biology, 2001. **152**(4): p. 669-82.
143. Wei, Y., et al., *Phosphorylation of histone H3 is required for proper chromosome condensation and segregation.* Cell, 1999. **97**(1): p. 99-109.
144. Zhang, S., et al., *Modification of histones by sugar beta-N-acetylglucosamine (GlcNAc) occurs on multiple residues, including histone H3 serine 10, and is cell cycle-regulated.* The Journal of biological chemistry, 2011. **286**(43): p. 37483-95.
145. Fong, J.J., et al., *beta-N-Acetylglucosamine (O-GlcNAc) is a novel regulator of mitosis-specific phosphorylations on histone H3.* The Journal of biological chemistry, 2012. **287**(15): p. 12195-203.
146. Macauley, M.S., et al., *Inhibition of O-GlcNAcase using a potent and cell-permeable inhibitor does not induce insulin resistance in 3T3-L1 adipocytes.* Chemistry & biology, 2010. **17**(9): p. 937-48.

147. Kimura, K., O. Cuvier, and T. Hirano, *Chromosome condensation by a human condensin complex in Xenopus egg extracts.* The Journal of biological chemistry, 2001. **276**(8): p. 5417-20.
148. Fisher, D., et al., *Phosphorylation network dynamics in the control of cell cycle transitions.* Journal of cell science, 2012. **125**(Pt 20): p. 4703-11.
149. Clarke, P.R., et al., *Dephosphorylation of cdc25-C by a type-2A protein phosphatase: specific regulation during the cell cycle in Xenopus egg extracts.* Molecular biology of the cell, 1993. **4**(4): p. 397-411.
150. Mueller, P.R., T.R. Coleman, and W.G. Dunphy, *Cell cycle regulation of a Xenopus Wee1-like kinase.* Molecular biology of the cell, 1995. **6**(1): p. 119-34.
151. Fujiki, R., et al., *GlcNAcylation of histone H2B facilitates its monoubiquitination.* Nature, 2011. **480**(7378): p. 557-60.
152. Dias, W.B., et al., *Regulation of calcium/calmodulin-dependent kinase IV by O-GlcNAc modification.* The Journal of biological chemistry, 2009. **284**(32): p. 21327-37.
153. Yi, W., et al., *Phosphofructokinase 1 glycosylation regulates cell growth and metabolism.* Science, 2012. **337**(6097): p. 975-80.
154. Macauley, M.S., et al., *Elevation of global O-GlcNAc levels in 3T3-L1 adipocytes by selective inhibition of O-GlcNAcase does not induce insulin resistance.* The Journal of biological chemistry, 2008. **283**(50): p. 34687-95.
155. Cheung, W.D., et al., *O-linked beta-N-acetylglucosaminyltransferase substrate specificity is regulated by myosin phosphatase targeting and other interacting proteins.* The Journal of biological chemistry, 2008. **283**(49): p. 33935-41.
156. Hart, G.W., et al., *Cross talk between O-GlcNAcylation and phosphorylation: roles in signaling, transcription, and chronic disease.* Annual review of biochemistry, 2011. **80**: p. 825-58.
157. Tan, E.P., et al., *Altering O-linked beta-N-Acetylglucosamine cycling disrupts mitochondrial function.* The Journal of biological chemistry, 2014. **289**: p. 14719-14730.
158. Ruan, H.B., et al., *O-GlcNAc Transferase Enables AgRP Neurons to Suppress Browning of White Fat.* Cell, 2014. **159**(2): p. 306-17.
159. Caldwell, S.A., et al., *Nutrient sensor O-GlcNAc transferase regulates breast cancer tumorigenesis through targeting of the oncogenic transcription factor FoxM1.* Oncogene, 2010. **29**(19): p. 2831-42.
160. Fang, B. and M.W. Miller, *Use of galactosyltransferase to assess the biological function of O-linked N-acetyl-d-glucosamine: a potential role for O-GlcNAc during cell division.* Experimental cell research, 2001. **263**(2): p. 243-53.
161. Slawson, C., et al., *Characterization of the O-GlcNAc protein modification in Xenopus laevis oocyte during oogenesis and progesterone-stimulated maturation.* Biochimica et biophysica acta, 2002. **1573**(2): p. 121-9.
162. Lefebvre, T., et al., *Modulation of O-GlcNAc glycosylation during Xenopus oocyte maturation.* Journal of cellular biochemistry, 2004. **93**(5): p. 999-1010.
163. Dehennaut, V., et al., *O-linked N-acetylglucosaminyltransferase inhibition prevents G2/M transition in Xenopus laevis oocytes.* The Journal of biological chemistry, 2007. **282**(17): p. 12527-36.

164. Dehennaut, V., et al., *Microinjection of recombinant O-GlcNAc transferase potentiates Xenopus oocytes M-phase entry.* Biochemical and biophysical research communications, 2008. **369**(2): p. 539-46.
165. Dehennaut, V., et al., *Identification of structural and functional O-linked N-acetylglucosamine-bearing proteins in Xenopus laevis oocyte.* Molecular & cellular proteomics : MCP, 2008. **7**(11): p. 2229-45.
166. Slawson, C. and F.E. Duncan, *Sweet action: The dynamics of O-GlcNAcylation during meiosis in mouse oocytes.* Mol Reprod Dev, 2015.
167. Shafi, R., et al., *The O-GlcNAc transferase gene resides on the X chromosome and is essential for embryonic stem cell viability and mouse ontogeny.* Proceedings of the National Academy of Sciences of the United States of America, 2000. **97**(11): p. 5735-9.
168. Yang, Y.R., et al., *O-GlcNAcase is essential for embryonic development and maintenance of genomic stability.* Aging Cell, 2012. **11**(3): p. 439-48.
169. Wang, T., et al., *Identification and characterization of essential genes in the human genome.* Science, 2015. **350**(6264): p. 1096-101.
170. Butkinaree, C., et al., *Characterization of beta-N-acetylglucosaminidase cleavage by caspase-3 during apoptosis.* The Journal of biological chemistry, 2008. **283**(35): p. 23557-66.
171. Park, H., et al., *Ewing sarcoma EWS protein regulates midzone formation by recruiting Aurora B kinase to the midzone.* Cell Cycle, 2014. **13**(15): p. 2391-9.
172. Yehezkel, G., et al., *O-linked beta-N-acetylglucosaminylation (O-GlcNAcylation) in primary and metastatic colorectal cancer clones and effect of N-acetyl-beta-D-glucosaminidase silencing on cell phenotype and transcriptome.* The Journal of biological chemistry, 2012. **287**(34): p. 28755-69.
173. Li, Q. and K. Kamemura, *Adipogenesis stimulates the nuclear localization of EWS with an increase in its O-GlcNAc glycosylation in 3T3-L1 cells.* Biochem Biophys Res Commun, 2014. **450**(1): p. 588-92.
174. Silk, A.D., A.J. Holland, and D.W. Cleveland, *Requirements for NuMA in maintenance and establishment of mammalian spindle poles.* J Cell Biol, 2009. **184**(5): p. 677-90.
175. Azuma, M., et al., *Ewing sarcoma protein ewsr1 maintains mitotic integrity and proneural cell survival in the zebrafish embryo.* PLoS One, 2007. **2**(10): p. e979.
176. Keembiyehetty, C., et al., *Conditional knockout reveals a requirement for O-GlcNAcase in metabolic homeostasis.* J Biol Chem, 2015.
177. Torres, C.R. and G.W. Hart, *Topography and polypeptide distribution of terminal N-acetylglucosamine residues on the surfaces of intact lymphocytes. Evidence for O-linked GlcNAc.* The Journal of biological chemistry, 1984. **259**(5): p. 3308-17.
178. Fardini, Y., et al., *O-GlcNAcylation: A New Cancer Hallmark?* Frontiers in endocrinology, 2013. **4**: p. 99.
179. Dias, W.B. and G.W. Hart, *O-GlcNAc modification in diabetes and Alzheimer's disease.* Molecular bioSystems, 2007. **3**(11): p. 766-72.
180. Kazemi, Z., et al., *O-linked beta-N-acetylglucosamine (O-GlcNAc) regulates stress-induced heat shock protein expression in a GSK-3beta-dependent manner.* The Journal of biological chemistry, 2010. **285**(50): p. 39096-107.
181. Chesterton, C.J., et al., *Studies on the control of ribosomal RNA synthesis in HeLa cells.* European journal of biochemistry / FEBS, 1975. **57**(1): p. 79-83.

182. Kim, H.R., H.S. Kang, and H.D. Kim, *Geldanamycin induces heat shock protein expression through activation of HSF1 in K562 erythroleukemic cells.* IUBMB life, 1999. **48**(4): p. 429-33.
183. Sawicki, S.G. and G.C. Godman, *On the differential cytotoxicity of actinomycin D.* The Journal of cell biology, 1971. **50**(3): p. 746-61.
184. Harju-Baker, S., et al., *Silencing of Agamma-globin gene expression during adult definitive erythropoiesis mediated by GATA-1-FOG-1-Mi2 complex binding at the -566 GATA site.* Molecular and cellular biology, 2008. **28**(10): p. 3101-13.
185. DiTacchio, L., et al., *Histone lysine demethylase JARID1a activates CLOCK-BMAL1 and influences the circadian clock.* Science, 2011. **333**(6051): p. 1881-5.
186. Obrig, T.G., et al., *The mechanism by which cycloheximide and related glutarimide antibiotics inhibit peptide synthesis on reticulocyte ribosomes.* The Journal of biological chemistry, 1971. **246**(1): p. 174-81.
187. Yang, W.H., et al., *Modification of p53 with O-linked N-acetylglucosamine regulates p53 activity and stability.* Nature cell biology, 2006. **8**(10): p. 1074-83.
188. Shi, F.T., et al., *Ten-eleven translocation 1 (Tet1) is regulated by O-linked N-acetylglucosamine transferase (Ogt) for target gene repression in mouse embryonic stem cells.* The Journal of biological chemistry, 2013. **288**(29): p. 20776-84.
189. Gloster, T.M., et al., *Hijacking a biosynthetic pathway yields a glycosyltransferase inhibitor within cells.* Nature chemical biology, 2011. **7**(3): p. 174-81.
190. Park, K., C.D. Saudek, and G.W. Hart, *Increased expression of beta-N-acetylglucosaminidase in erythrocytes from individuals with pre-diabetes and diabetes.* Diabetes, 2010. **59**(7): p. 1845-50.
191. Heinemeyer, T., et al., *Databases on transcriptional regulation: TRANSFAC, TRRD and COMPEL.* Nucleic acids research, 1998. **26**(1): p. 362-7.
192. Le Mee, S., O. Fromigue, and P.J. Marie, *Sp1/Sp3 and the myeloid zinc finger gene MZF1 regulate the human N-cadherin promoter in osteoblasts.* Experimental cell research, 2005. **302**(1): p. 129-42.
193. Myers, S.A., B. Panning, and A.L. Burlingame, *Polycomb repressive complex 2 is necessary for the normal site-specific O-GlcNAc distribution in mouse embryonic stem cells.* Proceedings of the National Academy of Sciences of the United States of America, 2011. **108**(23): p. 9490-5.
194. Ma, Z., D.J. Vocadlo, and K. Vosseller, *Hyper-O-GlcNAcylation is anti-apoptotic and maintains constitutive NF-kappaB activity in pancreatic cancer cells.* The Journal of biological chemistry, 2013. **288**(21): p. 15121-30.
195. de Queiroz, R.M., E. Carvalho, and W.B. Dias, *O-GlcNAcylation: The Sweet Side of the Cancer.* Frontiers in oncology, 2014. **4**: p. 132.

Appendix A

Supplementary Data: Chapter 3

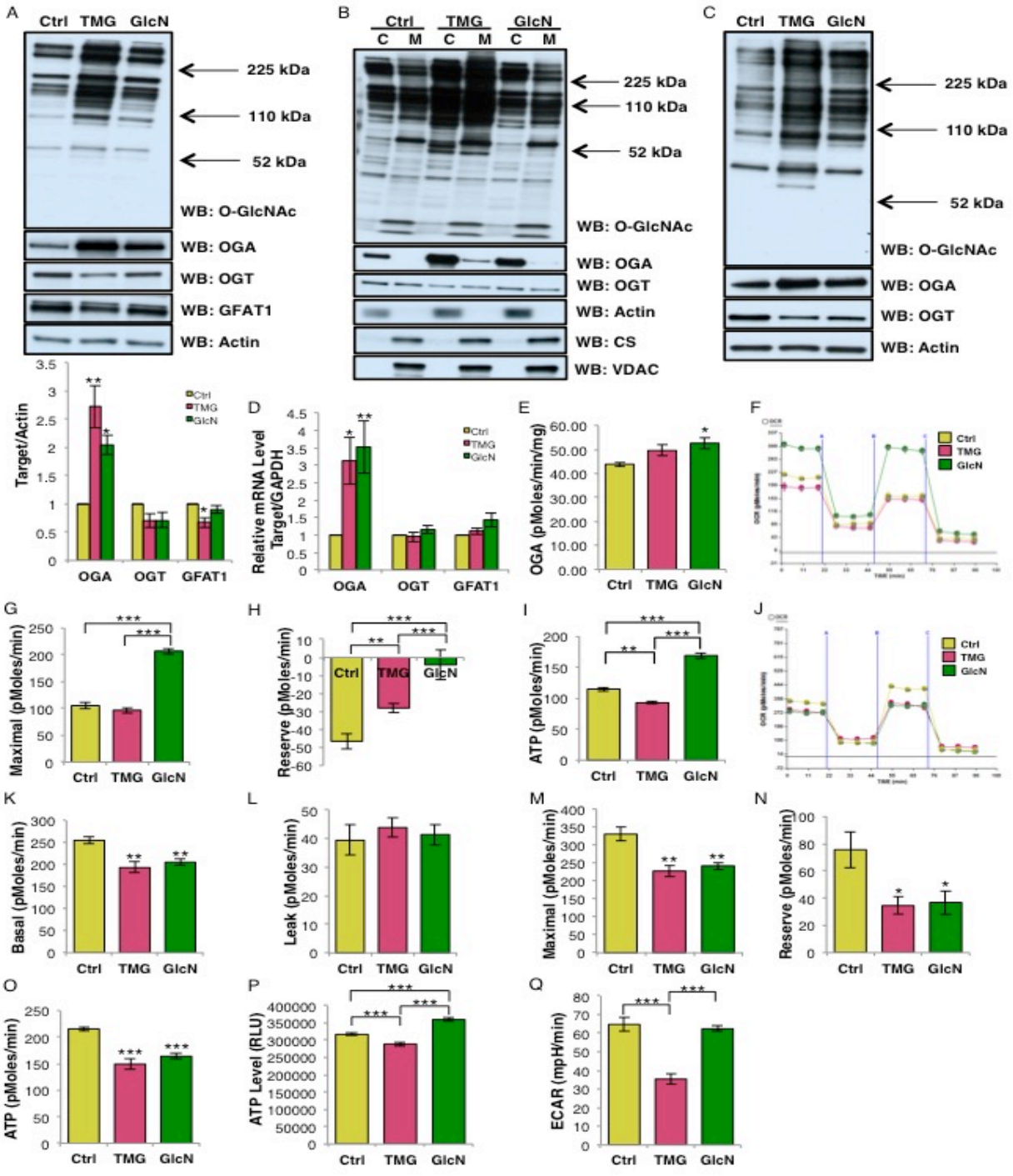

Figure A. 1: Prolonged TMG or GlcNAc treatment alters mitochondrial bioenergetics capacity

O-GlcNAc, OGT, OGA, GFAT1 levels of (A) whole cell, (B) cytoplasm and mitochondrial content in SH-SY5Y cells, and (C) NT2 whole cell. For whole cell or cytoplasmic extract, actin was used as loading control, while VDAC and citrate synthase (CS) was used as a loading control for mitochondrial extracts (n=3). (D) *OGA, OGT* (*MGEA5*), and *GFAT1* transcript levels were determined using qRT-PCR (n=3). (E) OGA activity (n=3). (F) Representative graph of the bioenergetics profile in SY5Y cells. (G) Maximal respiration rate, (H) reserve capacity rate, and (I) ATP production rate (average ± SEM, n=6). (J) Bioenergetics profile of NT2 cells, (K) basal respiration rate, (L) leak rate, (M) maximal respiration rate, (N) reserve capacity rate, and (O) ATP production rate (average ± SEM, n=6). NT2 cell representative plots showing (P) cellular ATP levels (average ± SEM, n=9) and (Q). glycolysis rate (n=6). * indicates significance $p < 0.05$. ** indicates significance $p < 0.01$. *** indicates significance $p < 0.001$.

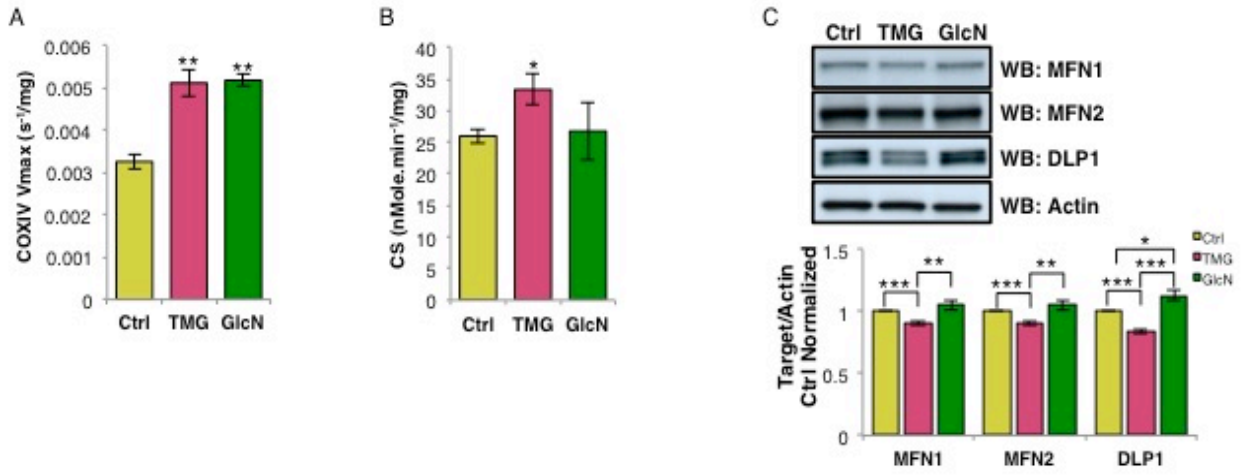

Figure A. 2: Prolonged TMG or GlcN treatment alter mitochondrial bioenergetics (cont.) Representative plots showing SY5Y (A) COXIV Vmax and (B) CS activity after being normalized with total protein concentration (n=3). (C) Mitofusin 1 (MFN1), Mitofusin 2 (MFN2), and Dynamin-like protein (DLP1) protein levels. Protein levels were first normalized to actin level, then normalized to control cells (n=3). * indicates significance $p < 0.05$. ** indicates significance $p < 0.01$. *** indicates significance $p < 0.001$.

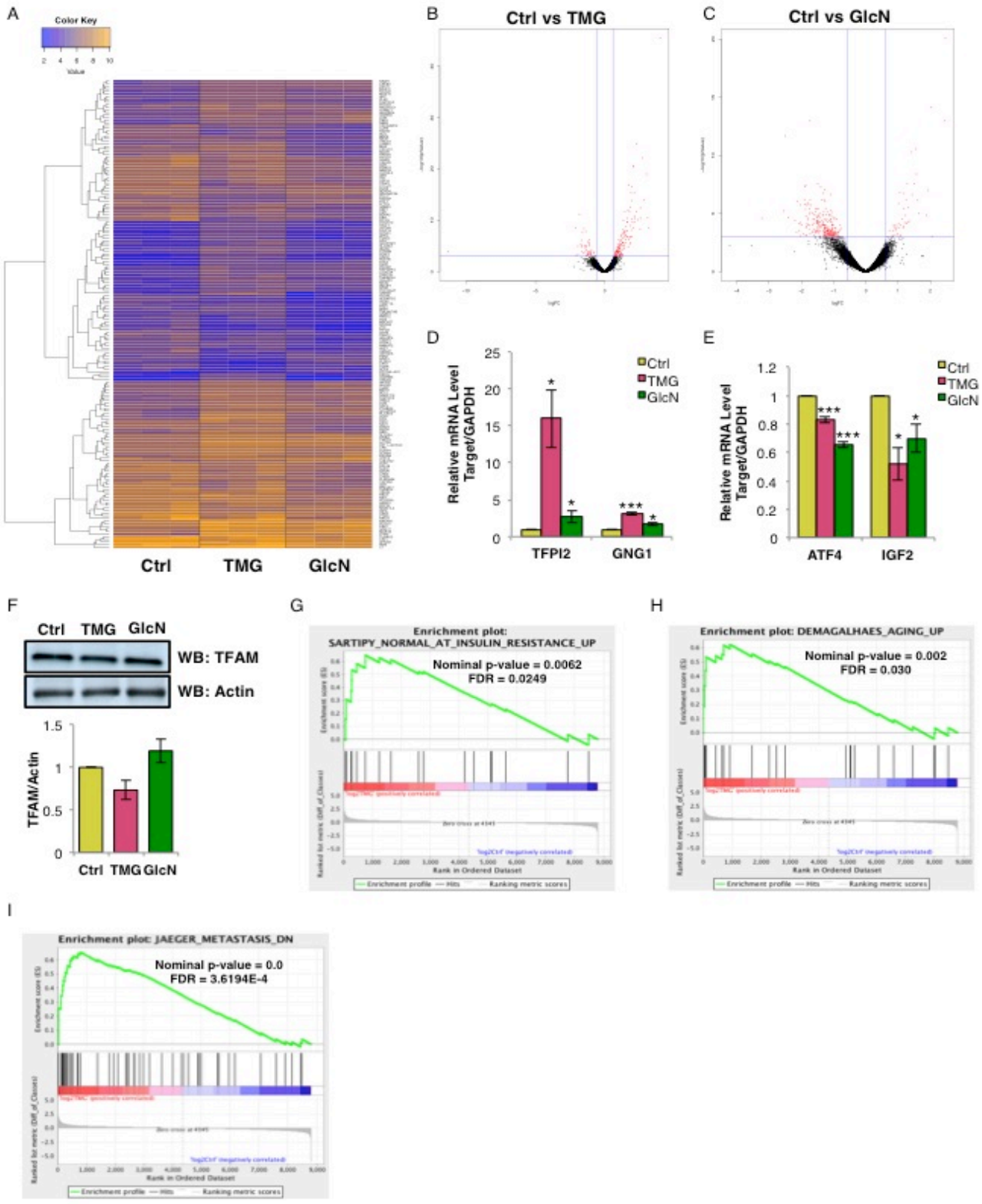

Figure A. 3: Transcriptome Alterations from Sustained TMG or GlcN treatment

(A) Heat map of top 100 genes with cpm (counts per million) of >10 in at least two of the three replicate samples generated from Next Generation RNA-Sequencing (RNA-seq) analysis. Volcano plots for (B) TMG and (C) GlcN compared to control cells. Orthogonal validation of (D) TFPI2 and GNG1 transcript levels and (E) ATF4 and IGF2 transcript levels (average ± SEM, n=3). (F) TFAM protein levels after actin level and control normalization (average ± SEM, n=3). Plots obtained from c2 gene sets from GSEA analysis comparing long-term TMG treatment to (G) insulin resistance (Sartipy_Normal_At_Insulin_Resistance_Up gene set), (H) aging (Demagalhaes_Aging_Up gene set), and (I) metastasis (Jaeger_Metastasis_DN gene set) gene sets. * indicates significance $p < 0.05$. ** indicates significance $p < 0.01$. *** indicates significance $p < 0.001$.

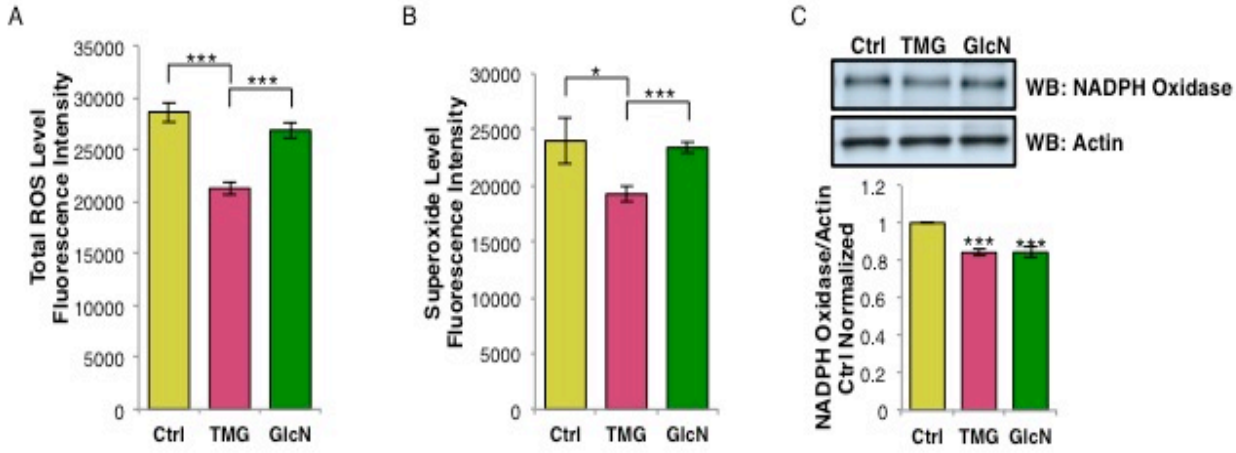

Figure A. 4: Prolonged TMG or GlcN treatment reduced ROS generation

(A) Total ROS and (B) superoxide level in NT2 cells (average ± SEM, n=9). (C) NADPH oxidase levels after prolonged TMG or GlcN treatment in SH-SY5Y cells (average ± SEM, n=3). * indicates significance $p < 0.05$. ** indicates significance $p < 0.01$. *** indicates significance $p < 0.001$.

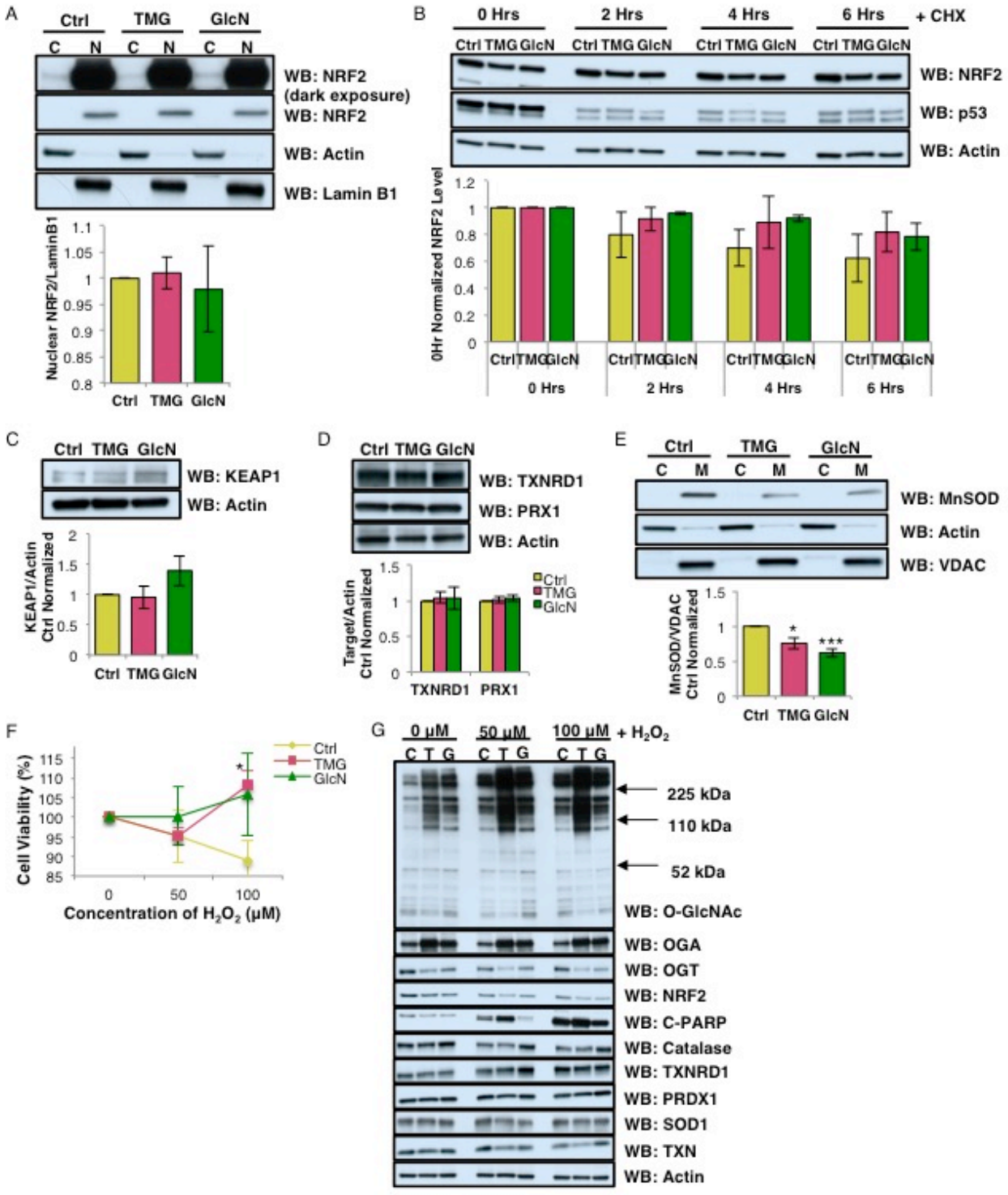

Figure A. 5: NRF2 localization, protein stability, and acute oxidative stress response were not altered by TMG or GlcN treatment

(A) NRF2 localization was not altered in TMG- or GlcN-treated SH-SY5Y cells. (B) NRF2 protein stability after cycloheximide treatment with p53 as positive control for the treatment. Actin was used as loading control, and the protein levels were further normalized with the

control. (C) KEAP1, (D) TXNRD1, and PRX1 protein levels in TMG- or GlcN-treated SY5Y cells. Actin was used as loading control, and the protein levels were further normalized with the control. (E) Mitochondrial MnSOD1 protein level is significantly decreased after TMG or GlcN treatment in SH-SY5Y cells. Cells were separated into cytoplasm and mitochondria fraction. VDAC was used as the loading control for mitochondrial fraction and actin was used as mitochondrial fraction negative control (average ± SEM, n=3). (F) Cell viability plot after acute oxidative stress test in TMG- or GlcN-treated SH-SY5Y cells (average, ± SEM, n=3). (G) O-GlcNAc, OGA, OGT, NRF2, C-PARP, Catalase, TXNRD1, PRDX1, SOD1 and TXN protein levels after 7 h of various concentrations H_2O_2 treatment (n=3).

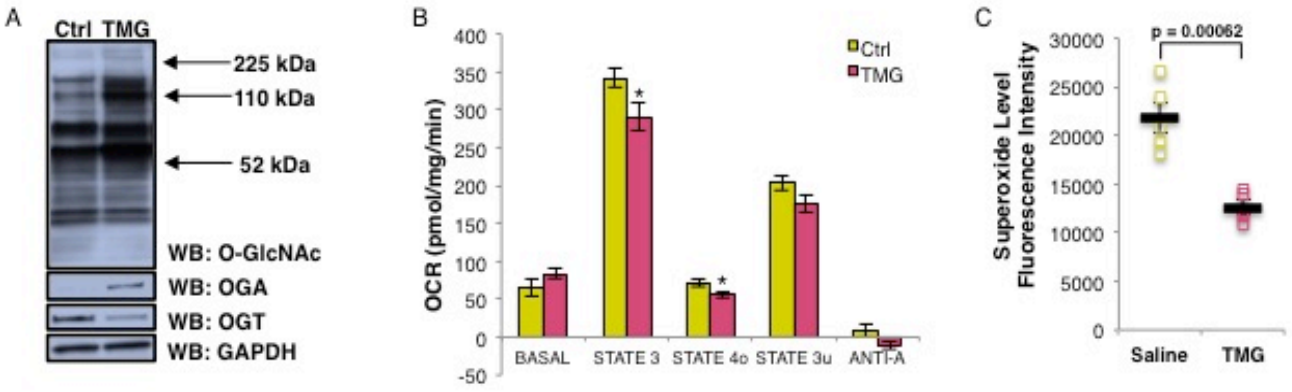

Figure A. 6: Long-term TMG injection decreased mitochondrial respiration and ROS generation in liver

(A) Total liver O-GlcNAcylation, OGT, and OGA protein level in prolonged TMG dosed mice (average, ± SEM, n=4). GAPDH is the loading control. (B) Mitochondrial respiration (C) and superoxide level in liver is reduced after prolonged TMG injection (average, ± SEM, n=5).

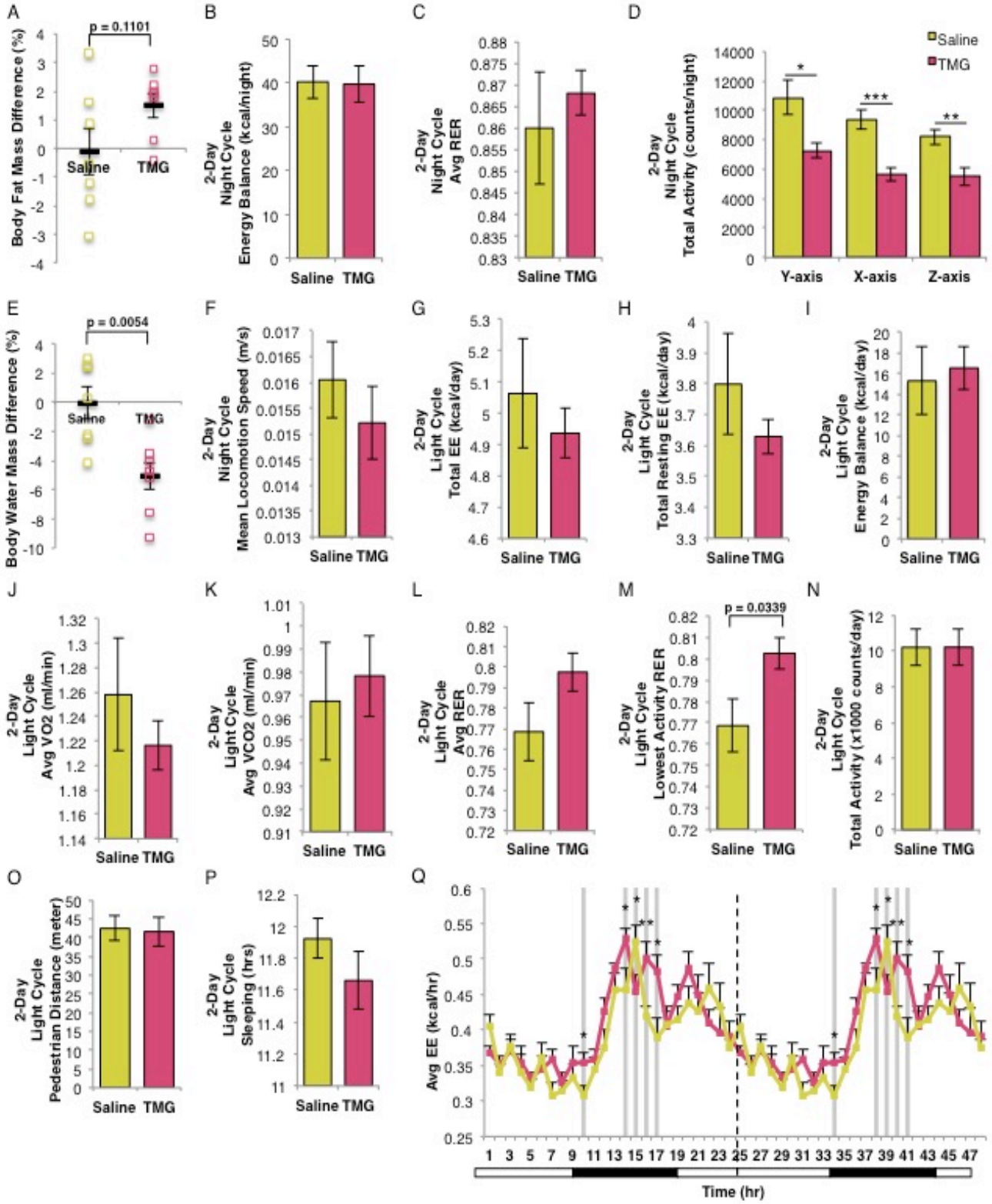

Figure A. 7: O-GlcNAc elevation altered energy metabolism in mice

(A) Body fat mass differences percentage calculated from the percentage difference of before and after injection (saline or TMG) (average, ± SEM, n=8). Representative plots illustrating nocturnal (B) energy balance (total energy intake – total energy expenditure), (C) average respiratory exchange ratio (RER), (D) total activity based on Y-axis, X-axis, and Z-axis beam breaks. (E) Body water mass difference percentage calculated by taking the percentage of the differences of water mass before and after injection (saline or TMG) (average, ± SEM, n=8). Representative plots of nocturnal (F) mean locomotion speed, (G) diurnal total EE, (H) total resting EE, (I) energy balance, (J) average VO_2, (K) average VCO_2, (L) average RER, (M) lowest activity RER, (N) total activity, (O) pedestrian distance, and (P) sleeping hours. (Q) The average EE for the last 24 h time after TMG injection was plotted. * indicates significance $p < 0.05$. ** indicates significance $p < 0.01$. *** indicates significance $p < 0.001$.

Appendix B: O-GlcNAc Cycling is Important in Regulating Mitotic Spindle Organization- *Part I*

Reproduced with permission from Tan, E.P., Caro, S., Potnis, A., Lanza, C., and Slawson, C. (2013). ***O-linked-N-Acetylglucosamine Cycling Regulates Mitotic Spindle Organization.*** *The Journal of Biological Chemistry 288(38):27085-99*

B.1 Introduction

The segregation of chromosomes into two daughter cells with perfect fidelity is crucial to the process of cell division. Daughter cell segregation is highly dependent upon the construction and organization of the mitotic spindle [106, 107]. As a cell enters mitosis, the duplicated chromosomes start to condense and spindle assembly begins. Microtubules radiate outward from the two centrosomes located at opposite poles of the cell and embed themselves into kinetochores assembled on the centromere of each chromosome [108]. In this manner, sister chromatids are attached to two microtubules from opposite centrosomes, and when the separation and segregation of these chromosomes ends, each daughter cell will contain an exact copy of all 23 chromosomes [109]. Mitotic success rests on the correct orientation of sister chromatids bound to microtubules. Problems at any point in this extensive yet rapid process are detrimental to both subsequent daughter cells. Defects in correct segregation of sister chromatids lead to mitotic catastrophe, apoptosis, or aneuploidy [110].

Mitotic phosphorylation cascades control spindle assembly and organization [111, 112]. Initially during prophase, cyclin-dependent kinase 1 (CDK1) phosphorylates proteins involved in nuclear envelope breakdown and spindle formation. Shortly thereafter, Aurora Kinase A (AurA) and Aurora Kinase B (AurB) phosphorylate the histone H3 variant CENPA, promoting microtubule attachment to kinetochores and chromosome alignment [111]. Polo-like Kinase 1

(PLK1) phosphorylates targets at the centrosomes, kinetochores, and kinetochore microtubules [113]. At the same time, the Chromosomal Passenger Protein Complex (CPC), composed of the proteins AurB, Survivin, Borealin, and the inner centromere protein (INCENP), localize to the spindle midzone to ensure the proper phosphorylation of substrates involved in condensation of chromosomes, correction of microtubule-kinetochore attachments, and the activation of the spindle assembly checkpoint [114-116]. As the enzymatic core of the CPC, activation of AurB is of extreme importance during mitosis [117, 118] and altered AurB activity can lead to improper chromosome segregation and cell division [119, 120].

In addition to phosphorylation, the post-translational modification of proteins with *O*-linked N-acetylglucosamine (*O*-GlcNAc) regulates cell cycle progression [121, 122]. *O*-GlcNAc occurs on serine or threonine residues of nuclear and cytoplasmic proteins consisting of the addition of a single N-acetylglucosamine moiety [35]. *O*-GlcNAcylation regulates many cellular processes including cell growth and survival [35]. Aberrant *O*-GlcNAcylation underlies various pathologies such as type II diabetes, neurodegenerative diseases and cancer [35]. Two highly abundant enzymes add or remove *O*-GlcNAc in response to the cellular environment in a process called *O*-GlcNAc cycling. *O*-GlcNAc transferase (OGT) adds *O*-GlcNAc to proteins using the metabolite UDP-GlcNAc (Uridine Diphospho-*N*-acetylglucosamine) while *O*-GlcNAcase (OGA) is responsible for its removal [35].

Increased expression of OGT leads to mitotic defects and an increased incidence of aneuploidy [121]. These results are partially due to alterations in mitotic signaling cascades [123]. CDK1 activity is severely reduced in cells with elevated OGT levels, due to an increase in the inhibitory phosphorylation of CDK1 mediated by alterations in the expression of upstream kinases and phosphatases [123]. Furthermore, OGT and OGA interact with AurB at the

midbody, and together, this signaling complex controls the post-translational state of midbody proteins [122]. OGT also associates with the mitotic spindle, and increased OGT expression hinders the actions of AurB by reducing phosphorylation of histones at the spindle [124]. These data demonstrate the vital role of *O*-GlcNAcylation in organizing events in mitosis.

Herein, we address the function of OGT and OGA in regulating the proper construction and activity of the mitotic spindle. We demonstrate that spindle size, shape and function are disrupted in OGT or OGA gain of function cells. The disruption of spindle architecture was mediated partially through impairment of spindle signaling pathways. CDK1 inhibitory phosphorylation was increased while AurB signaling was dramatically reduced at the spindle midzone as judged by histone H3 serine 10 phosphorylation. Importantly, OGT and OGA gain of function induced this phenotype; however, the OGA inhibitor Thiamet-G (TMG) in the gain of function cells was able to rescue the disrupted spindle phenotype correlated with an increase in histone phosphorylation. Together, these data suggest a novel mechanism in which the well-organized cycling of *O*-GlcNAc at the spindle regulates the proper formation and function of this mitotic apparatus.

B.2 Methods

B.2.1 Antibodies

All antibodies were used at a 1:1000 dilution for immunoblotting. pT288 AurA (1:200 for confocal staining, 3079), Survivin (2802), pS7 CENPA (2187), CENPA (2186), Histone H3 (9717), and pS10 histone H3 (1:500 for confocal staining, 9706) antibodies were all purchased from Cell Signaling Technologies. Hec1 (1:200 for confocal staining, ab3613), β-tubulin (1:1000 for confocal staining, ab6046), pT232 AurB (1:200 for confocal staining, ab61074), PLK1

(1:200 for confocal staining, ab17057), pT210 PLK1 (ab39068), pS10 histone H3 (1:5,000 for confocal staining, ab5176), INCENP (ab36453), Borealin (ab70910), CDC2 (ab18), pY15 CDC2 (ab47594), and AurA (ab13824) antibodies were purchased from Abcam. Actin (A2066), AurB (WHOOO9212M3), α-tubulin (1:1000 for confocal staining, T5168) and γ-tubulin (T6557) antibodies were purchased from Sigma. GFP was purchased from Santa Cruz (sc9996). Antibodies for OGT (AL-28, Al-35), OGA (341), and *O*-GlcNAc (110.6) were a gracious gift from the laboratory of Gerald Hart in the department of Biological Chemistry at the Johns Hopkins University School of Medicine.

B.2.2 Cell Culture

HeLa cells were cultured in DMEM (Sigma) supplemented with 10% Fetal Bovine Serum (FBS, Gemini) and 1% penicillin/streptomycin (Invitrogen). Cells were synchronized into M phase using the double thymidine release method, which allows for approximately 85-90% of the cells synchronization into M phase [121, 122]. Adenoviruses were used as previously described [121, 125]. Briefly, infections were performed at first thymidine release with each virus at a multiplicity of infection (MOI) of 100. Cells were treated with 10 μM Thiamet-G (TMG, SD Specialty Chemicals) at the time of the second thymidine release. Synchronization of HeLa cells at metaphase was performed by double thymidine block with 2mM thymidine [121], followed by release and treatment with S-trityl-cysteine (Tocris Bioscience) 6 hrs post-release [126]. Metaphase-anaphase cells were then harvested by mitotic shake-off 14 hrs. post-thymidine release. Cells were approximately 95% mitotic. Synchronization of HeLa cells at prophase was accomplished by incubation in DMEM media containing nocodazole for 18 hrs followed by mitotic shake-off resulting in approximately 95% of the cells in prophase [122]. Infection occurred 24 hours prior to nocodazole (Sigma) introduction [122].

B.2.3 Immunofluorescence Microscopy

Cells cultured on microscope slides were washed with 1X PBS (Phosphate Buffered Saline, Sigma) and then fixed with 4% Paraformaldehyde (Sigma) for 20 min. The paraformaldehyde was replaced by 1X PBS and slides were stored at 4°C. Cells were then permeabilized with 0.1% Triton X-100 (Sigma) in cold PBS for 20 min. Slides were washed with 1X PBS and then blocked with a TBST blocking solution (0.2% azide, 0.2% powdered dry milk, 12% chicken serum, 1% Bovine Serum Albumin, 100 mM glycine, 0.1% Triton-X 100 in 500mL Tris buffer pH 7.5, all reagents from Sigma except dry milk) for 1 hour. Primary antibody in blocking buffer solution was applied overnight. Slides were washed with TBST and then incubated with fluorescent secondary antibodies (1:1000, rabbit Alexa-fluor 488 nm A11008, mouse Alexa-fluor 488 nm A21202, rabbit Alexa-fluor 568 nm A10042, and mouse Alexa-fluor 568 nm A11004 Invitrogen) for 1 hour. DAPI solution (PBS, 0.01% Triton-X 100, 0.001% DAPI, Sigma) was applied for 20 min and slides were then washed and mounted on cover slips using ProLong Gold Anti-fade (Invitrogen) [122].

B.2.4 Cell Lysis and Histone Extraction

Cells were lysed in NP-40 Lysis Buffer (20 mM Tris-HCl pH 7.4, 150 mM NaCl, 1 mM EDTA, 1 mM DTT, 40 mM GlcNAc, and 1% NP-40, all reagents from Sigma) on ice for 30 minutes with occasional vortexing. Cellular debris was pelleted and the supernatant removed. For histones, the lysed pellet was washed twice with high salt (500 mM NaCl, Sigma) NP-40 lysis buffer and then resuspended in 0.25M HCl and vortexed vigorously for 15 minutes. The sample was pelleted again and the histone-enriched supernatant was transferred into a new tube. The pellet was subjected to the HCl treatment a second time, and the second supernatant added to the

first. Eight volumes of acetone were added to the supernatants and samples were incubated at -20° overnight. The acetone-precipitated histones were pelleted and washed with 0.1M HCl in acetone and then washed twice more with acetone alone. Pellets were air-dried and dissolved in a small amount of sterile water [127].

B.2.5 Immunoblotting

All electrophoretic separations were performed with 4-15% gradient polyacrylamide gels (Criterion Gels, Bio-Rad). Cell lysates were mixed with protein solubility mix (100mM Tris pH 6.8, 10mM EDTA, 8% SDS, 50% sucrose, 5% Beta-mercaptoethanol, 0.08% Pyronin-Y, all reagents from Sigma) and separated on gels, followed by transfer to PVDF membrane (Immobilon, Millipore). All antibodies were used at a 1:1000 dilution for immunoblots [121]. Blots were developed using HRP-conjugated secondary (anti-rabbit HRP 170-6515 and anti-mouse HRP 170-6516 Bio-Rad, anti-IgM HRP A8786 and anti-IgY HRP A9046 Sigma) and chemiluminescent substrate (HyGlo E2400 Denville Scientific). Blots were stripped in 100 mM glycine (Sigma) pH 2.5 for 1 hour, washed, and then treated as before. All western blots were repeated a minimum of 3 times using different experimental samples. For densitometry, images were scanned and quantified using ImageJ software (NIH).

B.2.6 Spindle Measurements

Measurement of spindle length, width, and angle as well as centrosome distance and HEC distribution was performed using ImageJ software (NIH) from multiple experiments.

B.2.7 Statistical Analysis

Statistical significance of the western blot densitometry was assessed via pairwise comparison with Bonferroni's correction.

B.3 Results

B.3.1 Gain of Function of OGT or OGA Disrupts Spindle Architecture

Since elevated expression of OGT or OGA induces mitotic exit defects and aneuploidy [121-123], we hypothesized that *O*-GlcNAc cycling is important for the formation of the mitotic spindle. We synchronized at M phase OGT/OGA gain of function HeLa cells or control cells expressing GFP. OGT gain of function cells showed an increase in total levels of *O*-GlcNAc, while OGA cells lowered *O*-GlcNAc levels (**Figure B.1A**). Synchronized cells were judged mitotic by the expression of Cyclin B with actin as a loading control. Next, we assessed how OGT/OGA gain of function affected spindle chromosome condensation. Spindles from each condition were measured over the course of 3 separate experiments. Both OGT and OGA gain of function caused an increase in chromosome condensation area (**Figure B.1B**). Condensed chromosome area was significantly larger in cells expressing both OGT and OGA while OGA inhibitor Thiamet-G (TMG) [128] (**Figure B.1A-B**) treatment significantly decreased chromosomal length, although width was larger than control (**Figure B.1C-D**). Not only did elevated OGT/OGA expression alter chromosome condensation but we also saw an increase in cells with multipolar spindles (**Figure B.1E**).

Next, we explored the positioning of the centrosome relative to the spindle midzone in cells expressing OGT or OGA. The distance between each centrosome and the midzone was greater in cells with the OGT or OGA gain of function (**Figure B.1F**); however, the spindle angle between the spindle midzone and the two centrosomes was not altered in these cells (**Figure B.1G**) [129]. We then measured the organization of the kinetochore. HEC1 (*Highly expressed in Cancer*) is a component of the Ndc80/HEC1 complex required for kinetochore microtubule attachment to the kinetochore [130]. HEC1 staining at the kinetochore is tightly localized to the centromere where the sister chromatids are paired in normal cells (**Figure B.1H**);

however, in OGT and OGA gain of function cells the HEC1 staining is more diffuse and less localized to the spindle midzone. The average area of the HEC1 staining is increased in these cells, matching the overall increase in condensation width with OGT/OGA gain of function (**Figure B.1H**). HEC1 expression was lower in both OGT and OGA gain of function cells (**Figure B.1J**); although TMG had little effect on HEC1 localization (**Figure B.1I**), expression of HEC1 after TMG treatment was also lower (**Figure B.1J**).

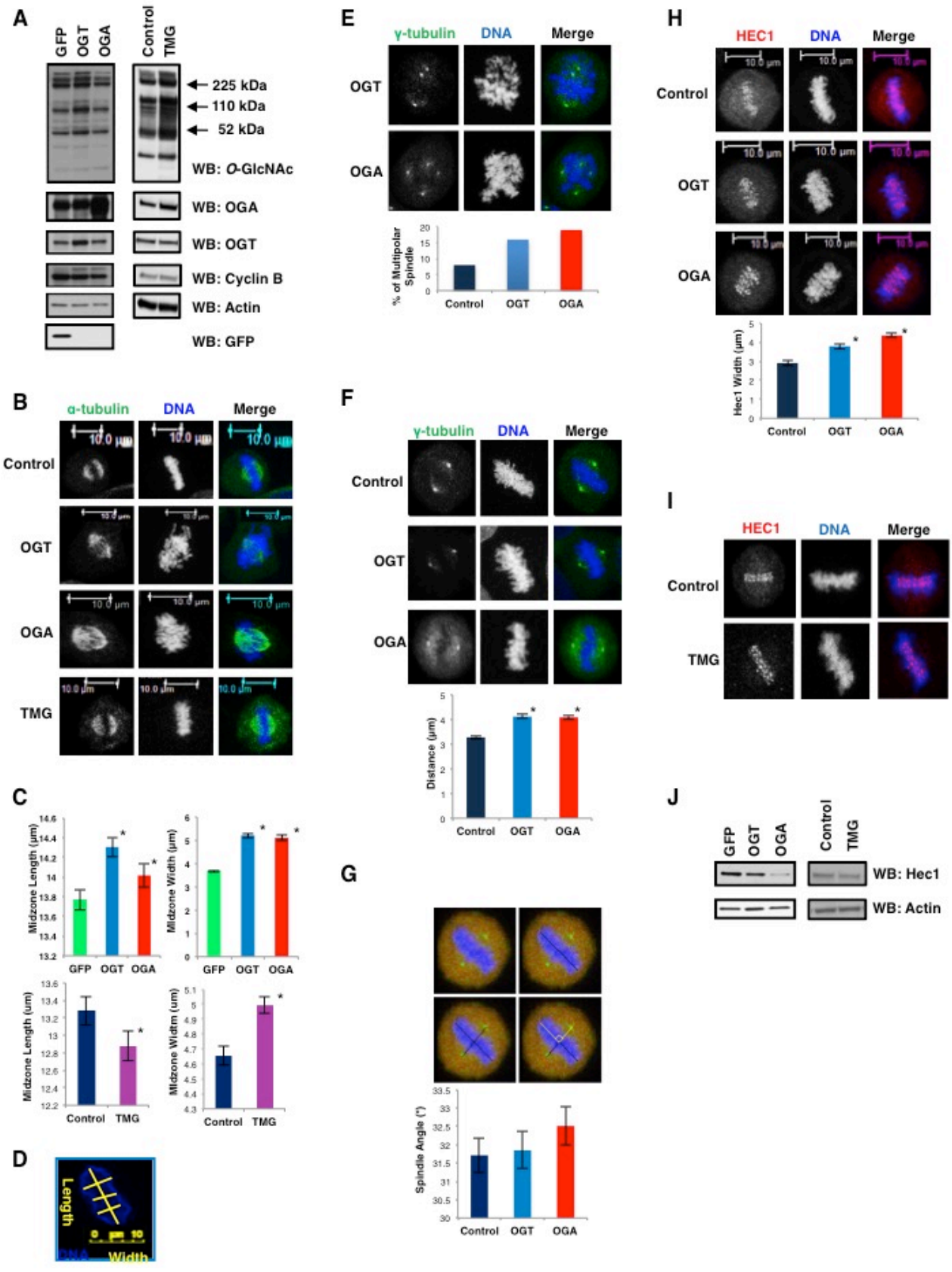
A
GFP
OGT
OGA
Control
TMG
225 kDa
110 kDa
52 kDa
WB: O-GlcNAc
WB: OGA
WB: OGT
WB: Cyclin B
WB: Actin
WB: GFP
B
α-tubulin
DNA
Merge
Control
OGT
OGA
TMG
C
Midzone Length (μm)
Midzone Width (μm)
Midzone Length (um)
Midzone Width (um)
GFP OGT OGA
Control TMG
D
Length
Width
DNA
E
γ-tubulin
DNA
Merge
OGT
OGA
% of Multipolar Spindle
Control OGT OGA
F
γ-tubulin
DNA
Merge
Control
OGT
OGA
Distance (μm)
Control OGT OGA
G
Spindle Angle (°)
Control OGT OGA
H
HEC1
DNA
Merge
Control
OGT
OGA
Hec1 Width (μm)
Control OGT OGA
I
HEC1
DNA
Merge
Control
TMG
J
GFP
OGT
OGA
Control
TMG
WB: Hec1
WB: Actin

Figure B. 1: OGT or OGA gain of function disrupts spindle architecture

(A) GFP, OGT or OGA gain of function or OGA inhibitor Thiamet-G treated HeLa cells were synchronized to M phase. Western blots were performed for O-GlcNAc, OGA, OGT, GFP, cyclin B, and actin. (B-D) DNA (blue) and α-tubulin (green) confocal imaging of M phase gain of function OGT/OGA cells, or cells treated with Thiamet-G. Midzone width and length (mean ± SEM, replicate number (n): nGFP = 195, nOGT = 193, nOGA = 198, nNT = 195, nTMG = 167, *P < 0.005 between GFP/NT vs. OGT/OGA or TMG) were quantified using ImageJ software as follows: first, the condensed chromatin area color was inverted in order to delineate the edge of the chromatin. Next, the chromatin was measured lengthwise and the width was measured 3 times from different sections and averaged. Yellow lines are a representative measurement. (E) Multipolar spindles were quantified from confocal images of DNA (blue) and γ-tubulin (green) M phase synchronized gain of function OGT/OGA cells. (F) DNA (blue) and γ-tubulin (green) were confocal imaged at M phase in OGT/OGA gain of function cells. Distance between each centrosome and the midzone was quantified (mean ± SEM, replicate number (n): nControl = 93, nOGT = 64, nOGA = 76, *P < 0.005 between Control vs. OGT/OGA). (G) Spindle angle measurement schematic in OGT/OGA gain of function cells. The perpendicular black lines originating from the centrosomes and the center of the spindle midzone were used to calculate spindle angle shown in yellow and plotted as a histogram. (H) DNA (blue) and HEC1 (red) were confocal imaged at M phase in OGT/OGA gain of function cells. Average width of HEC1 staining was quantified using ImageJ (mean ± SEM, replicate number (n): nControl = 21, nOGT = 47, nOGA = 50, *P < 0.005 between Control vs. OGT/OGA). (I) DNA (blue), α-tubulin (green), and HEC1 (red) were confocal imaged at M phase in TMG treated cells. (J) Western blot of HEC1 and actin in OGT/OGA gain of function and TMG treated cells.

B.3.2 OGA Gain of Function Reduces CPC Expression

The organization of the spindle is under the control of several mitotic kinases. CDK1 phosphorylates substrates during prophase, promoting nuclear envelope breakdown and activation of signaling networks regulated by the kinases PLK1, AurA, and AurB (**Figure B.2A**) [131, 132]. In turn, these kinases organize the mitotic spindle by phosphorylating substrates in specific regions of the spindle (**Figure B.2A**) [131, 133]. Increased OGT expression leads to increased inhibitory phosphorylation on CDK1 [123], suggesting that *O*-GlcNAcylation is important in the regulation of mitotic signaling events. We first measured whether OGT or OGA gain of function disrupts protein expression of AurA or PLK1. OGA gain of function lowered AurA and PLK1 levels while OGT had little effect (**Figure B.2B**). Previously, we reported that OGT gain of function lowers PLK1 expression slightly at M phase [123]; however, those cells were infected at the first thymidine block instead of the first release as in this study. The prolonged OGT over-expression likely promoted the decline in PLK1 expression. TMG treatment lowered PLK1 levels slightly (**Figure B.2B**). The distribution at the spindle of both AurA and PLK1 in OGT/OGA gain of function cells was no different than control (**Figure B.2C-D**). Next, we measured the expression of CPC proteins. OGA cells expressed lower protein levels of INCENP, survivin, and AurB (**Figure B.2E**). OGT cells produced little change while TMG treatment increased survivin protein expression (**Figure B.2E**). Localization of AurB, survivin and INCENP was no different than control; however, AurB staining was more diffuse in the OGA gain of function cells (**Figure B.2F-H**).

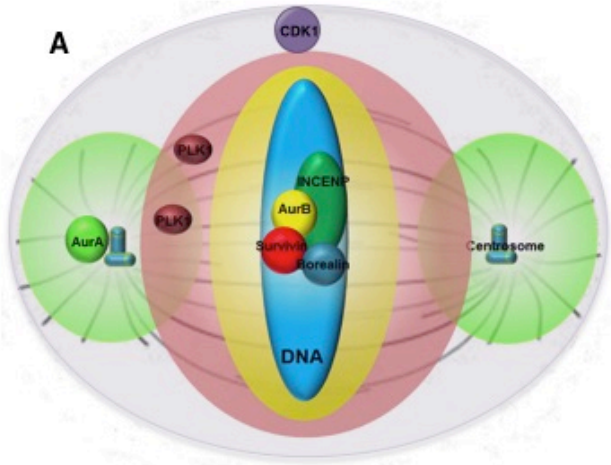
A
CDK1
PLK1
PLK1
INCENP
AurB
AurA
Survivin
Borealin
Centrosome
DNA

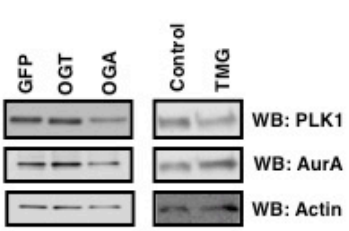
B
GFP
OGT
OGA
Control
TMG
WB: PLK1
WB: AurA
WB: Actin

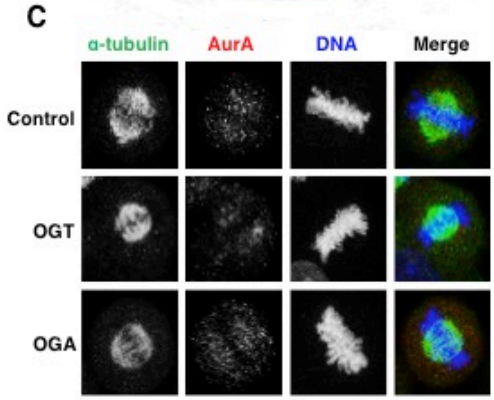
C
α-tubulin
AurA
DNA
Merge
Control
OGT
OGA

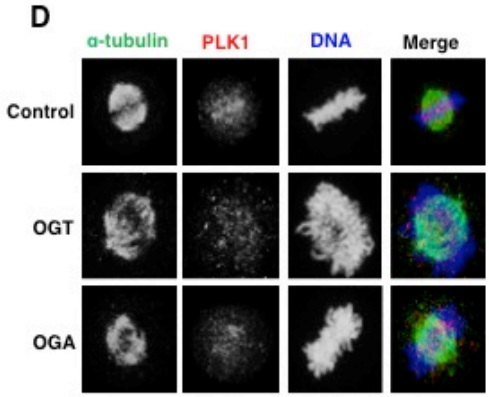
D
α-tubulin
PLK1
DNA
Merge
Control
OGT
OGA

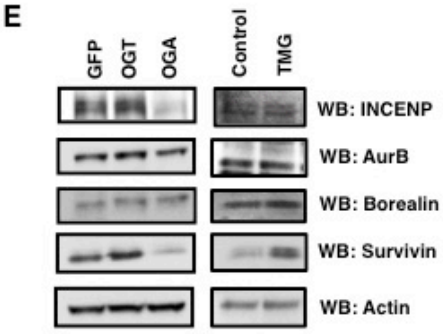
E
GFP
OGT
OGA
Control
TMG
WB: INCENP
WB: AurB
WB: Borealin
WB: Survivin
WB: Actin

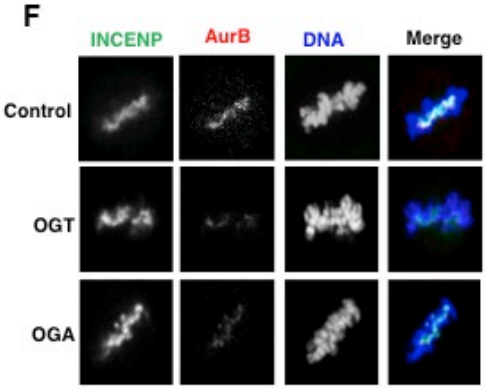
F
INCENP
AurB
DNA
Merge
Control
OGT
OGA

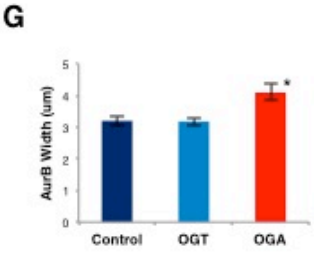
G
AurB Width (um)
0
1
2
3
4
5
Control
OGT
OGA
*

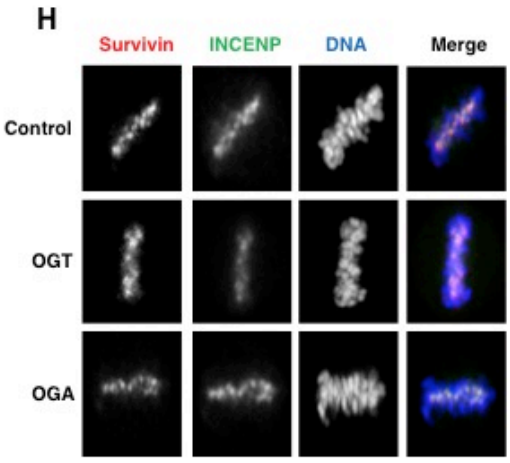
H
Survivin
INCENP
DNA
Merge
Control
OGT
OGA

Figure B. 2: Disrupted O-GlcNAc cycling alters spindle protein expression
(A) Spindle schematic of the locations and area of phosphorylation of mitotic kinases AurA, AurB, and PLK1. (B) M phase synchronized GFP/OGT/OGA gain of function or TMG treated cells were Western blotted for PLK1, AurA, and actin. (C) DNA (blue), α-tubulin (green), and AurA (red) were confocal imaged at M phase in OGT/OGA gain of function cells. (D) DNA (blue), α-tubulin (green), and PLK1 (red) were confocal imaged at M phase in OGT/OGA gain of function cells. (E) Western blot of CPC proteins AurB, INCENP, borealin, surviving, and actin as a load control (F) DNA (blue), INCENP (green), and AurB (red) were confocal imaged at M phase in OGT/OGA gain of function cells. (G) AurB width was quantified using ImageJ (mean ± SEM, replicate number (n): nControl = 45, nOGT = 35, nOGA = 43, *P < 0.005 between Control vs. OGA). (H) DNA (blue), INCENP (green), and survivin (red) were confocal imaged at M phase in OGT/OGA gain of function cells.

B.3.3 Phosphorylation of AurA, AurB, and PLK1 are Normal in the Gain of Function or TMG Treated Cells

Phosphorylation of AurA, PLK1, and AurB is required for full enzymatic activation; therefore, we measured whether OGT/OGA gain of function altered the activating phosphorylation on AurA, PLK1, and AurB. Activation of AurA occurs early in prophase and is mediated by AurA interactions with TPX2, Ajuba, and Bora [134-136]. This protein complex promotes AurA auto-phosphorylation at threonine 288 [137, 138]. In OGT/OGA gain of function cells, AurA phosphorylation was not significantly different from control cells (**Figure B.3A**). Since AurA is active in early prophase, we synchronized cells into prophase by nocodazole treatment. We saw a slight decline in AurA phosphorylation in these cells (**Figure B.3B**). We also measured phosphorylation in cells synchronized at the metaphase-anaphase transition after S-trityl-cysteine treatment. In these cells we saw no change in phosphorylation (**Figure B.3C**). Next, we measured the activating threonine 210 phosphorylation on PLK1 [139]. We observed no changes in PLK1 phosphorylation from M phase, prophase, or metaphase-anaphase synchronized OGT/OGA gain of function cells (**Figure B.3A-C**). These data agree with previous reports demonstrating no change in PLK1 phosphorylation in OGT gain of function cells. Finally, we looked at the AurB activating auto-phosphorylation on threonine 232 [140]. We saw no difference in AurB phosphorylation under different mitotic synchronization methods (**Figure B.3A-C**). OGA inhibition had no effect on the activating phosphorylation except for a slight but significant decline in phosphorylated PLK in prophase synchronized cells (**Figure B.3D-F**). We saw no disruption of localization at the spindle of phosphorylated AurA and PLK1 in OGT/OGA gain of function cells (**Figure B.3G-H**).

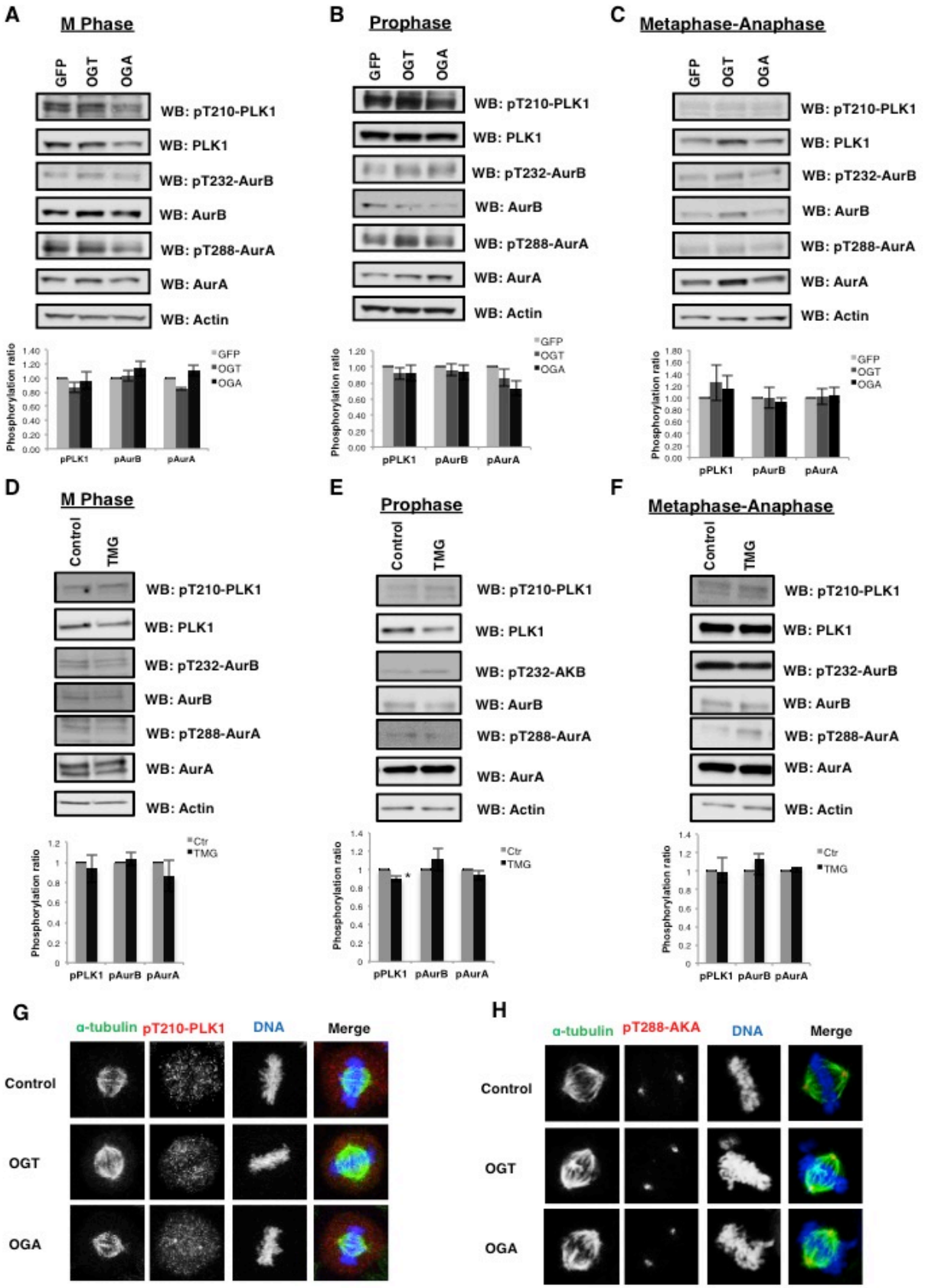
A
M Phase
GFP
OGT
OGA
WB: pT210-PLK1
WB: PLK1
WB: pT232-AurB
WB: AurB
WB: pT288-AurA
WB: AurA
WB: Actin
Phosphorylation ratio
pPLK1
pAurB
pAurA
B
Prophase
C
Metaphase-Anaphase
D
M Phase
Control
TMG
WB: pT232-AKB
Ctr
E
Prophase
F
Metaphase-Anaphase
G
α-tubulin
pT210-PLK1
DNA
Merge
Control
OGT
OGA
H
pT288-AKA

Figure B. 3: The effects OGT/OGA gain of function or TMG treatment on mitotic kinase phosphorylation

(A-C) GFP, OGT, or OGA gain of function cells were synchronized to (A) M phase, (B) prophase, (C) and metaphase-anaphase. Blots were probed for pT210-PLK1, PLK1, pT232-AurB, AurB, and pT288-AurA, AurA, and actin as a load control. (D-E) TMG treated cells were synchronized to (D) M phase, (E) prophase, (F) and metaphase-anaphase. Blots were probed for pT210-PLK1, PLK1, pT232-AurB, AurB, and pT288-AurA, AurA, and actin as a load control. Densitometry of kinase phosphorylation was firtst normalized to the kinases, then to the actin level. The densitometries were results from a minimum of 3 experiments, $*P < 0.005$ between GFP/NT vs. OGT/OGA or TMG. (G) DNA (blue), α-tubulin (green), and pT210-PLK1 (red) were confocal imaged at M phase in OGT/OGA gain of function cells. (H) DNA (blue), α-tubulin (green), and pT288-AurA (red) were confocal imaged at M phase in OGT/OGA gain of function cells.

B.3.4 CDK1 Inhibitory Phosphorylation is Altered in OGT/OGA Gain of Function Cells as Well as TMG Treated Cells

Previously, we reported an increase in the inhibitory phosphorylation of CDK1 in OGT gain of function cells [123]. Again, we synchronized cells either at M phase, prophase, or metaphase-anaphase and probed for CDK1 tyrosine 15 phosphorylation. Similar to previous reports, we continued to see a robust significant increase in tyrosine 15 phosphorylation in OGT gain of function cells; although, OGA gain of function cells did not have consistently elevated tyrosine 15 phosphorylation when only synchronized into M phase. This increase in CDK1 phosphorylation is consistently elevated in all prophase and metaphase-anaphase extracts (**Figure B.4A-C)**. TMG treated cells had higher levels of CDK1 phosphorylation in M phase synchronized cells, although the difference was not statistically significant (**Figure B.4D-F**); however, prophase synchronized cells had significantly lower CDK1 phosphorylation in the TMG treated samples, while metaphase-anaphase CDK1 phosphorylation was slightly lower compared to control. The difference in the TMG treated M phase extracts compared to the other synchronization methods is interesting and suggests that cells might be populating all the stages of M phases including telophase when CDK1 phosphorylation would be higher.

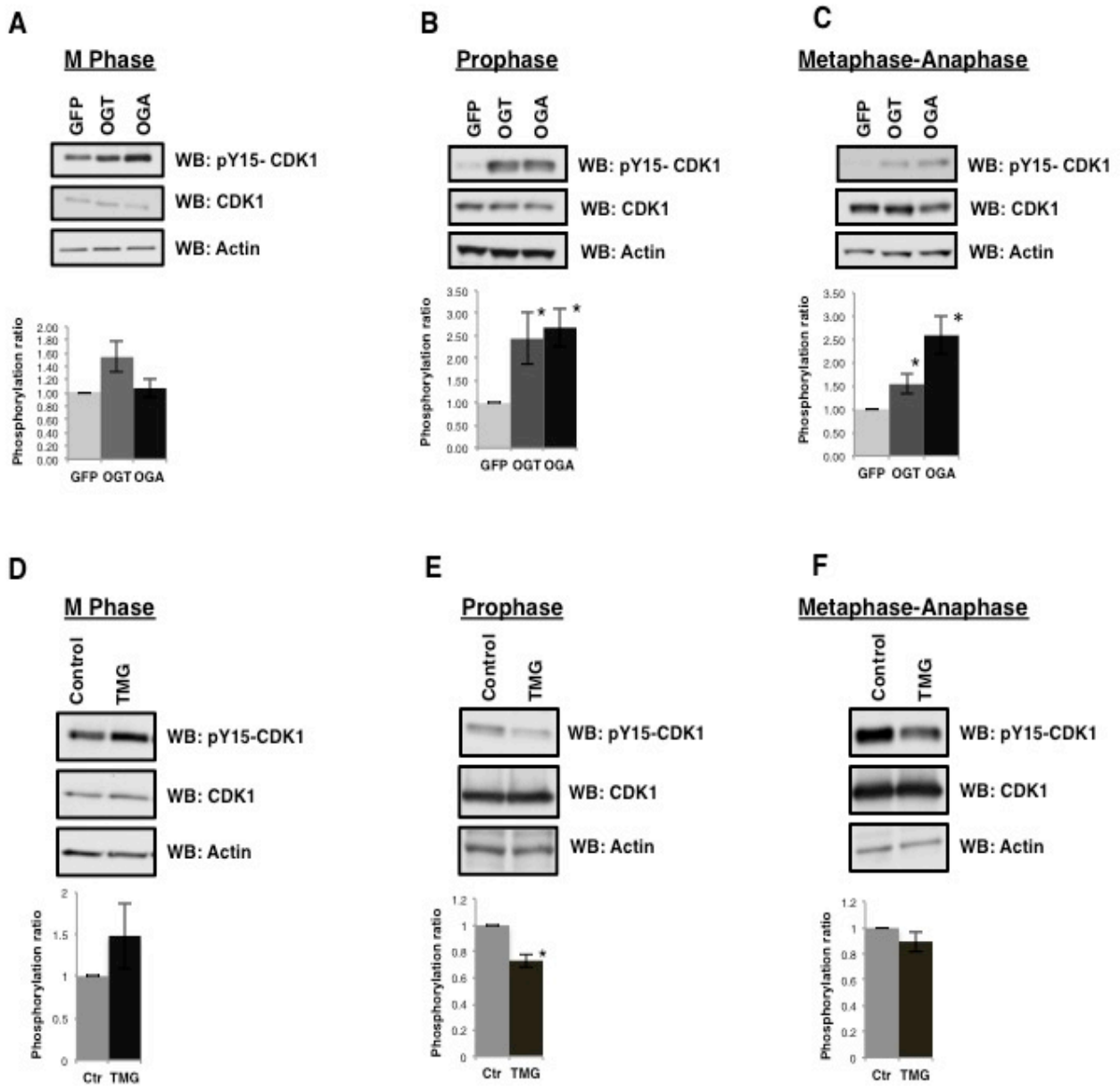

Figure B. 4: Altered O-GlcNAc cycling increases CDK1 inhibitory phosphorylation
(A-C) GFP, OGT, or OGA gain of function cells were synchronized to (D) M phase, (E) prophase, or (F) metaphase-anaphase. Western blots were probed for pY15-CDK1 and CDK1. (D-F) TMG treated cells were synchronized to (D) M phase, (E) prophase, or (F) metaphase-anaphase. Western blots from TMG treated M phase cells were probed for pY15-CDK1 and CDK1. Densitometry of CDK1 phosphorylation was normalized relative to the level of CDK1 and actin, then averaged from a minimum of 3 experiments, $*P < 0.005$ between GFP/NT vs. OGT/OGA or TMG.

B.3.5 OGT/OGA Gain of Function Cells Significantly Reduced Centromere Protein A Phosphorylation

We next looked to measure the activity of AurA and AurB toward spindle substrates in OGT/OGA gain of function cells. Centromere protein A (CENPA) is a histone variant that is phosphorylated at serine 7 by AurA in prophase, which in turn recruits INCENP and AurB to the spindle midzone where AurB phosphorylates CENPA serine 7 during late prophase and metaphase [111, 141]. CENPA serine 7 phosphorylation was depressed in mitotically synchronized OGT/OGA gain of function cells (**Figure 5A**). We synchronized cells in prophase where AurA is the predominate kinase toward CENPA serine 7 and again saw a slight loss of CENPA phosphorylation in the OGT gain of function cells. CENPA phosphorylation was not altered in OGA gain of function cells (**Figure 5B**). In order to ascertain the contribution of AurB toward CENPA phosphorylation, we measured phosphorylation in cells synchronized at the metaphase-anaphase transition. Serine 7 phosphorylation was significantly decreased in both OGT/OGA gain of function cells (**Figure 5C**). CENPA phosphorylation was not changed in cells treated with TMG (**Figure 5D-F**).

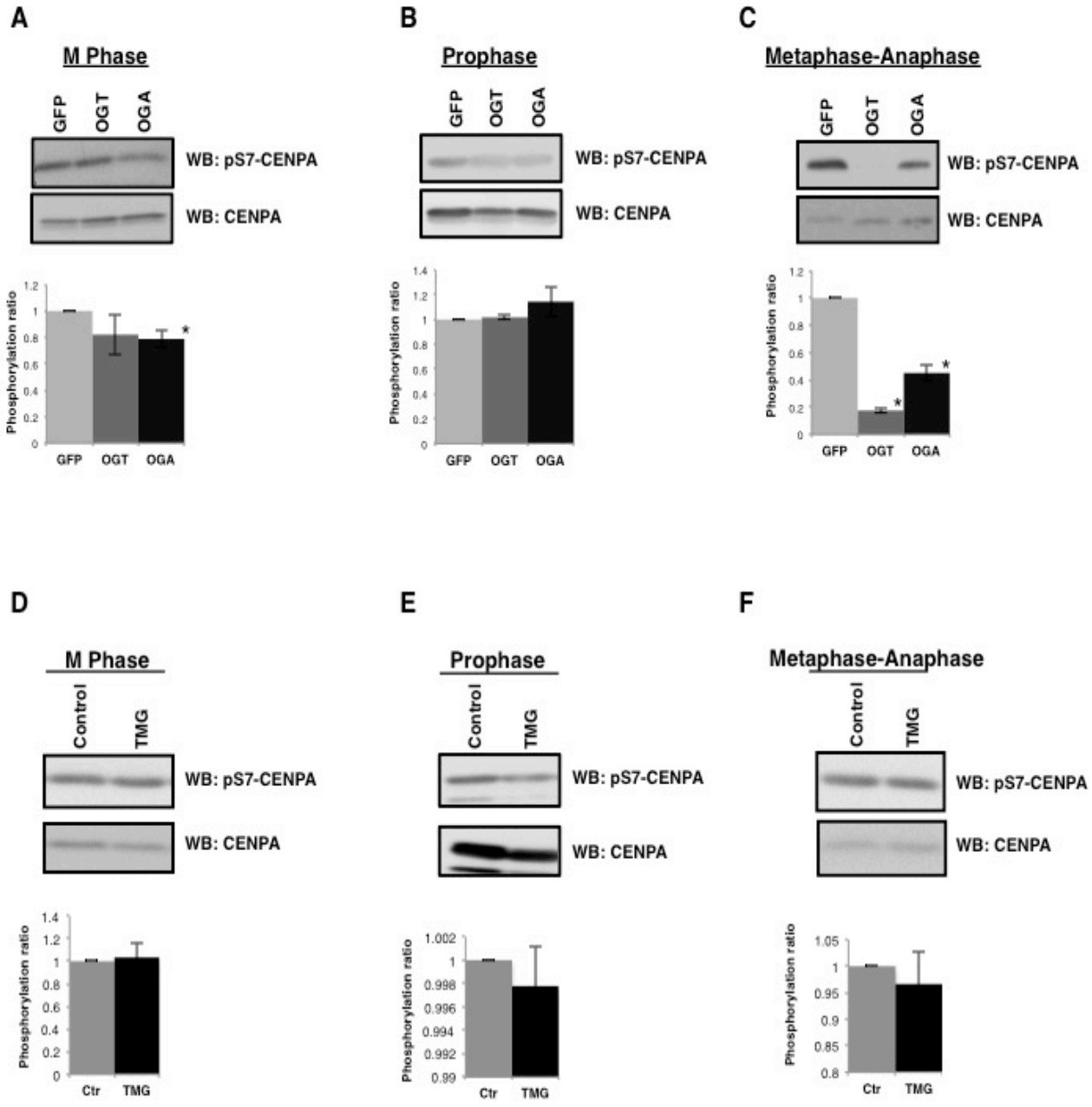

Figure B. 5: OGT or OGA gain of function disrupts AurB phosphorylation of CENPA
(A-C) GFP, OGT, or OGA gain of function cells were synchronized to (A) M phase, (B) prophase, (C) and metaphase-anaphase. Western blots were probed for pS7-CENPA and total CENPA. (D-F), TMG treated cells were synchronized to (D) M phase, (E) prophase, (F) and metaphase-anaphase. Western blots were probed for pS7- CENPA and total CENPA. Densitometry of pS7-CENPA was normalized relative to the level of CENPA and averaged from a minimum of 3 experiments, $*P < 0.005$ between GFP/NT vs. OGT/OGA or TMG.

B.3.5 Altered O-GlcNAc Cycling Disturbs Histone H3 Serine 10 Phosphorylation

We then measured the AurB mediated phosphorylation of serine 10 on histone H3, a marker for chromosome condensation [142, 143]. Histone H3 is modified by *O*-GlcNAc with the highest levels of H3 *O*-GlcNAcylation occurring during G_1 phase of the cell cycle [127, 144] while H3 *O*-GlcNAcylation appears lower in M phase [127, 145]. Others have reported an increase in *O*-GlcNAcylation at M phase [144]. We did not detect any appreciable levels of *O*-GlcNAc on mitotic histones (data not shown). Since H3 serine 10 phosphorylation (H3S10) is reduced in OGT gain of function cells [124], we acid extracted mitotic histones from both OGT and OGA gain of function cells. As previously reported [124], we saw a decrease in H3S10 phosphorylation in OGT gain of function cells at M phase (**Figure B.6A**). OGA gain of function cells had a significant decrease in H3S10 phosphorylation similar to the loss seen in OGT gain of function cells (**Figure B.6A**). In prophase synchronized cells, H3S10 phosphorylation was reduced, although not to the same extent as M phase synchronized cells (**Figure B.6B**). Metaphase-anaphase synchronized cells demonstrated a sharp reduction in H3S10 phosphorylation (**Figure B.6C**). When we visualized H3S10 phosphorylation at the spindle, we saw that staining was reduced at the condensed chromatin with some isolated areas being phosphorylated (**Figure B.6D**). TMG treated mitotically synchronized cells had slightly higher H3S10 phosphorylation (**Figure B.6E**). H3S10 and Aurora B phosphorylation at the condensed chromosomes was not altered in the TMG treated cells (**Figure B.6F**). Our results with TMG contradict earlier studies demonstrating that the OGA inhibitor PUGNAc reduced H3S10 phosphorylation [145]. We believe this is due to PUGNAc being a less selective OGA inhibitor than TMG that can produce pleotropic effects, likely leading to the discrepancy in the H3S10 phosphorylation [146].

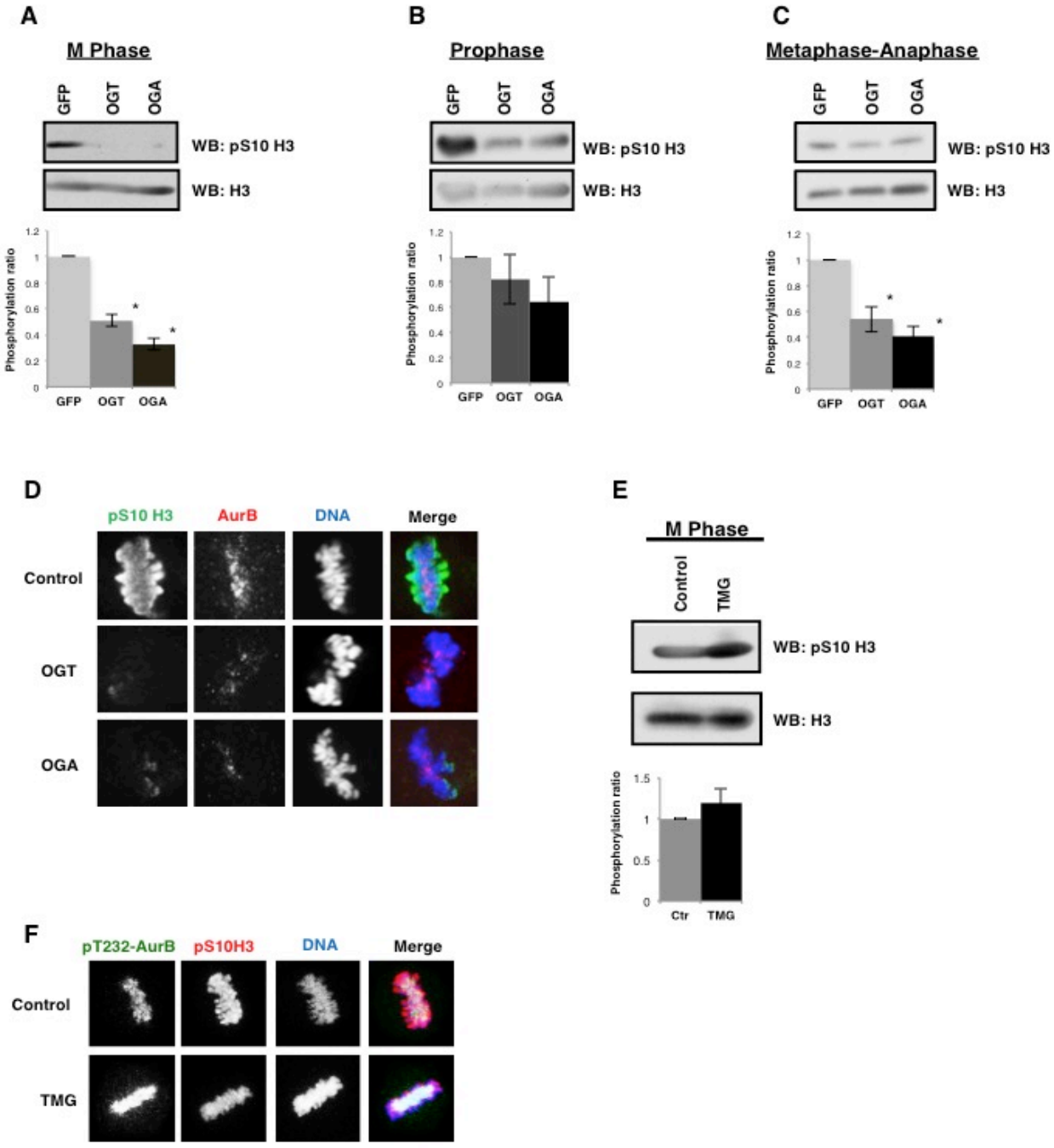

Figure B. 6: OGT or OGA gain of function lowers AurB phosphorylation of histone H3
(A-C) GFP, OGT, or OGA gain of function cells were synchronized to (A) M phase, (B) prophase, (C) and metaphase-anaphase. Western blots were probed for pS10 H3 and total H3. Western blots were probed for pS10-H3 and total H3. Densitometry of pS10-H3 was normalized relative to the level of H3 and averaged from a minimum of 3 experiments, $*P < 0.005$ between GFP vs. OGT/OGA. (D) DNA (blue), pS10-H3 (green), and AurB (red) were confocal imaged at M phase in OGT/OGA gain of function cells. (E) Control or TMG treated cells were synchronized to M phase and probed for pS10-H3 and total H3. Densitometry of pS10-H3 was

normalized relative to the level of H3 and averaged from a minimum of 3 experiments. (F) DNA (blue), pT232-AurB (green), and pS10-H3 (red) were confocal imaged at M phase after TMG treatment.

B.3.6 OGA Inhibition Rescues the Disrupted Spindle Phenotype

OGT and OGA gain of function consistently gave rise to disrupted spindle phenotypes. Contrary to OGT/OGA gain of function cells, TMG treated cells had smaller spindles and higher H3S10 phosphorylation. We investigated this apparent discrepancy in spindle size between chemical inhibition of *O*-GlcNAc removal and over-expression of the *O*-GlcNAc cycling enzymes. OGT/OGA gain of function or GFP control HeLa cells were synchronized into M phase via the double thymidine block method. We added TMG to these cells at the time of the G_1/S release. The cells were fixed, stained for tubulin and DNA 10 hours post second thymidine release, and chromosome condensation was measured. We measured spindles for each condition over the course of 3 separate experiments. Condensed chromosome area from gain of function OGT/OGA cells was considerably larger than GFP control cells (**Figure B.7A**). TMG treatment caused a significant reduction in condensation area in GFP control cells; surprisingly, TMG reversed the chromosome condensation errors in both the OGT/OGA gain of function cells (**Figure B.7A**). We then determined if TMG treatment combined with OGT/OGA gain of function changed the phosphorylation of AurA, AurB, PLK1, and CDK1. We saw little difference in the phosphorylation status of these kinases (**Figure B.7B**). Isolated histones from OGT/OGA gain of function cells had significantly lower H3S10 phosphorylation. Interestingly, treatment with TMG produced a trend of partially restored H3S10 phosphorylation that did not, however, achieve statistical significance (**Figure B.7C**).

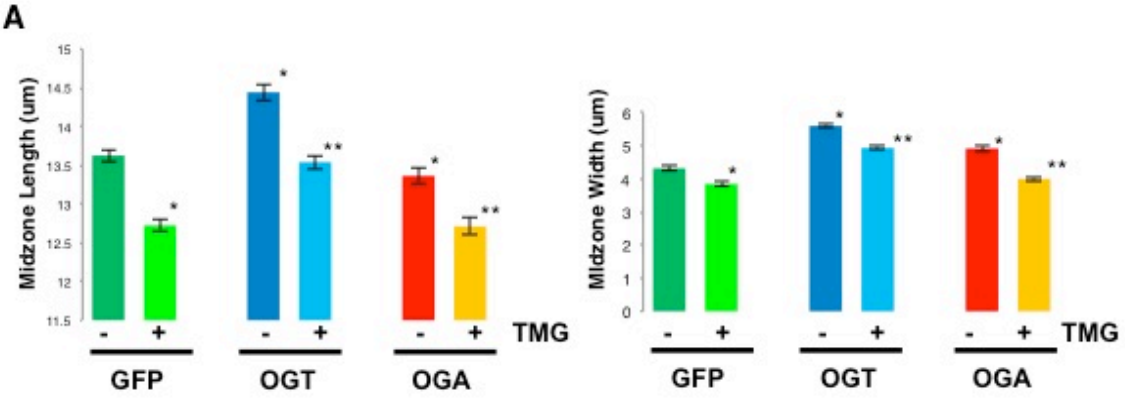
A
Midzone Length (um)
15
14.5
14
13.5
13
12.5
12
11.5
- + - + - + TMG
GFP OGT OGA
Midzone Width (um)
6
5
4
3
2
1
0
- + - + - + TMG
GFP OGT OGA

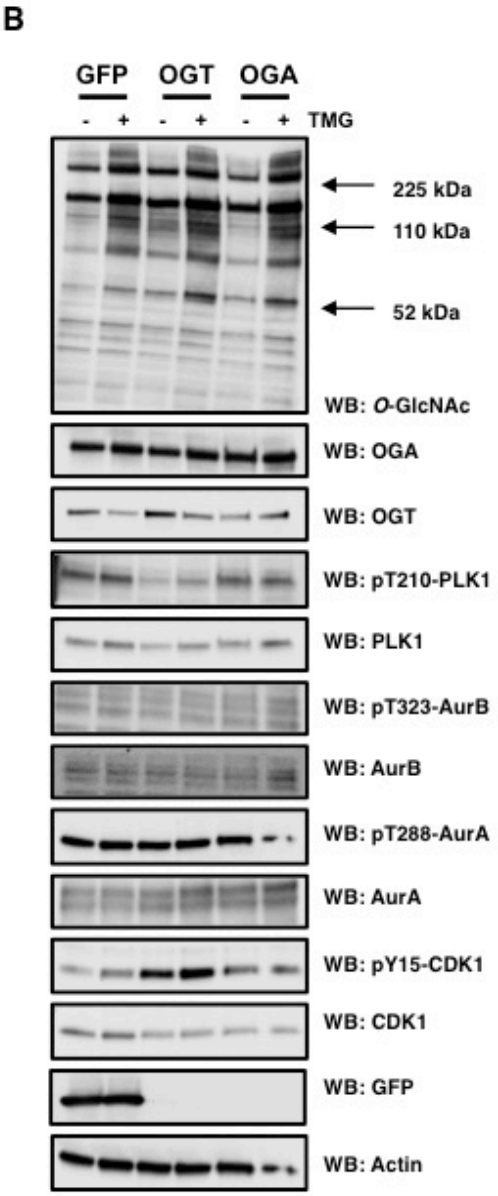
B
GFP OGT OGA
- + - + - + TMG
225 kDa
110 kDa
52 kDa
WB: O-GlcNAc
WB: OGA
WB: OGT
WB: pT210-PLK1
WB: PLK1
WB: pT323-AurB
WB: AurB
WB: pT288-AurA
WB: AurA
WB: pY15-CDK1
WB: CDK1
WB: GFP
WB: Actin

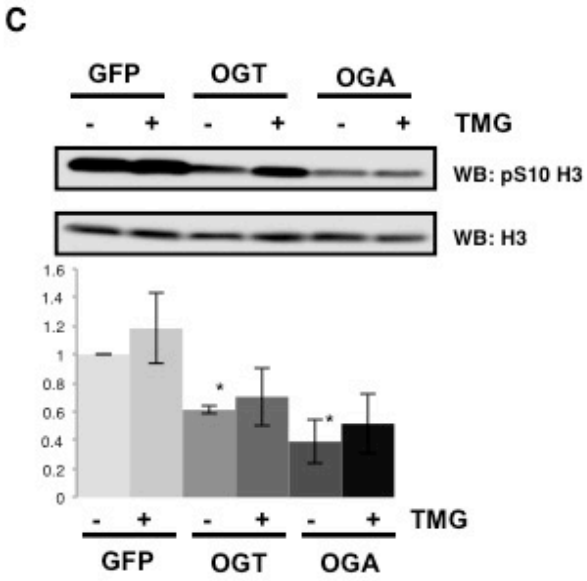
C
GFP OGT OGA
- + - + - + TMG
WB: pS10 H3
WB: H3
1.6
1.4
1.2
1
0.8
0.6
0.4
0.2
0
- + - + - + TMG
GFP OGT OGA

Figure B. 7: OGA inhibition rescued disrupted spindle phenotype in OGT/OGA gain of function cells

GFP, OGT, and OGA gain of function cells were synchronized to M phase and treated with TMG after second thymidine release. (A) Midzone width and length (mean ± SEM, replicate number (n): *nGFP* = 198, *nOGT* = 242, *nOGA* = 178, *nTMG/GFP* = 213, *nTMG/OGT* = 235, *nTMG/OGA* = 223, **P* < 0.005 GFP vs OGT/OGA, ***P* < 0.005 GFP/OGT/OGA vs TMG-GFP/TMG-OGT/TMG-OGA) were quantified using ImageJ software from confocal images stained for DNA and α-tubulin. (B). Western blots were probed for *O*-GlcNAc, OGT, OGA, pT210 PLK1, PLK1, pT323-AurB, AurB, pT288-AurA, AurA, pY15-CDK1, CDK1, GFP, and actin as a load control. (C) Western blots were probed for pS10 and total H3. Densitometry of H3 phosphorylation was normalized relative to the level of H3 and averaged from a minimum of 3 experiments, **P* < 0.005 between GFP vs. OGT/OGA.

B.4 Discussion

Disruptions in *O*-GlcNAc levels impair M phase progression, alter mitotic signaling cascades, change the distribution of chromatin marks, and promotes aneuploidy [121-124]. We show that either an OGT or OGA gain of function impairs the correct assembly of the mitotic spindle. Centrosome localization, kinetochore organization, and chromosome condensation are all disrupted, which in turn promotes an increase in multipolar spindles through impaired cytokinesis. The localization and phosphorylation of the mitotic kinases AurA, AurB, and PLK1 are not altered, but both CENPA and histone H3 phosphorylation are lower. Contrary to the phenotype of OGT/OGA gain of function cells, the OGA inhibitor TMG produced more condensed chromosomes, and rescued the disorganized spindle phenotype seen in OGT/OGA gain of function cells.

Previous work supports the fact that OGT and OGA gain of function cause a variety of spindle defects. OGT gain of function causes cytokinesis errors resulting in an increase in polyploidy; furthermore, this is accompanied by a large increase in chromosomal bridges, suggesting segregation defects [121, 124]. The effects of OGT/OGA gain of function on the spindle are likely through multiple mechanisms since many cellular processes control spindle size and shape, such as histone phosphorylation, tubulin polymerization, and condensin complex function [142, 143, 147]. OGA inhibitor TMG did reduce spindle length, although spindle width was wider than control cells. These data suggest that blocking the turnover of *O*-GlcNAc at the spindle with TMG induces structural changes to the spindle. Later when TMG was used in the gain of function cells, both DNA width and length were decreased in all samples, suggesting that blocking *O*-GlcNAc cycling will lead to a more condensed spindle phenotype. The alterations in *O*-GlcNAc cycling rate might be interfering with phosphorylation networks. For example, OGT

gain of function significantly alters the phosphorylation of at least one hundred mitotic proteins [123]. Disruption in *O*-GlcNAc cycling likely has some influence on the mitotic phosphorylation cascades that control spindle formation, such as CDK1 signaling.

Next, we explored the possibility that disrupted *O*-GlcNAc cycling was interfering with mitotic phosphorylation cascades. Our data point to an indirect relationship between the mitotic kinases AurA, AurB, and PLK1 with OGT/OGA. Alteration of *O*-GlcNAc cycling, either through gain of function or chemical inhibition, did not significantly alter the expression or phosphorylation of AurA, AurB, and PLK1. The expression of INCENP and survivin was lower in the OGA gain of function cells, but both still localized to the spindle. Importantly, only a substoichiometric amount of INCENP is needed to catalyze AurB autophosphorylation, suggesting that the amount of INCENP at the spindle in OGA gain of function cells is sufficient to activate AurB [140]. On the other hand, survivin protein levels were modestly higher when *O*-GlcNAc levels were elevated. The increased amount of survivin is due to either prolonged stability of the protein or a transcription/translation increase. Together, these data suggest that the CPC is still able to organize and promote AurB auto-phosphorylation as normal when *O*-GlcNAc cycling is disrupted. However, substrates of the CPC, such as serine 10 on histone H3, were not efficiently phosphorylated in OGT/OGA gain of function cells.

Increased OGT expression increases CDK1 inhibitory phosphorylations at threonine 14 and tyrosine 15 [123]. We demonstrate that OGA gain of function increases tyrosine 15 phosphorylation when synchronized to either prophase or metaphase-anaphase. Both OGT and OGA cause similar effects on CDK1 phosphorylation, suggesting that increased expression of OGT/OGA alters the rate of cycling, and this cycling rate is critical for the control of CDK1 phosphorylation. When we incubated cells with TMG, we saw a decrease at prophase, while in

mitotic and metaphase-anaphase extracts TMG appeared to have no effect. CDK1 phosphorylation is an exceedingly complex process. Multisite phosphorylation on CDK1 promote ultrasensitivity, the process in which increases in phosphorylation induce a threshold input, resulting in a switch like change in function [148]. The kinase-phosphatase system of Wee1 and Cdc25 control the phosphorylation of CDK1, but CDK1 activation leads to the downstream phosphorylation of these proteins and their inverse activation (Wee1 inhibition and Cdc25 activation), which in turn leads to the switch-like activation of CDK1 at M phase [148]. The Wee1-Cdc25 system can be restored by the actions of the phosphatase PP2A [149, 150]; however, at M phase CDK1 activity creates a feed-forward loop inactivating PP2A through phosphorylation [148]. *O*-GlcNAc cycling is likely affecting not only the Wee1-Cdc25 loop [123] but also the PP2A system. Cdc25 mRNA levels are lower in OGT gain of function cells and MYT1 kinase expression, which also controls CDK1 inhibitory phosphorylation, is elevated in these cells [123]. Additional control of the CDK1 switch by *O*-GlcNAc cycling would provide cells the ability to integrate changes in *O*-GlcNAc levels due to environmental signals into CDK1 activation and establish an even more sensitive control of CDK1 activation.

The effect the changes in *O*-GlcNAc cycling has on mitotic histone phosphorylation is likely not due to *O*-GlcNAcylation of histones. Indeed, histones are modified by *O*-GlcNAc and several sites have been mapped on H2A, H2B, and H4 [127, 151]. Histone H3 is also *O*-GlcNAc modified although the site has not been mapped by mass spectrometry [127, 145]. *O*-GlcNAcylation of histones is lower at M phase [127]. Zhang *et al.* argue through mutational studies that serine 10 is the site of *O*-GlcNAcylation, since a histone H3 mutant consisting of a serine 10 to alanine mutation was not efficiently modified by *O*-GlcNAc; however, this does not definitively argue for serine 10 being the *O*-GlcNAc site, but rather the serine to alanine

mutation impairs OGT activity toward histone H3 [144]. Our data does not support serine 10 being *O*-GlcNAcylated in mitotic cells. Should H3S10 be *O*-GlcNAcylated at M phase, we would anticipate increased H3S10 *O*-GlcNAcylation in OGT gain of function cells or after TMG treatment, but we could not measure H3S10 *O*-GlcNAcylation after elevation of *O*-GlcNAc levels. Furthermore, several groups detected less *O*-GlcNAc on H3 during M phase, suggesting that in mitotic cells serine 10 is not the main site of H3 *O*-GlcNAcylation [127, 145].

The reduction of H3S10 phosphorylation in OGT and OGA gain of function cells and the partial rescue of H3S10 phosphorylation by TMG suggest that we need to reexamine conceptually how *O*-GlcNAcylation regulates protein function. In many cases, the addition of the *O*-GlcNAc residue to a protein will have a direct effect on protein activity (**Figure B.8A**). For example, *O*-GlcNAcylation of calcium/calmodulin-dependent protein kinase IV blocks an activating phosphorylation site thereby reducing enzymatic activity [152], whereas *O*-GlcNAcylation of phosphofructokinase 1 blocks an allosteric regulation site and reduces enzymatic activity [153]. However, our data suggest a model in which *O*-GlcNAcylation can prime a protein for a potential physical interaction with other proteins, but full activation cannot be achieved until the *O*-GlcNAc is removed, which in turn leads to full activation of the protein complex (**Figure B.8B**).

Both OGT and OGA gain of functions cells have a similar disorganized spindle phenotype, while TMG treatment partially rescued this phenotype. Three possible mechanisms could explain these actions: the rate of *O*-GlcNAc removal is faster in gain of function cells leading to a disruption of protein-protein interactions facilitated by the *O*-GlcNAc modification; the over-expressed proteins are interacting with and disrupting other protein-protein interactions; or TMG is causing off-target effects. If mechanism two is correct, then TMG treatment in the

gain of function cells would not have any effect on the organization of the spindle, since *O*-GlcNAc levels are secondary to the increase in OGT/OGA protein expression; however, TMG restores spindle organization and H3S10 phosphorylation, arguing for mechanism one. TMG is a chemical inhibitor and could potentially have off-target effects that we can't completely rule out, but TMG has been demonstrated to be highly specific inhibitor of OGA and induces different cellular responses compared to previous generation OGA inhibitors like PUGNAc [128, 154].

Therefore, we propose a new model mechanism in which OGT *O*-GlcNAcylates proteins localized at the spindle midzone. As OGA is found in a complex with OGT [122, 155], OGA is therefore targeted to the spindle midzone by OGT. The *O*-GlcNAcylated spindle proteins facilitate the interaction of the CPC with spindle substrates [122]. Next, OGA removes the modification, and maximal activity of the CPC toward H3S10, occurs mediating a physiological response (**Figure B.8B**). Increased OGT or OGA expression would accelerate *O*-GlcNAc cycling and impair targeting of the CPC to substrates. TMG would elevate *O*-GlcNAcylation and promote the recruitment of the CPC toward spindle substrates like H3S10. TMG would also reduce OGA activity, providing enough time for the CPC to properly organize at the spindle midzone and phosphorylate H3S10. However, prolonged inhibition of OGA could be deleterious as well by stabilizing transient interactions or impairing the antagonizing actions of phosphatases or other proteins.

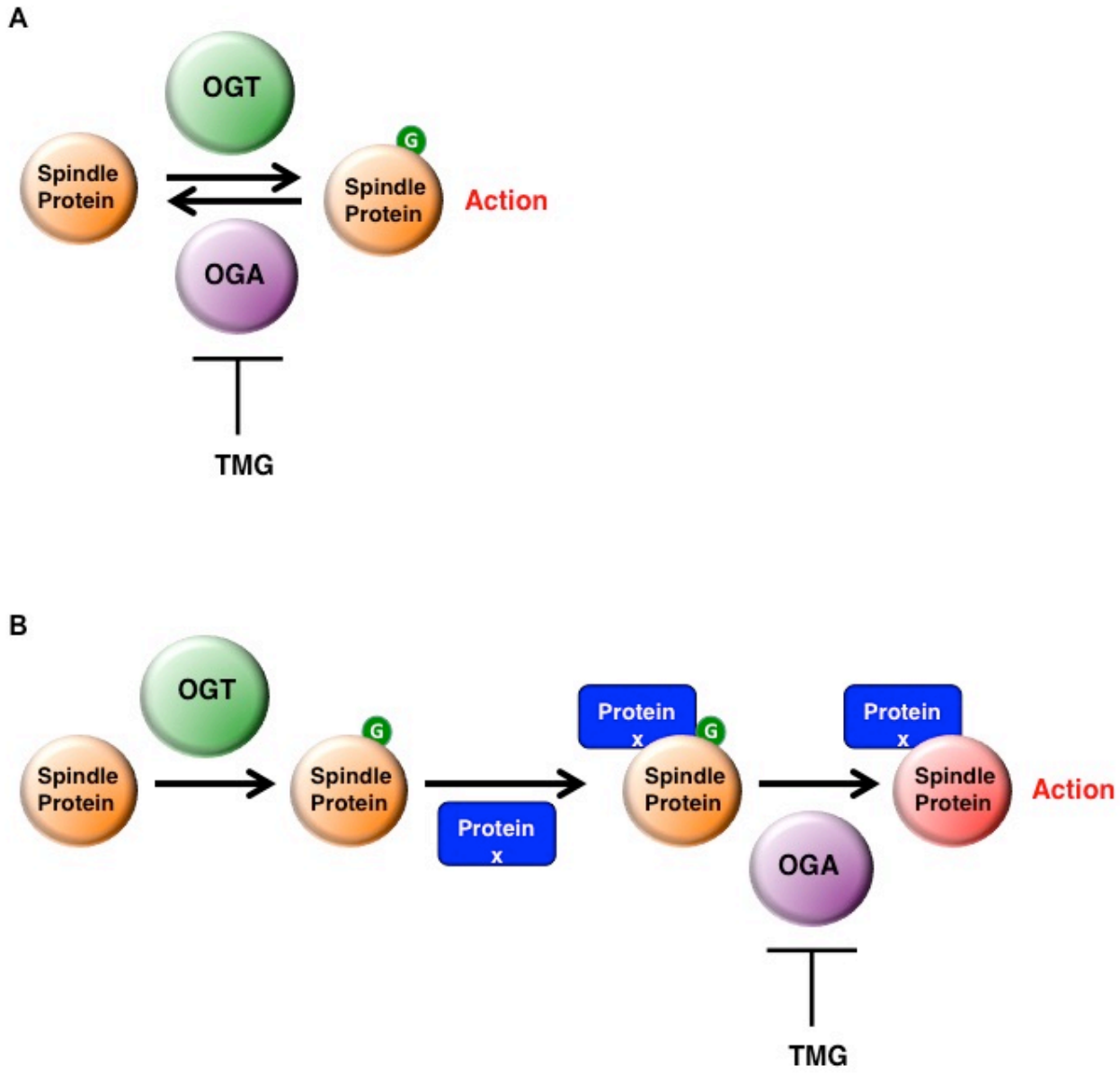

Figure B. 8: O-GlcNAc cycling regulates spindle function

(A) Schematic of O-GlcNAc cycling functioning as an on/off switch with addition of the O-GlcNAc residue (green) to a protein having direct effect on protein activity. (B) Schematic of O-GlcNAc cycling acting as a state machine in which the addition of the O-GlcNAc acts as a priming stage allowing for other spindle proteins (Protein X, blue) to interact with the O-GlcNAc modified spindle protein. Full activation is only achieved when O-GlcNAc is removed.

In conclusion the cycling of *O*-GlcNAc is a critical requirement for proper spindle organization. Alteration in the rate of *O*-GlcNAc cycling causes disorganized spindles, increases centrosome-spindle midzone distance, disrupts kinetochores, and causes an increase in multi-polar spindles. A potential contributing factor to the disorganized spindles is the reduction in AurB activity toward histone H3. OGA inhibition can reverse the phenotypes caused by an increase in *O*-GlcNAc cycling, and partially restore AurB activity toward H3. Our data suggest a novel mechanism by which *O*-GlcNAc cycling regulates the function of protein complexes. Furthermore, our data suggest a potentially new model of the role of *O*-GlcNAc cycling in regulating biological processes.

Appendix C: O-GlcNAc Cycling is Important in Regulating Mitotic Spindle Organization-*Part II*

Reproduced with permission from Zhang, Z., Tan, E.P., VadenHull, N.J., Peterson, K.R., and Slawson, C. (2016). ***Reduced O-GlcNAcase Expression Promotes Mitotic Errors and Spindle Defects.*** *Cell Cycle 15(10):1363-75.*

C.1 Introduction

O-GlcNAc is a single N-acetyl-glucosamine moiety linked via an oxygen residue to serine and threonine amino acids in nuclear, cytoplasmic, and mitochondrial proteins [35]. The modification is ubiquitously expressed in all metazoans and is essential for proper growth and development [156]. Two unique enzymes add or remove the modification on proteins. O-GlcNAc transferase (OGT) catalyzes the addition of N-acetyl-glucosamine to the hydroxyl group of serine and threonine residues while O-GlcNAcase catalyzes the removal of the modification [156]. O-GlcNAc cycling is the combined addition and removal of the modification. Dynamic cycling of O-GlcNAc is necessary for normal development, and cycling defects are implicated in metabolic syndromes, such as diabetes, cancer, and neurodegeneration [38, 40, 157-159]. Importantly, O-GlcNAc cycling defects have profound consequences for cell cycle progression [60].

Early studies in *Xenopus* oocytes demonstrated important roles for O-GlcNAc during progesterone mediated maturation. Microinjection of galactosyltransferase, an enzyme that caps terminal N-acetyl-glucosamine preventing OGA removal of the sugar moiety, induces maturation defects causing mitotic checkpoint activation and cell death [160]. Oocytes treated with the OGA inhibitor PUGNAc failed to mature properly [161], while microinjection of GlcNAc impaired maturation and spindle formation [162]. Additionally, inhibition of OGT

blocks the G_2/M transition during maturation [163], but microinjection of OGT promotes entry into M phase. Together, these data demonstrate that alteration to the rate of O-GlcNAc cycling affect the transition from G_2 to M phase in oocytes [164].

O-GlcNAc cycling plays an essential role in the regulation of both mitosis and meiosis. For example, HeLa cervical cancer cells over-expressing OGT or OGA have delayed exit from M phase and increased aneuploidy [121]. Interestingly, OGT localizes to both the mitotic and meiotic spindle, suggesting a critical role for O-GlcNAcylation at the spindle [121, 165, 166]. Numerous spindle and midbody associated proteins are modified by O-GlcNAc [123], suggesting that O-GlcNAcylation of spindle proteins is necessary for proper spindle development. The spindle seems especially sensitive to alterations in O-GlcNAc cycling. Over-expression of OGT/OGA leads to increased disorder of the spindle chromatids, while OGA inhibition with Thiamet-G (TMG) produces smaller more compact spindle chromatids [60]. Interestingly, TMG treatment can partially rescue the disordered spindle phenotype in both OGT and OGA over-expressing cells arguing that cells maintain a certain homeostatic level of O-GlcNAc cycling at the spindle. Disruptions in O-GlcNAc cycling likely have a pluripotent effect on spindle machinery. Increased O-GlcNAc cycling alters the phosphorylation of spindle proteins by mitotic kinases Aurora B and Polo Like Kinase 1 [122, 123]. Moreover, besides phosphorylation, impaired O-GlcNAc cycling disrupts other post-translational modifications on spindle proteins, such as methylation and acetylation [123, 124]. Together, these data demonstrate the essential role for O-GlcNAcylation in regulating cell cycle progression and spindle formation. Importantly, these data demonstrate that maintaining a homeostatic level of O-GlcNAc cycling at the spindle is crucial for organizing the spindle architecture, maintaining

the proper post-translational state of spindle proteins, and promoting proper segregation of the chromatids to the daughter cells.

Both OGT and OGA are essential genes, and a complete knockout of either gene would lead to senescence and cell death [167-169]; therefore, we generated OGA knockdowns cell lines with approximately 30% reduction in OGA activity. Now, we show that OGA knockdown cells have mitotic progression defects, altered spindle chromatid packing, and an increase in multipolar spindles. Furthermore, OGA knockdown cells displayed altered inhibitory phosphorylation on CDK1 (Y-15), which is required for inactivation of the Cyclin B/CDK1 complex [148]. Reduced OGA expression increased O-GlcNAcylation of EWS (Ewing Sarcoma Breakpoint Region 1 Protein), mislocalization of EWS at the spindle, and misalignment of the spindle midzone. These data demonstrate the importance of OGA for the proper progression and fidelity of mitosis, and suggest that O-GlcNAc cycling is an essential process regulating mammalian mitosis.

C.2 Methods

C.2.1 Antibodies

Antibodies for immunoblotting: OGT (AL-34, rabbit) and OGA (345, chicken) antibodies were gracious gifts from the Laboratory of Gerald Hart in the Department of Biological Chemistry at the Johns Hopkins University School of Medicine. O-linked N-acetylglucosamine antibody [RL2] (ab2739), β-tubulin (ab6046), NuMA (ab36999), pY15-CDK1 (ab47594), CDK1 (ab18), INCENP (ab12183), Shugoshin (ab58023), Aurora B (ab2254), pS10-Histone H3 (ab5176), and pT3-Histone H3 (ab78351) were purchased from Abcam. Survivin (2802), Histone H3 (5192), and pAurora A (Thr288)/ pAurora B (Thr232) /pAurora C (Thr198) (D13A11) antibodies were purchased from Cell Signaling. Actin (A2066), pRB (SAB400109), RB (Ab-780), α-tubulin

(T5168), Cyclin A (C4710), Cyclin B (C8831), Cyclin D (SAB4502602), and EWS (E4533) antibodies were purchased from Sigma. EWS (sc28327) antibody for western blotting was purchased from Santa Cruz. Goat anti-rabbit IgG HRP (170-6515) and goat anti-mouse IgG HRP (170-6516) were purchased from Bio-Rad.

C.2.2 Cell Culture and Generation of OGA Stable Knockdown Cells

HeLa cells were cultured in DMEM (D5796, Sigma) supplemented with 10% heat-inactivated fetal bovine serum (FBS, 100-106, Gemini) and 1% Penicillin-Streptomycin (P4333, Sigma) and incubated at 37 °C, 5% CO_2 in a 95% humidified incubator. Cell synchronization was performed as described previously [60].

Stable OGA knockdown cells lines were generated via electroporation. Briefly, two TRC lentiviral human OGA shRNA constructs 040 and 877 (RHS3979, Clone TRCN0000134040 and TRCN0000135877, Open Biosystem) and TRC lentiviral eGFP shRNA (RHS4459, Open Biosystem) were electroporated into HeLa cells by Ingenio Electroporation Solution (MIR 50114, Mirus) respectively according to manufacturer's instruction. HeLa cells were placed at 1 x 10^6 cells/ml in 100 mm dish and incubated overnight. Next day, cells were trypsinized and resuspended in Ingenio Electroporation Solution at 3 x 10^6 cells/ml. 250 µl of cell suspension was mixed with 5 µg of shRNA plasmid in a 0.4 cm electroporation cuvette (EC4, Midsci), and subjected to electroporation at voltage of 260 V and capacitance of 950 µF using exponential decay electroporator Gene Pulser Xcell Total System (1652660, Biorad). The cell mixture was immediately transferred to 2.5 ml of pre-warmed complete medium in a 6-well-plate and incubated for 48 hr. After 48 hr, puromycin (P8833, Sigma) was added to the medium at 1 mg/ml and continuously thereafter to generate the stable knock down cell lines.

C.2.3 Immunoprecipitation

Control or OGA knockdown HeLa cells were lysed on ice for 20 min in Nonidet P-40 (NP-40) Lysis Buffer (20 mM Tris-HCl, pH 7.4, 150 mM NaCl, 1 mM EDTA, 1 mM DTT, 40 mM GlcNAc, and 1% Nonidet P-40) supplemented with 1 mM PMSF, 1 mM sodium fluoride, 1 mM β-glycerophosphate, and 1X protease inhibitor cocktail I (leupeptin 1 mg/ml, antipain 1 mg/ml, benzamidine 10 mg/ml and 0.1% aprotinin). For immune precipitations, 0.5 mg of cell lysates were incubated with 0.5 μg of antibody in 1 ml reaction volume overnight while rotating at 4°C. Next, approximately 20 μl Protein G Sepharose 4 Fast Flow (17-0618-01, GE) slurry was added into each reaction, followed by end-to-end rotating at 4°C for 2 hr. Beads were washed 3 x 1 ml NP-40 Lysis Buffer supplemented with NaCl to a final concentration of 0.5 M. Washed beads were mixed with 20 μL 2X protein solubility mixture (50 mM Tris-HCl, pH 6.8, 5 mM EDTA, 4% SDS, 25% sucrose, 2.5% β-mercaptoethanol, 0.04% Pyronin-Y). Cell lysates were also mixed with 4X protein solubility mixture as input. The beads and input were heated at 95 °C for 2 min and subjected to immune blotting [60].

C.2.5 Immune Blotting

SDS-PAGE was performed with 4-15% gradient Criterion TGX Precast Gels (567-1084, Bio-Rad) and separated at 140 volts, followed by transfer to PVDF membrane (Immobilon, Millipore) at 0.4 Amps. Membranes were blocked with 3% BSA in TBST (25 mM Tris-HCl pH 7.6, 150 mM NaCl, 0.05 % Tween-20) at room temperature for 10 min, then incubated with primary antibody (1:1000) overnight at 4 °C. Membranes were washed with TBST for 5 x 5 min and incubated with HRP- conjugated secondary for 1 hr at RT (1:10,000), then washed again with TBST and developed using chemiluminescent substrate (HyGlo E2400; Denville Scientific). Membranes were stripped in 200 mM glycine, pH 2.5 at RT for 1 hr prior to

incubation with other primary antibodies. All immunoblotting results were repeated a minimum of three independent experiments.

C.2.6 Total RNA Isolation and RT-PCR

A minimum of 2 x 10^6 cells were resuspended in 1 mL TRI reagent solution (AM9738, Ambion) then incubated at room temperature for 5 min. Next, RNA was extracted using chloroform followed by a centrifugation. The upper phase containing RNA was collected and incubated with isopropanol. After centrifugation, precipitated RNA was washed once with 70% ethanol, air-dried and dissolved in nuclease free water.

1 µg of total RNA was mixed with iScript Reverse Transcription (RT) Supermix (170-8841, Bio-Rad). RNA was converted into cDNA using random primers according to the manufacturer's instructions. Briefly, samples were incubated in a thermal cycler (Model 2720, Applied Biosystems) using the following protocol: priming 5 min at 25 °C, RT 30 min at 42 °C, and RT inactivation 5 min at 85 °C. cDNA products were diluted with 100 µl of nuclease free water and analyzed by qPCR [68].

C.2.7 qPCR Assay

cDNA samples were analyzed by qPCR using SsoAdvanced Universal SYBR Green Supermix (172-5271, Bio-Rad) according to manufacturer's instruction. 2 µl of cDNA samples, SYBR Green Supermix, nuclease-free water, and primers for OGA were mixed for a total reaction volume of 20 µl. OGA primers were TTCACTGAAGGCTAATGGCTCCCG and ATGTCACAGGCTCCGACCAAGT. Next, the mixture was loaded into a 96-well PCR plate (AVRT-LP, MIDSCI) and loaded into a CFX96 Touch Real-Time PCR Detection System (185-5195, Bio-Rad). The qPCR protocol was the following: polymerase activation and DNA

denaturation 30 s at 95 °C, annealing/extension 5 s at 95 °C and 30 s at 60 °C, amplification with 40 cycles, and melt curve 65-95 °C with 0.5 °C increment 5 s/step **[68]**.

C.2.8 OGA Activity Assay

Whole cell lysates (60ug/reaction) were mixed with OGA reaction buffer for a total of 200 µl volume per reaction. O-GlcNAcase activity was assayed with 10 µl of 500 mM sodium cacodylate, pH 6.4, 3% bovine serum albumin, and 2 µl of 100 mM *p*-Nitrophenyl-*N-acetyl-β-D-glucosaminide* (*pNP-O-GlcNAc*, as substrate) at 37 °C for a total of two hours. The reactions were stopped with 100 µl of 500 mM sodium carbonate every 30 min and the absorbance at 400 nm was measured after all the reactions were stopped. Specific activity was calculated as described previously **[170]**.

C.2.9 Flow Cytometry

Double thymidine block synchronized HeLa cells were released and harvested at different time points (0 hr, 3 hr, 6 hr, 9 hr, and 12 hr) by trypsin digestion. Cells were washed in PBS, pelleted, and then resuspended in 1 ml of ice-cold PBS and followed by fixing with ice-cold 70% ethanol. Samples were stored at -20 °C until further use. Fixed cells were washed with ice-cold PBS and resuspended in PBS containing 0.1% (v/v) NP-40, 1 mg/ml RNase A, and 0.2% (w/v) propidium iodide **[121]**. Subsequently, cell cycle stages of cells were acquired by FACSDiva software using a BD LSRII at the University of Kansas Medical Center Flow Cytometry Core Laboratory. Data were analyzed using FlowJo.

C.2.10 Histone Purification

Histones were purified as described previously **[60]**. Briefly, cells were harvested and lysed, followed by acid extraction of the histones. After histones were quantified by Bradford assay, 5 µg of histone extract was separated by SDS-PAGE and probed for either histone phosphorylation or total histone H3.

C.2.11 Immunofluorescence Microscopy

Control or OGA KD cells were cultured on microscope slides and synchronized into G_1/S by double thymidine block. 9 hours after G_1/S release, cells were washed with 1X PBS fixation, followed by fixation with 4% paraformaldehyde (158127, Sigma) for 20 min. Cells were permeabilized with 0.1% Triton X-100 (T8787, Sigma) in PBS for 20 min and washed with 1X PBS prior to blocking with a TBST blocking solution (0.2% azide, 0.2% powdered dry milk, 12% chicken serum, 1% bovine serum albumin, 100 mM glycine, 0.1% Triton X-100 in Tris buffer pH 7.5, all reagents from Sigma except dry milk, Sun Fresh Supermarket) for 1 hr [60]. Slides were incubated with primary antibody (1:200 to 1:1000 depending on antibody) in blocking buffer overnight. Slides were 5 x 5 min washed with TBST and then incubated with fluorescent secondary antibodies (1:1000, rabbit Alexa-fluor 488 nm A11008, mouse Alexa-fluor 488 nm A21202, rabbit Alexa-fluor 568 nm A10042, or mouse Alexa-fluor 568 nm A11004 Invitrogen) for 1 hr. Slides were again washed 5 x 5 min in TBST. Slides were then places in a DAPI solution (PBS, 0.01% Triton X-100, 0.001% DAPI, Sigma) for 20 min followed by 2 washes with PBS. Slides were mounted on cover slips using ProLong Gold Anti-fade (P36930, Invitrogen) [171].

C.2.12 Image Analysis

Image analysis was performed as previously described using ImageJ software (NIH) [60].

C.2.13 Statistical Analysis

Statistical significance for the qPCR, OGA activity and spindle midzone width and length were assessed via SPSS-Statistics software by performing Paired-Samples T Test.

C.3 Results

C.3.1 Stable Knockdown of OGA Causes Cell Cycle Progression Defects

In order to understand the role of OGA activity on the cell cycle, we made stable OGA knockdown HeLa cells producing either GFP (control) or OGA (lines 040 and 877) knockdowns. The OGA knockdown (KD) cells 040 and 877 had approximately 30% reduction in the protein expression of OGA compared to control (**Figure C.1A**). Total cellular O-GlcNAc levels are not significantly affected by the reduction in OGA expression (**Figure C.1A**). Often a large expression change in OGT or OGA leads to concomitant change of the other O-GlcNAc cycling enzyme [68]. However, we do not see a significant reduction in OGT protein levels (**Figure C.1A**). Both 040 and 877 cells had reduced mRNA expression of the more common long form splice variant of OGA in these cells (**Figure C.1B**), while total OGA enzymatic activity was significantly reduced in these cells compared to control (**Figure C.1C**).

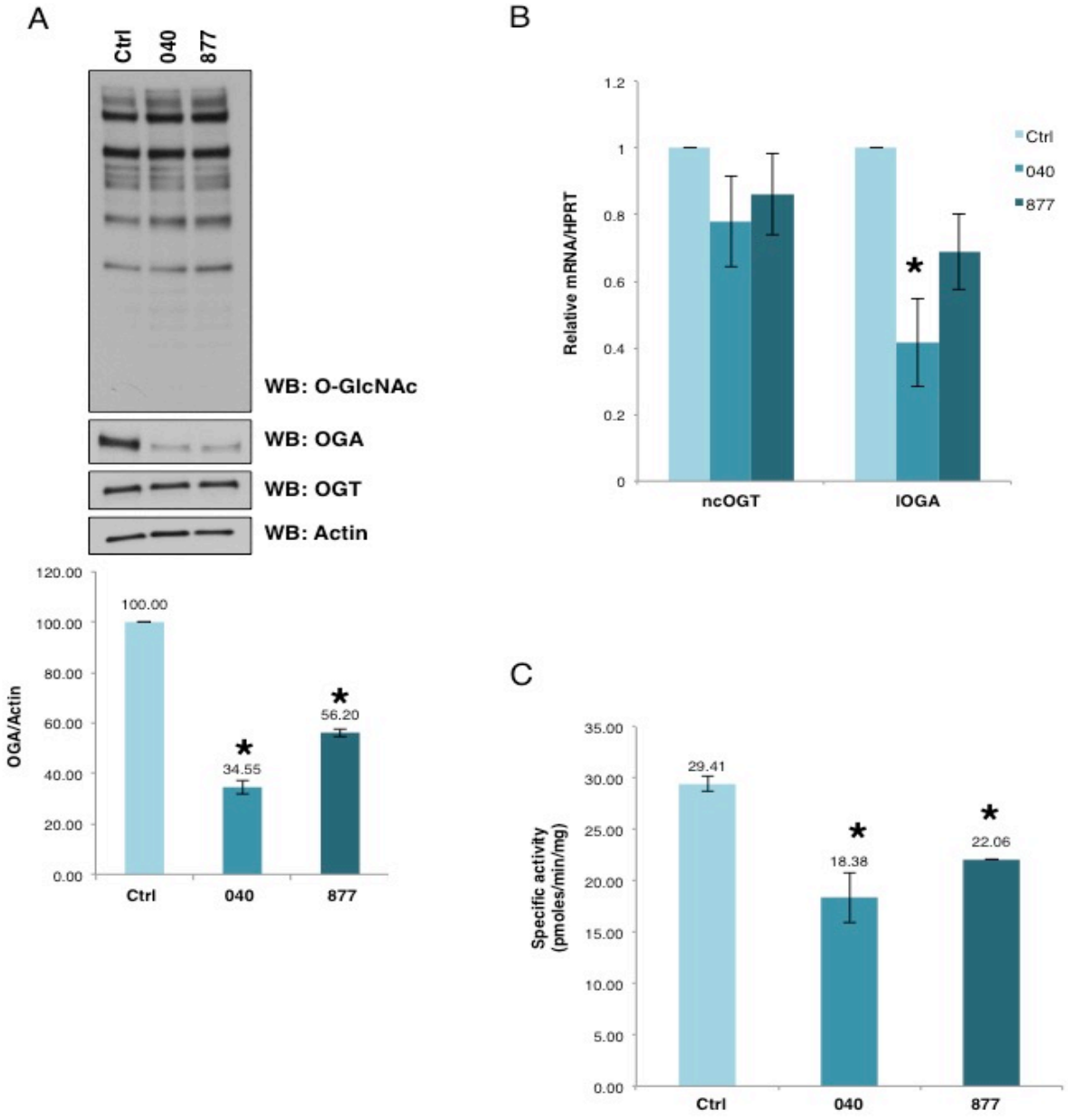

Figure C. 1: OGA expression is reduced in cell lines 040 and 877

(A) Stable shRNA mediated OGA knockdown HeLa cells lines were established with a significant decrease in OGA protein expression as judged by western blot. OGT protein expression was not significantly changed while total O-GlcNAc levels did increased slightly. (B), OGA mRNA is lower in both the 040 and 877 knockdown lines. (C) OGA enzymatic activity was significantly decreased in the stable OGA KD lines compared to the control cells. All experiments were performed with at least 3 biological replicates (* indicates $P < 0.05$, Student *t*-test).

Next, HeLa cells were synchronized in G_1/S phase [121] and then released into S phase, in which we then harvested time points every three hours up to 12 hours. Both the OGA 040 and 877 lines had increased O-GlcNAcylation and reduced OGA expression compared to control as judged by western blotting (**Figure C.2A**). Released cells were also harvested for cell cycle stage analysis by flow cytometry. Control and both OGA 040 and 877 cells moved through S phase at the same rate as control; however, both 040 and 877 cells displayed higher incidence of delayed M phase progression compared to the control cells (**Figure C.2B**). These OGA KD cells had prolonged M phase escape, corroborating previous finding demonstrating that over-expression of OGT or OGA also cause mitotic exit defects [121].

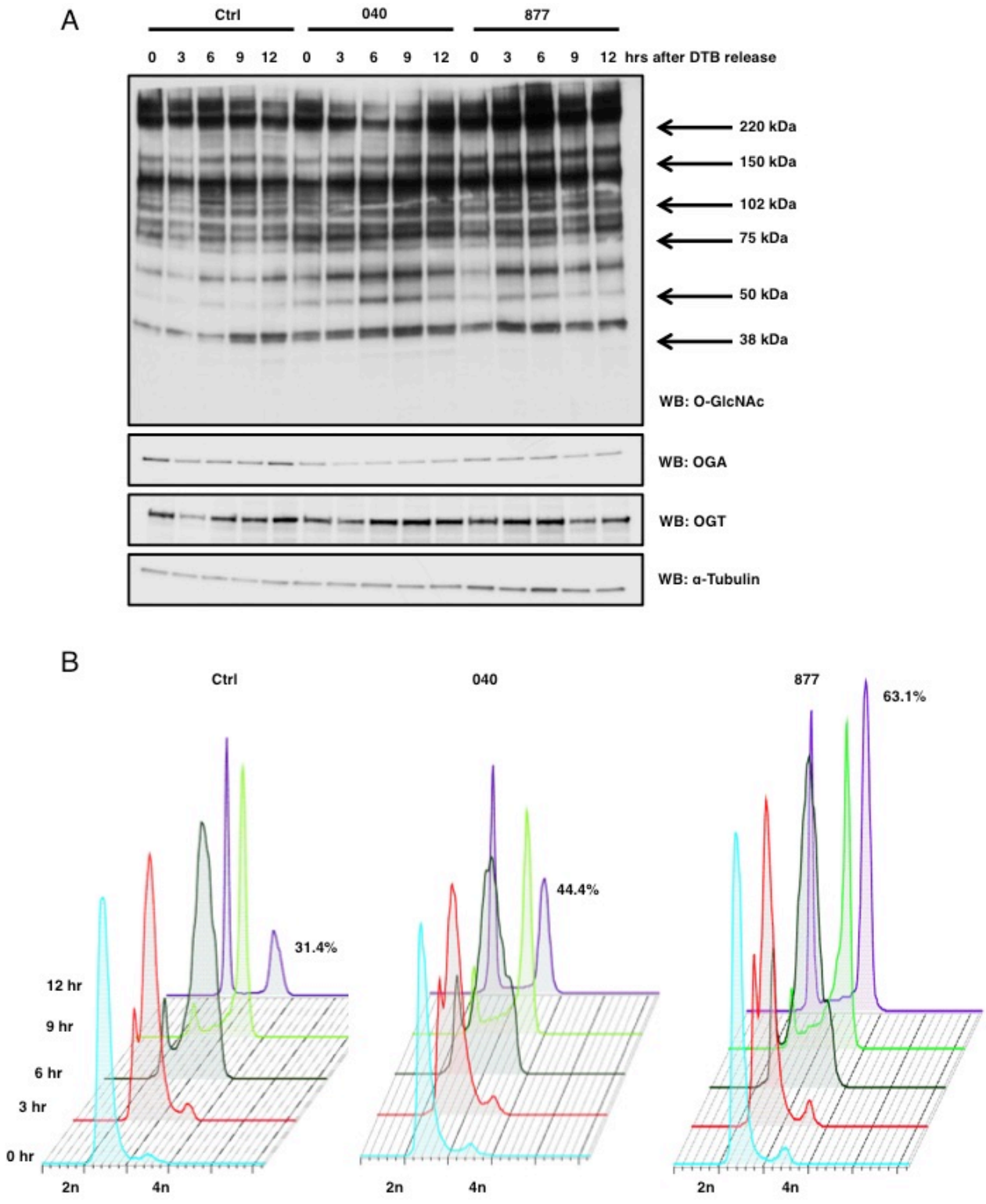

Figure C. 2: OGA KD cell lines show mitotic exit defects

(A) HeLa OGA KD and control cells were synchronized into G_1/S by double thymidine block and released. Time points were harvested every 3 hours post-release, and western blots for total O-GlcNAc, OGT, and OGA were performed while α-tubulin was used as a load control. (B) Control and OGA KD cells were again synchronized by double thymidine block and released into S phase. Cells were fixed every 3 hours, and DNA content was measured by flow cytometry. 12 hours post-release 44% of OGA 040 cells and 63% of OGA 877 cells were still in mitosis compared to 31% of cells in the control sample. All experiments were performed with at least 3 biological replicates.

Subsequently, we again released cells from G_1/S phase and probed time points for the expression of cyclins and phosphorylation of G_1/S phase checkpoint protein RB. Cyclin A had prolonged expression patterns in the OGA KD cells suggesting defects in G_2/M progression, while cyclin D expression was lower in the OGA KD cells, suggesting fewer cells progressing though G_1 phase (**Figure C.3A**). Cyclin B expression was initially higher in the two knockdown cells, but then decreased below control levels only to increase again at the 12 hour release point. Likely, cyclin B protein levels are altered due to the defects in mitotic progression. These results confirm that the OGA KD cells are progressing slower through M phase. The phosphorylation of G_1/S checkpoint point protein RB was also higher in these cells compared to control (**Figure C.3B**) demonstrating a higher percentage of OGA knockdown cells in S or M phase. These findings are consistent with previous data obtained from over-expressed OGT and OGA cells [121].

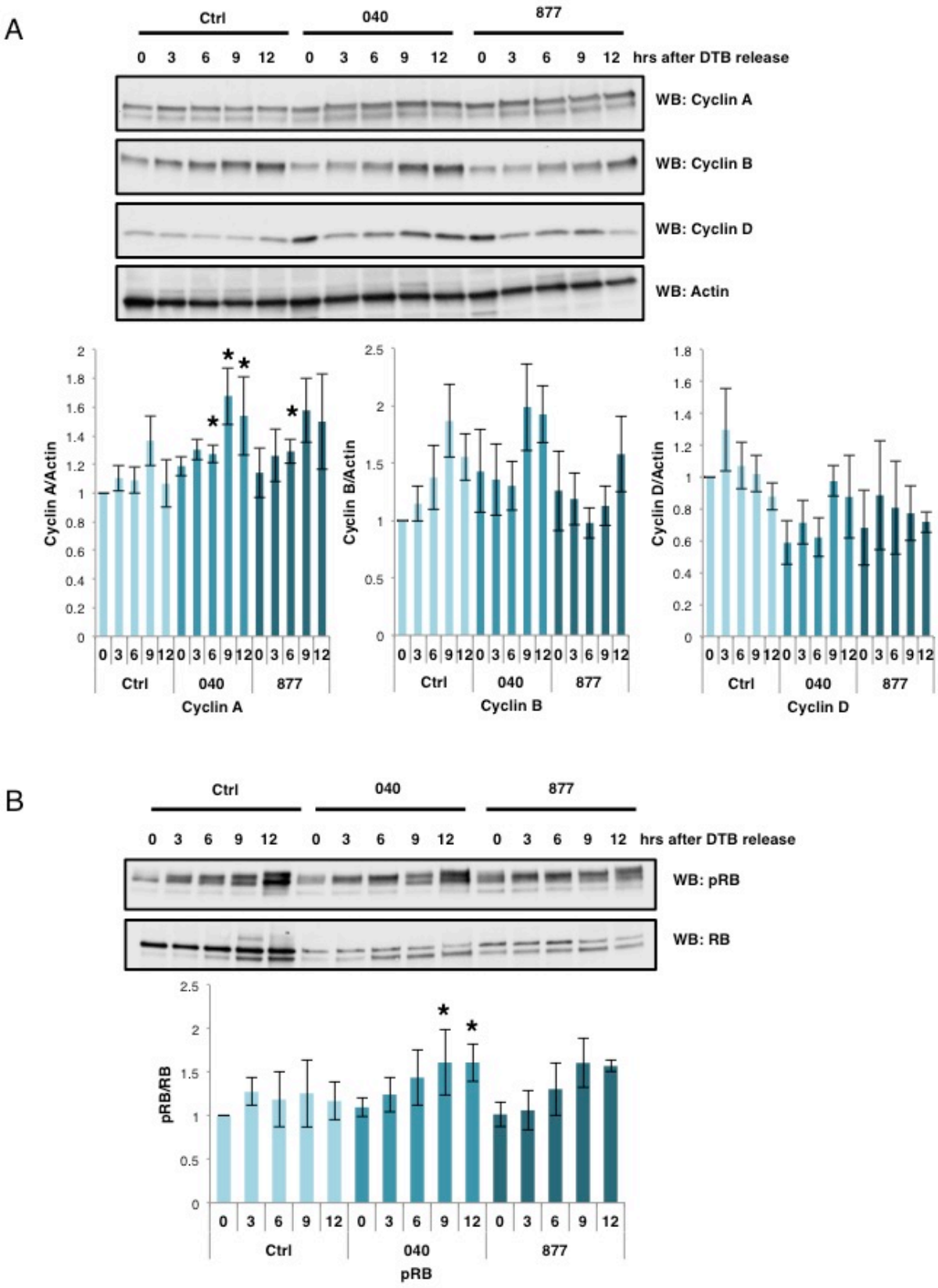

Figure C. 3: Cyclin expressions are disrupted in OGA knockdown cells

Control and OGA KD cells were synchronized into G_1/S by double thymidine block and released. Time points were harvested every 3 hours for western blot analysis. (A) In the OGA 040 and 877 cells, expression of cyclin A, B, and D are altered. Cyclin A has higher maximal expression in both OGA KD cell lines, while Cyclin B expression is higher at time zero for both OGA 040 and 877. Cyclin D expression is lower in both 040 and 877 cell lines compared to control. Expression of actin was used as a load control. (B) Phosphorylated RB and RB Western blots were performed as in (A). RB phosphorylation is elevated in the later time points in the OGA KD cells. Graphs show normalized densitometric analysis for phosphorylation of RB, or Cyclin(s) A, B, or D protein expression. Signals were first normalized with actin then normalized with each of its time-point matched control as indicated (n = 3-4; *, $p < 0.05$ versus control). Data are expressed as means ± S.E. Ctrl = Control, 040 = OGA040, 877 = OGA877. All experiments were performed with at least 3 biological replicates.

C.3.2 OGA Knockdown Shortens Spindle Chromatids and Increases Multi-polar Spindles

Previously, we demonstrated that over-expression of OGT or OGA caused defects in spindle formation [60]. In these cells, spindles were elongated and poorly condensed. The spindle defects caused by OGT and OGA over-expression increased the population of aneuploid cells [121]. In order to determine if OGA knockdown cells produced defective spindles and increased aneuploidy, we stained OGA knockdown and control cells for β-tubulin and DNA and counted the number of cells with aberrant spindles or that were multinucleated (**Figure C.4A**). Both OGA KD cell lines had an increase in multipolar spindles compared to control (**Figure C.4B**). These data corroborate previous experiments performed in colorectal carcinoma cells in which OGA knockdown caused an increase in polyploidy [172]. Next, we measured the length and width of the condensed DNA in metaphase spindles. Both OGA 040 and 877 showed a significant reduction in the length and width of the condensed chromatid DNA compared to control cells (**Figure C.4C-E**). Interestingly, these results are opposite to OGT and OGA over-expression studies and are more similar to cells treated with Thiamet-G (TMG), a selective OGA inhibitor, suggesting that reduced O-GlcNAc cycling either caused by OGA inhibition or OGA KD produces shorter, more condensed spindles [60].

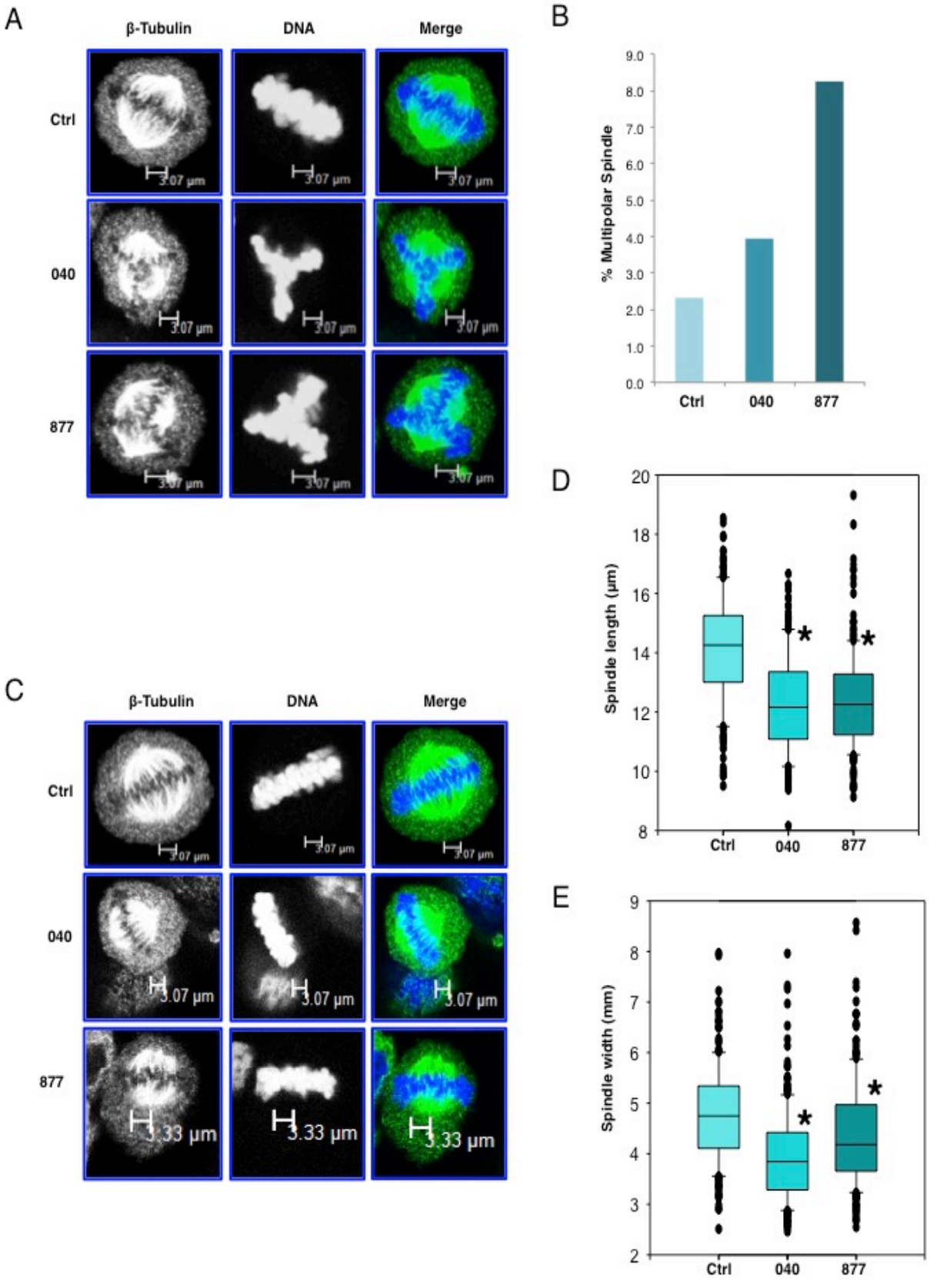
A
β-Tubulin
DNA
Merge
Ctrl
040
877
3.07 µm
3.33 µm
B
% Multipolar Spindle
9.0
8.0
7.0
6.0
5.0
4.0
3.0
2.0
1.0
0.0
Ctrl
040
877
C
β-Tubulin
DNA
Merge
Ctrl
040
877
3.07 µm
3.33 µm
D
Spindle length (µm)
20
18
16
14
12
10
8
Ctrl
040
877
*
E
Spindle width (mm)
9
8
7
6
5
4
3
2
Ctrl
040
877
*

Figure C. 4: Multipolar spindles and chromatid compaction are increased in OGA knockdown cells

(A) Cells were imaged for β-tubulin and DNA. For each cell line, 200 cells were counted and the percentage of cells with multipolar spindles was determined. (B) Both 040 and 877 cell lines have an increased percentage of multipolar spindles compared to control cells. (C) Cells were again stained for β-tubulin and DNA, and cells without visible signs of multipolar spindles were used in the measurement of chromatid length and width. (D) For each cell line, 200 cells at metaphase-anaphase had their chromatid length measure using ImageJ. OGA knockdown cells had significantly shorter spindle chromatids than control. (E) For spindle chromatid width, samples were measured across the two ends and middle of the DNA and averaged. Both 040 and 877 OGA knockdown cells had significantly thinner spindle chromatids then control cells (* indicates $P < 0.05$, Student *t*-test).

C.3.3 OGA Knockdowns Influences Mitotic Signaling Cascades

Alterations in mitotic O-GlcNAcylation increase the inhibitory phosphorylation on Cyclin Dependent Kinase 1 (CDK1) at threonine 14 (T14) and tyrosine 15 (Y15) [60, 123]. Phosphorylation at these sites inhibits CDK1 activity and links CDK1 activation to O-GlcNAc cycling. Therefore, we probed mitotic OGA KD cells for CDK1 Y15 phosphorylation and found that both OGA KD cell lines increased CDK1 Y15 phosphorylation (**Figure C.5A**). Interestingly, we did not see the increase in CDK1 Y15 phosphorylation in the OGA KD lines when cells were synchronized at prophase using nocodazole (**Figure C.5B**). Importantly, inhibitory phosphorylation in the OGA KD cells was lower, suggesting that the effect of OGA KD on CDK1 activation occurs later in M phase. Synchronization into metaphase-anaphase by thymidine release and treatment with kinesin inhibitor *S*-trityl-cysteine increased CDK1 inhibitory Y15 phosphorylation in both OGA KD cell lines (**Figure C.5C**).

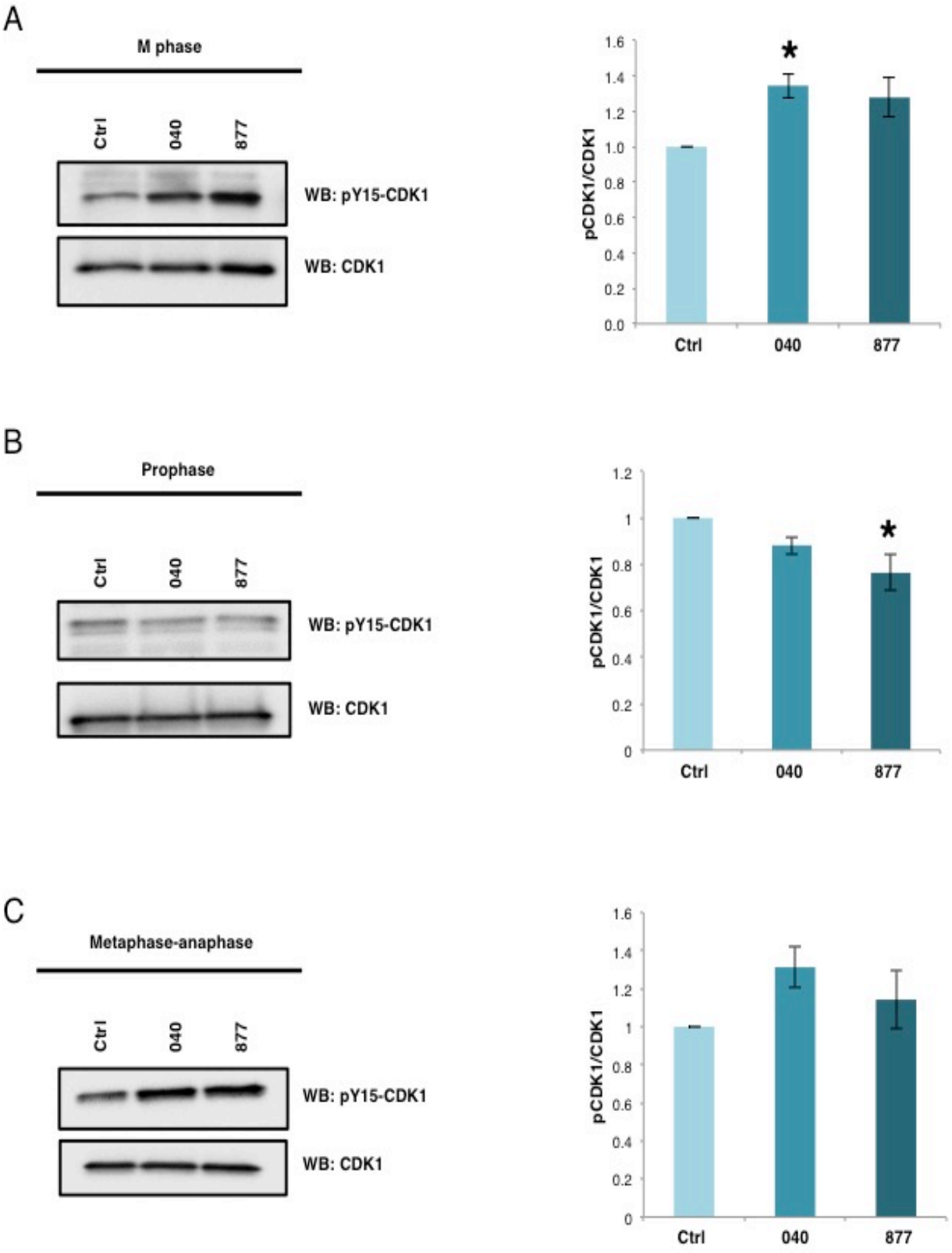

Figure C. 5: Inhibitory phosphorylation of tyrosine 15 of CDK1 is higher OGA KD cells

(A-C) Cells were synchronized into M phase by double thymidine block and harvested 9 hours post release (A) overnight treatment with nocodazole to synchronize cells into prophase (B) or treatment 6 post-release from double thymidine block with STC and harvested 14 hours post-release (C). Lysates were probed for phosphorylated Y15 CDK1 and total CDK1. Graphs show densitometry values of phosphorylation of CDK1 in OGA knockdown samples at the different stages of M phase. Signals were normalized first with CDK1 then followed by the control for each sample as indicated ($n = 3$; *, $p < 0.05$ versus control). Data are presented as means ± S.E. All experiments were performed with at least 3 biological replicates.

Spindle associated kinases like Aurora B kinase (AurB) interact with OGT and OGA at M phase [122, 123], and disruptions in O-GlcNAcylation affect the phosphorylation of AurB substrates such as vimentin and histones [60, 122]. Therefore, we measured the expression of AurB and AurB interacting partners in double thymidine released control and OGA KD cells. As a result, there was no significant difference in the expression of AurB or AurB interacting partners INCENP, Survivin (part of the chromosomal passenger protein complex, CPC), and Shugoshin; nor did we see changes in AurB activating phosphorylation (**Figure C.6A**). No change was seen in the localization of AurB, INCENP, or Survivin at the mitotic spindle (**Figure C.6B-C**); however, there was reduced localization of Survivin at the spindle midzone (**Figure C.6C**).

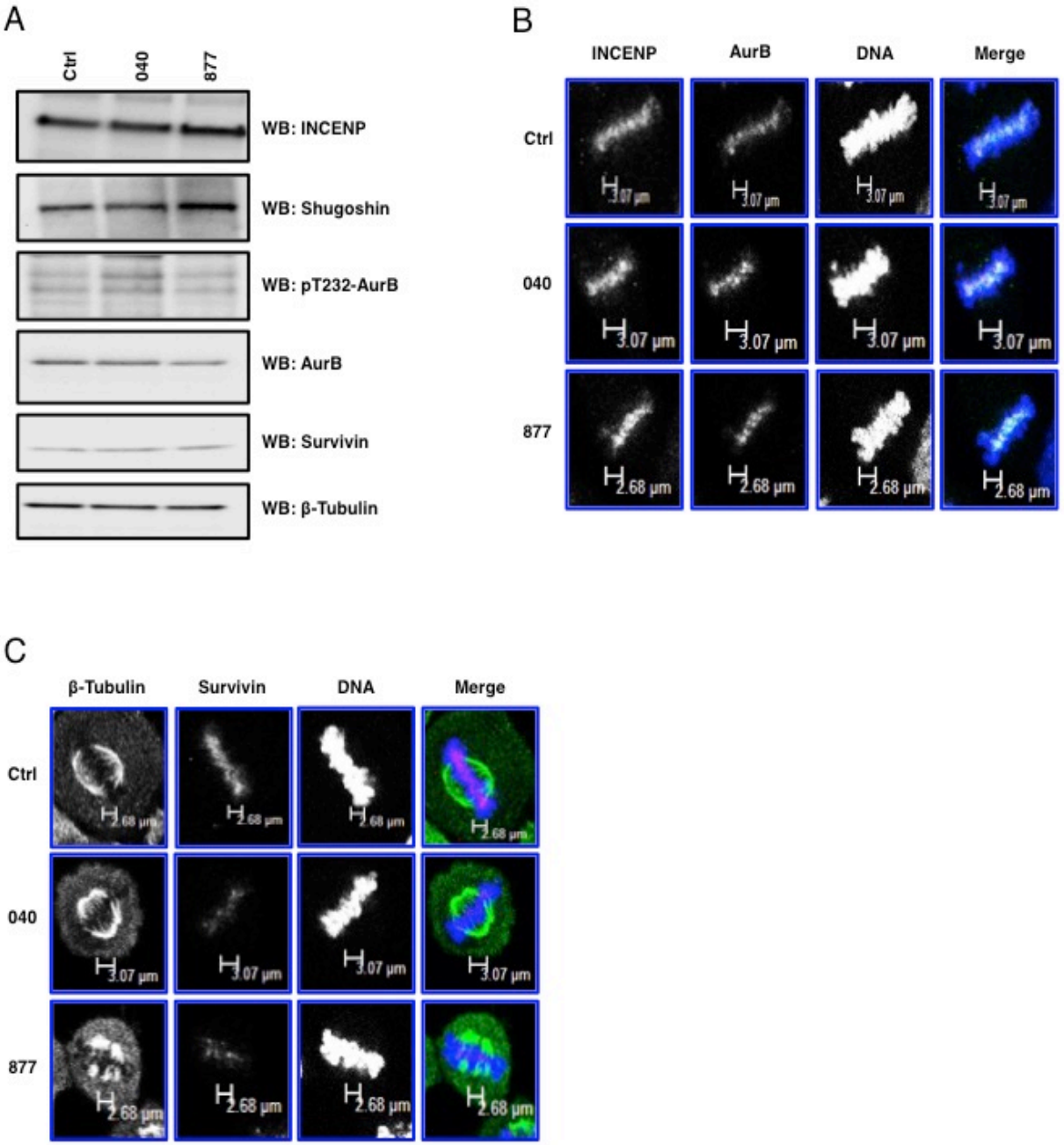

Figure C. 6: OGA knockdown had little effect on the expression or localization of the chromosomal passenger protein complex

(A) Protein expression of AurB and the other components of the CPC were unchanged in the OGA KD cells. (B) Localization of AurB and INCENP is unchanged in the OGA KD cells. (C) Localization of Survivin was reduced at the spindle midzone in the OGA KD cells. All experiments were performed with at least 3 biological replicates.

OGT and OGA over-expression reduces AurB phosphorylation of histone H3 serine 10 [60]. When histone H3 serine 10 (pS10H3) and threonine 3 phosphorylation (pT3H3) were measured in cells synchronized at M phase, prophase, or metaphase-anaphase, there were no significant differences in histone phosphorylation in 040 cells. Whereas, there was a significant reduction pT3H3 in the OGA 877 KD cells synchronized into M phase (**Figure C.7A-C**).

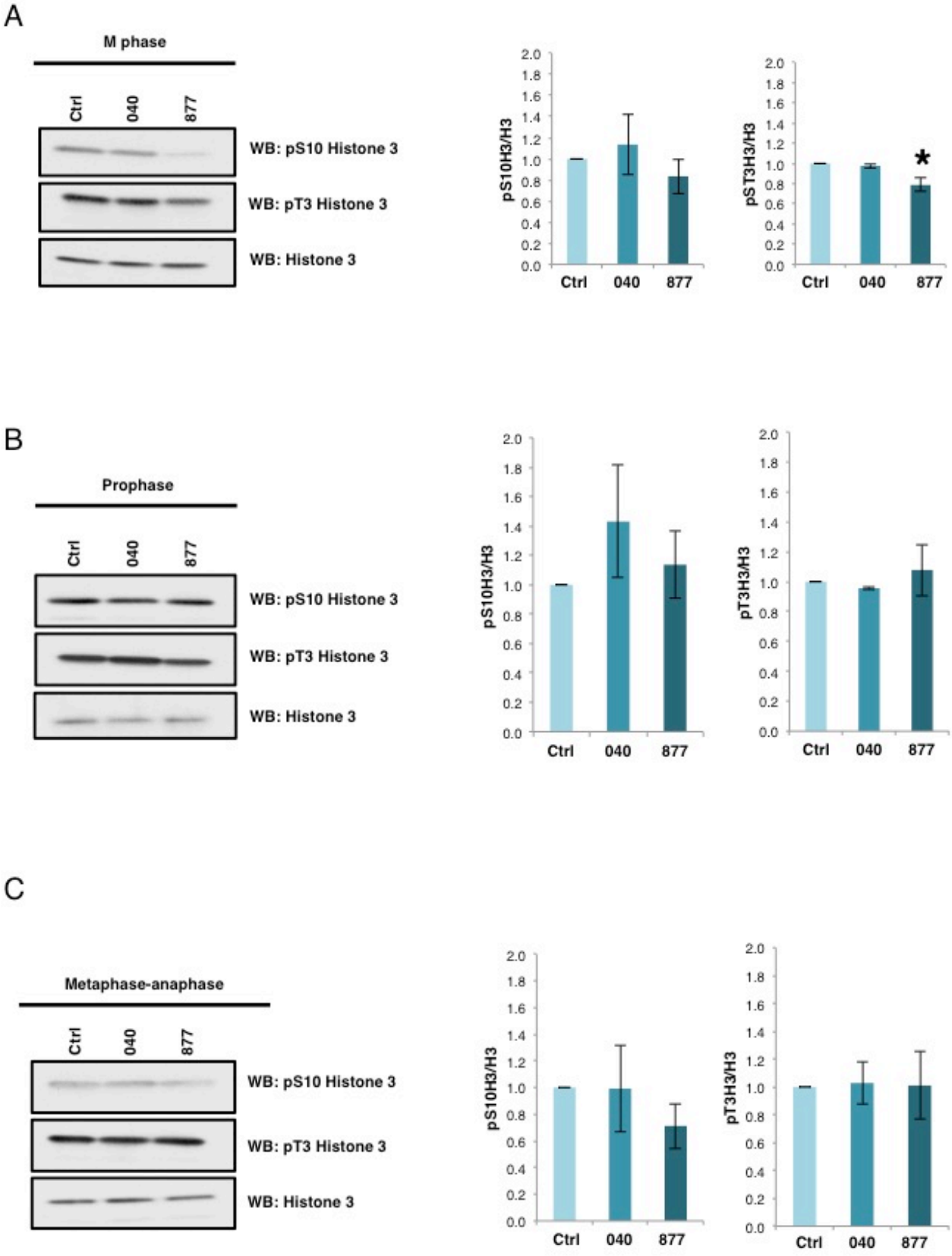
A
M phase
Ctrl
040
877
WB: pS10 Histone 3
WB: pT3 Histone 3
WB: Histone 3
pS10H3/H3
pST3H3/H3
*
B
Prophase
pT3H3/H3
C
Metaphase-anaphase

Figure C. 7: OGA 877 KD cells have reduced histone H3 phosphorylation

Cells were synchronized into M phase by double thymidine block and release **A**, prophase by nocodazole treatment **B**, or metaphase-anaphase with STC. **C**, Histones were purified by acid extraction and phosphorylation of histone H3 Serine 10 and Threonine 3 was measured. H3 T3 phosphorylation was lower in the double thymidine block and released 877 cells. Graphs of normalized densitometric analysis for phosphorylation of S10H3 or T3H3 to total histone H3 ($n = 3$; *, $p < 0.05$ versus control). Data are expressed as means ± S.E. All experiments were performed with at least 3 biological replicates.

C.3.4 OGA Knockdown Increases Mitotic O-GlcNAcylation of NuMA and EWS and Disrupts EWS Spindle Localization

We next explored the O-GlcNAcylation status of two known O-GlcNAc modified proteins, NuMA (Nuclear Mitotic Apparatus Protein) and EWS (Ewing Sarcoma Breakpoint Region 1 Protein), in the OGA knockdown cells [123, 173]. NuMA is a centrosome protein involved in organizing the centrosome to the cells cortex. We previously identified O-GlcNAc sites on NuMA and demonstrated that changes in OGT expression caused NuMA to localize to the cortex [123, 174]. We immunoprecipitated NuMA from prophase extracts and measured the level of O-GlcNAcylation on the protein. O-GlcNAc on NuMA was significantly increased in the OGA KD cells compared to control (**Figure C.8A**). These data demonstrate that reduced O-GlcNAc cycling increases O-GlcNAcylation on a spindle associated protein.

EWS is a RNA and DNA binding protein involved in numerous cellular functions; in particular, EWS helps recruits AurB to the spindle midzone during M phase [171]. Since previous report suggested that EWS is involved in organizing the spindle, we then measured O-GlcNAcylation and the localization of EWS to metaphase-anaphase spindles [175]. EWS O-GlcNAcylation was significantly increased on EWS in the OGA KD cells (**Figure C.8B**). Next, to demonstrate whether the localization of EWS is affected in OGA KD cells, we performed immunocytochemistry using anti-EWS antibody. As a result, EWS was evenly distributed throughout the cytoplasm in metaphase control cells. However, spindle localization of EWS was no longer associating with the center of the dividing cell (**Figure C.9A**). Scoring of the cells with the aberrant distribution of EWS demonstrated that there is a higher percentage of cells with aberrant localization of EWS in both OGA KD 040 and 877 cells compared to control. This

result suggests that normal level of O-GlcNAc cycling is required for proper localization of EWS during mitosis (**Figure 9B**).

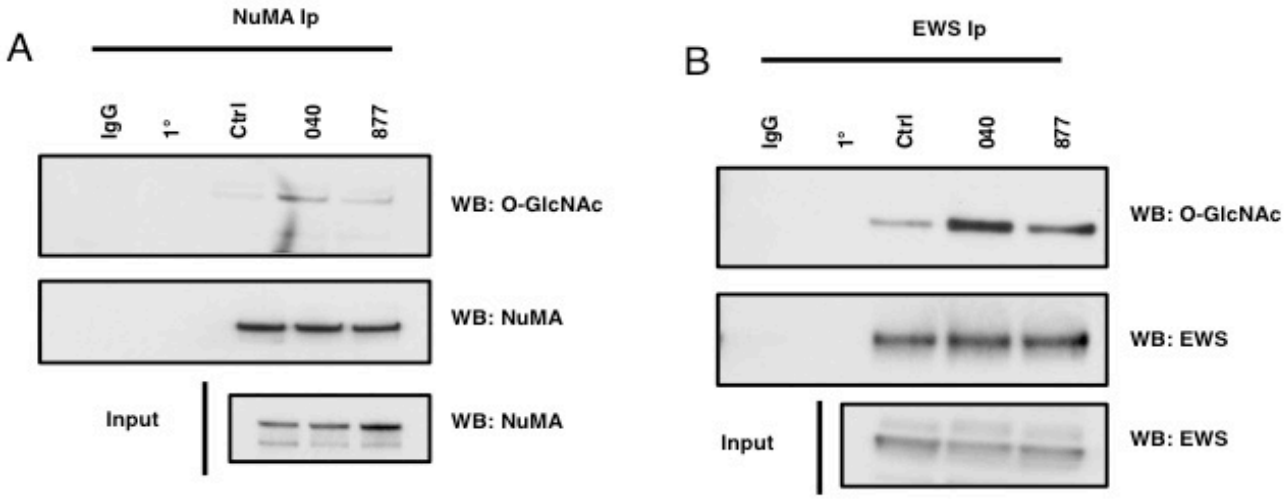

Figure C. 8: NuMA and EWS O-GlcNAcylation increases in OGA knockdown cells
(A-B) NuMA and EWS were precipitated from prophase extracts using specific antibodies to NuMA or EWS. Blots were then probed for O-GlcNAc using the RL-2 O-GlcNAc antibody. Both NuMA and EWS O-GlcNAcylation were increased in 040 and 877 OGA knockdown cells. All experiments were performed with at least 3 biological replicates.

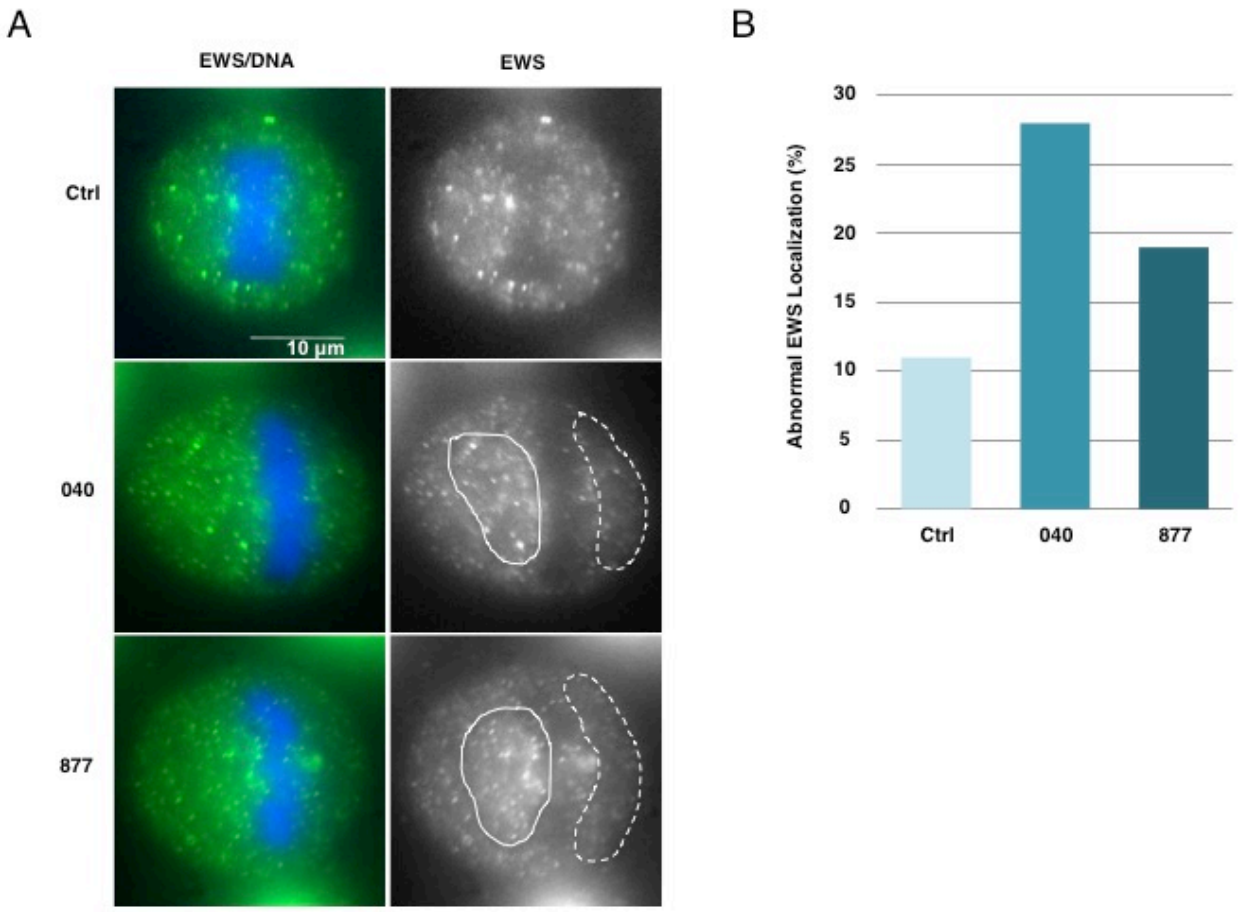

Figure C. 9: EWS spindle localization is disrupted in OGA knockdown cells
(A) (Left) EWS visualized with an anti-EWS antibody. Area with clustered EWS signal is shown with white line. Area with sparse EWS signal is shown with dashed white line. (Right) merged images of DNA stained with DAPI (blue) and EWS (green) visualized with an anti-EWS antibody. (B) The percentage of cells with aberrant localization of EWS (n=300 metaphase cells, per sample).

C.4 Discussion

We generated two stable OGA knockdown cell lines in order to understand the effect of reduced O-GlcNAc removal on cell cycle progression and M phase dynamics. Both cell lines had an approximate 20-30% reduction in activity and protein expression (**Figure 1**). Although the OGA KD cells grow at a normal rate as control, the KD cells show mitotic progression defects when synchronized into G_1/S and released (**Figure C.2**), and the expression of Cyclins D, A, and B was disrupted in these cells (**Figure C.3**). At M phase, the inhibitory phosphorylation of CDK1 was also increased (**Figure C.5**). KD cells had more compact chromatids, misaligned spindles, and had higher incidence of anueploidy than control. Finally, EWS was mislocalized from the spindle (**Figure C.4** and **C.9**). Together, these data demonstrate the importance of O-GlcNAc cycling in regulating mitotic progression and spindle function.

Recently, several labs have generated OGA embryonic knockout mice [168, 176]. The loss of OGA led to almost complete perinatal lethality in these animals with a variety of developmental defects [168, 176]. OGA -/- MEF (mouse embryonic fibroblast) demonstrated reduced growth rates, failure to resume cell cycle progression after serum starvation-reactivation, and these cells had an increase in polyploidy [168]. Interestingly, OGA knockdowns in colorectal cancer cells also had an increase in polyploidy [172]. Our data corroborates the mitotic defects seen in either OGA knockout mice or knockdown cells. Clearly, OGA has an important role in maintaining the fidelity of mitotic progression. Since OGA 040 and 877 KD cells had tighter chromatid packing at the spindle midzone correlating with chromatid packing after OGA inhibition [60], these data suggest that maintaining a homeostatic level of O-GlcNAc is necessary for chromatid packing at the midzone. Likely the rate of O-GlcNAc cycling is a regulatory mechanism for chromatid condensation.

Previously, we proposed that the rate of O-GlcNAc cycling was critical for proper mitotic progression [60]. We demonstrated that faster cycling caused by either over-expression of OGT or OGA led to large, unstructured chromatids at metaphase; however, pharmacological inhibition of OGA with Thiamet-G (TMG) produced tighter spindle chromatids, and treatment of OGT/OGA over-expressing cells with TMG partially restored spindle chromatid compaction [60]. The OGA KD cell lines 040 and 877 phenocopied the TMG treated cells demonstrating more compact spindle chromatids. Treatment with TMG slows O-GlcNAc cycling by blocking the removal of O-GlcNAc and establishes a state of increased O-GlcNAcylation. OGA knockdown also reduces O-GlcNAc cycling and increased O-GlcNAcylation. We previously proposed that increased O-GlcNAcylation caused specifically by reduced O-GlcNAc cycling would promote protein-protein interactions, but these O-GlcNAc mediated protein complexes would not be fully functional until the O-GlcNAc was removed [60]. The reduced O-GlcNAc cycling rate of the OGA KD cells is potentially promoting increased protein-protein interactions at the spindle and causing the more compact chromatid structure. However, the more compact chromatid structure is not without consequence. The OGA KD cells have a higher rate of multipolar spindles (**Figure C.4B**) than the control cells leading to loss of chromatid segregation fidelity. These data support the argument that O-GlcNAc cycling rates are critical for proper spindle development and function, and alterations in O-GlcNAc cycling will reduce segregation fidelity and promote aneuploidy.

Since O-GlcNAc affects numerous cellular pathways, the chromatid spindle phenotype is likely due to numerous factors. However, we did demonstrate increased EWS O-GlcNAcylation and mislocalization at the spindle (**Figure C.8B** and **C.9**). EWS is a multi-functional protein that is localized at the spindle during metaphase and helps to target AurB to the spindle midzone.

Although we saw no disruption in AurB midzone localization, we did measure an increase in midzone alignment errors. These data suggest that O-GlcNAcylation controls EWS spindle localization and potentially EWS spindle function. Because we cannot entirely exclude the possibility of O-GlcNAcylation of other unknown protein impairing the AurB alignment, future studies are required to identify the causal mechanisms of this phenotype.

Importantly, disruption in the rate of O-GlcNAc cycling either by over-expression of OGT/OGA, knockdown of OGA, or pharmacological inhibition of OGA modulates CDK1 inhibitory phosphorylation [60, 123]. CDK1 is the master regulator of M phase entry and is regulated not just by Cyclin B expression but also by inhibitory and activating phosphorylations [148]. Due to the importance of CDK1 in initiating mitotic entry, CDK1 activation is likely tied to O-GlcNAc homeostasis. Alterations in O-GlcNAc homeostasis either through nutritional flux, stress, or disease development could signal to the cell to reduce CDK1 activity until cellular conditions improve. How O-GlcNAc homeostasis regulates CDK1 phosphorylation is unclear but likely resides in the upstream kinases or phosphatases that regulate CDK1 inhibitory phosphorylation. Further investigation into O-GlcNAc control of CDK1 is warranted.

In conclusion, these data demonstrate the key role of OGA function in promoting cell cycle progression and spindle fidelity. These data argue that in the case of mitotic progression the cycling rates of O-GlcNAc are more important for biological function than absolute stoichiometry of O-GlcNAc on proteins. Therefore, understanding the interactions of OGT and OGA with the mitotic machinery will provide new insight into the critical role for O-GlcNAc in controlling mammalian mitosis.

Appendix D: O-GlcNAc Cycling Regulation

Reproduced with permission from Zhang, Z., Tan, E.P., VadenHull, N.J., Peterson, K.R., and Slawson, C. (2014). ***O-GlcNAcase Expression is Sensitive to Changes in O-GlcNAc Homeostasis.*** *Frontier Endocrinology 5:206.*

D.1 Introduction

O-linked *N*-acetylglucosamine (*O*-GlcNAc) is a post-translational modification (PTM) first discovered by Gerald W. Hart and Carmen-Rosa Torres in 1984 when they used bovine milk galactosyltransferase (GalT1) to probe for terminal *N*-acetylglucosamine moieties on glycoconjugates of T-cells [177]. *O*-GlcNAc is a reversible modification that is ubiquitously expressed in higher eukaryotes and involves the attachment of a single β-*N*-acetylglucosamine residue to serine or threonine residues in nuclear and cytosolic proteins. *O*-GlcNAc transferase (OGT) is the enzyme that adds the *O*-GlcNAc modification, whereas, *O*-GlcNAcase (OGA) removes it [35]. Because uridine diphosphate-*N*-acetyl-glucosamine (UDP-GlcNAc), the end point of the hexosamine biosynthetic pathway is the high-energy donor substrate for OGT, *O*-GlcNAcylation is sensitive to nutrient availability [156]. Furthermore, the removal and addition of *O*-GlcNAc termed *O*-GlcNAc cycling is a highly dynamic process, and *O*-GlcNAc cycling rates affect transcription regulatory pathways, cell cycle progression, and respiration [35, 36, 156, 157]. More importantly, an imbalance in the homeostasis of *O*-GlcNAc contributes to the development of diseases, including cancer, diabetes, and Alzheimer's [35, 36, 178, 179].

Since *O*-GlcNAcylation plays a significant role in regulating a wide panel of cellular processes, understanding the regulation of OGT and OGA is important. Several studies report that the expression of OGT and OGA is sensitive to changes in total cellular *O*-GlcNAc levels [121, 180]. Elevation of *O*-GlcNAc levels via pharmacological inhibition of OGA causes OGT

protein expression to decrease and OGA protein expression to increase [121]. A rapid decrease in OGA protein expression occurs in mice embryonic fibroblasts when OGT is knocked out [180]. Although we know that alterations to homeostatic levels of *O*-GlcNAc affect OGT and OGA expressions the mechanism by, through which cells adjust OGT and OGA expression as *O*-GlcNAc levels fluctuate is still unclear.

To further address how cells adjust OGT and OGA protein expression in response to alterations in *O*-GlcNAc levels, we measured in different cell lines OGT and OGA protein and mRNA expression and stability after pharmacological inhibition of OGA. In these experiments we are able to show that the OGA mRNA levels are more sensitive compared to OGT in response to the alterations in *O*-GlcNAc. Altogether, our data show that the expression of OGT and especially OGA is sensitive to changes in *O*-GlcNAc levels, and OGA expression is critical in maintaining cellular *O*-GlcNAc homeostasis.

D.2 Methods

D.2.1 Antibodies and Reagents

All primary and secondary antibodies used for immunoblotting were used at a 1:1000 and 1:10,000 dilution respectively. Anti-O-linked N-acetylglucosamine antibody [RL2] (ab2739) was purchased from Abcam. Antibodies for OGT (AL-34) and OGA (345) were gracious gifts from the laboratory of Gerald Hart in the Department of Biological Chemistry at the Johns Hopkins University School of Medicine. Actin (A2066) antibody and anti-chicken IgY HRP (A9046) were was purchased from Sigma. ChIP grade mouse (G3A1) mAb IgG1 isotype control (5415) and RNA polymerase II antibody, clone CTD4H8 (05-623) were purchased from Cell Signaling

Technologies and Millipore, respectively. Anti-rabbit HRP (170-6515) and anti-mouse HRP (170-6516) were purchased from Bio-Rad.

All reagents were purchased form Sigma unless otherwise noted. Cycloheximide (CHX, C7698, Sigma) was used at 50 μg/ml for HeLa cells and 25 μg/ml for K562 cells [181, 182]. Actinomycin D (AMD, A1410, Sigma) was used at 0.5 μg/ml for HeLa cells and 5 μg/ml for K562 cells [182, 183].

D.2.2 Cell Culture

HeLa cells and SH-SY5Y neuroblastoma cells were cultured in DMEM (**Invitrogen**) supplemented with 10% fetal bovine serum (FBS, Gemini) and 1% penicillin/streptomycin (**Invitrogen**). K562 cells were cultured in RPMI-1640 (**Invitrogen**) supplemented with 10% fetal bovine serum, 1X MEM non-essential amino acids solution (Invitrogen), 1 mM sodium pyruvate (Invitrogen), 2.5 mM HEPES, and 1% penicillin/streptomycin. Cells were treated with 10 μM Thiamet-G (TMG, S.D. Specialty Chemicals) for 6 hrs, 8 hrs, 24 hrs or 48 hrs with fresh TMG supplied daily. Cells were also pretreated with CHX and AMD for 4 hr and 0.5 hr respectively, followed by TMG treatment for 8 hr and 6 hr respectively. Cells were infected with OGT, OGA, or GFP virus at a multiplicity of infection (MOI) of 75 for 24 hr. After different treatments, cells were harvested for western blot, quantitative PCR (qPCR) or chromatin immunoprecipitation (ChIP) assay.

D.2.3 Immunoblotting

Cells were lysed on ice for 30 min in Nonidet P-40 (NP-40) Lysis Buffer (20 mM Tris-HCl, pH 7.4, 150 mM NaCl, 1 mM EDTA, 1 mM DTT, 40 mM GlcNAc, and 1% Nonidet P-40) with 1 mM PMSF, 1 mM sodium fluoride, 1 mM β-glycerophosphate, and 1X protease inhibitor cocktail I (leupeptin 1 mg/ml, antipain 1 mg/ml, benzamidine 10 mg/ml and 0.1% aprotinin).

Cell lysates were mixed with 4X protein solubility mixture (100 mM Tris-HCl, pH 6.8, 10 mM EDTA, 8% SDS, 50% sucrose, 5% β-mercaptoethanol, 0.08% Pyronin-Y). All electrophoresis was performed with 4–15% gradient polyacrylamide gels (Criterion Gels, Bio-Rad) and separated at 120 volts, followed by transfer to PVDF membrane (Immobilon, Millipore) at 0.4 Amps. Blots were blocked by 3% BSA in TBST (25mM Tris-HCl, pH 7.6, 150 mM NaCl, 0.05 % Tween-20) at RT for 20 min, then incubated with primary antibody at 4 °C overnight. After washing with TBST for 5 X 5 min, blots were incubated with HRP- conjugated secondary for 1 hr at room temperature, then washed with TBST again and developed using chemiluminescent substrate (HyGlo E2400; Denville Scientific). Blots were stripped in 200 mM glycine, pH 2.5 at room temperature for 1 hr and probed with different primary antibodies. All immunoblotting results were repeated in three independent experiments [60]. OGA and OGT relative protein levels were measured by analyzing the bands density using ImageJ 1.48 (http://imagej.nih.gov/ij/download.html) then normalized to the density of actin. All experiments were repeated three times and average relative fold changes were calculated.

D.2.4 Total RNA Isolation and RT-PCR

Total RNA was isolated by TRI reagent solution (AM9738, Ambion) according to manufacture's instruction. Briefly, 2 x 10^6 cells were resuspended by 1 mL TRI Reagent Solution. Then 200 µl of chloroform was added to extract RNA. After spinning down, upper phase containing total RNA was collected and incubated with an equal amount of isopropanol. RNA pellets were then precipitated by centrifugation, washed once with 70% ethanol, air-dried and dissolved in nuclease free water (Invitrogen).

RNA concentration was measured by Nanodrop 2000c (Thermo) and 1 μg of total RNA was used for reverse transcription (RT) using iScript Reverse Transcription Supermix (170-8841, Bio-Rad) following manufacturer's instruction. 10 μl of each completed reaction mix was incubated in a thermal cycler (Model 2720, Applied Biosystems) using the following protocol: priming 5 min at 25 °C, RT 30 min at 42 °C and RT inactivation 5 min at 85°C. cDNA products were diluted with 90 μl nuclease free water and analyzed by qPCR. All qPCR results were repeated in three independent experiments [184].

D.2.5 ChIP Assay

K562 cells were harvested by centrifugation at 1,000 g for 5 min and washed twice with 1X PBS. Cells were then cross-linked by 2 mM EGS (21565, Pierce) in PBS at room temperature for 30 min, followed by 1% formaldehyde (BP531-25, Fisher) for another 10 min. Cross-linking reaction was terminated by 125 mM glycine. Cell pellets were collected and lysed on ice for 30 min by cell lysis buffer (10 mM Tris-HCl, pH 8.1, 10 mM NaCl, 0.5% NP-40) with protease inhibitors. Chromatin was collected by spinning down and the pellets were resuspended in cold nuclear lysis buffer (50 mM Tris-HCl, pH 8.1, 10 mM EDTA, 1% SDS, 25% glycerol) with protease inhibitors. 300 μl of nuclear lysis buffer was used to resuspend chromatin from 2 x 10^6 cells.

Chromatin DNA was sheared to the size of 100-300 bp by sonication (Model Q800R, Active Motif) with the following protocol: amplification 75%, pulse On 15 s, pulse Off 45 s, temperature 3°C. 200 μl of sheared chromatin was diluted by adding 1 ml of ChIP buffer (20 mM Tris-HCl pH8.1, 1.2% Triton X-100, 1.2 mM EDTA, 20 mM NaCl) with protease inhibitors. 2 μg of control IgG and specific antibody was added to diluted chromatin, respectively, followed by end to end rotation at 4 °C overnight. At the same time, 12 μl of

diluted chromatin was saved as input and processed later. Next day, 30μl of PBS washed M-280 sheep anti-mouse IgG Dynabeads (11204D, Invitrogen) was add to the chromatin, followed by rotating at 4 °C for 4 hr. Dynabeads were separated by DynaMag-2 Magnet (12321D, Invitrogen) and subsequently washed with 1 ml of the following buffer for 5 min at 4 °C: wash buffer 1 (0.1% SDS, 1% Triton X-100, 2 mM EDTA, 20 mM Tris-HCl pH 8.0, 150 mM NaCl), wash buffer 2 (0.1% SDS, 1% Triton X-100, 2 mM EDTA, 20 mM Tris-HCl pH 8.0, 300 mM NaCl), wash buffer 3 (0.1% SDS, 1% Triton X-100, 2 mM EDTA, 20 mM Tris-HCl pH 8.0, 500 mM NaCl), wash buffer 4 (0.25 M LiCl, 1% NP-40, 1% Sodium Deoxycholate, 1 mM EDTA, 10 mM Tris-HCl pH 8.0) and TE buffer (10 mM Tris-HCl, pH 8.0, 1 mM EDTA).

Complexes were eluted from beads with 500 μl elution buffer (1% SDS, 0.1 M $NaHCO_3$, 40 mM Tris-HCl, pH 8.0, 10 mM EDTA) and added with 200 mM NaCl. Eluates and inputs were treated at the same time with RNase A (EN0531, Thermo) at 65°C overnight, followed by proteinase K (25530-031, Invitrogen) treatment for 2 hr. DNA was extracted by phenol/chloroform/isoamyl alcohol (AC327111000, Fisher) and precipitated by glycogen (10814-010, Invitrogen) and ethanol [185]. DNA pellets were air dried, dissolved in 50 μl nuclease free water, and analyzed by qPCR.

D.2.6 qPCR Assay

cDNA or ChIP DNA samples were analyzed by qPCR using SsoAdvanced Universal SYBR Green Supermix (172-5271, Bio-Rad) according to manufacturer's instruction. Briefly, 2 μl of cDNA or 5 μl of ChIP DNA samples, SYBR green supermix, nuclease free water, and primers (Table 1) for the target gene were mixed with a total reaction volume of 20 μl. A 96-well PCR plate (AVRT-LP, Midsci) with the mixture was loaded to CFX96 Touch Real-Time PCR

Detection System (185-5195, Bio-Rad) with the following protocol: polymerase activation and DNA denaturation 30 s at 95°C, amplification denaturation 5 s at 95 °C, and annealing 30 s at 60°C or 62°C with 40 cycles, and melt curve 65°C-95°C with 0.5°C increment 5 s/step.

D.2.1 Data Analysis

Quantification cycle (Cq) value was recorder by CFX Manager™ software. For cDNA qPCR data, dynamic range of RT and amplification efficiency was evaluated before using ΔΔCq method to calculate relative gene expression change. For ChIP DNA qPCR data, Cq value was normalized to percentage of input. Data generated in three independent experiments was presented as means ± standard error and analyzed using two-tailed Student *t* test with $P < 0.05$ as significant difference.

D.3 Results

D.3.1 Alterations in O-GlcNAc Levels Changes the Protein Expression of OGT and OGA

Previous reports demonstrated that different pharmacological inhibitors of OGA, PUGNAc and GlcNAc-thiazoline, rapidly increase the protein expression of OGA [121, 122]. We explored this phenomenon using another highly selective inhibitor of OGA Thiamet-G (TMG)[128]. We altered the *O*-GlcNAc levels of SH-SY5Y neuroblastoma, HeLa cervical carcinoma, and K562 leukemia cells with TMG and measured *O*-GlcNAc, OGT, and OGA levels at various time points up to 48 hrs of TMG treatment. OGA protein expression increased while OGT protein expression decreased gradually in the prolonged TMG treatment time points (**Figure D.1A-C**). Additionally in SY5Y cells, we used adenoviral-mediated OGT or OGA infection to alter *O*-GlcNAc levels. Green Fluorescent Protein (GFP) was used as a control for the adenoviral infection. Cells over-expressing OGT showed an elevation in *O*-GlcNAc levels and a slight increase in OGA protein expression compared to control, while cells over-expressing OGA

showed a decrease in *O*-GlcNAc levels and a slight increase in OGT protein expression compared to control (**Figure D.1D)**.

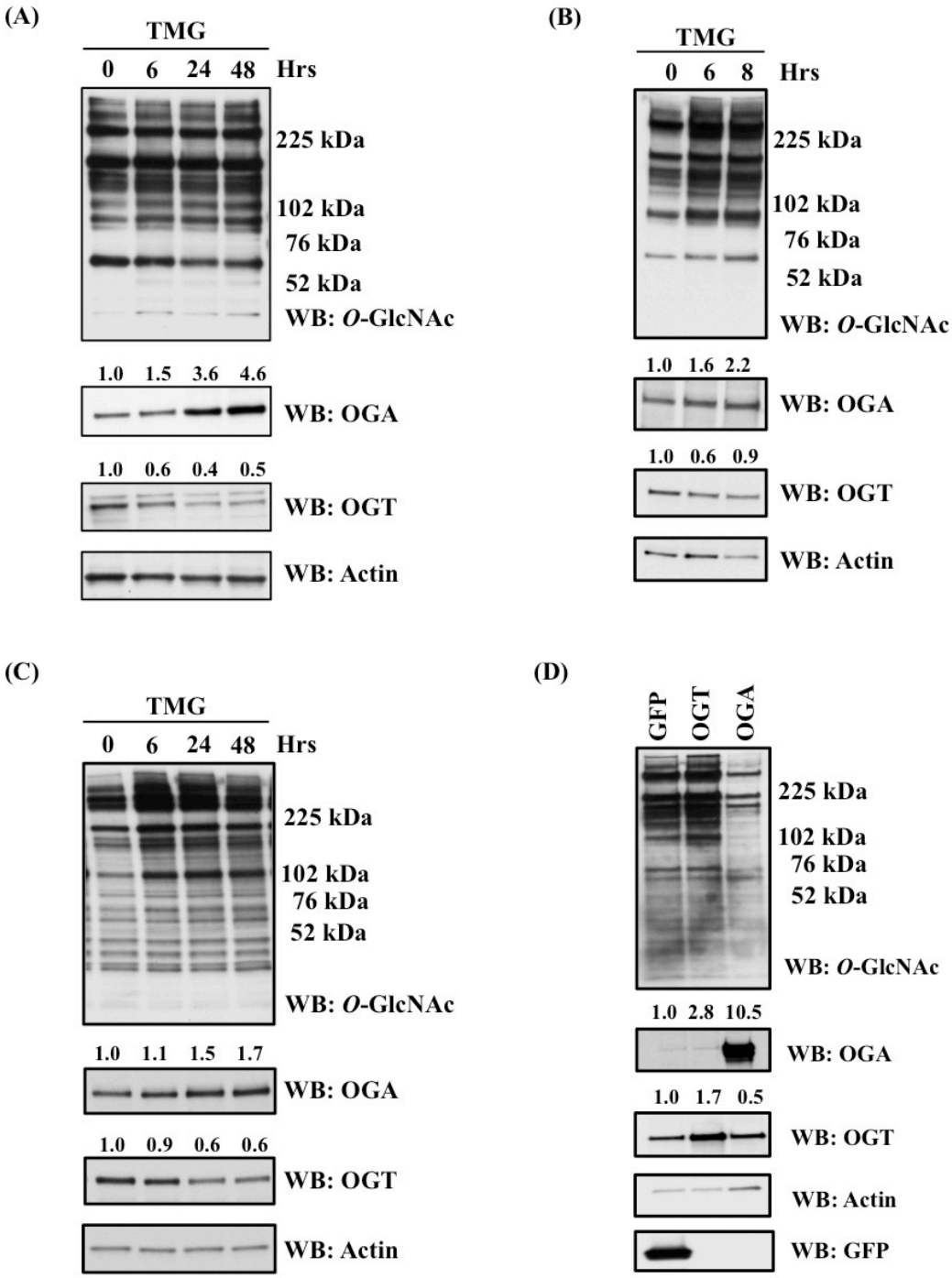

Figure D. 1: OGA protein level was increased after TMG treatment

(A) SH-SY5Y neuroblastoma cells, (B) HeLa cervical cells, and (C) K562 leukemia cells were treated with 10 μM TMG for indicated time. (D) SH-SY5Y cells were infected with GFP, OGT, and OGA adeno-virus at 75 MOI for 24 hours. Cells were lysed, overall O-GlcNAc level, OGA and OGT protein levels were analyzed by western blot with actin as a loading control. Average fold change for OGT and OGA is listed on the blots.

D.3.2 TMG Does Not Stabilize OGA Protein

In order to explore the reason why TMG increases OGA protein level, we asked the question does TMG increase OGA protein stability. We pretreated cells with cyclohexamide (CHX) to inhibit protein translation [186]. We treated HeLa (**Figure D.2A**) and K562 (**Figure 2B**) cells with TMG and observed a robust increase in OGA protein level (**Figure D.2A-B,** Lane 2) compared to control cells without any treatment (**Figure 2A and B,** Lane 1). When HeLa cells were treated with CHX, OGT protein levels were dramatically decreased compared to control, and we did not observe much of a decrease in OGA protein expression (**Figure D.2A,** Lane 3). However, both OGT and OGA protein levels were dramatically decreased after CHX treatment in K562 cells (**Figure D.2B,** Lane 3) compared to control. Combination of CHX and TMG did not change the OGA or OGT protein levels (**Figure D.2A-B,** Lane 4) compared to CHX treatment only, suggesting that the TMG-mediated increase in OGA protein expression was not due to increased stability of the protein.

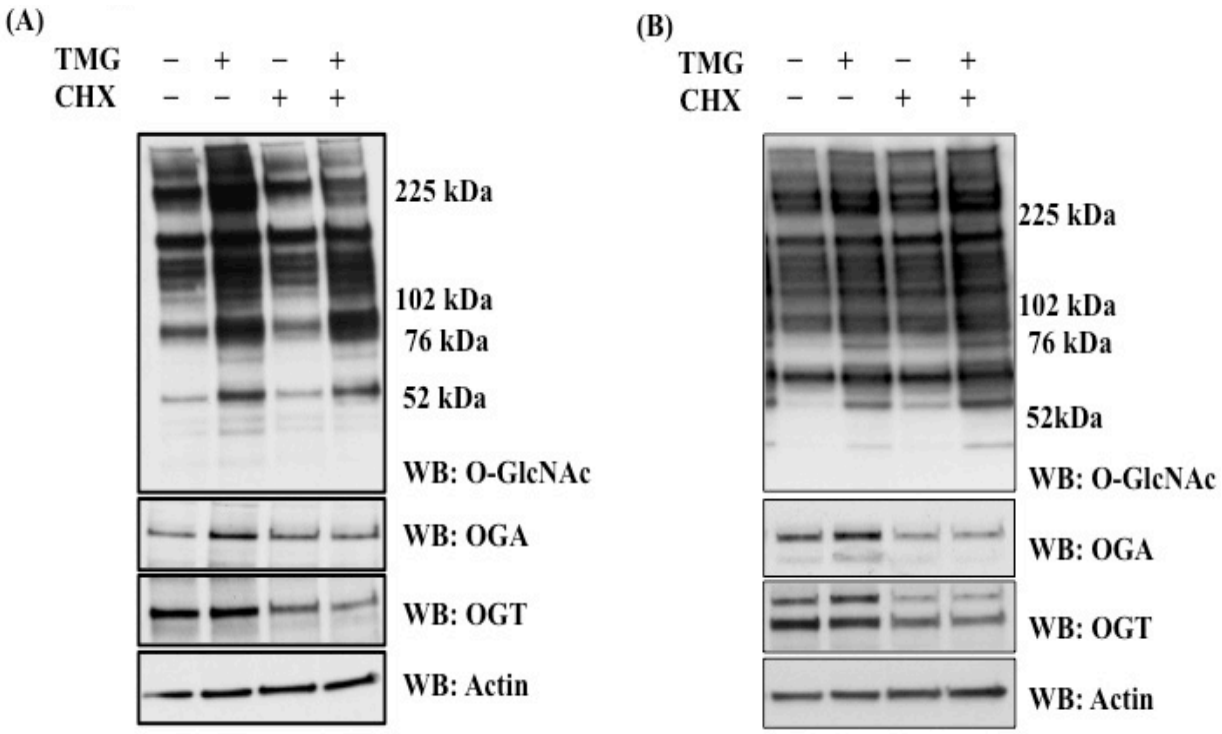

Figure D. 2: TMG does not stabilize OGA protein

(A) HeLa cells and (B) K562 cells were treated with TMG, CHX (protein translation inhibitor), and CHX+TMG. Cells were lysed, overall O-GlcNAc level, OGA and OGT protein level were analyzed by western blot, with actin as loading control.

D.3.3 TMG Transcript Level is Increased After TMG Treatment

Next, we investigated if OGT or OGA transcript level were altered after TMG treatment. We analyzed OGA mRNA level in SH-SY5Y (**Figure D.3A**), HeLa (**Figure D.3B**) and K562 (**Figure 3C**) cells. We found OGA mRNA level was increased from 6 hrs TMG treatment in all three cell lines, and was still elevated above control after 48 hr TMG treatment (**Figure D.3A-C**). The OGA mRNA level corresponded with the increase in protein level in **Figure D.1**. However, the OGT mRNA level did not significantly change (**Figure D.3D-F**). We also demonstrated that the corresponding OGA and OGT mRNA levels increased slightly, but not significantly, when OGT or OGA were overexpressed in SH-SY5Y cells (**Figure D.3G-H**).

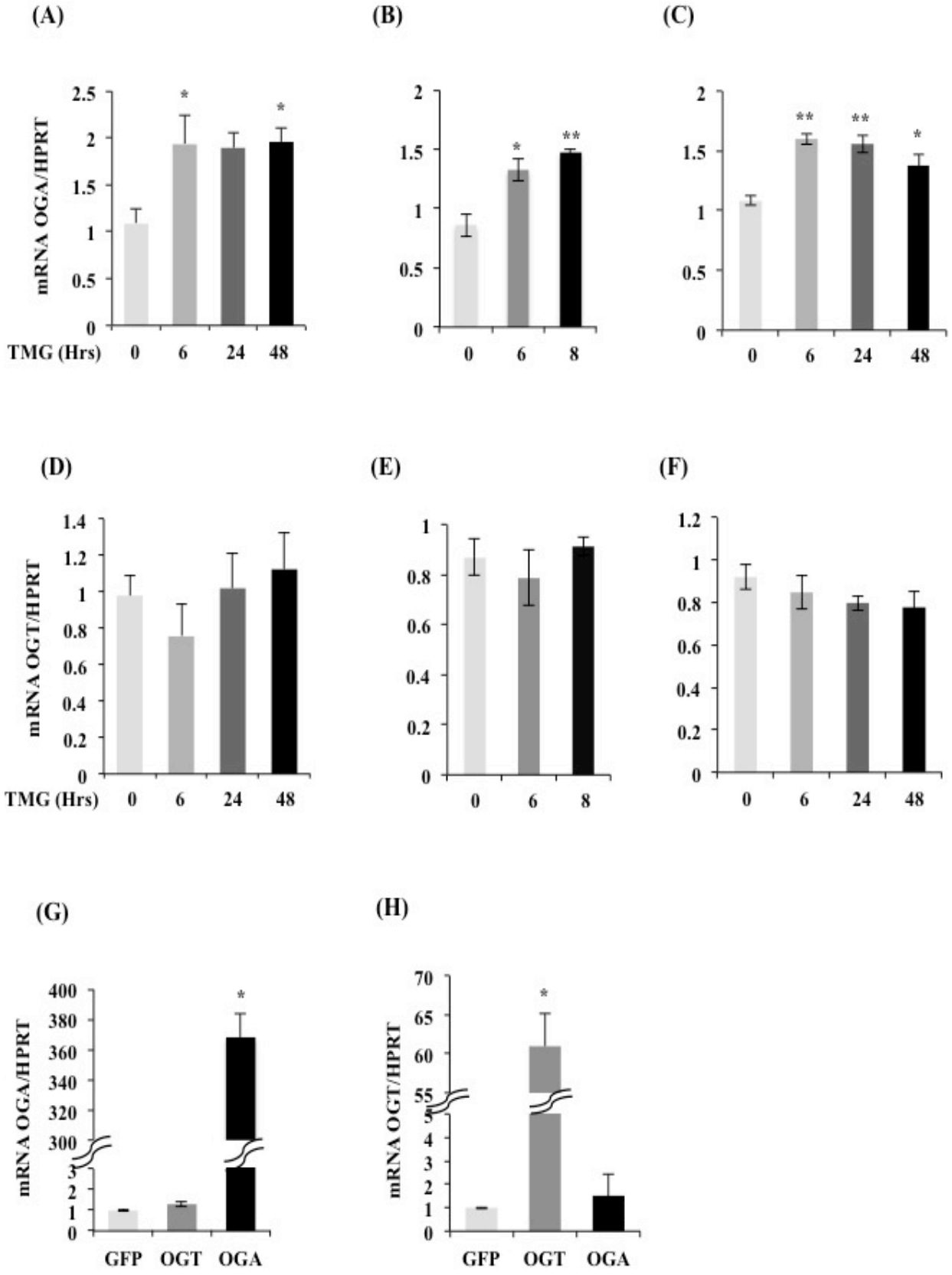
(A)
(B)
(C)
mRNA OGA/HPRT
TMG (Hrs) 0 6 24 48
0 6 8
0 6 24 48
(D)
(E)
(F)
mRNA OGT/HPRT
TMG (Hrs) 0 6 24 48
0 6 8
0 6 24 48
(G)
(H)
mRNA OGA/HPRT
GFP OGT OGA
mRNA OGT/HPRT
GFP OGT OGA

Figure D. 3: OGA mRNA level was increased after TMG treatment

After TMG treatment, relative OGA mRNA level in (A) SH-SY5Y, (B) HeLa, and (C) K562 cells, as well as OGT mRNA level in (D) SH-SY5Y, (E) HeLa, and (F) K562 cells were analyzed by qPCR. Both (G) OGA mRNA level and (H) OGT mRNA level in SH-SY5Y cells infected with GFP, OGT, and OGA adenovirus at 75 MOI for 24 hr respectively were also analyzed by qPCR. Hypoxanthine-guanine phosphoribosyltransferase (HPRT) served as internal control. * indicates $P < 0.05$ and ** indicates $P < 0.01$, compared with control (TMG 0 hr or GFP), n=3, Student *t*-test.

D.3.4 TMG Does Not Stabilize OGA mRNA

Next, we asked the question is increased OGA mRNA level after TMG treatment due to stabilized OGA mRNA. Actinomycin D (AMD), a RNA synthesis inhibitor was used to test OGA mRNA stability. TMG treated HeLa cells showed an increase of OGA mRNA level compared to control cells without any treatment (**Figure D.4A**). When cells were treated with AMD, both OGA and OGT mRNA levels were dramatically decreased compared to control (**Figure 4A** and **B**). Combination of AMD and TMG did not change the OGA and OGT mRNA levels compared to AMD treatment only (**Figure D.4A-B**). The same results were observed when using K562 cells (**Figure D.4C-D**).

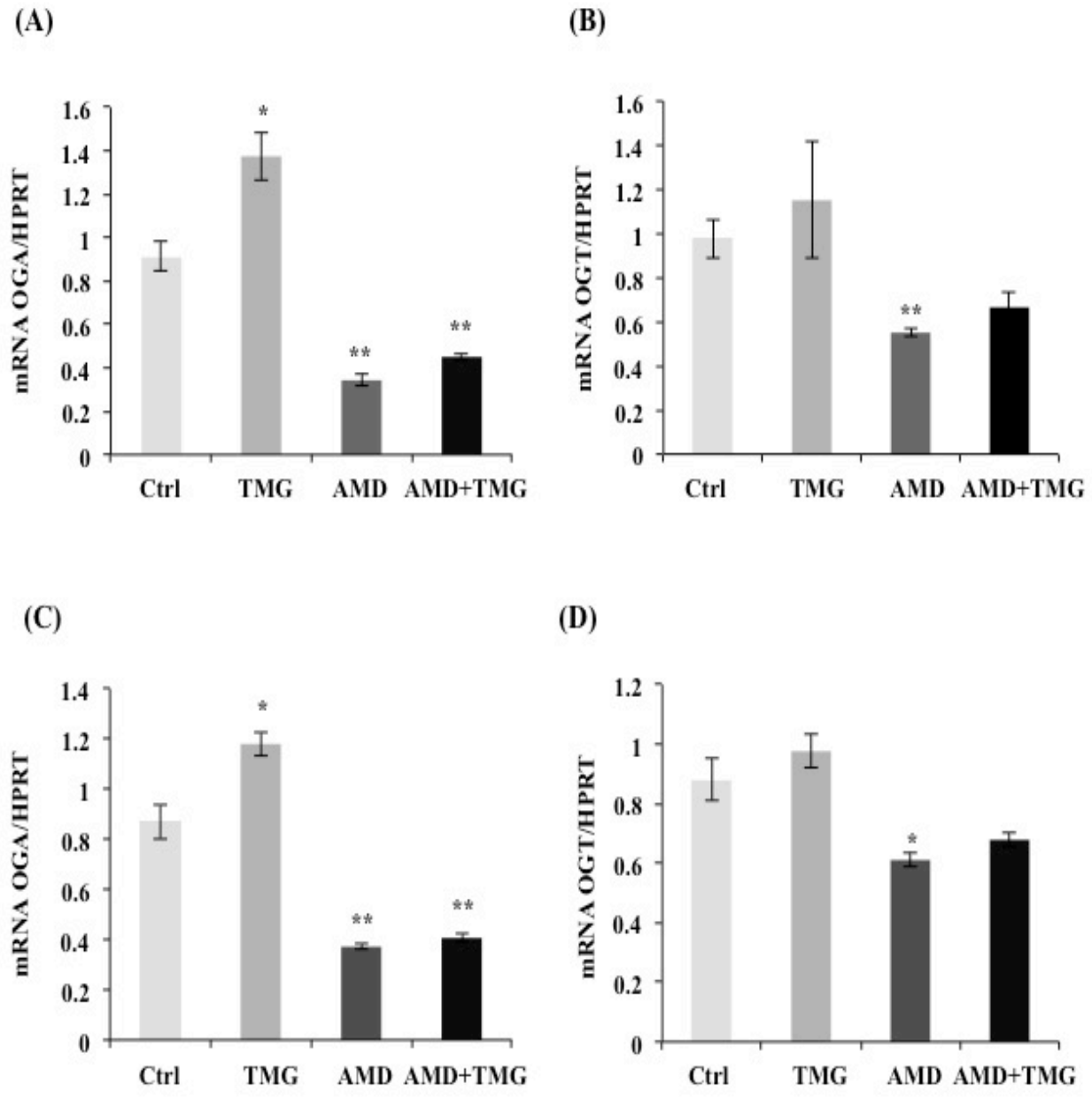

Figure D. 4: TMG does not stabilize OGA mRNA

HeLa cells (A and B) and K562 cells (C and D) were treated with TMG, AMD (RNA transcription inhibitor), and AMD+TMG, respectively. (A) OGA (A and C) and OGT (B and D) mRNA level were analyzed by qPCR, with HPRT as internal control. * indicates $P < 0.05$ and ** indicates $P < 0.01$, compared with control, n=3, Student *t*-test.

D.3.5 RNA Pol II Occupancy is Decreased at OGA Transcription Start Site (TSS) After 48 hrs TMG Treatment

We next investigated RNA Pol II occupancy at the OGA TSS via RNA Pol II chromatin immunoprecipitation. In control K562 cells, RNA Pol II was bound to OGA TSS with less binding at upstream (-1000) and downstream (+2700) of the TSS. However, after 48 hr TMG treatment, RNA Pol II occupancy was decreased at the OGA TSS compared to control cells (**Figure D.5A**). Normal mouse IgG ChIP was used as a negative control (**Figure D.5B**).

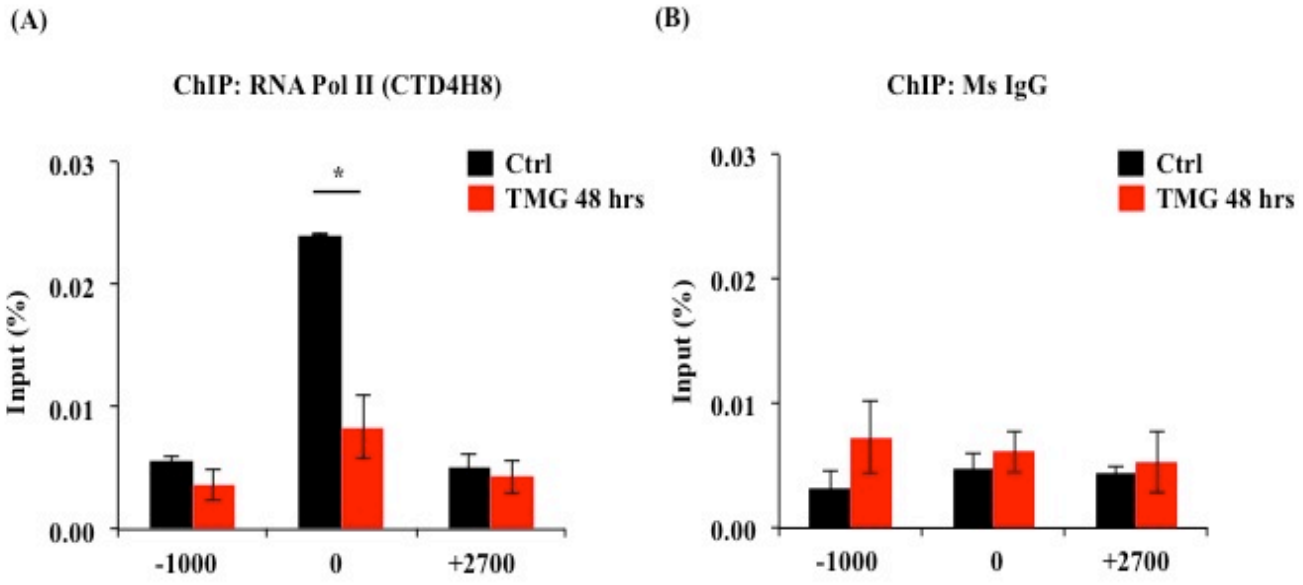

Figure D. 5: RNA Pol II occupancy at OGA TSS was decreased after 48 hrs TMG treatment in K562 cells

(A) RNA Pol II ChIP assay was performed on control and 48 hrs TMG treated cells. ChIP DNA was analyzed by qPCR using a set of primer targeting 1000bp upstream of OGA TSS (-1000), OGA TSS (0) and +700bp downstream of OGA TSS (+2700). * indicates $P < 0.05$, n=3, Student *t*-test. (B) Normal mouse IgG ChIP served as a negative control.

D.4 Discussion

The production of uridine diphosphate-N-acetyl-glucosamine (UDG-GlcNAc), the substrate for OGT, integrates various metabolic substrates allowing the *O*-GlcNAc modification to act as a nutrient sensor [156]. Consequently, cells are sensitive to changes in *O*-GlcNAc levels due to nutritional and metabolic flux and will adjust cellular functions accordingly. Possibly, prolonged alterations in homeostatic levels of *O*-GlcNAc will cause the protein expression of OGT and OGA to change in an effort to restore *O*-GlcNAc homeostasis [156]. Exactly how cells sense alterations to homeostatic levels of *O*-GlcNAc and adjust OGT and OGA expression to compensate for the changes in *O*-GlcNAcylation is unclear. For example, pharmacological inhibition of OGA rapidly increases cellular *O*-GlcNAc levels; however, the protein expression of OGA will also increase in response to the elevation of *O*-GlcNAc [121, 122]. We sought to explore the mechanism as to how OGT and OGA protein expression changes in response to alterations in cellular *O*-GlcNAc levels. In agreement with previous reports, we found an increase in OGA protein expression as quickly as 8 hr in HeLa cells and 24 hr in K562 and SY5Y cells after treatment with TMG. OGT protein expression also decreased at these later time points (**Figure D.1**). Due to the fact that increased levels of *O*-GlcNAc can increase the stability of proteins such as p53 [187] and TET (ten-eleven translocation) [188], we postulated that increased O-GlcNAc could stabilize OGA. K562 or HeLa cells exposed to cycloheximide in the presence of TMG showed no difference in the stability of either OGT or OGA (**Figure D.2**) suggesting that the increase in OGA protein expression was not due to increased stability and more likely to an increase of OGA transcripts.

Importantly, decreased *O*-GlcNAc levels do not necessarily increase OGT levels in all cell types; for example, blocking GFAT (glutamine fructose-6-phosphate amidotransferase)

activity with 6-diazo-5-oxo-L-norleucine (DON) in HeLa cells lowered *O*-GlcNAc levels but did not increase OGT protein expression [121]. On the other hand, OGA protein levels quickly decreased after *Cre*-mediated knockout of OGT in mouse embryonic fibroblasts [180], but OGA knockdown in colon cancer cells did not significantly decrease OGT protein expression [172]. Changes in OGA protein expression appear more sensitive to changes in *O*-GlcNAc than OGT in HeLa cells, while both OGT and OGA expression significantly change in SY5Y cells (**Figure D.1**). Over-expression of OGA did not substantially influence OGT protein expression (**Figure D.1**), and OGT over-expression did not change OGA expression (**Figure D.1**). Recently the development of a selective OGT inhibitor allowed for a dramatic reduction in cellular *O*-GlcNAcylation [189], which in turn caused OGA protein expression to rapidly decrease with only a minimal increase in OGT protein expression [189]. The dynamic change in OGA protein expression was seen in the development of disease as well. In red blood cells of prediabetic individuals, OGA expression was significantly increased [190], and OGA protein levels correlated with increased blood glucose in these prediabetic patients. These data suggest that higher blood glucose levels promote increased flux through the hexosamine biosynthetic pathway leading to elevated OGT activity, followed by OGA protein levels increasing to restore cellular *O*-GlcNAc homeostasis in erythrocyte precursor cells. Together, these data support the hypothesis that if OGT acts as a nutrient sensor allowing for rapid changes in *O*-GlcNAcylation due to alterations to either the extracellular or intracellular environment, then OGA should be less sensitive to nutrient changes and more sensitive to acute or chronic changes in *O*-GlcNAcylation.

In order to respond to acute or chronic changes in *O*-GlcNAc levels, cells rapidly and dramatically alter the expression of OGA mRNA (**Figure D.3**). In the case of OGT, we did not

detect a significant change in OGT mRNA levels after TMG treatment. The rapid increase in OGA mRNA levels after TMG treatment would argue that either OGA transcripts were more stable or transcriptional activity at the OGA promoter was increasing. We tested transcript stability by inhibiting RNA polymerase II with AMD [183]. Interestingly, OGA and OGT transcript levels were not more stable after TMG treatment in the presence of AMD (**Figure D.4**) suggesting that the increase in OGA mRNA levels with TMG was due to an increase in OGA gene transcription.

Next, we performed ChIP at the OGA promoter with an antibody that recognized all forms of RNA Pol II (phosphorylated and non-phosphorylated forms). After 48 hrs of prolonged TMG treatment in K562 cells, total RNA Pol II at the promoter was decreased compared to the control samples (**Figure D.5**). Although we expected to find an increase of RNA Pol II occupancy at the OGA promoter, the observed decrease might be due to the prolonged TMG treatment. We have yet to explore RNA Pol II occupancy at the OGA promoter after an acute TMG treatment (for example 6 hrs), which might yield a different result and needs to be studied further. The mRNA levels of OGA in K562 cells did begin to decrease at the 48-hr TMG treatment, suggesting that the OGA promoter might become inactive after prolonged TMG treatment.

Many transcription factors are modified by *O*-GlcNAc [35] and likely alteration of the *O*-GlcNAcylation level of a transcription factor could mediate the change in OGA transcription. We used the predictive software TFSEARCH (http://www.cbrc.jp/research/db/TFSEARCH.html) to identify potential transcription factor binding sites in the first 1000 base pairs upstream of the OGA transcription start site [191]. Among the transcription factor-binding sites in this sequence, GATA and MZF were the most

predicted transcription factors. Due to the essential and ubiquitous expression of OGA [156], we anticipated that several housekeeping transcription factors might bind to this region, but we found only few of these. Interestingly, both GATA and MZF are important transcription factors regulating hemopoietic development [184, 192]. Perhaps the increased in OGA expression in prediabetic red blood cells [190] was partially due to changes in either of these two proteins. *O*-GlcNAcylation changes might lead to alteration of GATA or MZF occupancy at the OGA promoter. Some GATA family members are modified by *O*-GlcNAc [193]; thus, this presents an interesting avenue to explore in more detail.

Together, our data demonstrate that OGA protein and mRNA expression is sensitive to cellular levels of *O*-GlcNAc. Some disease states have OGA expression uncoupled from *O*-GlcNAc levels [194]. In many different cancers, *O*-GlcNAc homeostasis appears to be disrupted with increased OGT protein expression and *O*-GlcNAc levels [195]. Several pancreatic cancer cell lines have increased *O*-GlcNAc levels when compared to an immortalized control cell line; importantly, OGT protein expression was increased while OGA protein expression was decreased [194]. The uncoupling of OGA expression to *O*-GlcNAc homeostasis could be an indicator of cancer progression and suggests that an increase of OGA protein expression would be beneficial therapeutically. Determining how *O*-GlcNAc regulates OGA expression and transcription will be crucial for understanding the biology of *O*-GlcNAcylation and how *O*-GlcNAc homeostasis is disrupted in disease.